

# DISSERTATION

submitted to the  
Combined Faculties for the Natural Sciences and for Mathematics  
of the Ruperto-Carola University of Heidelberg, Germany  
for the degree of  
Doctor of Natural Sciences

presented by  
Dipl.-Phys. Jochen Dingfelder  
born in Saarbrücken

Oral examination: 22. January 2003



**Search for Anomalous Production  
of Single Top Quarks  
with the H1 Experiment at HERA**

Referees: Prof. Dr. Franz Eisele  
Prof. Dr. Christof Wetterich



## Kurzfassung

Eine Suche nach der Produktion einzelner Top-Quarks durch flavor-ändernde neutrale Ströme in  $ep$ -Kollisionen wird vorgestellt. Die Suche ist motiviert durch die Beobachtung von Ereignissen mit dem H1-Detektor, die ein isoliertes Lepton sowie einen hohen fehlenden und einen hohen hadronischen Transversalimpuls aufweisen. Die Häufigkeit und Topologie dieser Ereignisse ist mit Standardmodellprozessen nur schwer in Einklang zu bringen. Das Ziel dieser Arbeit ist eine umfassende Suche nach der Produktion von Top-Quarks. Zerfälle des Top-Quarks in ein  $b$ -Quark und ein  $W$  Boson werden sowohl für leptonische als auch für hadronische Zerfallsmoden des  $W$ -Bosons untersucht. Die Trennung des Top-Signals vom Standardmodelluntergrund erfolgt mittels einer multivariaten Analyse. Die gesamten mit dem H1-Experiment aufgenommenen HERA I Daten, entsprechend einer integrierten Luminosität von  $118 \text{ pb}^{-1}$ , werden untersucht. Als Resultat dieser Analyse wird gefunden, daß ein Teil der beobachteten Leptonereignisse kinematisch deutlich besser zu Top-Produktion als zu Standardmodellprozessen paßt. Anomale Top-Produktion müßte auch an einer Erhöhung der beobachteten Ereignisrate mit hadronischen  $W$ -Zerfällen sichtbar sein. Es wird keine signifikante Abweichung vom Standardmodelluntergrund beobachtet. Die Kombination aller Zerfallskanäle in einer Likelihoodanpassung ergibt einen Wirkungsquerschnitt für die Produktion einzelner Top-Quarks von  $0.31^{+0.16}_{-0.15} \text{ pb}$  bei  $\sqrt{s} = 320 \text{ GeV}$ . Diese Kombination liefert eine deutlich bessere Beschreibung der Daten als das Standardmodell alleine. Aufgrund der momentan noch kleinen Anzahl von Top-Kandidaten wird auch eine Ausschlußgrenze für den Wirkungsquerschnitt der Top-Produktion und für die Stärke der flavor-ändernden Kopplung ermittelt. Für die  $tu\gamma$ -Kopplungskonstante ergibt sich  $\kappa_{tu\gamma} < 0.25$  mit 95% CL. Dieses Resultat verbessert die existierenden Ausschlußgrenzen anderer Experimente bei LEP und am TeVatron.

## Abstract

A search for single top quark production mediated by flavor changing neutral currents in  $ep$  collisions is presented. The search is motivated by the observation of events with an isolated lepton, missing transverse momentum and large hadronic transverse momentum in the H1 detector. The rate and topology of these events is found to be unlikely for Standard Model processes. The goal of this thesis is a comprehensive search for top quarks. Decays of top quarks in a  $b$ -quark and a  $W$  boson are searched for in both the leptonic and the hadronic decay modes of the  $W$ . The top signal is discriminated from Standard Model background processes in a multi-variate analysis. The full HERA I data set taken with the H1 detector is used, corresponding to an integrated luminosity of  $118 \text{ pb}^{-1}$ . As a result of this analysis, it is found that a part of the observed lepton events is kinematically more consistent with top production than with Standard Model processes. Anomalous top production should also be visible as an increased event rate for hadronic  $W$  decays. No significant deviation from the Standard Model background is observed. The combination of all decay channels in a likelihood fit yields a cross-section for single top production of  $0.31^{+0.16}_{-0.15} \text{ pb}$  at  $\sqrt{s} = 320 \text{ GeV}$ . This combination gives a much better description of the data than the Standard Model alone. Due to the presently small number of top candidates, also an exclusion limit is set on the single top production cross-section and the flavor changing neutral current coupling. An upper limit on the  $tu\gamma$ -coupling of  $\kappa_{tu\gamma} < 0.25$  at 95% CL is established, which extends into a region of parameter space not excluded by other experiments at LEP and TeVatron.



*For my parents  
and my brother*





# Contents

<b>1</b>	<b>Introduction</b>	<b>1</b>
<b>2</b>	<b>Theoretical Overview</b>	<b>3</b>
2.1	Introduction to Single Top Production . . . . .	3
2.2	FCNC Top Production at HERA . . . . .	7
2.2.1	Kinematics of $ep$ Scattering . . . . .	8
2.2.2	Kinematics of Top Production at HERA . . . . .	8
2.2.3	Cross-Section . . . . .	9
2.2.4	Top Quark Decays . . . . .	10
2.3	Standard Model Background Processes . . . . .	11
2.3.1	$W$ Production . . . . .	11
2.3.2	Lepton-Pair Production . . . . .	14
2.3.3	Deep Inelastic Scattering . . . . .	14
2.3.4	Photoproduction . . . . .	17
2.3.5	Multi-Jet Production . . . . .	18
2.4	Monte Carlo Generators . . . . .	19
<b>3</b>	<b>The H1 Experiment at HERA</b>	<b>21</b>
3.1	The HERA Collider . . . . .	21
3.2	The H1 Detector . . . . .	22
3.2.1	H1 Coordinate System . . . . .	23
3.2.2	Calorimetry . . . . .	24
3.2.3	The Inner Tracking System . . . . .	27
3.2.4	The Muon System . . . . .	29
3.2.5	Time-of-Flight Detectors . . . . .	30
3.2.6	Luminosity System . . . . .	30
3.3	Trigger and Data Acquisition . . . . .	31
3.4	Detector Simulation . . . . .	32
<b>4</b>	<b>General Data Pre-Selection</b>	<b>33</b>
4.1	Run Selection and Detector Status . . . . .	33
4.2	Event Vertex . . . . .	34
4.3	Data Sets and Luminosities . . . . .	34
4.4	Non- $ep$ Background Rejection . . . . .	34

<b>5</b>	<b>Lepton Identification and Hadronic Reconstruction</b>	<b>37</b>
5.1	Lepton Identification . . . . .	37
5.1.1	Electron Candidates . . . . .	37
5.1.2	Muon Candidates . . . . .	39
5.2	Hadronic Final State Reconstruction . . . . .	40
5.2.1	Combination of Tracks and Clusters . . . . .	40
5.2.2	Jet Algorithm . . . . .	41
5.2.3	Hadronic Calibration . . . . .	42
<b>6</b>	<b>Top Search in the Semi-Leptonic Decay Channel</b>	<b>45</b>
6.1	“Isolated Leptons” at HERA . . . . .	45
6.2	Isolated Lepton Selection and $W$ Production . . . . .	46
6.2.1	Pre-Selection . . . . .	47
6.2.2	Backgrounds to $W$ Production . . . . .	48
6.2.3	Selection of Events with $W$ Bosons . . . . .	50
6.3	How Likely is the Excess at high $P_T^X$ ? . . . .	59
6.4	Kinematic Reconstruction of Top Decays . . . . .	63
6.4.1	Reconstruction of the Neutrino . . . . .	65
6.4.2	Reconstruction of the $b$ -Jet and the Top Mass . . . . .	69
6.5	Observables to Discriminate Top and $W$ Production . . . . .	73
6.5.1	Choice of Observables . . . . .	73
6.5.2	Possibility of $b$ -Quark Identification . . . . .	78
6.5.3	Shape Analysis . . . . .	78
6.6	Cut-Based Search for Top Quarks . . . . .	80
6.6.1	Definition of the Cuts . . . . .	81
6.6.2	Systematic Uncertainties and Results . . . . .	81
6.7	Likelihood Discriminator . . . . .	84
6.7.1	Likelihood Method . . . . .	85
6.7.2	Approximation of Correlations . . . . .	86
6.7.3	Performance and Results . . . . .	88
6.8	Summary . . . . .	93
<b>7</b>	<b>Top Search in the Hadronic Decay Channel</b>	<b>97</b>
7.1	Pre-Selection of Multi-Jet Events . . . . .	97
7.1.1	Standard Model Background and Background Normalization . . . . .	98
7.1.2	Control Distributions . . . . .	99
7.2	Selection of Events with High $E_T$ and a $W$ Candidate . . . . .	100
7.3	Observables to Discriminate Top and QCD Background . . . . .	103
7.4	Cut-Based Top Search . . . . .	106
7.4.1	Definition of the Cuts . . . . .	106
7.4.2	Systematic Uncertainties . . . . .	107
7.4.3	Results . . . . .	109
7.5	Likelihood Discriminator . . . . .	110
7.5.1	Application of the Likelihood Method . . . . .	111
7.5.2	Results and Comparison to Cut-Based Analysis . . . . .	111
7.6	Summary . . . . .	113

<b>8</b>	<b>Statistical Evaluation of the Likelihood Analyses</b>	<b>115</b>
8.1	Maximum-Likelihood Fit of the Top Signal . . . . .	115
8.1.1	Description of the Maximum-Likelihood Fit . . . . .	115
8.1.2	Results of the Maximum-Likelihood Fit . . . . .	117
8.1.3	Inclusion of Systematic Errors . . . . .	118
8.1.4	Combination of Channels . . . . .	121
8.1.5	Compatibility of Semi-Leptonic and Hadronic Channels . . . . .	122
8.2	Probability of the Top Interpretation . . . . .	124
8.3	Exclusion Limit on Top Cross-Section and FCNC Coupling . . . . .	125
8.4	Comparison with Other Experiments . . . . .	129
8.4.1	Single Top at TeVatron . . . . .	129
8.4.2	Single Top at LEP . . . . .	129
8.4.3	Isolated Leptons and Single Top at ZEUS . . . . .	130
8.4.4	Outlook for FCNC Single Top Production . . . . .	131
8.5	Summary . . . . .	132
<b>9</b>	<b>Summary and Outlook</b>	<b>135</b>
<b>A</b>	<b>Event Displays of Isolated Leptons at High Hadronic <math>P_T</math></b>	<b>139</b>
<b>B</b>	<b>Spin Correlations in Top Quark Decays</b>	<b>145</b>
<b>C</b>	<b>Transformed Observables and Correlation Matrices</b>	<b>147</b>
C.1	Electron Channel . . . . .	148
C.2	Muon Channel . . . . .	149
C.3	Hadronic Channel . . . . .	150
<b>D</b>	<b>Discriminating Observables after Cut on the Lepton Charge</b>	<b>151</b>
<b>E</b>	<b>Event Displays of Top Candidates in the Hadronic Channel</b>	<b>153</b>
<b>F</b>	<b>Study of Systematic Uncertainties for the Signal Fit</b>	<b>156</b>
F.1	Hadronic Channel . . . . .	156
F.2	Electron Channel . . . . .	157
F.3	Muon Channel . . . . .	158
	<b>List of Figures</b>	<b>161</b>
	<b>List of Tables</b>	<b>164</b>
	<b>Bibliography</b>	<b>165</b>
	<b>Acknowledgements</b>	<b>173</b>



# Chapter 1

## Introduction

Over the last four decades, experiments at colliders with high energies have made major contributions to particle physics. At the highest energies available at the time, new fundamental particles have been discovered. In the 1970's, *charm*- and *beauty*-flavored particles were produced and detected in electron-positron collisions for the first time. 1983 was marked by the discovery of the electroweak gauge bosons  $W^\pm$  and  $Z^0$  in proton-antiproton collisions. The latest landmark discovery was made in 1994, when the heaviest elementary particle known to date, the *top* quark, was found in proton-antiproton collisions.

On the theoretical side, this period of particle discoveries was accompanied by the development and elaboration of the so-called Standard Model (SM) of particle physics. In this model, the basic constituents of matter, leptons and quarks, interact via the exchange of gauge bosons: photons,  $W^\pm$ ,  $Z^0$  bosons and the gluons, representing the electroweak and strong forces, respectively. The Standard Model has been extremely successful in describing all experimental data up to this day (except for the neutrino masses, which are now known to be non-zero). Still it is generally believed that it cannot be the ultimate theory of particle physics. The many free parameters of this theory, coupling constants and masses, are considered as rather annoying in a fundamental theory. The belief that the Standard Model is just an effective theory, valid only at the experimental energies accessible today, is widespread. At higher energies it may have to be replaced by a theory with higher degrees of symmetry and less free parameters.

The top quark with its extremely large mass of about 175 GeV (more than 30 times heavier than the second heaviest quark, the beauty quark with 4.5 GeV) could play a crucial role for the discovery of new physics at large energy scales. In several proposed extensions to the Standard Model, signs of new physics are expected first in the top sector. Up to now only about 100 top quarks have been observed at the TeVatron proton-antiproton collider. The observation of top quarks at other existing collider experiments would be a surprise because the predicted Standard Model rates for single top production are negligibly small. Production mechanisms beyond the Standard Model would therefore have to be involved in order to observe top quarks.

The HERA collider at DESY in Hamburg is the only existing electron-proton collider to date. With its center-of-mass energy of 320 GeV, it is one of the few facilities in the world on the high energy frontier of particle physics. The available center-of-mass

energy is kinematically sufficient for the production of single top quarks. Single top production might be possible in flavor changing neutral current (FCNC) interactions, where an up or charm quark coming from the proton is converted into a top quark by interaction with a photon or  $Z^0$  boson emitted from the electron. In the Standard Model, FCNC processes proceed only at loop level, and thus are strongly suppressed. However, several interesting extensions of the Standard Model would allow a detectable rate for single top production in FCNC interactions. Top production at HERA leads to spectacular experimental signatures from top quark decays. The top quark decays almost always into a beauty quark and a real  $W^+$  boson. This  $W^+$  boson decays leptonically into  $e^+\nu_e$ ,  $\mu^+\nu_\mu$ ,  $\tau^+\nu_\tau$  or hadronically into  $q\bar{q}'$ . For the leptonic  $W$  decay channel, an isolated lepton with high transverse momentum is expected in the detector. The escaping neutrino would cause a large missing momentum in the detector. It is very exciting that candidate events with this signature have been observed. They will be discussed in detail in this thesis.

The subject of this thesis is the investigation of single top quark production at HERA as seen in the H1 detector. All  $W$  boson decay channels mentioned above, except the tau channel, are investigated separately. Methods for the suppression of Standard Model background mimicking signatures of top quark decays are developed and applied, using multi-variate techniques. The obtained results are evaluated on a statistical basis, exploiting the different shapes of discriminating observables. The probability of a contribution from single top production in the data is studied.

Preliminary results of this single top analysis have been reported in [1, 2].

This thesis is organized as follows:

- Chapter 2 gives a theoretical overview of single top production within and beyond the Standard Model. Also relevant Standard Model background processes are introduced.
- Chapter 3 introduces the H1 experiment and the HERA collider.
- Chapter 4 presents preparatory steps of the data analysis. A general data pre-selection ensuring a reasonable data quality for all later selection steps is performed.
- Chapter 5 explains the identification of leptons and hadronic jets in the H1 detector.
- Chapters 6 and 7 constitute the main part of the data analysis. The single top search in the semi-leptonic and the hadronic decay channels of the top quark are discussed. These chapters describe the complete event selection. A focus lies on maximizing the sensitivity to a possible top signal, e.g. by using a likelihood analysis.
- Chapter 8 presents the statistical evaluation of the likelihood analysis. The results are compared to single top searches at other experiments.
- Chapter 9 summarizes the results and gives an outlook.
- The appendix gives supportive information for different analysis steps and contains graphical displays of interesting data events.

# Chapter 2

## Theoretical Overview

In this chapter, the theoretical foundations for the single top analysis are presented. In the first part, some properties of the top quark and the production of single top quarks at HERA within and beyond the Standard Model are discussed. In the second part, all relevant background processes to single top production are introduced. Finally, the Monte Carlo generators used to simulate signal and background processes are presented.

### 2.1 Introduction to Single Top Production

Since its discovery in  $p\bar{p}$  collisions at the TeVatron in 1994 [3, 4], the top quark has attracted considerable attention both from the theoretical and the experimental point of view. There are several reasons for this. The top quark is the heaviest of all elementary particles observed until today. The currently most precise determination of the top mass is  $174.3 \pm 5.1 \text{ GeV}^1$  [5], measured directly in decays of pair-produced top quarks at the TeVatron. Due to the large top mass close to the electroweak symmetry breaking (EWSB) scale, the properties of the top quark could reveal information on the nature of EWSB, address questions in flavor physics or provide insight to new physics originating at a higher mass scale. Another consequence of its large mass is that the top quark decays rapidly ( $\tau \sim 10^{-24} \text{ s}$ ) before hadronization takes place and top-flavored meson states can form. Hence the top quark allows a determination of the properties of the quark itself, which is not possible for any of the lighter quarks. For instance, spin correlations in top decays  $t \rightarrow bW$  can be studied without any disturbances from fragmentation. It is widely believed that deviations from the Standard Model might be first observed in the top sector.

The production of  $t\bar{t}$  pairs is at present only possible at the TeVatron with its large center-of-mass energy of 1.8 TeV. However, the center-of-mass energies of the HERA and LEP colliders lie above the top production threshold and would thus kinematically allow the production of single top quarks. However, the expected rates for single top production in the Standard Model are extremely low. The single top cross-section in  $e^+e^-$  collisions at LEP was estimated to be of the order  $\mathcal{O}(10^{-4}) \text{ fb}$  [74] and thus totally negligible. At the TeVatron, the single top cross-section is 1.7 pb (0.7 pb) for  $W$ -gluon

---

<sup>1</sup>Natural units are used throughout this thesis ( $c = 1, \hbar = 1$ ). As a result, energies and momenta are given in GeV.

fusion ( $W^*$ ) processes [6], but still not large enough to be sensitive with the currently accumulated luminosity.

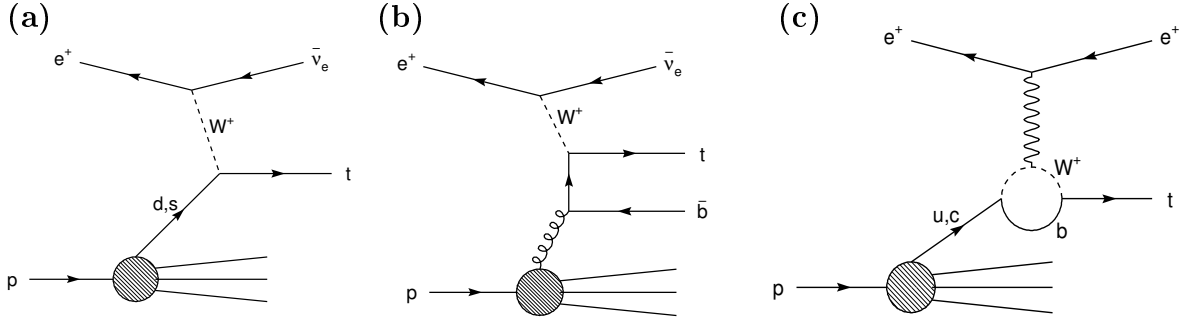


Figure 2.1: Example diagrams for Standard Model single top production at HERA. (a) Charged current process with the  $W$  coupling to a light down-type quark ( $d, s$ ) in the proton, (b) charged current process involving a  $b$ -quark, (c) flavor changing neutral current process at loop-level (penguin).

In electron-proton collisions at HERA, single top quarks could be produced via  $W$  exchange (charged current) or via photon or  $Z$  exchange (neutral current) according to the diagrams in figure 2.1.

- *Charged current top production at HERA:*

Two possible diagrams for single top production via  $W$  exchange at HERA are shown in figure 2.1 (a) and (b). The cross-sections for these charged current processes were estimated using the CompHEP [8] program. The cross-section for process (a) is of the order  $\mathcal{O}(10^{-2} \text{ fb})$  for the couplings of the  $W$  to either a  $d$ - or a  $s$ -quark in the proton. It is suppressed by the respective CKM matrix elements, since a transition between a quark in the first or second generation ( $d$ - or  $s$ -quark) to the third generation ( $t$ -quark) is involved. Process (b), which involves a  $b$ -quark, has a significantly larger cross-section, since the CKM matrix element  $|V_{tb}|$  is approximately one. It is of the order  $\mathcal{O}(1 \text{ fb})$ , which is however still too small to produce an observable rate of top events. Altogether, the production of  $\approx 0.1$  single top event is expected in the data collected with the H1-experiment so far.

- *Neutral current top production at HERA:*

In order to produce a top quark via exchange of a neutral gauge boson, the neutral current would have to induce a change of flavor of the struck quark in the proton ( $u \rightarrow t$  or  $c \rightarrow t$ ). In the Standard Model, processes with flavor changing neutral currents (FCNC) can only arise via higher order radiative corrections, and are highly suppressed. Hence FCNC top production in the Standard Model is negligible. An example diagram for such a process at loop-level is shown in figure 2.1 (c).

Due to the large suppression in the Standard Model, single top production offers a high sensitivity to new physics. An observation of single top quarks would unambiguously signal the presence of new physics.



To allow for single top production beyond the Standard Model, an enhancement of FCNC interactions would be needed. Flavor changing neutral current interactions can be described by using a model-independent effective Lagrangian. This effective Lagrangian contains operators in an expansion series in powers of  $1/\Lambda$ , where  $\Lambda$  denotes the characteristic mass scale for the new interactions [9, 10]. The effective Lagrangian is added to the Standard Model Lagrangian:

$$\mathcal{L} = \mathcal{L}_{\text{SM}} + \mathcal{L}_{\text{eff}} = \mathcal{L}_{\text{SM}} + \frac{1}{\Lambda} \mathcal{L}_1 + \frac{1}{\Lambda^2} \mathcal{L}_2 + \dots, \quad (2.1)$$

where  $\mathcal{L}_1, \mathcal{L}_2, \dots$  are Lagrangian's containing new interactions with operators of dimension five, six,  $\dots$ .

In this thesis, the most general effective Lagrangian, proposed in [9], is considered which describes tree-level FCNC top quark interactions involving electroweak bosons. It can be written as follows:

$$\mathcal{L}_{eff} = \sum_{U=u,c} i \frac{e e_U}{\Lambda} \bar{t} \sigma_{\mu\nu} q^\nu \kappa_{\gamma,U} U A^\mu \quad (2.2)$$

$$+ \frac{g}{2 \cos \theta_W} \bar{t} \left[ \gamma_\mu (v_{Z,U} - a_{Z,U} \gamma^5) + i \frac{1}{\Lambda} \sigma_{\mu\nu} q^\nu K_{Z,U} \right] U Z^\mu + \text{h.c.}, \quad (2.3)$$

where  $\sigma_{\mu\nu} = (i/2) [\gamma^\mu, \gamma^\nu]$ ,  $\theta_W$  is the Weinberg angle,  $q$  the four-momentum of the exchanged boson,  $e$  and  $g$  denote the gauge couplings relative to the gauge groups with  $U(1)$  and  $SU(2)$  symmetries respectively,  $e_U$  denotes the electric charge of up-type quarks,  $A^\mu$  and  $Z^\mu$  the fields of the photon and  $Z$  boson. The scale up to which the effective theory is assumed to hold is given by the parameter  $\Lambda$ . By convention,  $\Lambda$  is set to the mass of the top quark ( $\Lambda = m_t$ ). The FCNC couplings of the top quark are the magnetic couplings  $\kappa_{\gamma,U}$  ( $K_{Z,U}$ ) to an up-type quark  $U = u, c$  and a photon ( $Z$  boson) and the vector (axial vector) couplings  $v_{Z,U}$  ( $a_{Z,U}$ ) to an up-type quark  $U = u, c$  and a  $Z$  boson.

The above Lagrangian could be the effective, low-energy theory of a more fundamental theory. Examples of theories extending the Standard Model and leading to enhanced FCNC top interactions are :

- *Models with dynamical symmetry breaking:*

Models with dynamical breaking of certain symmetries can lead to an enhancement of FCNC couplings [11]. When the electroweak symmetry is dynamically broken, providing a dynamical mechanism for the mass generation, non-diagonal (vector) couplings to the  $Z$  naturally appear. Couplings to massless bosons might also be generated, for example in models where the mass hierarchy arises from the breaking of a larger symmetry, e.g.  $SU(3)_L \times SU(3)_R$ . This was considered in [12], where the possibility of anomalous single top production at HERA was first pointed out.

- *Two-(Multi-)Higgs-Doublet models:*

In model with two or more Higgs doublets, FCNC couplings can occur at tree-level [14]. An example diagram is shown in 2.2 (a) with couplings of a flavor

changing Higgs boson to a  $c$ -quark and to a  $u$ -quark or a top quark. This diagram thus represents an effective FCNC coupling.

- *Supersymmetry:*

New couplings of sparticles to Standard Model particles can produce effective FCNC couplings. In the Minimal Supersymmetric Standard Model (MSSM), the enhancements of FCNC couplings are probably not large enough to allow an observation of single top production [9]. In supersymmetric models with R-parity violation, some enhancement might be possible [15, 16]. An example is shown in figure 2.2 (b), where the effective FCNC coupling arises via a product of R-parity violating couplings  $\lambda'_{i1k} \times \lambda'_{i3k}$  of a slepton ( $i^{\text{th}}$  generation) to Standard Model quarks ( $k^{\text{th}}$  generation) and to an up or top quark.

- *Models with exotic quarks:*

Exotic quark singlets appear in many grand unified and string theories [17]. Single top production can be enhanced by mixing with these singlet quarks. If the exotic quarks are heavy, no new particles would be observed in top decays, if their masses lie above the top threshold (the same argument holds of course for supersymmetric particles or any other new heavy particles).

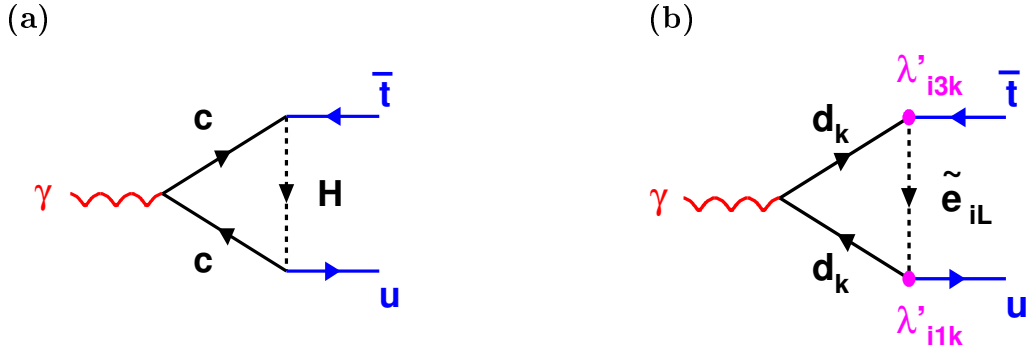


Figure 2.2: Example diagrams of processes with effective FCNC couplings. These effective couplings can for instance be produced by exchange of a flavor changing Higgs boson (a) or exchange of a slepton (b).

The enhancement of FCNC couplings can experimentally be tested by studying the production rate or the decay branching ratios of top quarks. For example, the CDF Collaboration searched for rare top decays into a light quark and a photon or  $Z$  boson and set the following exclusion limits at 95% CL [18]:

$$BR(t \rightarrow u\gamma) + BR(t \rightarrow c\gamma) < 3.2\% \quad (2.4)$$

$$BR(t \rightarrow uZ) + BR(t \rightarrow cZ) < 33\% \quad (2.5)$$

This limit can be compared to the size of the branching ratios for  $t \rightarrow cV$  ( $V = \gamma, Z$ ) predicted by the above mentioned models, as given in table 2.1. These estimates give an impression of the enhancement of flavor changing neutral current couplings expected in various theoretical models. Branching ratios up to about 1% seem to be possible in some theories.

Theoretical Model	$BR(t \rightarrow cV)$
Standard Model	$\sim 10^{-13} - 10^{-12}$
Two-Higgs-Doublet Models	$\sim 10^{-9} - 10^{-8}$
Supersymmetry	$\sim 10^{-9} - 10^{-8}$
Multi-Higgs-Doublet Models	$\sim 10^{-6} - 10^{-5}$
Singlet Quarks	$\sim 10^{-2}$
Dynamical EWSB	$\sim 10^{-2}$

Table 2.1: Estimates of the branching ratios for decays  $t \rightarrow cV$  ( $V = \gamma, Z$ ) in different models with flavor changing neutral current interactions [9].

## 2.2 FCNC Top Production at HERA

With a sizeable FCNC coupling, single top production at HERA may proceed in a process as shown in figure 2.3. The top search in this analysis does not rely on any assumptions concerning the underlying theory and a priori allows all flavor changing couplings to be present.

Top quarks could be produced by transforming an up-type quark ( $u, c$ ) in the proton into a top quark via photon exchange with an anomalous coupling  $\kappa_\gamma$ . In diagram 2.3 only a coupling to the photon is shown, but also a coupling to the  $Z$  boson is possible. Before we further discuss the characteristics of this process, it is useful to give a brief introduction to the kinematics of  $ep$  scattering.

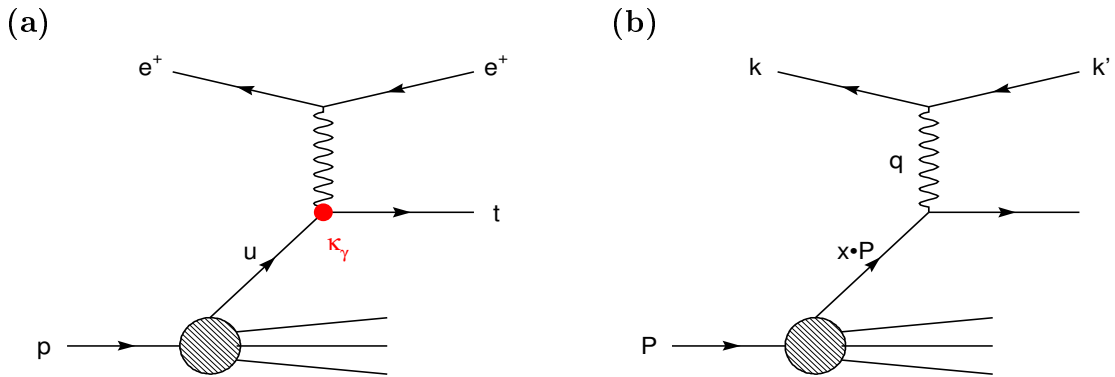


Figure 2.3: (a) Feynman diagram of FCNC top production at HERA with an anomalous coupling  $\kappa_\gamma$  of the top quark to an  $u$ - or  $c$ -quark and a photon. In (b) the same diagram is shown, but labeled with the corresponding momentum four-vectors of the particles.

### 2.2.1 Kinematics of $ep$ Scattering

The following four-vectors are used for the different particles involved in the scattering process (see figure 2.3 (b)):

- $k$ : incoming electron  $e$
- $k'$ : outgoing electron  $e'$  (neutrino  $\nu_e$ )
- $P$ : incoming proton  $p$
- $q$ : exchanged gauge boson  $\gamma, Z (W)$

The center-of-mass energy of the electron-proton system (neglecting the electron and proton masses) is given by:

$$\sqrt{s} = \sqrt{(k + P)^2} \approx \sqrt{4E_e^0 E_p} = 320 \text{ (300) GeV} \quad \text{at HERA} . \quad (2.6)$$

The four-momentum transfer in the  $ep$  scattering is:

$$q = k - k' . \quad (2.7)$$

The following set of lorentz-invariant variables is commonly used to describe the kinematics of  $ep$  scattering:

$$Q^2 = -q^2 \quad (2.8)$$

$$x = \frac{Q^2}{2Pq} \quad (2.9)$$

$$y = \frac{Pq}{Pk} . \quad (2.10)$$

The quantity  $Q^2$  is the negative four-momentum transfer squared and corresponds to the *virtuality* of the exchanged gauge boson. The quantities  $x$  and  $y$  are the dimensionless Björken scaling variables, that take on values between 0 and 1. The scaling variable  $x$  is the fractional momentum of the proton that the struck quark in the proton carries. The scaling variable  $y$  corresponds to the relative energy transfer to the proton in its rest frame, i.e. the *inelasticity* of the scattering process.

The kinematic variables  $x, y, Q^2, s$  are connected with each other according to the following relation:

$$Q^2 = xys . \quad (2.11)$$

Hence for a given center-of-mass energy  $\sqrt{s}$ , the kinematics of deep inelastic scattering is uniquely determined by only two variables.

### 2.2.2 Kinematics of Top Production at HERA

We now come back to the discussion of the process in figure 2.3 (a). In single top production via a flavor changing neutral current, the contribution from  $Z$  exchange in the  $t$ -channel is suppressed due to the large mass of the propagator. Hence the

cross-section is dominated by photon exchange. The anomalous magnetic and vector couplings to the  $Z$  boson are neglected in the following.

In order to produce the large top quark mass<sup>2</sup> of 175 GeV, the quark that interacts with the exchanged boson must carry a large momentum fraction  $xP$ . Also the electron must give away a large fraction of its energy. The center-of-mass energy of the photon-quark system,  $\sqrt{\hat{s}}$ , has to be greater than the top quark mass:

$$\sqrt{\hat{s}} = \sqrt{xy s} \approx \sqrt{4xy E_e^0 E_p} > 175 \text{ GeV} \Rightarrow xy > 0.3 . \quad (2.12)$$

As a result, both  $x$  and  $y$  must have values above 0.3. Figure 2.4 shows distributions of the kinematical variables  $Q^2, x, y$  for generated single top events. For these large values of  $x$  (corresponding to quark momenta above  $\sim 280$  GeV), the contribution from sea quarks is very small. The sensitivity of HERA is naturally much higher for the coupling  $\kappa_{tu\gamma}$  than for  $\kappa_{tc\gamma}$  due to the larger  $u$ -valence-quark density compared to the  $c$ -quark density at large  $x$ . Therefore only single top production involving a coupling to the  $u$ -quark is considered here. Also the charge conjugate anti-top production in a  $\gamma - \bar{u}$  fusion process is strongly suppressed (by roughly a factor of 80 [8, 13]). It is thus shown that HERA has the largest sensitivity for the coupling of the top quark to an  $u$ -quark and a photon ( $\kappa_\gamma = \kappa_{tu\gamma}$ ).

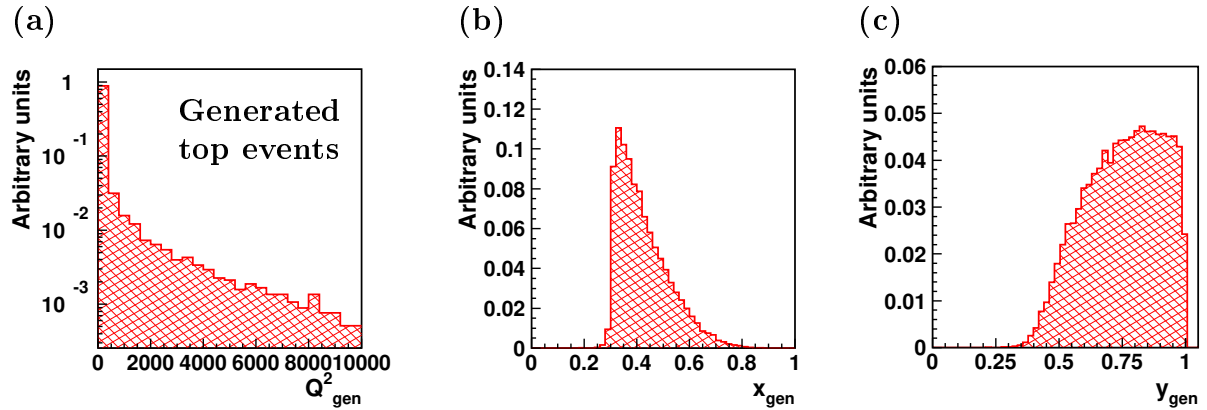


Figure 2.4: Kinematic distributions of generated single top events from FCNC top production at HERA.

### 2.2.3 Cross-Section

The calculation of the cross-section for the FCNC process presented in figure 2.3 was carried out using the CompHEP [8, 13] program. For a fixed value of the coupling strength of  $\kappa_{tu\gamma} = 0.1$ , the single top cross-section at  $\sqrt{s} = 320$  GeV is:

$$\sigma(et \rightarrow etX, \sqrt{s} = 320 \text{ GeV}) = 0.093 \text{ pb} . \quad (2.13)$$

This result includes next-to-leading order (NLO) corrections from a recent calculation published in [19], which increases the leading order cross-section by 25%. Figure 2.5

<sup>2</sup>Throughout this analysis, a central value for the top quark mass of 175 GeV is assumed.

shows the total cross-section obtained by the NLO calculation as a function of the  $ep$  center-of-mass energy and as a function of the top mass. A strong dependence of the cross-section on  $\sqrt{s}$  and  $m_t$  is seen. A variation of  $m_t$  by  $\pm 5\%$  causes about 20% uncertainty in the total cross-section. The 7% increase in  $\sqrt{s}$  from 300 GeV to 320 GeV (the two center-of-mass energies used at HERA between 1994 and 2000) leads to a 45% increase of the total cross-section.

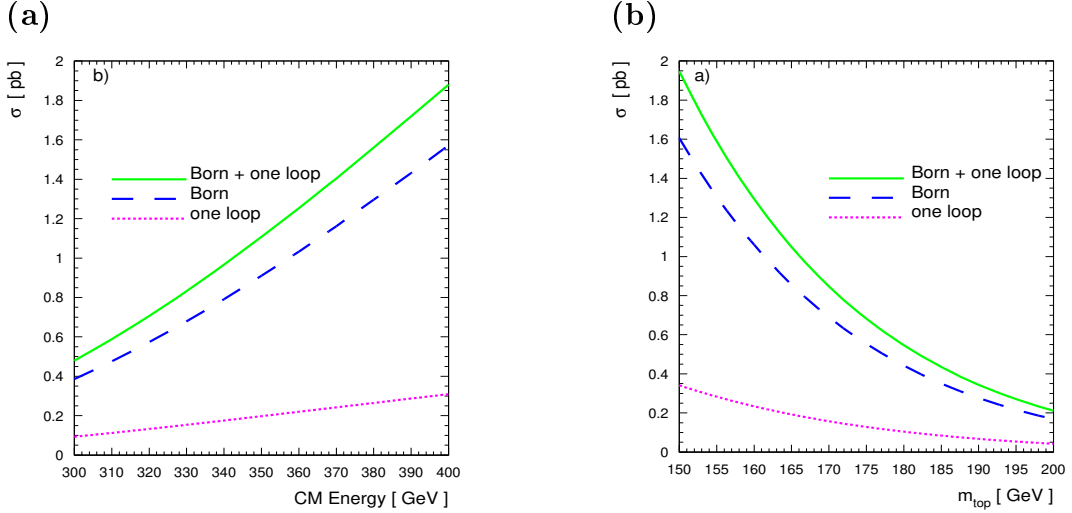


Figure 2.5: Born, one-loop, and Born+one-loop cross-section for the FCNC single top production as a function of the center-of-mass energy (a) and the top quark mass (b). The cross-section calculation uses the top mass as scale and a value of  $\kappa_{tu\gamma} = 0.1$ . Due to different conventions in the definition of the Lagrangian (and thus in  $\kappa_{tu\gamma}$ ), the absolute values of the cross-section cannot directly be compared to the result in equation 2.13. Taken from [19].

### 2.2.4 Top Quark Decays

In the Standard Model, the top quark decays almost to 100% into a  $b$ -quark and a  $W$  boson. The  $W$  boson decays either leptonically ( $W \rightarrow \ell \nu_\ell$ ) or hadronically ( $W \rightarrow q \bar{q}'$ ). The branching ratios of the top quark decays thus correspond to those of the  $W$  decays. They are summarized in table 2.2.

Decay mode	Branching ratio
$W \rightarrow e \nu_e$	10.7 %
$W \rightarrow \mu \nu_\mu$	10.6 %
$W \rightarrow \tau \nu_\tau$	10.7 %
$W \rightarrow q \bar{q}'$	68.0 %

Table 2.2: Branching ratios of the top quark and the  $W$  boson decays [5].

The signatures of top quark decays in the semi-leptonic decay channel ( $t \rightarrow b\ell\nu_\ell$ ) are a hadronic jet from the  $b$ -quark with high transverse momentum, a lepton and substantial missing transverse momentum due to the undetectable neutrino. In the hadronic decay channel ( $t \rightarrow bqq'$ ), three quark-jets with high transverse momentum are expected.

## 2.3 Standard Model Background Processes

The main background for single top quark decays with subsequent leptonic decay of the  $W$  boson ( $t \rightarrow bW \rightarrow b\ell\nu_\ell$ ) are processes that have a charged lepton<sup>3</sup> or a neutrino in the final state. For hadronic decays of the  $W$  ( $t \rightarrow bW \rightarrow bqq'$ ), processes which produce at least three energetic hadronic jets contribute to the background. All Standard Model processes that might lead to top-like final state topologies are discussed in the following, starting with the main background sources in the semi-leptonic channel.

### 2.3.1 $W$ Production

The dominant Standard Model process for the semi-leptonic decay channel of the top quark is the production of real  $W$  bosons. They can be produced in the processes:

$$e^\pm p \rightarrow e^\pm XW^\pm \quad \text{and} \quad e^\pm p \rightarrow \bar{\nu}^{(-)} XW^\pm ,$$

whereby the cross-section for the second process is an order of magnitude smaller compared to the first. Figure 2.6 shows a typical leading order diagram for Standard Model  $W$  production at HERA. Here a quark from the proton is scattered on the electron via photon or  $Z$  exchange, and in addition a  $W$  boson is radiated from the quark line. The radiation of an on-shell  $W$  from the quark is suppressed by the large mass of the  $W$ , therefore the cross-section for  $W$  production<sup>4</sup> is very small. The total cross-section amounts to 1.1 (1.3) pb [20] for electron-proton center-of-mass energies of 300 (320) GeV, which corresponds to the production of roughly 100  $W$  bosons in the currently available data at H1. The process is dominated by the exchange of low- $Q^2$  photons. The beam electron is scattered into the main detector in about 25% of events.

To calculate the full process  $ep \rightarrow eXW$ , seven diagrams must be taken into account in the leading order. They are shown in figure 2.8. Diagrams (a), (b) and (e) give the largest contribution to the amplitude. Diagram (e) contains a triple gauge boson coupling. In diagrams (c) and (d), the real  $W$  is radiated from the electron line. Their contribution is small due to the suppression by the two  $W$  propagators. Diagrams (f) and (g) contain off-shell  $W$ 's and are needed to ensure gauge invariance.

The experimental signatures of  $W$  production with subsequent decay  $W \rightarrow \ell\nu$  are a lepton with high transverse momentum and a substantial amount of missing transverse momentum due to the neutrino, which cannot be detected. In decays  $W \rightarrow qq'$ , two

<sup>3</sup>For simplicity, charged leptons are in the following referred to only as "leptons"  $\ell$ , in contrast to neutrinos  $\nu$ .

<sup>4</sup>In this thesis, the term " $W$  production" is frequently used as a short form for "Standard Model  $W$  production", which does not include the production of real  $W$  bosons in top decays.

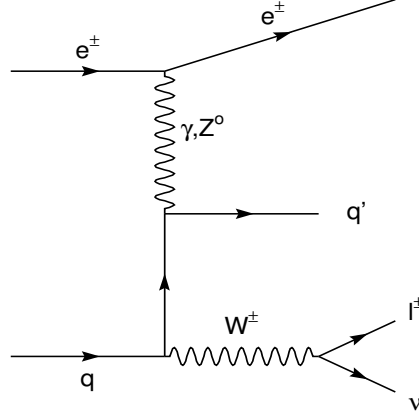


Figure 2.6: One of the dominant leading order diagrams for Standard Model  $W$  production at HERA.

hadronic jets are observed. In addition to the lepton and neutrino or the two jets, the struck quark from the proton can be seen as hadronic jet in the detector. This jet and the  $W$  decay products are expected to be well separated from each other, since they come from two different vertices in the diagram shown in figure 2.6.

The transverse momentum spectrum of the scattered quark falls off steeply, because  $W$  production is dominated by low momentum transfers and the radiation of the  $W$  boson does in general not lead to a large transverse momentum of the quark. For decays  $W \rightarrow \ell\nu$ , this is the main distinction between the signatures of  $W$  and single top production, since the transverse momentum distribution of the  $b$ -quark from the top decay has a Jacobian peak at  $\frac{m_t^2 - m_W^2}{2m_t} \sim 69$  GeV (see figure 2.7).

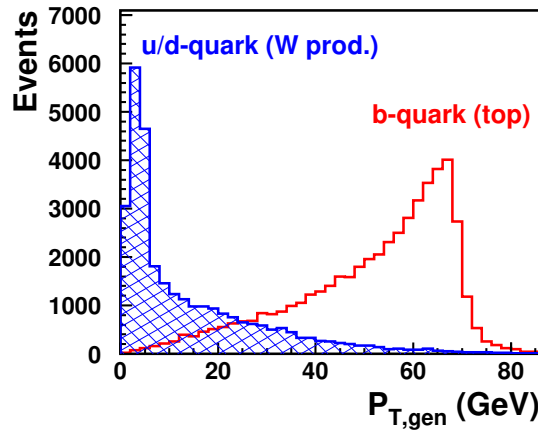
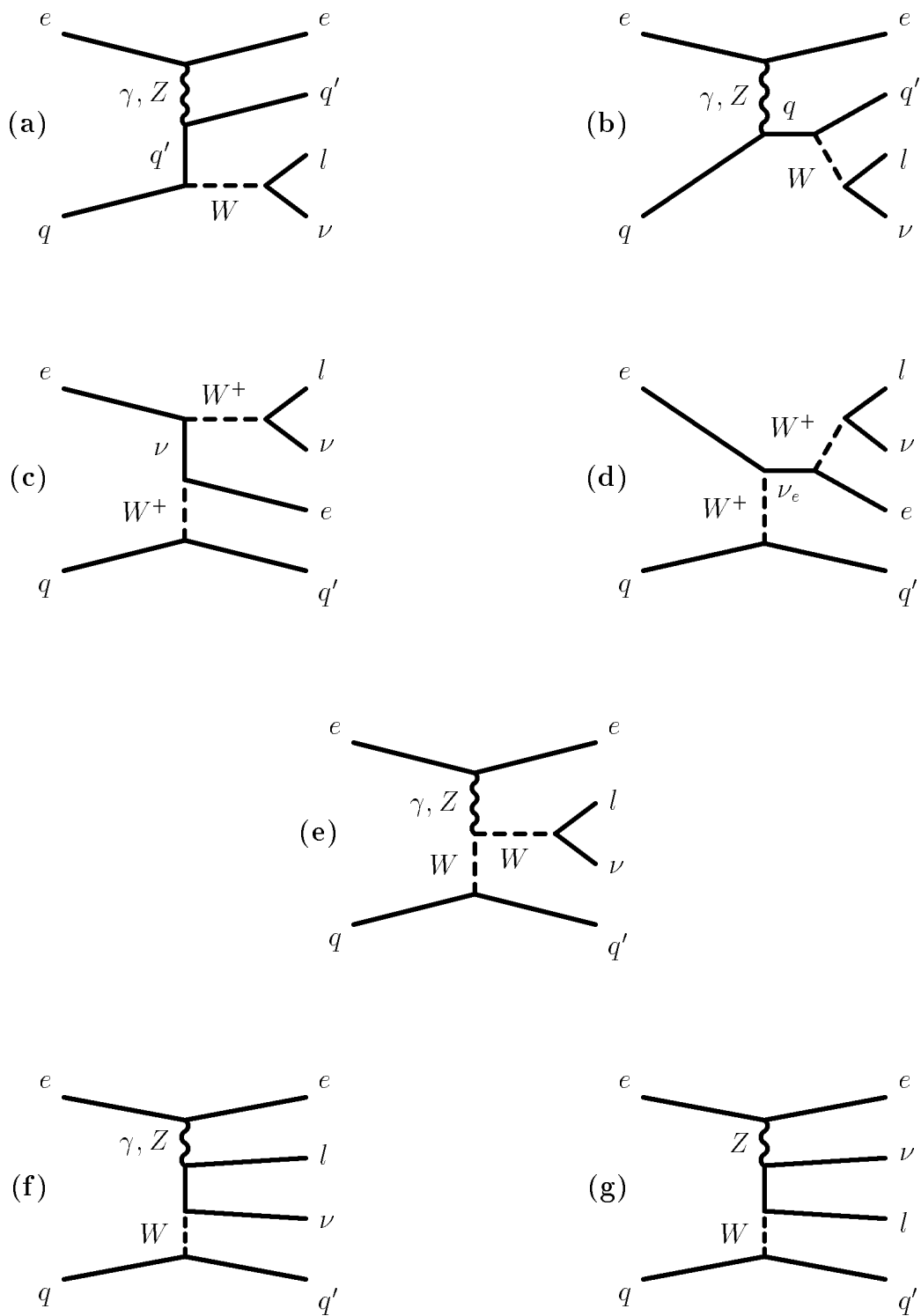


Figure 2.7: Generated transverse momentum distribution of the scattered  $u/d$ -quark in simulated  $W$  production events compared to the  $b$ -quark from simulated top decays.



Figure 2.8: Leading order diagrams for  $W$  production in the process  $eq \rightarrow eq' \ell \nu$ .

### 2.3.2 Lepton-Pair Production

The production of lepton pairs at HERA is mainly possible through photon-photon interactions. A quasi-real photon radiated from the electron interacts with a photon radiated from the proton. The two photons then produce a lepton-anti-lepton pair,  $ep \rightarrow e\ell^+\ell^-X$ . The dominant diagram for this process is shown in figure 2.9. The total photon-photon cross-section is large, but falls off very steeply with the transverse momenta of the produced leptons ( $\propto P_{T,\ell}^{-3}$ ).

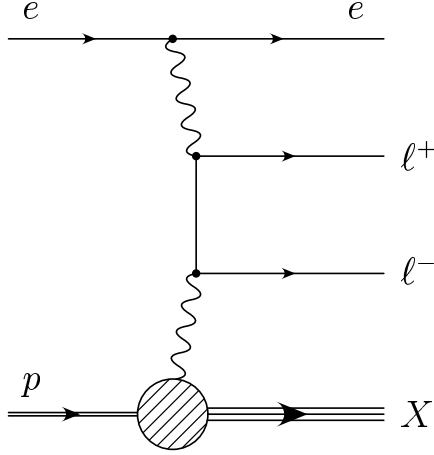


Figure 2.9: Dominant diagram for lepton pair production in photon-photon collisions.

The signatures of photon-photon collisions are in general two leptons with opposite charges. However, it can happen that only one lepton is detected, for instance if the other lepton is lost in the beam pipe. This is not unusual, since the polar angle distributions of the produced leptons have maxima for large and small polar angles, i.e. in the backward and forward regions. However, due to the steeply falling transverse momentum spectrum of the produced leptons, the background from photon-photon collisions for large lepton transverse momenta is rather small.

The interaction on the proton vertex can be elastic or inelastic. For inelastic processes, an additional hadronic jet ( $X$ ) formed by the scattered quark can be seen in the forward region of the calorimeter. For high momentum transfers on the electron side, the scattered electron is observed in the main detector.

### 2.3.3 Deep Inelastic Scattering

Electron-proton scattering via the exchange of a gauge boson, that has a virtuality large enough to resolve the substructure of the proton, is called *Deep Inelastic Scattering* (DIS). This is the case for momentum transfers  $Q^2 \approx 1 \text{ GeV}^2$ , corresponding to a spatial resolution of  $\approx 10^{-15}m$ . If the exchange boson is a photon or a  $Z$ , one speaks of *neutral current* (NC) DIS, if a  $W^\pm$  is exchanged, one calls it *charged current* (CC) DIS:

$$\text{NC} : \quad ep \rightarrow eX \quad (2.14)$$

$$\text{CC} : \quad ep \rightarrow \nu_e X . \quad (2.15)$$

Here  $X$  denotes the hadronic final state in the event. Figure 2.10 shows an illustration of a general DIS process.

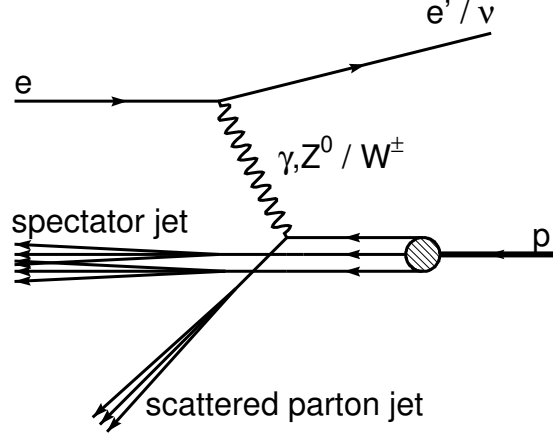


Figure 2.10: Illustration of deep inelastic electron-proton scattering.

In the *Quark-Parton-Model*, deep inelastic scattering is described as elastic scattering of the electron off a point-like constituent in the proton, a so-called *parton*. The partons are interpreted as the quarks in the proton. The struck quark is scattered into the detector. It fragments and forms a well-collimated jet. The remaining quarks, that do not participate in the hard scattering process, are called *spectator quarks*. They form the *proton remnant* (or *spectator jet*). The proton remnant usually disappears in the beam pipe, but can also be visible in the very forward region of the detector.

At HERA energies, photon exchange dominates the  $ep$  scattering cross-section.  $Z$  and  $W$  exchange contributes only at large  $Q^2$ , because the cross-section is suppressed by the large  $Z$  and  $W$  masses:

$$\frac{\sigma(Z, W^\pm)}{\sigma(\gamma)} \propto \frac{Q^2}{Q^2 + M_{Z, W^\pm}^2} \quad (2.16)$$

The double differential cross-sections for neutral and charged current DIS with respect to  $x$  and  $Q^2$  are given by:

**NC cross-section:**

$$\frac{d^2\sigma_{NC}(e^\pm p)}{dx dQ^2} = \frac{4\pi\alpha^2}{xQ^4} \left[ y^2 x F_1 + (1-y) F_2 \mp y(1-\frac{y}{2}) x F_3 \right] \quad (2.17)$$

**CC cross-section:**

$$\frac{d^2\sigma_{CC}(e^\pm p)}{dx dQ^2} = \frac{G_F^2}{2\pi} \left( \frac{M_W^2}{M_W^2 + Q^2} \right)^2 \left[ y^2 x F_1 + (1-y) F_2 \mp y(1-\frac{y}{2}) x F_3 \right] . \quad (2.18)$$

Here  $\alpha$  is the fine structure constant,  $G_F$  the Fermi constant, and  $F_1, F_2, F_3$  denote the proton structure functions. In the Quark-Parton-Model,  $F_1$  and  $F_2$  can be expressed as sum of the quark and anti-quark densities in the proton, and  $F_3$  as difference between the quark and anti-quark densities.

### Kinematic Reconstruction

As already mentioned in section 2.2.1, the complete kinematics of  $ep$  scattering can be described with only two variables for a fixed value of  $\sqrt{s}$ . Neutral current events are over-constrained, since the measurements of the electron and hadron energies and polar angles yield four variables. In charged current events, only the two variables of the hadronic final state can be measured. There are different methods to reconstruct the kinematic variables  $x, y, Q^2$ , for instance:

- *Electron method*: The kinematic variables are determined from the energy ( $E_e$ ) and the polar angle ( $\theta_e$ ) of the scattered electron:

$$Q_e^2 = 4E_e^0 E_e \cos\left(\frac{\theta_e}{2}\right) \quad , \quad y_e = 1 - \frac{E_e}{E_e^0}(1 - \cos(\theta_e)) \quad , \quad x_e = \frac{Q_e^2}{y_e s} \quad . \quad (2.19)$$

- *Hadron method (Jacquet-Blondel-method)*: The kinematic variables are reconstructed using the energy and the polar angle of the hadronic final state. First some quantities of the hadronic final state are introduced (the index  $h$  runs over all hadronic final state particles):

$$(E - P_z)_{had} = \sum_h (E_h - P_{z,h}) \quad , \quad P_T^{had} = \sqrt{\left(\sum_h P_{x,h}\right)^2 + \left(\sum_h P_{y,h}\right)^2} \quad (2.20)$$

$$\tan\left(\frac{\theta_{had}}{2}\right) = \frac{(E - P_z)_{had}}{P_T^{had}} \quad . \quad (2.21)$$

One obtains for the kinematic variables:

$$y_{JB} = \frac{(E - P_z)_{had}}{2E_e^0} \quad , \quad Q_{JB}^2 = \frac{(P_T^{had})^2}{1 - y_{JB}} \quad , \quad x_{JB} = \frac{Q_{JB}^2}{s y_{JB}} \quad . \quad (2.22)$$

A detailed description of further reconstruction methods can be found in [21]. The *double angle (DA) method* still deserves mentioning, since it is used for the energy calibration of the calorimeters in section 5.2.3. It uses the angles of the electron and the hadronic final state and is to first order independent of the calorimetric energy measurements.

The signatures of deep inelastic scattering are an electron and a jet for neutral current interactions and a jet with missing transverse momentum in the event for charged current interactions. The electron in neutral current events together with missing momentum caused for instance by fluctuations in the energy measurement can fake the signature of a  $W$  boson in the detector. Since the cross-section for neutral current DIS is large, it is a non-negligible background for top and  $W$  production. Also charged current events are important, since they already have a neutrino in the event. An additional lepton signature can be produced by misidentification of a hadron or photon as a lepton. However, as discussed before, the charged current cross-section is much smaller than the neutral current cross-section.

### 2.3.4 Photoproduction

*Photoproduction* ( $\gamma p$ ) is defined as interactions where the momentum transfer is approximately zero ( $Q^2 \approx 0$ ) and the exchanged photon is quasi-real. The scattered electron barely changes its direction and is lost in the beam pipe. At HERA, photoproduction and deep inelastic scattering can only be distinguished by the fact that the scattered electron is or is not detected. For value  $Q^2 > 2 \text{ GeV}^2$ , the electron can be seen in the main detector. If the electron is detected in the electron tagger,  $Q^2$  lies in the interval:

$$10^{-8} \text{ GeV}^2 < Q^2 < 0.01 \text{ GeV}^2 . \quad (2.23)$$

Photoproduction is the dominant process at HERA. It has a total cross-section of  $\sim 150 \mu\text{b}$ . The largest part of the cross-section comes from soft (low-energetic) interactions. However, also particles with high transverse momenta ( $P_T$ ) may be produced in photoproduction, allowing perturbative QCD calculations to be made using the high  $P_T$  as a hard scale for the process.

#### Equivalent Photon Approximation

In the limit  $Q^2 \rightarrow 0$ ,  $ep$  scattering can be reduced to a photon-proton interaction. The variable  $y$  then obtains a simple meaning. According to equation 2.19,  $y$  becomes:

$$y \approx 1 - \frac{E_e}{E_e^0} = \frac{E_\gamma}{E_e^0} , \quad (2.24)$$

i.e. it is the fraction of the electron energy that the photon carries into the hard subprocess. The  $ep$  cross-section can be factorized into the photon-proton cross-section and a term describing the flux of radiated photons:

$$\frac{d^2\sigma_{ep}}{dydQ^2} = \frac{d^2F_\gamma(y, Q^2)}{dydQ^2} \cdot \sigma_{\gamma p} , \quad (2.25)$$

where  $F_\gamma(y, Q^2)$  denotes the photon flux. This factorization is called *Equivalent Photon Approximation*. The photon flux contains a transverse component,  $F_\gamma^T$ , and a longitudinal component  $F_\gamma^L$ . While real photons can only be transversally polarized, virtual photons can also be longitudinally polarized. As in photoproduction the exchanged photons are almost real, the longitudinal polarization state can be neglected. The photon flux is then given by the *Weizsäcker-Williams-Approximation* (WWA):

$$\frac{d^2F_\gamma(y, Q^2)}{dydQ^2} \approx \frac{d^2F_\gamma^T(y, Q^2)}{dydQ^2} = \frac{\alpha}{2\pi y Q^2} \left( 1 + (1 - y)^2 - 2\frac{m_e^2 y^2}{Q^2} \right) . \quad (2.26)$$

#### Hard Photoproduction

The large center-of-mass energy at HERA allows hard interactions of real photons with the partons in the proton. These hard processes produce collimated *jets* of particles with large transverse momenta in the final state. There are two different classes of hard interactions, the so-called *direct* and *resolved* processes:

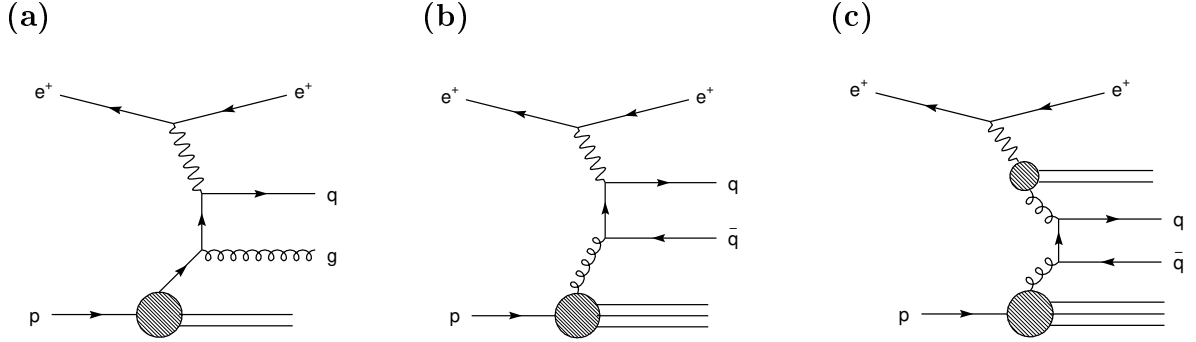


Figure 2.11: Feynman diagrams for different photoproduction processes in leading order: (a) QCD Compton process (direct), (b) boson-gluon-fusion (direct), and (c) resolved photon process.

- *Direct Processes:* The photon couples as a point-like particle to a parton in the proton. Direct processes in leading order of the strong coupling constant  $\mathcal{O}(\alpha_s)$  are the *QCD Compton process* and the *boson-gluon-fusion* (see figure 2.11 (a) and (b)).
- *Resolved Processes:* The photon does not interact as a point-like particle, but fluctuates into an unbound quark pair or a vector meson and then interacts strongly with a parton in the proton. One can say that the inner hadronic structure of the photon is resolved, and a parton from the photon scatters on a parton from the proton. An example diagram is shown in figure 2.11 (c). If the photon fluctuates into a vector meson, one speaks of *Vector Meson Dominance (VMD)*, if it fluctuates into a quark-anti-quark pair and interacts before a meson could be formed, it is called an *anomalous resolved process*.

In analogy to the definition of  $x$  in DIS as the fraction of the proton momentum that the quark carries, a quantity  $x_\gamma$  is introduced, which is the fraction of the photon momentum that the parton from the photon carries. Direct processes are therefore characterized by  $x_\gamma \approx 1$ , while resolved processes have  $x_\gamma < 1$  and hence carry less energy into the scattering process. The partons from the photon, that do not participate in the hard interaction, fragment into a hadronic *photon remnant*, which can be found in the backward region of the detector.

### 2.3.5 Multi-Jet Production

The main background to single top production in the hadronic channel is due to QCD multi-jet production in photoproduction and neutral current DIS. The production of three or more jets proceeds through radiation of additional hard gluons and thus involves higher order QCD processes. Three-jet production is a process of order  $\mathcal{O}(\alpha_s^2)$  in the strong coupling constant. Since currently no simulation including higher orders in  $\alpha_s$  is available, such processes are approximated using a parton shower approach in the so-called *leading logarithmic approximation*. This leading-log approximation is based

on the DGLAP [22] evolution equations. Two example diagrams for 3-jet production with initial and final state gluon radiation (parton showering) are shown in figure 2.12.

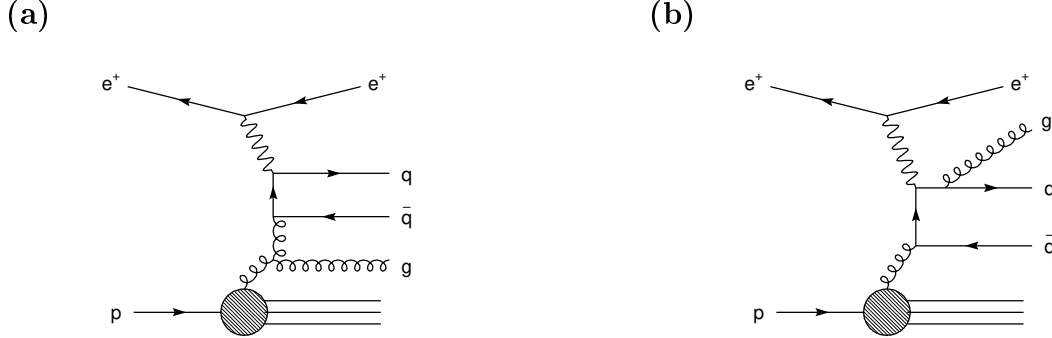


Figure 2.12: Example Feynman diagrams for 3-jet production with a gluon radiated in the initial state (a) or in the final state (b).

## 2.4 Monte Carlo Generators

This section is concerned with the simulation of all the processes discussed in the previous sections. A simulation of both signal and background processes for the single top analysis is performed. At the first stage of the Monte Carlo simulation, events are generated on the parton level. Then they are converted into observable particles. These particles are then put through a full simulation of the detector response. The detector simulation is explained in section 3.4. In the following, all Monte Carlo generators used in this analysis are discussed.

### FCNC Single Top Production (ANOTOP)

The simulation of the single top signal relies on the event generator ANOTOP. It uses the matrix elements of the full  $2 \rightarrow 4$  process  $e + q \rightarrow e + t \rightarrow e + b + W \rightarrow e + b + f + \bar{f}'$ . The matrix elements were obtained with the CompHEP [8] program. The use of the full matrix elements allows a proper description of angular distributions for the top quark decays. The numerical integration of the amplitudes and the generation of events according to the differential cross-section is performed with the BASES/SPRING [23] package. The MRST LO parton densities are used for the proton structure [24]. The parton densities are evaluated at the top mass scale in analogy to the lepton production of heavy quarks. Higher order QCD corrections are simulated using the *leading-log parton shower approach*. Parton showers in both the initial and the final state are simulated.

### ***W* Production (EPVEC)**

The most important Standard Model background in the semi-leptonic channel is the production of real  $W$  bosons with subsequent leptonic decay. The production of electroweak vector bosons ( $W$  and  $Z$ ) is modeled with the EPVEC [25] event generator. It includes all leading order diagrams for  $W$  production presented in figure 2.8.

### **Lepton-Pair Production (LPAIR)**

The production of lepton pairs in photon-photon collisions, where one photon comes from the electron and the other from the proton, is simulated using the LPAIR [26] generator. Both elastic and quasi-elastic processes ( $Q^2 < 4 \text{ GeV}^2$ ), as well as inelastic processes ( $Q^2 > 4 \text{ GeV}^2$ ) are generated.

### **NC and CC DIS (RAPGAP, DJANGO)**

To estimate the background contribution from neutral current DIS for both the semi-leptonic and the hadronic channels, the generator RAPGAP [27] is used. DIS Events are generated for  $Q^2 > 4 \text{ GeV}^2$ . To simulate the multi-jet topologies relevant for the hadronic channel of the top analysis, higher order QCD corrections are implemented as parton showers. For some control studies, also the generator DJANGO is used. The background from charged current DIS is simulated with the DJANGO [28] event generator, which includes first order QED radiative corrections. The simulation of real bremsstrahlung photons is included based on HERACLES [29]. QCD radiation is treated according to the Color Dipole Model [30] and implemented using ARIADNE [31]. The generation of the hadronic final state is based on the string fragmentation model [32].

### **Photoproduction (PYTHIA)**

The main background in the hadronic channel is 3-jet photoproduction. Both direct and resolved photoproduction is modeled with the PYTHIA [33] generator (more precisely, not only photoproduction events, but all low- $Q^2$  events up to  $Q^2 = 4 \text{ GeV}^2$  have been generated with PYTHIA). It relies on the first order QCD matrix elements and uses leading-log parton showers to simulate higher orders. The hadronization of the outgoing partons is performed using the Lund-String-Model [32]. Both light and heavy quark flavors are generated. The GRV LO (GRV-G LO) parton densities [34] are used for the proton (photon) structure. PYTHIA is run in the photon-proton mode. In order to simulate the photon flux using the Weizsäcker-Williams-Approximation, the PYTHIA generator is interfaced to IJRAY [35]. Since only the  $2 \rightarrow 2$  process is implemented and higher orders are only approximated, PYTHIA is not able to describe the absolute 3-jet cross-section. Therefore the prediction from PYTHIA is scaled to the observed number of data events (see section 7.1).



# Chapter 3

## The H1 Experiment at HERA

This chapter gives an overview of the H1 experiment at the HERA<sup>1</sup> collider. The H1 detector is described with a focus on the components most relevant for the presented measurements.

### 3.1 The HERA Collider

HERA is the worldwide only electron proton collider. The HERA accelerator ring has a circumference of 6.4 km and is situated in a tunnel about 10-15 m below the surface at the DESY<sup>2</sup> laboratory in Hamburg, Germany. It consists of two storage rings, one for positrons or electrons<sup>3</sup>, and one for protons.

Figure 3.1 shows the HERA collider facility with the main accelerator ring and the various pre-accelerators. After several accumulation and acceleration steps, the electrons and protons are injected in opposite directions into the HERA storage ring, where they are accelerated to their final energy. Bending magnets in the curved sections of the ring force the particles on a 'circular' orbit. Since the particles are accelerated by an RF voltage, there are no continuous beams but *bunches* of particles. Electrons and protons are stored in up to 220 bunches with  $10^{10}$  to  $10^{11}$  particles each. The time interval between two consecutive bunches is 96 ns, corresponding to a bunch crossing frequency of 10.4 MHz.

During the data taking period 1994-97, HERA was operated with positrons ( $e^+$ ) of final energy  $E_e = 27.5$  GeV and protons of final energy  $E_p = 820$  GeV. In 1998, the proton energy was increased to  $E_p = 920$  GeV and HERA was running with electrons ( $e^-$ ). Since mid of 1999 until the shutdown in fall 2000, HERA was again operated with positrons. The available center-of-mass energy of the  $ep$  collisions is thus:

$$\sqrt{s} \approx \sqrt{4E_e^0 E_p} \approx 320 \text{ (300) GeV} \quad \text{for } E_p = 920 \text{ (820) GeV} . \quad (3.1)$$

The electron and proton beams are brought to collisions in two interaction regions in the North Hall and the South Hall of the HERA ring. Around these interaction

---

<sup>1</sup>Hadron-Elektron-Ring-Anlage

<sup>2</sup>Deutsches Elektronen-Synchrotron

<sup>3</sup>the term *electron* will be used from now on referring to both electrons and positrons, irrespectively of their electric charge. Distinction will be made explicit when required.

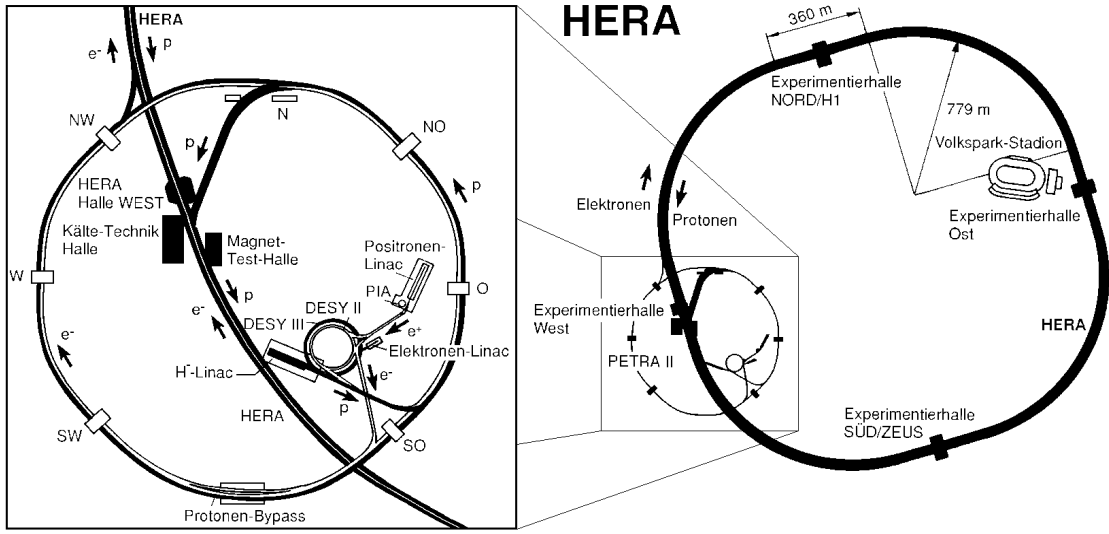


Figure 3.1: The HERA collider facility with the main HERA storage ring (right) and an enlarged view of the pre-accelerator system (left).

regions the H1 and ZEUS detectors were installed. There are two more experiments, the fixed target experiments HERA-B and HERMES, which use only one of the beams. The HERA-B experiment investigates the production of heavy flavor quarks (Charm, Beauty) from interactions of the proton beam halo with a wire target. The HERMES experiment measures collisions of the longitudinally polarized electron beam with polarized  $H_2$ , D or He gas targets to study the spin structure of the nucleon.

A very important ingredient for the derivation of a cross-section is the luminosity  $L$ . It is the proportionality factor which connects the interaction rate  $dN/dt$  and the cross section  $\sigma$ :

$$\frac{dN}{dt} = L \cdot \sigma \quad (3.2)$$

Thus the total number of events in a scattering reaction depends on the integrated luminosity  $L = \int \mathcal{L} dt$ . The cross section has the dimension of length squared; usually it is specified in barn ( $[1 \text{ b} = 10^{-28} \text{ m}^2]$ ). Accordingly, the integrated luminosity is measured in inverse barn.

HERA is currently starting a phase of operation at higher luminosity. In September 2000, HERA operation was shut down to carry out a major luminosity upgrade of the HERA machine and the collider experiments. New super-conducting quadrupole magnets were inserted close to the H1 and ZEUS interaction regions. The goal is to achieve an increase in luminosity by a factor of five. Also the detectors have undergone major upgrade programmes.

### 3.2 The H1 Detector

The H1 detector is designed to measure the complete final state in HERA  $ep$  collisions. This final state typically consists of many particles of various species, e.g. electrons,

muons, photons and neutral and charged hadrons (mostly pions). The particles are often produced in jets with high particle densities. The requirement to measure all these particles is met by the complex detector design as shown in fig. 3.2. The huge H1 apparatus fills out a volume of  $\approx 1800 \text{ m}^3$  and weighs about 2800 tons. It covers almost the complete solid angle of  $4\pi$  with some unavoidable losses due to the feed through of the beam pipe. The design of the H1 detector resembles the typical layout of modern collider detectors. Starting from inside to outside the following components are installed:

- A system of central and forward tracking chambers arranged around the beam pipe is used to measure trajectories and momenta of charged particles.
- The tracking system is surrounded by electromagnetic and hadronic calorimeters. They measure positions and energies of neutral and charged particles and identify electrons and hadrons.
- Outside the hadronic calorimeter a super-conducting coil provides a homogenous magnetic field parallel to the beam axis. This allows to measure the momenta of charged particles in the plane perpendicular to the beam axis with the tracking system.
- The outermost part of the detector is formed by a system of chambers for identifying muons and measuring their trajectories.

Because of the non-equal beam energies the detector design is asymmetric with respect to the beam axis. In the hemisphere around the proton direction, denoted as 'forward region', the H1 detector is equipped with higher granularity than in the 'backward region', e.g. in the calorimeters. A more detailed description of the H1 detector can be found in [36, 37].

In the following we will discuss in more detail the detector components most relevant for this analysis.

### 3.2.1 H1 Coordinate System

In this thesis we will naturally use detector coordinates. The cartesian coordinate system of the H1 detector is defined as follows: Its origin is placed at the nominal  $ep$  interaction point, situated at the geometrical center of the central tracking chambers (see figure 3.2). The  $z$ -axis points in the proton flight direction, the  $y$ -axis points upwards and the  $x$ -axis points towards the HERA ring center. The  $x - y$  plane is referred to as the transverse plane. The polar angle  $\theta$  is defined with respect to the positive  $z$ -axis, the azimuthal angle  $\phi$  with respect to the positive  $x$ -axis.

For ultra-relativistic particles, the *pseudorapidity*  $\eta$  is often used instead of  $\theta$ . It is defined as:

$$\eta = -\ln \left( \tan \left( \frac{\theta}{2} \right) \right)$$

and transforms linearly under Lorentz boosts along the  $z$ -axis.

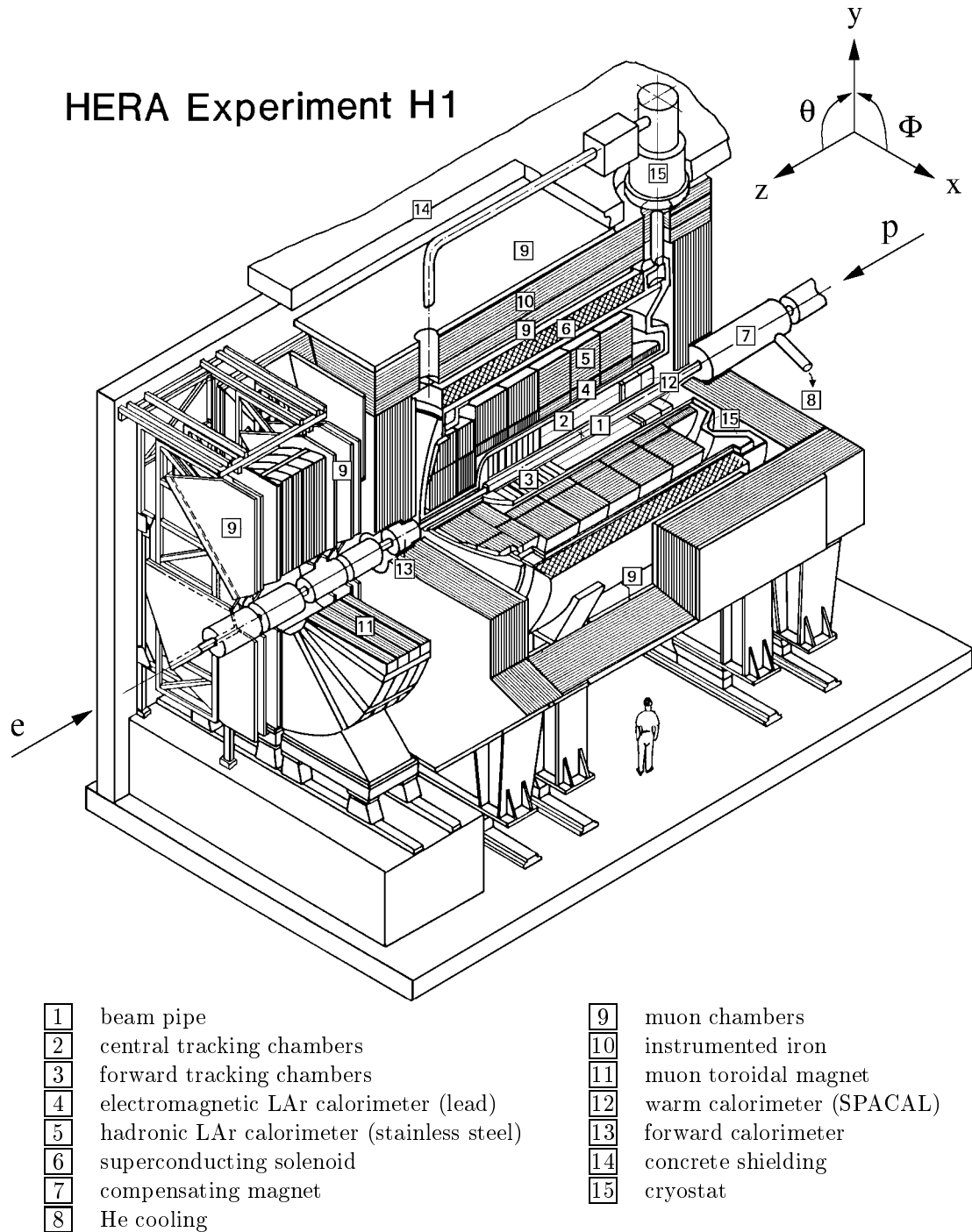


Figure 3.2: The H1-Detector.

### 3.2.2 Calorimetry

#### The Liquid Argon Calorimeter System

The Liquid Argon Calorimeter (*Liquid-Argon* LAr) is the most important detector for measuring the energies of the final state particles from  $ep$  interactions. It covers an angular range of  $4^\circ \leq \theta \leq 154^\circ$ . The calorimeter is housed in a single cryostat inside

the superconducting coil. The latter fact ensures that particles originating from  $ep$  interactions traverse only little amount of dead material before entering the calorimeter.

The advantages of LAr calorimetry, as exploited in this detector, are stability, simple electronic calibration, good homogeneity and fine segmentation. This allows an accurate determination of energy and direction of the scattered electron and a precise measurement of the energy flow of the hadronic final state. In the following an overview of the H1 LAr calorimeter system is presented, for details see [38].

Figure 3.3 shows a longitudinal section of the H1 LAr calorimeter. The calorimeter is segmented along the  $z$ -direction into an 8 wheel self-supporting structure (starting backward BBE, CB1, CB2, CB3, FB1, FB2, OF, IF). Each wheel is further divided in the azimuthal direction into eight identical units, the so-called octants. Figure 3.4 shows a transverse section of one calorimeter wheel in the central region (CB).

From inside to outside the LAr calorimeter is built up of absorber plates interleaved with LAr interspaces. In the inner part the electromagnetic section is located, where lead is used as absorber material with a total thickness of about 20 (30) radiation lengths in the central (forward) region. In the outer part the hadronic section is situated, where steel is used as absorber material. The total hadronic absorption length is about  $5 \lambda$  in the central and  $8 \lambda$  in the forward area. The orientation of the absorber plates was chosen such that the angle of incidence of particles originating from the  $ep$  interaction point is always larger than 45 degrees. This ensures that the energy resolution is independent of the particle direction.

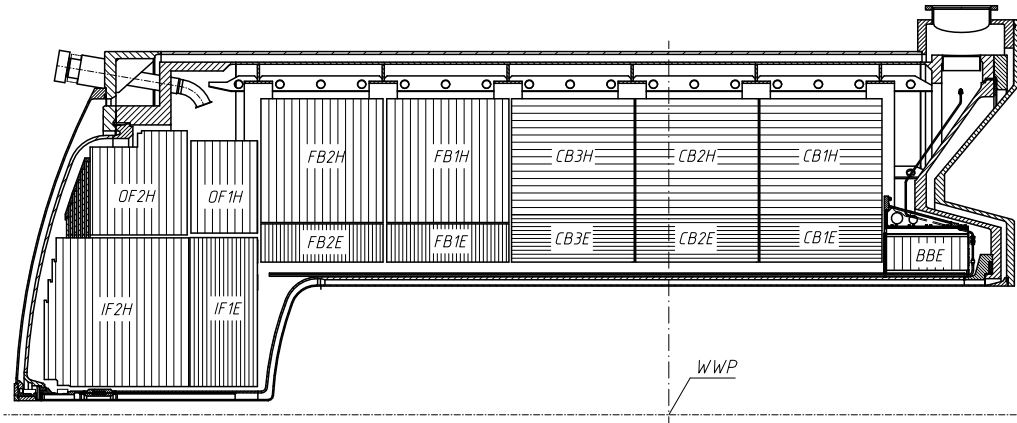


Figure 3.3: Longitudinal section of the Liquid Argon Calorimeter.

The basic transverse granularity of the electromagnetic readout cells is about 3 cm. In BBE, CB1 and CB2 the cell sizes are roughly doubled. Longitudinally the number of segments increases from three (barrel region) to six (forward region).

In the hadronic part of the LAr calorimeter the number of segments increases from four (barrel region) to six (forward region). The fine granularity allows for a precise spatial measurement of electromagnetically interacting objects and an effective separation of electron and pions.

The H1 LAr calorimeter is non-compensating and the response ratio of electrons and pions is at 10 GeV about 1.35. Due to the  $\pi_0$  fluctuations the response to hadrons has a

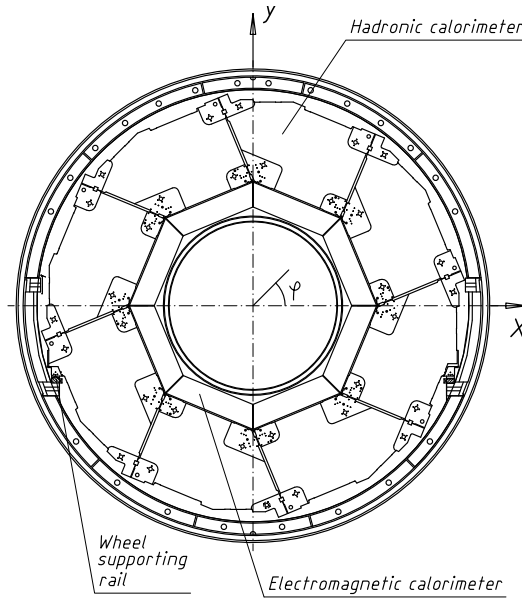


Figure 3.4: Transverse section of the Liquid Argon Calorimeter.

significant non-Gaussian contribution at larger energies which deteriorates the energy resolution. This can be improved by using a software energy weighting technique which was first applied in the CDHF experiment. The H1 LAr calorimeter was designed such that the fine granularity allows to identify the large high density energy deposits due to the primary electromagnetic component in the jet and due to the  $\pi_0$  component in the hadronic showers. The response of the electromagnetic and hadronic component is equalized and hereby the  $\pi_0$  fluctuations are reduced.

The energy resolution of electromagnetically and hadronically interacting particles was determined in test beam measurements [39],[40] and results in

$$\Delta E/E = 15 \% / \sqrt{E/\text{GeV}} \oplus 1 \%$$

for electrons and

$$\Delta E/E = 70 \% / \sqrt{E/\text{GeV}} \oplus 2 \%$$

for pions.

### The SPACAL Calorimeter

The SPACAL Calorimeter provides calorimetric information in the backward region, where it covers the range  $155^\circ < \theta < 178^\circ$ . Its main task is to measure the scattered electron in low  $Q^2$  DIS events ( $1 < Q^2 < 150 \text{ GeV}^2$ ).

The SPACAL is a scintillating fibre 'spaghetti' calorimeter with lead absorbers. Incident particles develop into a shower in the lead. Charged shower particles cause the fibres to scintillate and the light is transported to photomultipliers, where it is collected.

The SPACAL consists of two parts, an inner electromagnetic section and an outer hadronic section. The electromagnetic section is 28 radiation lengths deep. It contains cells of transverse size  $(40.5 \text{ mm})^2$ , which ensures a good position resolution. In

total 1192 channels are read out. The energy resolution, as obtained in test beam measurements, is

$$\frac{\sigma_E}{E} = \frac{(7.1 \pm 0.2)\%}{\sqrt{E/\text{GeV}}} \oplus (1.0 \pm 0.1)\%. \quad (3.3)$$

In the relevant energy range for the scattered electron ( $\approx 8 - 30$  GeV), the absolute energy scale is known with a precision of better than 1%. The hadronic section of the calorimeter is made up of cells with transverse size  $(119 \text{ mm})^2$ . In total 136 channels are read out. The total length of the electromagnetic and hadronic section corresponds to two interaction lengths.

The SPACAL signals are read out with an excellent time resolution of 1 ns, which is exploited in the first level trigger of the experiment (see below) to reject background events.

### 3.2.3 The Inner Tracking System

The inner tracking system measures the trajectories of charged particles. By combining all detector signals originating from the same particle, the polar and azimuthal angles as well as the extrapolated  $xy$ - and  $z$ -position of the track at the  $ep$ -interaction point are determined. The high spatial resolution allows to detect secondary vertices of decaying particles, e.g.  $K_s^0$  and  $\Lambda$  decays.

The superconducting magnet solenoid, surrounding the tracking system and the LAr calorimeter, creates a homogenous magnetic field of about 1.15 Tesla parallel to the  $z$ -axis. In this field charged particles are forced on curved tracks with a radius  $r \sim p_T$  in the  $xy$ -plane, where  $p_T$  is the transverse momentum. This relation is exploited to determine  $p_T$  from the measurement of  $r$ .

The inner tracking chambers can be subdivided into three subsystems, as illustrated in figure 3.5. Integrated into the system are layers of proportional chambers. These are used for triggering events with tracks and for a fast determination of the  $z$ -coordinate of the interaction point.

#### Central Tracking Chambers

Figure 3.6 shows a transverse section of the H1 central tracking chambers.

Covering in total the angular region  $25^\circ < \theta < 155^\circ$ , they consist of the following interleaved layers of roughly cylindrical shaped detectors around the beam pipe:

- Central silicon tracker (CST) consisting of two detector layers.
- Inner and outer multi-wire proportional chambers (CIP and COP), each consisting of two detector layers.
- Inner and outer large drift chambers (CJC1 and CJC2), with 24 and 32 signal wires respectively.
- Inner and outer  $z$ -drift chambers (CIZ and COZ), each equipped with four signal wire planes.

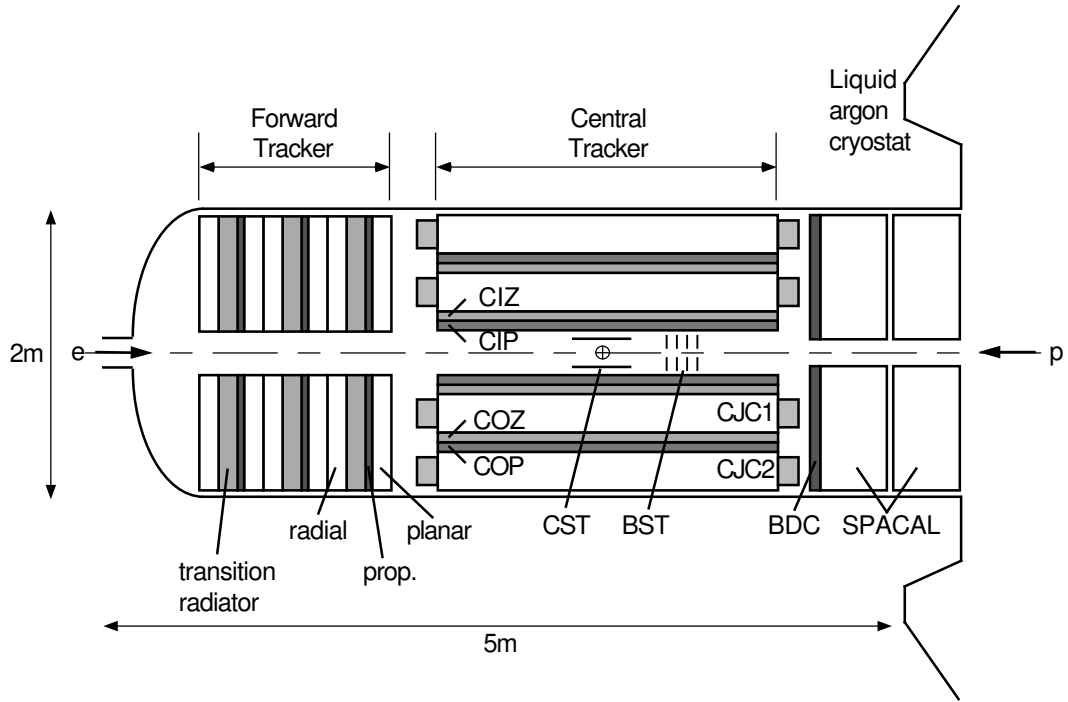


Figure 3.5: Longitudinal section of the H1 tracking system (1995 the backward electromagnetic calorimeter BEMC was replaced by the SPACAL).

The most important subsystems are the two jet chambers CJC1 and CJC2, denoted as CJC. In the CJC the wires are strung parallel to the  $z$ -axis. The wire signal induced by a charged particle allows to measure the  $r$ - $\phi$ -coordinate of the particle with a precision of  $\approx 170 \mu\text{m}$ . The  $z$ -coordinate of the particle is measured by comparing the collected charge on the two ends of the wire, resulting in a rather coarse resolution of  $\sigma_z \approx 35 \text{ mm}$ . A much better precision of  $\sigma_z \approx 400 \mu\text{m}$  is achieved with the  $z$ -chambers CIZ and COZ, where the wires are strung perpendicular to the  $z$ -axis. The innermost H1 central tracking detector is the central silicon tracker CST. It can measure up to two points of the track's trajectory very accurately. This allows to determine the track's position at the  $ep$ -interaction point with such precision, that one obtains sensitivity to decays from long-lived heavy flavor hadrons (containing a charm or beauty quark). Table 3.1 summarizes the achieved hit resolutions of the different central tracking detectors.

	$\sigma_{r\phi} [\text{mm}]$	$\sigma_z [\text{mm}]$
CST	0.0012	0.0025
CJC1/CJC2	0.170	35
CIZ	28	0.4
COZ	58	0.4

Table 3.1: Spatial resolutions of the H1 central tracking chambers.



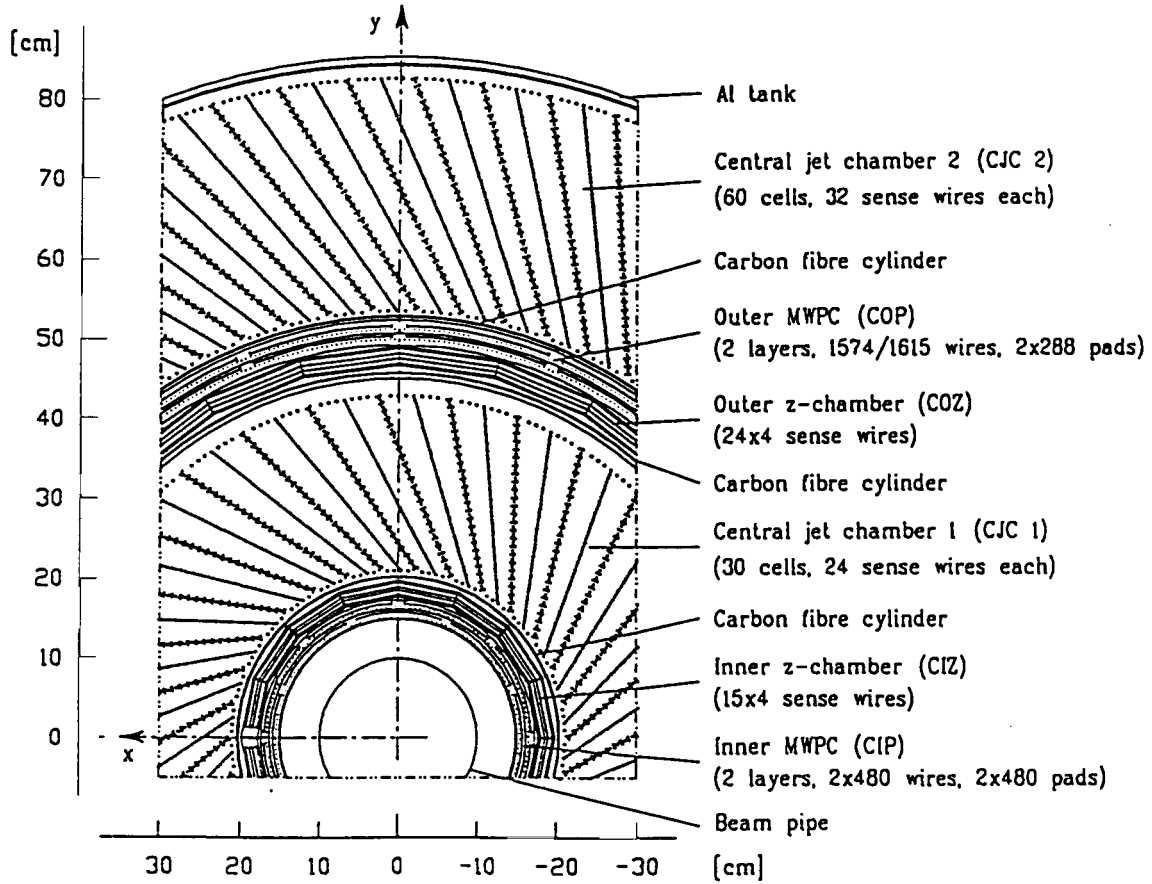


Figure 3.6: Transverse section through the tracking system.

For tracks passing through all layers of the CJC an effective momentum resolution has been obtained of

$$\frac{\sigma(p_T)}{p_T} \approx 0.01 \cdot p_T(\text{GeV}). \quad (3.4)$$

### Forward Tracking Chambers

The forward tracker consists of three identical super-modules, covering the angular region  $7^\circ < \theta < 25^\circ$ . Each super-module contains three planes of planar drift chambers, a multi wire proportional chamber, a transition radiation detector and a radial drift chamber. Subsequent planar drift chamber planes are rotated by  $60^\circ$ .

### 3.2.4 The Muon System

The H1 muon system is divided into the Central Muon Detector which consists of the iron return yoke instrumented with limited streamer tubes, and the Forward Muon Detector. The main purpose of these detectors is to identify tracks from muon particles and to measure their direction. Due to large amounts of material in front of and inside the muon detectors, the muons suffer from large multiple scattering, which does only allow for a rough measurement of the muon momenta.

### Central Muon Detector

The Central Muon Detector (“Instrumented Iron”) covers the angular region  $5^\circ \leq \theta \leq 171^\circ$  and allows to detect muons with an energy greater than about 1.5 GeV. It consists of ten iron layers, each 7.5 cm thick, interleaved with limited streamer tubes. Both at the inside and the outside of the iron three streamer tube layers are attached in addition. The signal wires in the streamer tubes enable to measure the muon position perpendicular to the wires with a resolution of about 3 to 4 mm. Five of the layers are equipped with strip electrodes running perpendicular to the wires. This allows to measure the muon position parallel to the wires with an accuracy of about 10 to 15 mm. Single layer efficiencies of about 80% are reached. The Central Muon Detector is subdivided into four subdetectors (forward end cap, forward and backward barrel and backward end cap), covering different polar angular regions and with different orientations of wires and strips. Because of limited geometrical acceptance, e.g. due to support structures, the muon reconstruction efficiency is limited to about 90%.

The instrumented iron in addition serves as a “Tail Catcher” calorimeter to measure hadronic energy leaking from the LAr and SPACAL calorimeters. For this purpose pad electrodes with analogue readout are used, which are glued on the limited streamer tubes in eleven layers.

### Forward Muon Detector

The forward muon detector complements the H1 Muon System in the forward direction.

It is situated between 6.4 m and 9.4 m forward of the nominal  $ep$  interaction vertex and covers polar angles  $4^\circ \leq \theta \leq 17^\circ$ . It consists of six double layers of drift chambers, three on either side of the toroid magnet providing a field of roughly 1.6 Tesla. Only muons with momenta of at least 5 GeV will reach and pass through this detector and thus can be detected.

### 3.2.5 Time-of-Flight Detectors

The Time-of-Flight detectors are vital for the rejection of non- $ep$  interactions. A major source of such interactions are the so-called beam-gas and beam-wall events, where protons interact with the residual gas inside the beam pipe or with the beam pipe wall. Such background events are decorrelated in time and space with the desired  $ep$  interactions, which occur at the precisely known electron proton bunch crossing times. The Time-of-Flight detectors consist of several large scintillator counters located at various places around the H1 detector. Non- $ep$  background is rejected by requiring that the arrival time of particles in the scintillators is inside a time window as defined from the electron-proton bunch crossing times.

### 3.2.6 Luminosity System

At H1 the luminosity is measured with the Bethe–Heitler process [41] ( $ep \rightarrow e'\gamma p$ ). The cross section of this reaction is large and well known. The measurement consists of counting the Bethe–Heitler event rate and then using equation 3.2 to determine the luminosity.

The luminosity system of the H1 experiment consists of two segmented crystal Cherenkov counters. One is the electron tagger at  $z_{ET} = -33.4$  m, the other the photon tagger at  $z_{PD} = -102.9$  m.

The electron tagger is located directly beneath the electron beam pipe and accounts for the scattered electron from the Bethe–Heitler process. The photon leaves the upwards bent proton beam pipe and hits the photon tagger. Electrons and photons are identified in coincidence. The background is restricted requiring that the energy sum  $E_{ET} + E_{PD}$  has to be in the range of the electron beam energy  $E_e$ .

In addition to the luminosity measurement the luminosity system is also used to identify photoproduction events ( $Q^2 < 0.01$  GeV<sup>2</sup>) and DIS events with additional bremsstrahlung of the incoming electron (ISR).

### 3.3 Trigger and Data Acquisition

The H1 trigger has to distinguish between  $ep$  interactions and background reactions during data acquisition. The rate of non-empty events, i.e. with significant detector signals, is about 100 kHz. It is completely dominated by background processes such as beam-wall events. The trigger has to reject these events while retaining the desired  $ep$  interactions. Finally the event rate must be reduced to  $\approx 10$  Hz that can be stored on tape.

The trigger system consists of four levels (L1 to L4). The first level trigger provides a decision whether an event should be kept or not within  $2.5 \mu\text{s}$ . An event is kept if one of 128 *subtriggers* has fired. These subtriggers are logical combinations of *trigger elements*, which are signals provided by the individual subdetector components. In the second and third trigger levels, the signals of the different components can be topologically connected. The fourth trigger level performs a fast reconstruction of the whole detector information to verify the decision of the previous levels.

The events that are accepted by trigger level four (L4) are written to tape. To obtain a further reduction of the data, the events are classified in different physical event classes after a delay of some hours (offline). This classification is also called trigger level five (L5). It is based on the complete reconstruction of the detector information. The so classified events are written to tape (production output tape POT) with all details of the reconstruction and to disk (data summary tape DST) in a reduced format. For the present analysis the data are used in the DST format.

#### Triggering of Events in the Single Top Analysis

The triggering of events that are studied in this analysis uses mainly information from the Liquid Argon Calorimeter. To trigger events in the semi-leptonic decay channel, the five subtriggers developed in the H1 analysis of neutral and charged current DIS [45] are used (subtriggers ST67,75,66,71,77). They are mainly based on the following two trigger elements. The *LAr-electron* trigger element signals a high electromagnetic energy deposit in a trigger “tower” of the Liquid Argon Calorimeter pointing towards the event vertex, as caused by an electron from a  $W$  decay. For electron energies above 11 GeV, the trigger efficiency exceeds 99% [45]. The *LAr-ETmiss* trigger element signals an imbalance of transverse energy measured in the Liquid Argon Calorimeter, as

caused by an energetic neutrino from a  $W$  decay. The efficiency for events with missing calorimetric transverse momentum,  $P_T^{calo}$ , is 98% when  $P_T^{calo} > 25$  GeV and 50% when  $P_T^{calo} = 12$  [45]. In order to increase the efficiency for events with muons, also muon triggers are exploited, which signal a pattern consistent with a minimum ionizing particle in the muon system in coincidence with tracks in the tracking detector. The muon triggers have a rather low efficiency of 35% (9%) for muons with polar angles  $\theta_\mu > 35^\circ$  ( $\theta_\mu < 35^\circ$ ) [54]. In the hadronic decay channel, events are expected to have a large amount of hadronic energy in the calorimeter. For the high transverse energies required for the events studied in this analysis, they are triggered based on the amount of transverse energy in the the Liquid Argon Calorimeter with an efficiency of close to 100%.

### 3.4 Detector Simulation

Section 2.4 introduced the Monte Carlo simulations of the  $ep$  physics processes studied in this thesis. The discussion ended at the so-called generator level. At this level, all generated final state particles are available as four-vectors, describing the particle momenta. To allow for comparisons with “real” events, the measurement process with the H1 detector must be simulated for these particles. The first step of this detector simulation is the tracking of the generated particles through the detector. A GEANT [42]-based application is used. This step includes the tracking in the magnetic field, secondary particle generation and shower development. In the next step, the response of the active detector parts, e.g. sense wires, is simulated, resulting in an output very similar to that for “real” events. Finally the trigger response is simulated. The events produced in this way are fed through the same reconstruction software as the data.

# Chapter 4

## General Data Pre-Selection

The analysis presented in this thesis uses the full HERA I data set taken in the years 1994-2000. Before a selection of events according to physics points of view can be carried out, it must be assured that only events are selected, for which the detector was fully operational. In addition, background events that were not produced in electron-proton collisions must be rejected. The criteria used in this general data pre-selection are summarized in this section. Since top quarks are searched for in three different decay channels ( $t \rightarrow be\nu$ ,  $t \rightarrow b\mu\nu$ ,  $t \rightarrow bq\bar{q}'$ ), no common pre-selection for all channels can be performed.

### 4.1 Run Selection and Detector Status

The periods of data taking at HERA are divided into so-called "luminosity fills", which are defined by one filling of electrons in the HERA ring. Each luminosity fill is again divided into different "runs", which last up to two hours. The detector conditions during one run are rather stable, but may vary within one luminosity fill. Only runs with stable detector and triggering conditions, classified as "Good" or "Medium" quality runs are used in this analysis.

In order to assure a good measurement of the events, the subdetectors necessary for the analysis must be fully operational. Therefore the status of all detector components is monitored. To guarantee operational readiness, nominal high-voltage values and functioning readout are required for the following components:

- Liquid Argon Calorimeter
- SPACAL
- Central Jet Chambers (CJC1 and CJC2)
- Central Proportional Chambers (CIP and COP)
- Luminosity system
- Time of flight system (TOF)

The calorimeters, in particular the Liquid Argon Calorimeter, are indispensable for this analysis. The central tracking chambers are needed for the determination of the electron proton interaction vertex and a reliable track measurement of charged particles, while the central proportional chambers are essential for the triggering. The operation of the luminosity system allows the determination of the data luminosity.

## 4.2 Event Vertex

An electron proton interaction vertex, the so-called primary vertex, is required for each event. To reconstruct the vertex, both central and forward tracks are used. The  $z$ -position of the vertex must lie within

$$-40 \text{ cm} < z_{\text{vertex}} < 100 \text{ cm} \quad (4.1)$$

around the nominal interaction point. This requirement ensures a reliable measurement of the event within the detector acceptance. In addition, it rejects events that do not come from  $ep$  interactions, which will be discussed in more detail in section 4.4.

## 4.3 Data Sets and Luminosities

All HERA I data collected from 1994 until the shutdown in 2000 are exploited to search for top quarks. The different data sets together with their integrated luminosities, center-of-mass energies and charge of the beam electron are specified in table 4.1.

Data Sets	1994-1997	1998-1999	1999-2000
Beam	$e^+p$	$e^-p$	$e^+p$
$\sqrt{s}$	300 GeV	320 GeV	320 GeV
$L = \int \mathcal{L} \, dt$	37.0 pb $^{-1}$	13.6 pb $^{-1}$	67.8 pb $^{-1}$

Table 4.1: Summary of the data sets used in this thesis.

With the above mentioned run selection and detector status requirements, the analyzed data sample corresponds to a total integrated luminosity of

$$L_{\text{tot}} = 118.4 \pm 1.8 \text{ pb}^{-1}. \quad (4.2)$$

The accuracy of the luminosity measurement is estimated to be 1.5%.

## 4.4 Non- $ep$ Background Rejection

The rate of events produced in  $ep$  collisions is substantially smaller than the rate due to non- $ep$  interactions. The majority of these interactions is rejected by the Time-of-Flight system described in section 3.2.5. A large part is also removed by the vertex

requirements. Still, it is essential to reach an effective suppression of the remaining non- $ep$  background recorded with the H1 detector. The main background sources are muons from cosmic rays or beam-halo muons. The latter originate from the decays of charged pions produced in beam-gas and beam-wall events. These muons cause tracks in the tracking system or produce showers in the calorimeter, which can be misidentified as electrons or hadrons. Halo muons traverse the detector in horizontal direction, cosmic muons mainly in vertical direction. Beam-gas and beam-wall interactions do not only cause significant background, when a halo muon is produced, but also when other secondary particles are scattered into the H1 detector. The following cuts and background finders are used to reject non- $ep$  background:

- **Timing:** The timing of the event determined from the drift time in the Central Jet Chamber ( $t_0(CJC)$ ) must be consistent with the time of the bunch crossing.
- **Topological background finders:** A standard set of background finders, implemented in the program package QBGFMAR [43], is used to reject topologies typical for cosmic or halo muons by searching for long and narrow signatures in combinations of different detector components (Instrumented Iron, Liquid Argon Calorimeter, CJC, SPACAL).
- **Cut on  $E - P_z$ :** If all particles produced in an  $ep$  collision are detected and correctly measured, the total  $E - P_z$  in the event must have a value of twice the incoming electron energy ( $E_e^0$ ):

$$E - P_z = E_p - P_{z,p} + E_e^0 - P_{z,e}^0 = 2E_e^0 . \quad (4.3)$$

Values of up to  $\sim 75$  GeV can be due to fluctuations in the energy measurement. Much larger values can only be produced by energetic non- $ep$  interactions or by an "overlay" of more than one interactions in the recorded event. Therefore an upper cut on the visible  $E - P_z$  is applied:

$$(E - P_z)_{vis} < 75 \text{ GeV} . \quad (4.4)$$

After applying all the above cuts, the non- $ep$  background is suppressed to a negligible level. In the final data selections, this is further verified by a visual scan of all candidates events.





# Chapter 5

## Lepton Identification and Hadronic Reconstruction

The search for top quark decays presented in this thesis depends on a good particle identification and a reliable measurement of hadronic energies. For the semi-leptonic decay channel, an excellent identification of electrons and muons from  $W$  decays is essential. It is described in the first part of this chapter. The second part is concerned with the reconstruction of the hadronic final state, the jet finding, and the calibration of hadronic energies.

### 5.1 Lepton Identification

#### 5.1.1 Electron Candidates

The identification of electrons is based on the electron finding algorithm QESCAT [44] used as standard in H1. Electrons are searched for in the Liquid Argon Calorimeter and the SPACAL. Electrons found in the backward region in the SPACAL are candidates for the scattered beam electron. In this analysis, they are only used to constrain the kinematics of top events at high momentum transfers in the semi-leptonic decay channel. Since top production proceeds at large  $y$ , i.e. the scattered beam electron loses a large fraction of its initial energy, the minimum energy required for electron candidate is chosen to be 2 GeV. Electrons from  $W$  decays have high transverse momenta and are expected to be found in the Liquid Argon Calorimeter. The following discussion will concentrate on electrons in the Liquid Argon Calorimeter

Electron candidates are identified by the presence of a compact cluster of energy in the electromagnetic part of the Liquid Argon Calorimeter. Detector regions that allow no reliable measurement of the electron candidate, such as  $\phi$ - and  $z$ -cracks between calorimeter modules, are excluded by applying fiducial cuts. The energy cluster must be associated with a track having a distance of closest approach<sup>1</sup> of less than 12 cm. The requirement of an associated track serves as discrimination between electrons and

---

<sup>1</sup>The distance of closest approach (DCA) is defined as the perpendicular distance between the center of gravity of the energy cluster and the tangent to the extrapolated track at its impact point on the calorimeter front.

photons, since an electron-photon separation based purely on calorimetric information is not possible.

The polar and azimuthal angles ( $\theta_e, \phi_e$ ) of the electron are determined from the center of gravity of the electromagnetic cluster and the reconstructed primary vertex. The electron energy ( $E_e$ ) is determined from the cluster energy and is calibrated using the standard procedure developed in [45]. The calibration constants were determined separately for each calorimeter wheel, using neutral current DIS events, kinematically reconstructed with two different methods (DA- and  $\omega$ -method). Since the statistics of neutral current events in the forward region of the detector is low, also elastic QED Compton events and events from  $\gamma\gamma \rightarrow e^+e^-$  were used. The mean fractional energy shift from the absolute electromagnetic energy scale obtained with this calibration is shown in figure 5.1. The systematic uncertainty on the energy scale quoted in [45] is represented by the shaded error band. In this analysis, electrons from top or  $W$  decays are expected mainly in the forward region, and an overall systematic uncertainty on the electromagnetic energy scale of 3% is assumed.

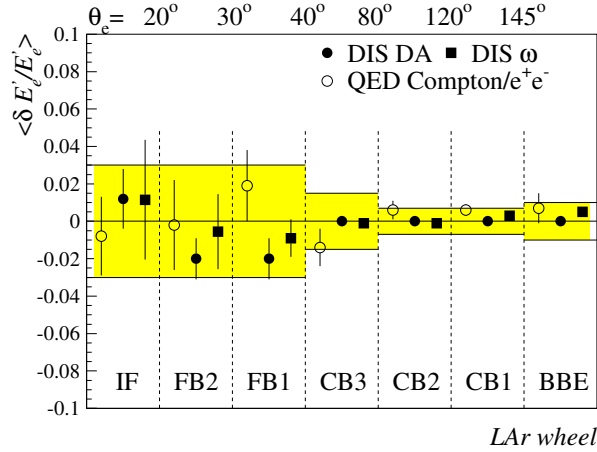


Figure 5.1: The mean fractional energy shift  $\delta E_e / E_e$  from the absolute energy scale obtained by two different reconstruction methods (DA-method,  $\omega$ -method). The error band shows the systematic uncertainty on the energy scale. Taken from [45].

A sample of neutral current events (data taken in the year 2000) has been used to study the efficiencies of the electron finding and the cluster-track association. To determine the electron finding efficiency, a monitor sample is defined by using an independent electron identification algorithm based on a cone jet finder [46]. Electrons are identified as purely electromagnetic jets with exactly one isolated track, that matches the momentum measured in the calorimeter. Details can be found in [47]. The electron finding efficiency is defined as the fraction of monitor electrons which are identified by QESCAT. As shown in the lower plot of figure 5.2 it is found to be 98% up to largest values of the electron energy. It agrees well with the simulation within  $\sim 2\%$ . A cluster-track efficiency can be defined by using a superset of electrons identified by only using the QESCAT finder. The efficiency is computed as the fraction of the QESCAT electrons for which a matched track is found with distance of closest approach to the cluster

of less than 12 cm. As can be seen in figure 5.2 in the upper plot, the cluster-track efficiency in the data is  $\sim 96\%$ . It is about 2-3% lower than in the Monte Carlo simulation (DJANGO). In the very forward region ( $\theta_e < 20^\circ$ ), the efficiency to find an associated track is much smaller. In this region, however, the neutral current statistics is very low. The small discrepancies between data and Monte Carlo simulation seen for the electron identification and the cluster-track association are taken into account as systematic uncertainties in the electron channel of the top search.

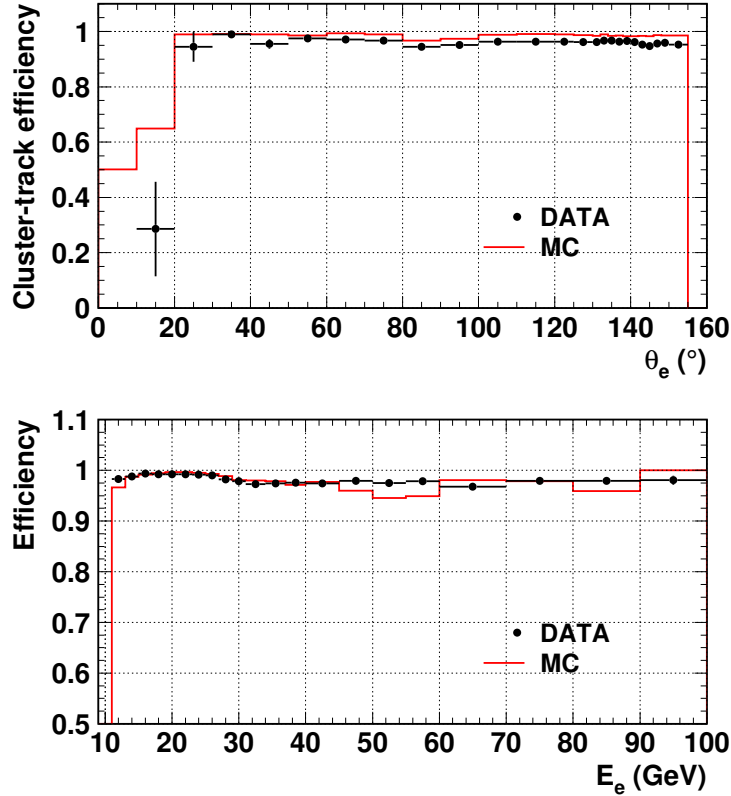


Figure 5.2: Cluster-track efficiency (upper plot) and electron finding efficiency (lower plot) as determined for electrons in the Liquid Argon Calorimeter.

### 5.1.2 Muon Candidates

As minimal ionizing particles, muons penetrate the whole detector and generally deposit only little energy in the calorimeter. They are measured as tracks in the inner tracking chambers and identified by their tracks in the dedicated muon detectors. Muons leave signatures in the following detector components (depending on their polar angle):

- Central/Forward inner tracking system
- Liquid Argon Calorimeter
- Instrumented Iron
- Forward Muon Detector

Muon candidates are accepted if they have an inner track and a muon signature in the Instrumented Iron, or if they are measured in the Forward Muon Detector. Their transverse momentum must be larger than 1 GeV. If the muon candidate is not associated with a forward muon track, it must have an inner track linked to either a track in the Iron or associated with an energy deposit in the Iron within a cone of radius 0.5 around the track. The momentum of the muon is determined from the measurement of the track curvature in the inner tracking system. If a forward muon track exists, the momentum measurement in the Forward Muon Detector is used. For polar angles below  $12.5^\circ$ , muons with only a signature in the Instrumented Iron are rejected, because hits in this region can be produced by scattering in the beam pipe.

In this analysis, only muons that are isolated with respect to other particles are searched for. Therefore they must have less than 8 GeV of energy in the Liquid Argon Calorimeter within a cone of radius 0.5 around the muon track. Further isolation requirements are applied later in the selection of events with  $W$  bosons. With these selection criteria, muons are identified with an efficiency of  $\sim 90\%$  ( $\sim 70\%$ ) in the central (forward region) of the detector. The systematic uncertainty on the muon identification efficiency is about 5%.

## 5.2 Hadronic Final State Reconstruction

The hadronic final state is defined as the sum of all hadronic particles measured in the detector. The reconstruction of the hadronic final state can be done in different ways, for instance using only calorimeter clusters, since hadronic energy is predominantly measured in the Liquid Argon Calorimeter. However, if only clusters are used, the measured hadronic energy tends to be underestimated. Two reasons for this are:

1. Noise cuts are applied to reduce the effect of electronic noise in the calorimeter cells. These cuts also remove a fraction of real hadronic energy in low-energetic clusters.
2. Before particles reach the calorimeter, they can lose some of their energy due to interactions with dead material in the detector.

The reliability of the hadronic final state reconstruction can be improved by combining information from the calorimeter and the inner tracking chambers, as discussed in the following section.

### 5.2.1 Combination of Tracks and Clusters

The momentum measurement of the central tracking system is superior to the calorimetric measurement for charged particles with low momenta. Therefore it is useful to combine tracking information with calorimetric information to reconstruct the hadronic final state. With increasing momentum, the momentum measurement of charge particles with the tracking system deteriorates, whereas the calorimetric measurement improves. For this reason, only tracks with a transverse momentum below 2 GeV are considered, that are reconstructed in the Central Jet Chamber. The combination of

tracks and clusters is performed by the algorithm FSCOMB, developed in [48], which meticulously avoids double counting of energies using the following prescription:

- Well-measured central tracks, that are constrained to the primary vertex, are extrapolated to the calorimeter front face.
- All energy deposits in the electromagnetic (hadronic) calorimeter within a cylinder of radius 25 (50) cm around the impact point of the track are summed up and assigned to the track.
- In case the energy in the cylinder exceeds the track momentum, the calorimetric energy is used and the track is discarded.
- In case the energy in the cylinder is smaller than the track momentum, the track is taken and the corresponding calorimetric energy is neglected. Therefore clusters are removed one after another, in the order of increasing distance to the track impact point, until their energy equals the track energy.
- Low-momentum tracks that do not reach the calorimeter due to their large curvature are also used.

All remaining tracks and clusters form the so-called *combined objects*. A reconstruction of the hadronic final state with these combined objects improves the hadronic energy resolution and reduces the uncertainty on the energy scale, as shown for instance in [49].

### 5.2.2 Jet Algorithm

Quarks from heavy particle decays or partons emerging from the hard scattering process cannot directly be observed in the detector. Since they carry non-zero color charge, they fragment into collimated showers of hadrons, called *jets*. In principle, a jet comprises the information about the kinematics of the initial quark or gluon. However, due to the production of many low-energetic hadrons in the hadronization process, the jet does not exactly reflect the kinematics of the quark or gluon. A number of jet algorithms have been developed in order to minimize the effects of this long-distance hadronization.

In this thesis, jets are reconstructed using the longitudinally invariant  $k_T$  algorithm [50, 51]. The variables used to characterize each jet are chosen with regard to the invariance under boosts along the beam axis. They are the transverse energy  $E_T = E \sin(\theta)$ , the azimuthal angle  $\phi$ , and the pseudorapidity  $\eta = -\ln(\tan(\frac{\theta}{2}))$ .

The  $k_T$  algorithm starts with a list of objects ("*protojets*"), which in our case are the combined objects defined in the previous section 5.2.1. These protojets are grouped together in the following recursive procedure to form the final jets:

- For each protojet, a separation to the beam axis is defined as:

$$d_i = E_{T,i}^2 . \quad (5.1)$$

- A separation between protojets is defined for each pair of protojets:

$$d_{ij} = \min(E_{T,i}^2, E_{T,j}^2) \cdot \frac{R_{ij}^2}{R^2} , \quad (5.2)$$

where  $R_{ij} = \sqrt{(\eta_i - \eta_j)^2 + (\phi_i - \phi_j)^2}$  is the distance between protojet  $i$  and  $j$  in the  $\eta - \phi$  plane, and  $R$  is a fixed separation parameter (cone radius) chosen to be equal one.

- The smallest of all  $d_i$  and  $d_{ij}$  is labeled  $d_{min}$ .
- If  $d_{min}$  is one of the  $d_{ij}$ , the protojets  $i$  and  $j$  are merged into a new protojet  $k$  with:

$$E_{T,k} = E_{T,i} + E_{T,j} , \quad (5.3)$$

$$\eta_k = (E_{T,i}\eta_i + E_{T,j}\eta_j)/E_{T,k} , \quad (5.4)$$

$$\phi_k = (E_{T,i}\phi_i + E_{T,j}\phi_j)/E_{T,k} . \quad (5.5)$$

- If  $d_{min}$  is one of the  $d_i$ , the protojet  $i$  is not merged with another protojet. It is removed from the list of protojets and added to the final list of jets.

This procedure is repeated until all objects are associated with a jet. The jets which are formed last are the ones with highest  $E_T$  (since  $d_i = E_{T,i}^2$ ) and thus the most relevant ones in the search for top quark decays. In this analysis, jets are required to have a minimum transverse momentum of 4 GeV.

### 5.2.3 Hadronic Calibration

Due to detector effects, caused by imperfections or inhomogeneities of different parts of the calorimeter, and due to an unprecise knowledge of the correct hadronic energy scale, the energies of jets and of the hadronic final state need to be corrected.

A calibration of the hadronic energy scale is performed using the absolute calibration method developed in [52]. The main principle of the method is to impose the transverse momentum balance between the electron and the hadronic final state in neutral current events as correction to the measured hadronic energies. A high  $Q^2$  neutral current sample with one identified electron and exactly one jet is used.

The quantities used in the calibration procedure are the transverse momentum and polar angle of the hadronic final state:

$$P_T^{had} = \sqrt{\left(\sum_h P_x^h\right)^2 + \left(\sum_h P_y^h\right)^2} , \quad (5.6)$$

$$\tan\left(\frac{\theta_{had}}{2}\right) = \frac{\sum_h (E - P_z)_h}{P_T^{had}} , \quad (5.7)$$

where the index  $h$  runs over all hadronic final state particles, and the polar angle of the jet:

$$\tan\left(\frac{\theta_{jet}}{2}\right) = \frac{\sum_j (E - P_z)_j}{P_T^{jet}} , \quad (5.8)$$

where the index  $j$  runs over all hadronic final state particles belonging to the jet.

As a comparison, the hadronic transverse momentum in neutral current events can also be calculated with the double angle method, using the polar angle of the hadronic final state and the electron:

$$P_T^{DA} = \frac{2E_e^0}{\tan\left(\frac{\theta_e}{2}\right) + \tan\left(\frac{\theta_{had}}{2}\right)} . \quad (5.9)$$

The  $P_T$ -balance is calculated as the ratio of the measured hadronic transverse momentum and the transverse momentum calculated with the double angle method:

$$P_{T,bal} = \frac{P_T^{had}}{P_T^{DA}} . \quad (5.10)$$

The calibration is carried out in two steps. First a *relative calibration* between data and Monte Carlo simulation is performed. In the second step, an *absolute calibration* of the hadronic energy is achieved.

- *Relative Calibration:*

Data and Monte Carlo are compared in different regions of the jet polar angle,  $\theta_{jet}$  (i.e. for the different calorimeter wheels), using the ratio:

$$\frac{(P_{T,bal})^{Data}}{(P_{T,bal})^{MC}} . \quad (5.11)$$

This  $P_T$ -balance ratio is used to correct for detector effects, that lead to different descriptions of hadronic energies in the data and the Monte Carlo simulation.

- *Absolute Calibration:*

As a second step, an absolute hadronic energy scale is reached by shifting the  $P_T$ -balance to one. This is done for data and Monte Carlo separately, taking the transverse momentum calculated with the double angle method as reference. The correction factors are again determined for each calorimeter wheel and as a function of  $P_T^{DA}$ .

Selection of neutral current sample
1 electron with $P_T^e > 10$ GeV
1 jet with $\theta_{jet} > 7^\circ$
$P_T^{had}/P_T^e > 0.35$
$P_T^e/P_T^{DA} > 0.88$ (suppresses events with ISR)
$E - P_z > 42$ GeV (suppresses events with ISR)

Table 5.1: Selection criteria for a sample of neutral current events used to check the hadronic energy calibration, as proposed in [52].

The calibration is carried out separately for the data taken between 1994-1997 and 1998-2000. It has been checked using a large sample of neutral current events defined

by the cuts in table 5.1, as proposed in [52]. Figure 5.3 shows the improved resolution after the calibration and the shift of the underestimated hadronic energy scale to the correct value. The  $P_T$ -balance as a function of  $P_T^{DA}$  is shown for data and Monte Carlo. A good agreement is seen. An uncertainty of 4% on the hadronic energy scale is quoted, which is found to be a conservative choice.

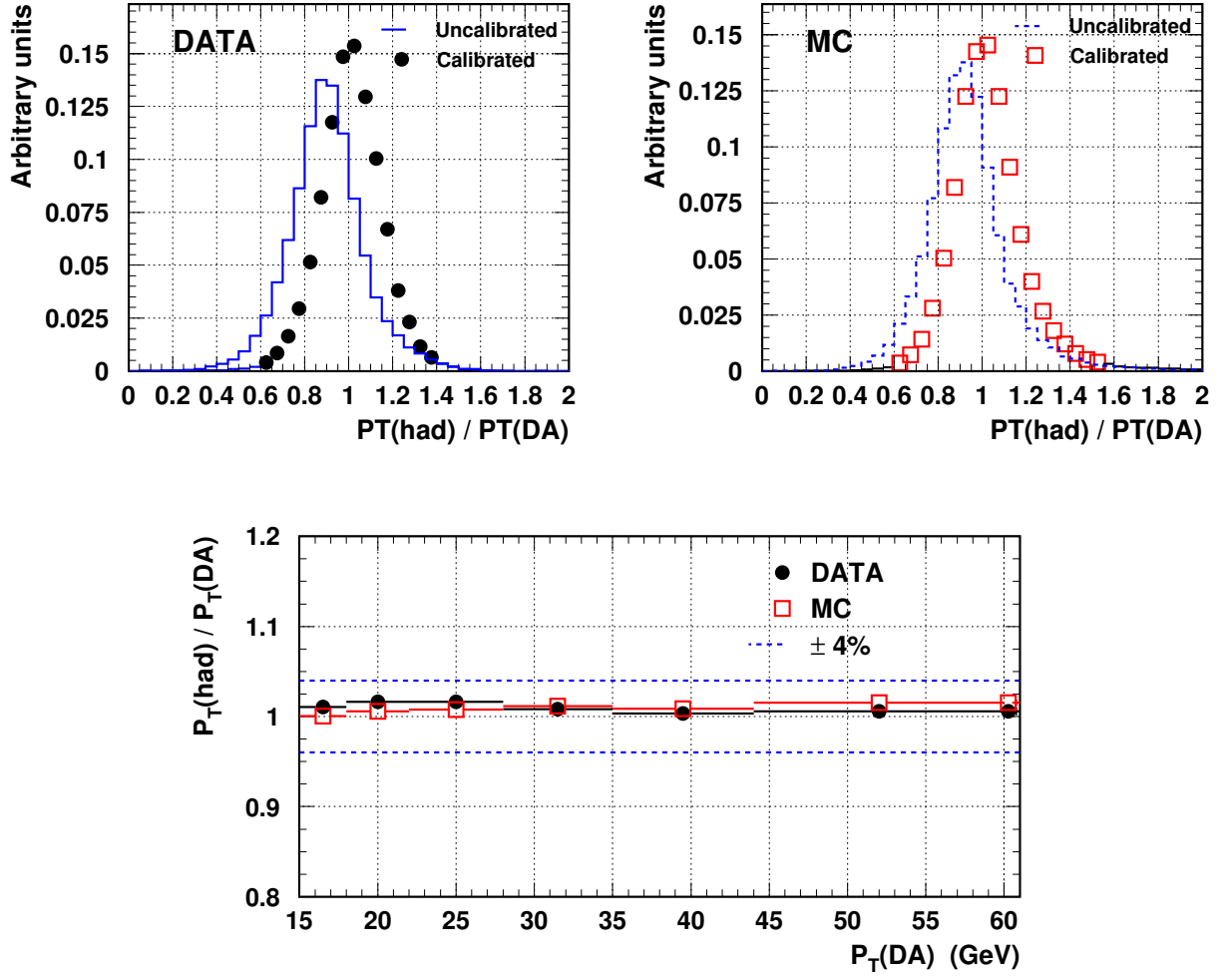


Figure 5.3: The  $P_T$  balance  $P_T^{had}/P_T^{DA}$  is shown for data and Monte Carlo before and after the calibration of the hadronic energy scale (upper plots). The lower plot shows the  $P_T$  balance as a function of  $P_T^{DA}$ .



# Chapter 6

## Top Search in the Semi-Leptonic Decay Channel

In this chapter, the search for single top quark production in the semi-leptonic decay channel, i.e. for decays  $t \rightarrow bW \rightarrow b\ell\nu_\ell$ , is presented. It is motivated by the observation of events with a high- $P_T$  lepton and missing transverse momentum in the H1 detector. This topology suggests the presence of a  $W$  boson in the event. Since  $W$  bosons also emerge from top decays, the selection of events containing a  $W$  serves as basis for the top analysis and is discussed first. A main emphasis is put on the kinematic reconstruction of top quark decays, for instance the reconstruction of the neutrino kinematics, as well as on the choice of observables that can be used to separate a potential top signal from Standard Model processes. The selection of top candidates is performed using both a simple cut-based analysis and a more refined likelihood analysis. Different analysis techniques are applied and compared to each other to maximize the sensitivity to the top signal. The optimized reconstruction and selection techniques presented in this chapter serve also as preparation for the analysis of the data expected from upgraded HERA II in the next years.

### 6.1 “Isolated Leptons” at HERA

In the data collected between 1994 and 1997, the H1 experiment recorded six events with a high- $P_T$  lepton, clearly isolated from other particles in the detector (therefore the name “isolated lepton”), and substantial missing transverse momentum in the event [54]. In one of these events, the high- $P_T$  lepton is an electron, in the other five events they are muons. The observed event topology is so striking, that the first event  $e^+p \rightarrow \mu^+X$  observed in 1994 was worth a publication of its own [53]. Various processes within and beyond the Standard Model have been discussed as possible origin. As an example, lepton flavor violating processes were studied, which lead to a conversion of the incoming electron into a muon. However, the missing transverse momentum in the event could not be explained. The most probable Standard Model interpretation is the production of a real  $W$  boson with subsequent leptonic decay, as introduced in section 2.3.1. The missing transverse momentum is then attributed to the neutrino emerging from the  $W$  decay. Three of the five events, however, exhibit a large transverse

momentum of the hadronic final state, which is an improbable kinematic property for  $W$  production. One of these beautiful events is shown in figure 6.1.

In the following years between 1998 and 2000, more isolated lepton events have been observed. Again some of these events possess an unexpectedly high transverse momentum of the hadronic final state. A large hadronic transverse momentum together with a  $W$  in the event is the typical topology for top decays with subsequent leptonic decay of the  $W$ . One goal of this analysis is to study whether the observed isolated lepton events are more compatible with  $W$  production or with the production of single top quarks.

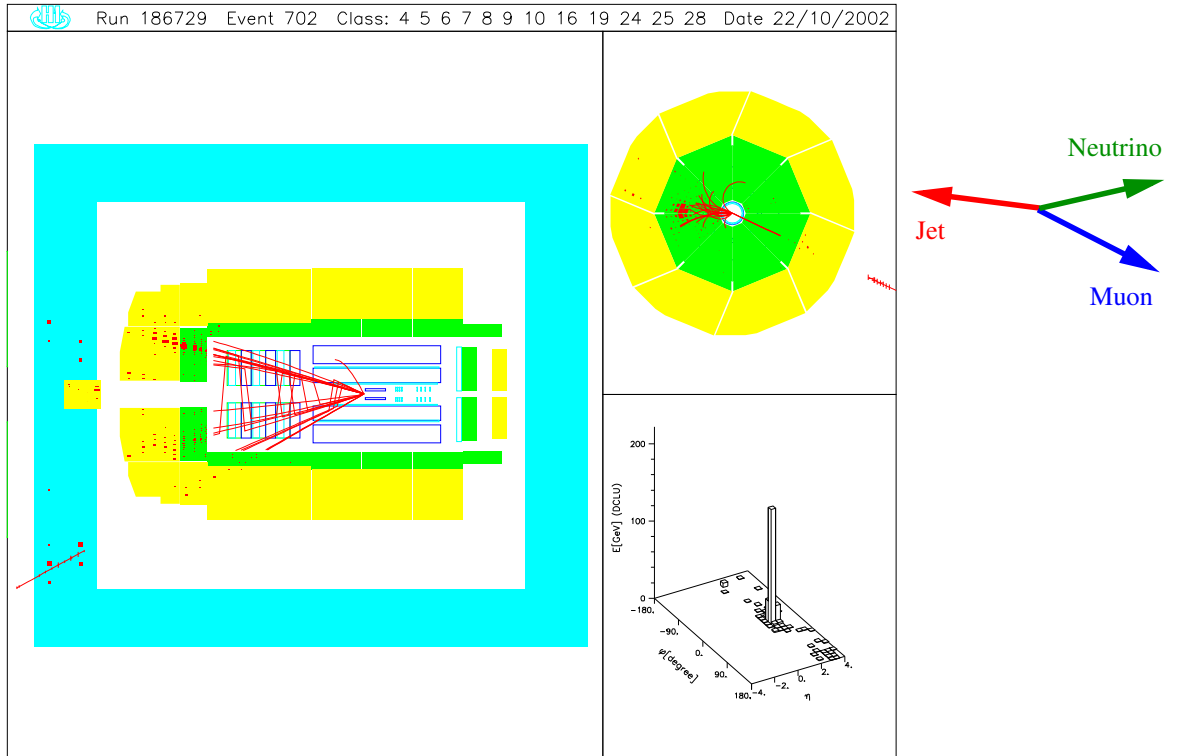


Figure 6.1: Event with a high- $P_T$  muon ( $P_T^\mu = 51_{-11}^{+17}$  GeV), identified by its track in the muon system, and a large missing transverse momentum ( $P_T^{miss} = 28$  GeV). The missing transverse momentum becomes obvious as acoplanarity between the muon and the hadronic final state in the transverse plane. This event has a large hadronic transverse momentum of 67 GeV.

## 6.2 Isolated Lepton Selection and $W$ Production

The selection of events containing  $W$  bosons (called “ $W$  selection” in the following) serves as basis for the search for top quark decays  $t \rightarrow bW \rightarrow b\ell\nu_\ell$  presented in this thesis. At first a pre-selection of events with an isolated lepton and missing transverse momentum is carried out. After the pre-selection, cuts are applied to separate  $W$  production from backgrounds due to other Standard Model processes.

### 6.2.1 Pre-Selection

A pre-selection of isolated lepton events is carried out to obtain a data sample of manageable size for the final  $W$  selection and the top analysis. The following variables are used:

- $\theta_\ell$  : the polar angle of the lepton.
- $P_T^\ell = \sqrt{(P_x^\ell)^2 + (P_y^\ell)^2}$  : the transverse momentum of the lepton.
- $P_T^X = \sqrt{(\sum_h P_x^h)^2 + (\sum_h P_y^h)^2}$  : the transverse momentum of the hadronic final state (the index  $h$  runs over all particles in the hadronic final state).
- $P_T^{calo} = \sqrt{(\sum_i P_x^i)^2 + (\sum_i P_y^i)^2}$  : the total transverse momentum measured in the calorimeter (the index  $i$  runs over all energy deposits in the calorimeter). It is also referred to as the *calorimetric missing transverse momentum*.
- $D_{track}$  : the distance in the pseudorapidity-azimuth ( $\eta - \phi$ ) plane between the lepton and the closest track not associated to the lepton. It is defined by:

$$D_{track} = \sqrt{(\eta_\ell - \eta_{track})^2 + (\phi_\ell - \phi_{track})^2}. \quad (6.1)$$

- $D_{jet}$  : the distance in the  $\eta - \phi$  plane between the lepton and the closest jet, defined in analogy to equation 6.1.

### Kinematic Cuts

The pre-selection criteria common to both the electronic and muonic decays of the  $W$  are the presence of a lepton (an electron or a muon identified as described in section 5.1.1 or 5.1.2) with transverse momentum  $P_T^\ell > 10$  GeV in the polar angle range  $5^\circ < \theta_\ell < 145^\circ$ . In addition, a missing calorimetric transverse momentum  $P_T^{calo} > 12$  GeV is required as a sign of a high- $P_T$  neutrino that escaped detection. Even though  $P_T^{calo}$  is measured only in the calorimeter, it is also used to pre-select events with missing transverse momentum in the muon channel, where the real missing  $P_T$  can differ from  $P_T^{calo}$ , because muons deposits only little energy in the calorimeter. However, applying the cut on  $P_T^{calo}$  ensures an efficient triggering of  $W$  candidate events in both channels.

The kinematic criteria mentioned above represent safe requirements for the selection of  $W$  bosons, since the transverse momentum spectra of the decay lepton and the decay neutrino have Jacobian peaks at  $\sim 40$  GeV, i.e. half the value of the  $W$  mass. Their polar angle distribution has its maximum in the forward direction close to  $\sim 15^\circ$ .

### Isolation of the Lepton

An additional pre-selection requirement is the spatial isolation of the lepton candidate in the detector. Asking for lepton isolation removes a large amount of background with fake leptons or with leptons in or close to a jet. To ensure the isolation of electron candidates, the amount of energy deposited in a region close to the electron cluster is

restricted. Therefore all energy deposits in a cone of radius one around the direction of the electron candidate are summed up and compared to the energy of the electron cluster itself. Electron candidates are accepted as isolated if the hadronic energy around the electron cluster does not exceed 3% of the electron energy, i.e.  $\frac{E_{cone}}{E_e} < 1.03$ .

In the muon channel, a minimum distance in  $\eta - \phi$  of the muon track with respect to other tracks and with respect to jets is required. The isolation cuts for muons are  $D_{track} > 0.5$  and  $D_{jet} > 1.0$ .

## 6.2.2 Backgrounds to $W$ Production

There are two different types of background that can mimic a leptonic  $W$  decay:

- *Background with real lepton and fake missing  $P_T$ :*

The first type of background events contains a true lepton, but a fake missing transverse momentum. For example, this can be the case for neutral current DIS and lepton-pair production in photon-photon collisions. The fake transverse momentum is either due to fluctuations in the hadronic or electromagnetic energy measurements or due to large energy losses outside of the calorimeter acceptance. Also semi-leptonic heavy flavor decays produce real leptons. However, the transverse momentum of these leptons is low compared to  $W$  decays.

- *Background with real missing  $P_T$  and fake lepton:*

The second type of background has a true missing transverse momentum, attributed to a neutrino, but a falsely identified lepton. This can be the case for charged current DIS, where either a radiated photon or a hadron, which deposits a compact cluster of energy in the electromagnetic calorimeter, e.g.  $\pi^0 \rightarrow \gamma\gamma$ , is misidentified as an electron.

The process with the largest total cross-section at HERA is photoproduction. However, for photoproduction events both a fake lepton and fake missing  $P_T$  is in general needed to mimic  $W$  production. Hence the background contribution from photoproduction is rather small. Also non- $ep$  background events such as interactions of cosmic or halo muons can cause a missing transverse momentum, they are however already suppressed using the topological background finders and cuts described in section 4.4.

## Event Yields of the Pre-Selection

The pre-selection criteria for the electron channel yield 3063 data events compared to a total Standard Model expectation of 3165.8 events. At this stage, the Standard Model expectation is dominated to  $\sim 98\%$  by neutral current DIS. The remaining background from other processes is due to charged current DIS, electron-pair production and photoproduction to about equal parts. The expectation for  $W$  production amounts to only 12.5 events.

The main background to  $W$  production in the electron channel is neutral current DIS. The missing transverse momentum comes from energy losses or fluctuations in the energy measurement. These lead to a tail in the  $P_T^{calo}$  distribution up to values of 25-30 GeV. It is a priori not clear, how well the detector simulation describes these

effects. In figure 6.2, the  $P_T^{\text{calo}}$  distribution for a study sample of neutral current DIS events is shown. The comparison of the data with the Monte Carlo prediction from DJANGO shows that for large values of  $P_T^{\text{calo}}$ , the data undershoot the prediction. However, the data are reasonably well described within about 30%, which reflects the size of the uncertainty on the background prediction for this analysis.

In  $ep$  collisions, the yield for events containing a muon in the final state is naturally much lower than for electrons. Therefore the  $W$  selection in the muon channel already starts on the basis of only a few events and a much smaller Standard Model expectation. The dominant Standard Model process that produces muons at HERA is the pair production in photon-photon interactions, as explained in section 2.3.2. Muons from heavy flavor decays have relatively small transverse momenta, and the cut  $P_T^\mu > 10$  GeV as well as the isolation cuts already eliminate most of these events. Neutral Current DIS and photoproduction with falsely identified muons give some small contribution to the background. Charged Current DIS is negligible. The pre-selected muon sample contains 31 data events in agreement with the expectation of 26.5 events. The  $W$  contribution amounts to 4.0 events.

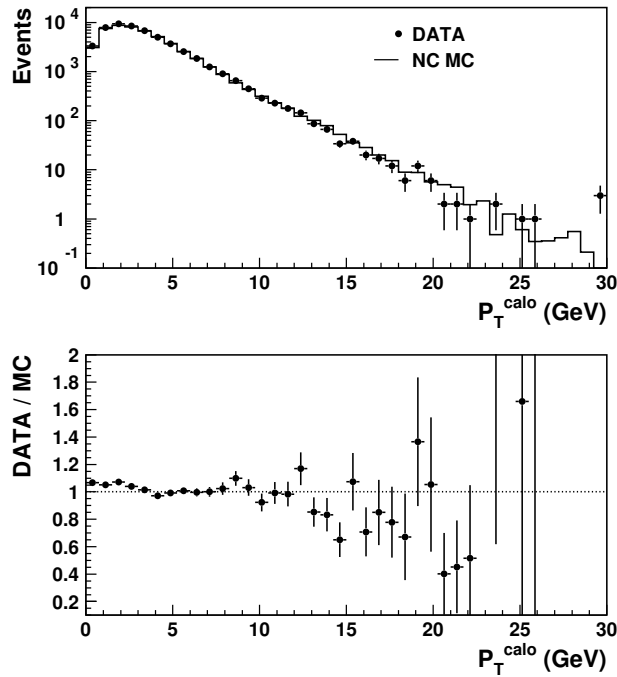


Figure 6.2: Distribution of the missing transverse momentum measured in the calorimeter for a study sample of data events from neutral current DIS compared to the Monte Carlo prediction from DJANGO. In the lower plot, the ratio of the observed data and the Monte Carlo prediction is shown.

## Control Distributions

Kinematic distributions of the pre-selected data samples and the Monte Carlo samples of the Standard Model background processes are presented in figure 6.3 for the electron channel and in figure 6.4 for the muon channel. The Monte Carlo simulations are normalized according to the integrated luminosity of the data. The dark shaded histogram corresponds to  $W$  production. The main background process, i.e. neutral current DIS in the electron channel and muon-pair production in the muon channel, is shown as open histogram. The other background processes are summed up and are represented by the hatched histogram. The data are displayed as black dots with error bars representing the statistical errors.

For each channel, distributions of the transverse momentum and polar angle of the lepton as well as the transverse momenta  $P_T^{calo}$  and  $P_T^X$  are shown. The data and Monte Carlo distributions are in agreement within the error band shown for the total Standard Model expectation. The presented error corresponds to the quadratic sum of the systematic errors assumed for the  $W$  expectation and for the expectation of the other Standard Model processes. An error of 30% is given to the  $W$  prediction modeled by EPVEC. It is taken from the cross-section calculation in [25]. As for the background processes, control distributions for events with  $P_T^{calo}$  above 12 GeV were studied in [55] using data samples specifically enriched for each of the Standard Model backgrounds. A 30% error is deduced for these processes from the agreement between data and Monte Carlo distributions. For neutral current DIS, this error is consistent with the result obtained from the study shown in figure 6.2.

### 6.2.3 Selection of Events with $W$ Bosons

Starting from the pre-selected isolated lepton sample, an optimized set of kinematic cuts, which has been developed in [55, 56], is used to discriminate a potential  $W$  signal from other Standard Model processes. A number of kinematic quantities are calculated for each event, which are either sensitive to undetected energetic particles or exploit some other kinematic property that has a good discrimination power to reject non- $W$  background. These quantities are defined as follows:

- $P_T^{miss}$  : the total missing transverse momentum, reconstructed from all detected final state particles, including muons. The presence of a muon in the event, which in general deposits only a small fraction of its energy in the calorimeter, causes  $P_T^{miss}$  to differ from  $P_T^{calo}$ .
- $(E - P_z)_{vis} = \sum E_i(1 - \cos \theta_i)$ , where the index  $i$  runs over all detected final state particles. If no energy is lost in the event, the visible  $E - P_z$  equals twice the energy of the incoming electron:  $(E - P_z)_{vis} = 2E_e^0 = 55$  GeV. By definition, this quantity is insensitive to energy losses in proton direction (positive  $z$ -direction).

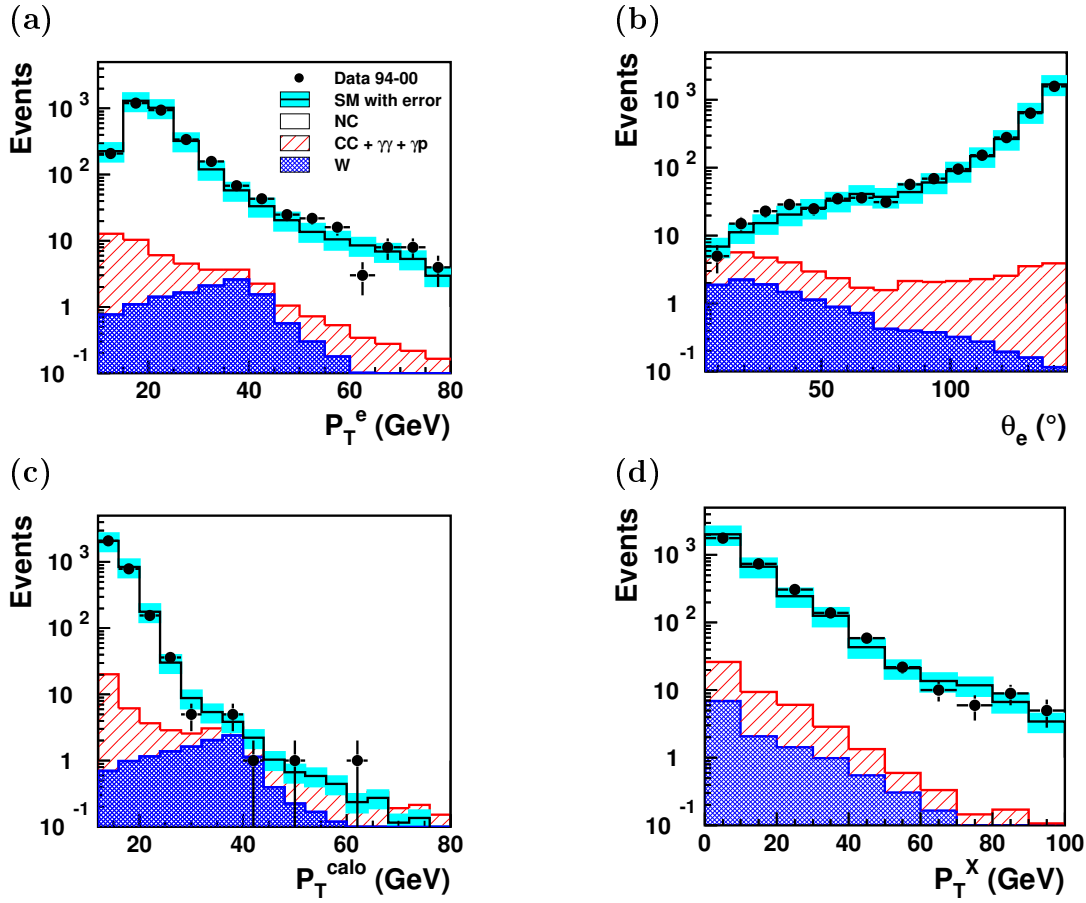


Figure 6.3: Control distributions of the pre-selected data and Monte Carlo samples in the electron channel. (a) The transverse momentum of the electron, (b) the polar angle of the electron, (c) the calorimetric missing transverse momentum in the event, and (d) the transverse momentum of the hadronic final state  $X$ .

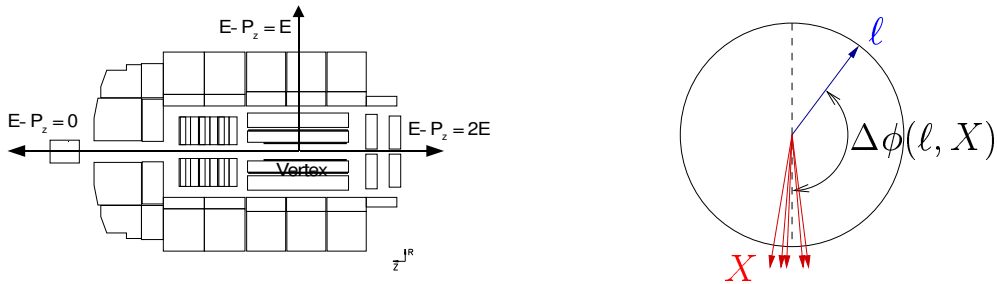


Figure 6.5: Illustration of the quantity  $E - P_z$  and the acoplanarity  $\Delta\phi(\ell, X)$ .

- $\Delta\phi(\ell - X)$  : the azimuthal angle between the lepton and the hadronic final state. It corresponds to the acoplanarity of the event in the transverse plane.
- $\zeta_\ell^2 = 4E_\ell E_e^0 \cos^2(\theta_\ell/2)$ , where  $E_\ell$  denotes the energy of the lepton. If the lepton is the scattered beam electron,  $\zeta_\ell^2$  is equal to the momentum transfer  $Q^2$ .
- $\frac{V_{ap}}{V_p}$  : a measure of the azimuthal balance in the event. It is defined as the ratio of

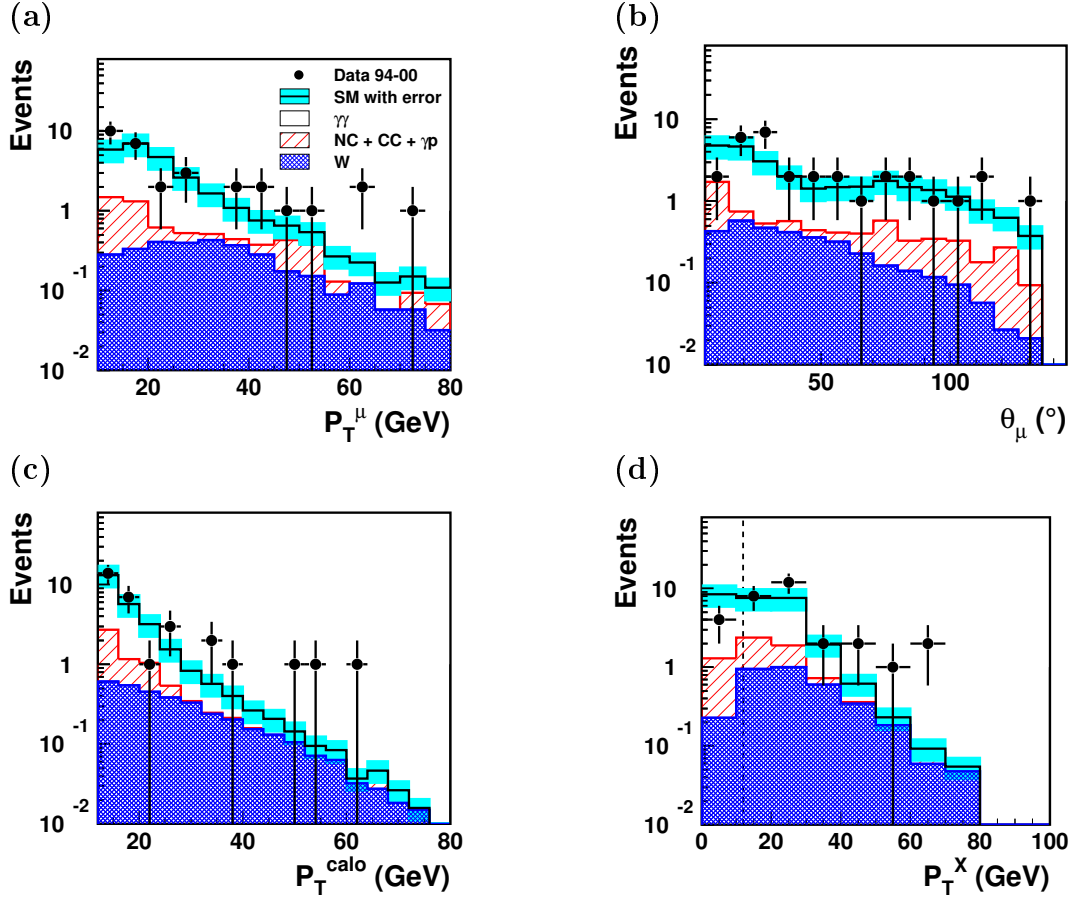


Figure 6.4: Control distributions of the pre-selected data and Monte Carlo samples in the muon channel. (a) The transverse momentum of the muon, (b) the polar angle of the muon, (c) the calorimetric missing transverse momentum in the event, and (d) the transverse momentum of the hadronic final state  $X$ .

the anti-parallel to parallel components of the calorimetric transverse momentum with respect to the direction of the hadronic transverse momentum.

$$V_p = \sum_i \frac{\vec{P}_{T,i} \cdot \vec{P}_T^X}{P_T^X} \quad \text{over all energy deposits } i \text{ with } \vec{P}_{T,i} \cdot \vec{P}_T^X > 0 \quad (6.2)$$

$$V_{ap} = -\sum_i \frac{\vec{P}_{T,i} \cdot \vec{P}_T^X}{P_T^X} \quad \text{over all energy deposits } i \text{ with } \vec{P}_{T,i} \cdot \vec{P}_T^X < 0 \quad (6.3)$$

This quantity was developed in the H1 analysis of neutral and charged current DIS at high  $Q^2$  [45].

### $W$ Selection Cuts in the Electron Channel

After the pre-selection of isolated electron events, the expectation from  $W$  production is about a factor of 250 below the one from neutral current DIS. As a first step to reach a reasonable signal to background ratio, the neutral current contribution needs



to be drastically reduced. This is achieved with a set of "Anti-NC cuts" that exploit the following characteristics of neutral current DIS ( $ep \rightarrow eX$ ):

1.  $\Delta\phi(\ell - X)$  : Due to transverse momentum conservation, the scattered electron and the hadronic final state generally form an angle of  $180^\circ$  in azimuth. If the missing transverse momentum in the event is due to fluctuations in the energy measurement, it will point either along the direction of the hadronic system or the electron. In this case, the angle  $\Delta\phi(\ell - X)$  still tends to be close to  $180^\circ$ . Events with a real neutrino from a  $W$  decay exhibit a flat distribution. A cut  $\Delta\phi(\ell - X) < 160^\circ$  is applied to suppress neutral current DIS.
2.  $(E - P_z)_{vis}$  : The distribution of the visible  $E - P_z$  for neutral current DIS peaks at 55 GeV. Energies lost in the very forward direction cause in general only a small decrease in the measured  $(E - P_z)_{vis}$ . Decays  $W \rightarrow \ell\nu$  naturally have much smaller values due to the neutrino. Therefore only events with  $E - P_z < 50$  GeV are selected. This cut is only applied if the electron candidate has the same charge as the incoming beam electron.
3.  $\zeta_e^2$  : If the scattered electron is misinterpreted as electron from the  $W$  decay, the quantity  $\zeta_e^2$  is identical to the momentum transfer  $Q^2$ . The neutral current cross-section falls off steeply with  $Q^2$ . Thus neutral current events generally have small values of  $\zeta_e^2$ , while leptonic  $W$  decays produce large values. A two-dimensional cut is applied on  $\zeta_e^2$  as a function of the calorimetric missing transverse momentum. For  $P_T^{calo} < 25$  GeV,  $\zeta_e^2$  is required to be above 5000 GeV<sup>2</sup>. For  $P_T^{calo} > 25$  GeV, the expectation from neutral current DIS is already quite low and no cut on  $\zeta_e^2$  is imposed.

The cuts dedicated to reduce the neutral current DIS background are summarized in table 6.1 and are indicated as dashed lines in the corresponding distributions in figure 6.6. In the data, 31 events remain for 32.4 expected. The contribution from  $W$  production amounts to 9.3 events.

After imposing the "Anti-NC cuts", neutral current DIS is still the largest background contribution. However, also charged current DIS and photoproduction are now relevant. In a second step, further cuts are applied to reduce the remaining background:

1. *Electron isolation with respect to tracks and jets*: In addition to the calorimetric electron isolation used in the pre-selection, the same isolation criteria as used for the muons are also found to be useful for electrons. In charged current DIS and photoproduction events, the electron candidate is in general falsely identified. If a hadron is misidentified as electron, there are often other tracks or hadronic activity close to the electron candidate, leading to low values of  $D_{track}$  or  $D_{jet}$ . This can be seen in figure 6.7 (a) and (b). Also radiative charged current events with a converted photon ( $\gamma \rightarrow e^+e^-$ ), misinterpreted as a single electron in the electromagnetic calorimeter, cause small values of  $D_{track}$ . To remove these backgrounds, a minimum distance to the closest track,  $D_{track} > 0.5$ , and to the closest jet,  $D_{jet} > 1.0$ , are required as additional isolation criteria. Since particle showers can be produced in interactions of the electron with the end cap of the

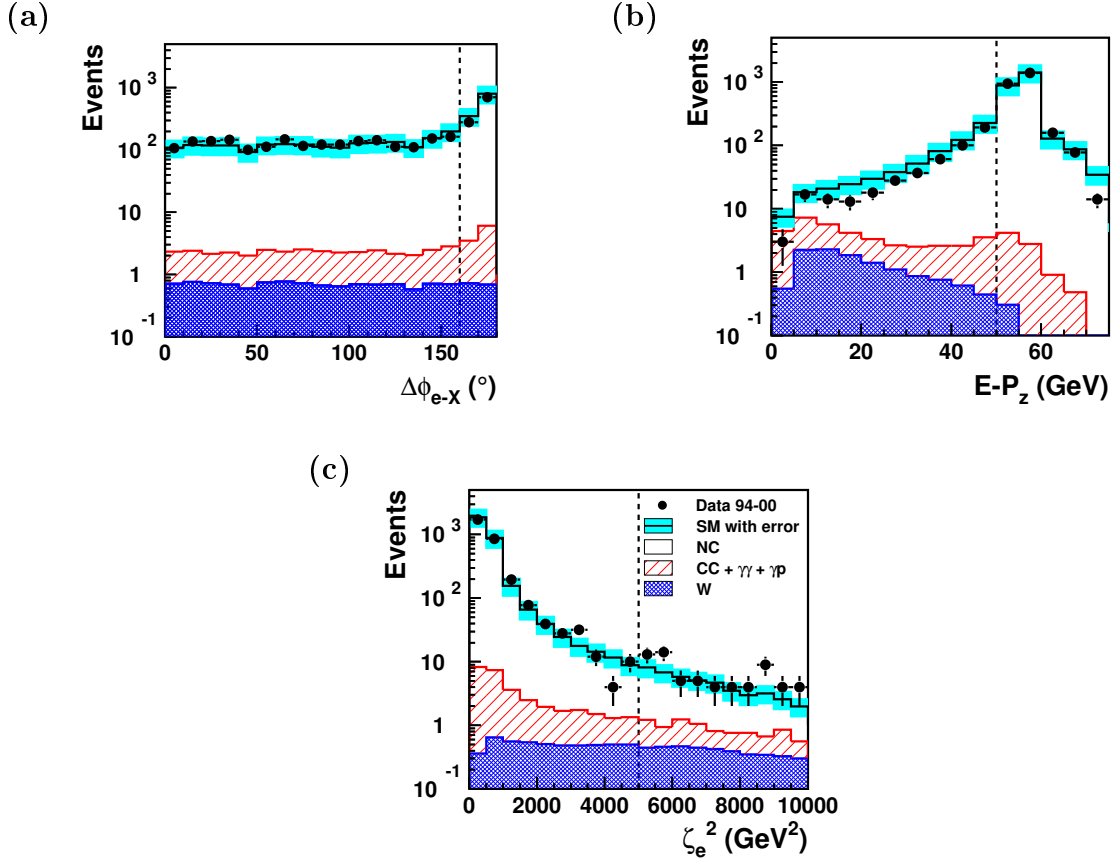


Figure 6.6: Distributions of the observables used to reduce the background from neutral current DIS in the pre-selected electron sample. The values of the applied "Anti-NC cuts" are indicated as dashed lines. The cut  $\zeta_e^2 > 5000 \text{ GeV}^2$  is only applied for  $P_T^{calo} < 25$ .

Central Jet Chamber or dead material in the forward region of the detector, the cut on  $D_{track}$  is only applied for  $\theta_e > 45^\circ$ .

2. *Azimuthal balance  $\frac{V_{ap}}{V_p}$* : The quantity  $\frac{V_{ap}}{V_p}$  can be interpreted as the fraction of energy in the direction of the calorimetric missing transverse momentum. Events from neutral current DIS and photoproduction tend to have large values of  $\frac{V_{ap}}{V_p}$ . Events in which the missing momentum is due to high- $P_T$  particles that deposit no or only little energy in the calorimeter, such as neutrinos or muons, have low values of  $\frac{V_{ap}}{V_p}$ . A two-dimensional cut is applied as a function of the electron transverse momentum  $P_T^e$ . It is illustrated in figure 6.7.

After all selection cuts,  $W$  production dominates the Standard Model expectation. The  $W$  contribution amounts to 70%. The overall efficiency for the selection of events  $W \rightarrow e\nu$  is estimated with the EPVEC generator to be 40%. The final results of the  $W$  selection in the electron channel are presented together with the results in the muon channel, which is discussed in the following section.

Pre-selection	Anti-NC cuts	Further background suppression
$5^\circ < \theta_e < 145^\circ$	$\Delta\phi(e - X) < 160^\circ$	$D_{track} > 0.5$
$P_T^e > 10 \text{ GeV}$	$(E - P_z)_{vis} < 50 \text{ GeV}$	$D_{jet} > 1.0$
$P_T^{calo} > 12 \text{ GeV}$	$\zeta_e^2 > 5000 \text{ GeV}^2$ for $P_T^{calo} < 25$	$\frac{V_{ap}}{V_p} < 0.5$ ( $< 0.15$ for $P_T^e < 25 \text{ GeV}$ )
$\frac{E_{cone}}{E_e} < 1.03$		

Table 6.1: Summary of the cuts used to select decays  $W \rightarrow e\nu$ . The pre-selection criteria for the electron channel are shown in the first column. The second column shows the cuts for the suppression of neutral current DIS. The third column contains the additional cuts to reject the remaining Standard Model background.

### $W$ Selection Cuts in the Muon Channel

In the muon channel, the main emphasis must be put on the reduction of muon-pair production in photon-photon collisions. A set of cuts similar to the ones used in the electron channel is exploited to enhance the  $W$  component relative to the background processes. These cuts are listed in table 6.2 and are discussed below:

1. *Number of isolated muons:* Muons from photon-photon collisions are often produced in backward or in forward direction. Hence one of the two muons frequently disappears in the beam pipe and escapes detection. Events in which both muons are detected are removed by asking for only one isolated muon. The isolation condition for the second muon is essential, since events with muons in or close to a jet, for instance from semi-leptonic decays of a  $b$ -quark, should of course not be rejected.
2.  $\Delta\phi(\mu - X)$  : In inelastic muon-pair production, where one muon is lost in the beam pipe, the angle between the detected muon and the hadronic final state is usually  $180^\circ$ . A cut  $\Delta\phi(\mu - X) < 170^\circ$  thus efficiently suppresses photon-photon events. Also other Standard Model backgrounds are significantly reduced by this cut.
3.  $P_T^{miss}$  : As mentioned earlier, the real missing transverse momentum in events with muons differs from the calorimetric missing transverse momentum,  $P_T^{calo}$ . Therefore events with  $P_T^{calo} > 12 \text{ GeV}$  can still be balanced in transverse momentum, if the muon  $P_T$ -measurement in the tracker is taken into account. Such events are rejected by requiring also  $P_T^{miss}$  to be above 12 GeV.
4.  $P_T^X$  : In contrast to the electron channel, the background contribution becomes less and less important towards higher values of  $P_T^X$ . The peak in the first bin of the  $P_T^X$  distribution in figure 6.8 corresponds to elastic muon-pair production, i.e. events in which the proton stays intact and no or only little hadronic final state is visible. To remove these elastic events, a cut at 12 GeV is imposed on

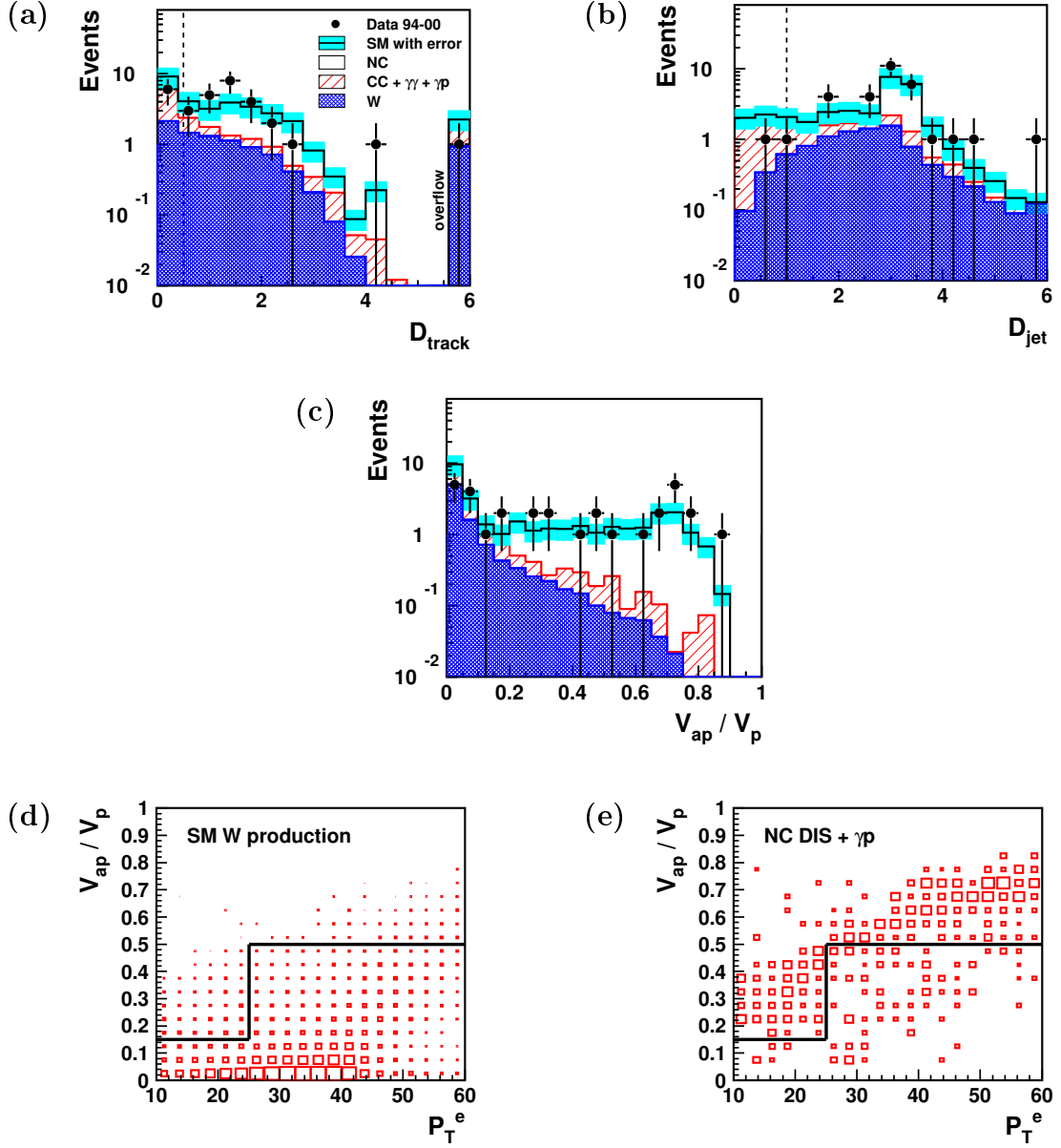


Figure 6.7: Distributions of the observables used to further reduce non- $W$  background in the electron channel after the neutral current suppression is applied. The cuts are indicated as dashed lines in the one-dimensional histograms (a) and (b) and as solid lines in the correlation plots (d) and (e).

$P_{\text{T}}^X$ . Since for muon events the  $P_{\text{T}}^{\text{calo}}$  requirement acts effectively as a cut on the hadronic transverse momentum, the additional cut on  $P_{\text{T}}^X$  causes no significant loss of  $W$  efficiency.

5.  $\frac{V_{\text{ap}}}{V_{\text{p}}}$ : Corresponding to the electron channel, a two-dimensional cut is applied on the azimuthal balance  $\frac{V_{\text{ap}}}{V_{\text{p}}}$  as a function of  $P_{\text{T}}^{\text{calo}}$  to reduce the remaining

background from neutral current DIS and photoproduction. It is illustrated in figures 6.8 (f) and (g).

Pre-selection	Background suppression
$5^\circ < \theta_\mu < 145^\circ$	$\Delta\phi(\mu - X) < 170^\circ$
$P_T^\mu > 10 \text{ GeV}$	$P_T^X > 12 \text{ GeV}$
$P_T^{calo} > 12 \text{ GeV}$	$P_T^{miss} > 12 \text{ GeV}$
$D_{track} > 0.5$	$\# \text{ isolated } \mu = 1$
$D_{jet} > 1.0$	$\frac{V_{ap}}{V_p} < 0.5$ ( $< 0.15$ for $P_T^{calo} < 25 \text{ GeV}$ )

Table 6.2: Summary of the pre-selection in the muon channel and the cuts used to reject non- $W$  background.

This muon selection results in a  $W$  contribution of close to 90%. The overall efficiency of selecting  $W$ 's is  $\sim 15\%$ . For large values of the hadronic transverse momentum ( $P_T^X > 25 \text{ GeV}$ ), approximately the same  $W$  efficiency of  $\sim 40\%$  is reached in the electron and in the muon channel.

### Results of the $W$ Selection

The final event yields of the  $W$  selection in both channels are summarized in tables 6.3 and 6.4. They are presented for different ranges of the hadronic transverse momentum. The contributions from  $W$  production and from all other Standard Model processes are also given separately.

In figures 6.9 (a) and (c), the transverse mass distributions of the lepton-neutrino system are shown. The transverse mass is defined as the invariant mass of the two (massless) vectors obtained by projecting the lepton and neutrino momenta onto the transverse plane:

$$M_T^{\ell\nu} = \sqrt{(|\vec{P}_T^\ell| + |\vec{P}_T^{miss}|)^2 - (\vec{P}_T^\ell + \vec{P}_T^{miss})^2}. \quad (6.4)$$

The transverse momentum of the hypothetical neutrino from the  $W$  decay corresponds to the missing transverse momentum in the event. The  $M_T^{\ell\nu}$  distributions of the data events are compatible with a Jacobian peak close to the  $W$  mass for both channels, as expected from the  $W$  simulation. This result nicely supports the  $W$  hypothesis of the observed events.

As can be seen from the  $P_T^X$  spectra in figures 6.9 (b) and (d) and the event numbers in tables 6.3 and 6.4, there is a clear excess of data events for large values of  $P_T^X$ , observed in both the electron and muon channels. Combining both channels for  $P_T^X > 25 \text{ GeV}$ , eleven isolated lepton events are observed for  $3.67 \pm 0.96$  expected. The following section discusses the degree of agreement between the observed  $P_T^X$  constellation and the  $P_T^X$  spectra predicted by the Standard Model.

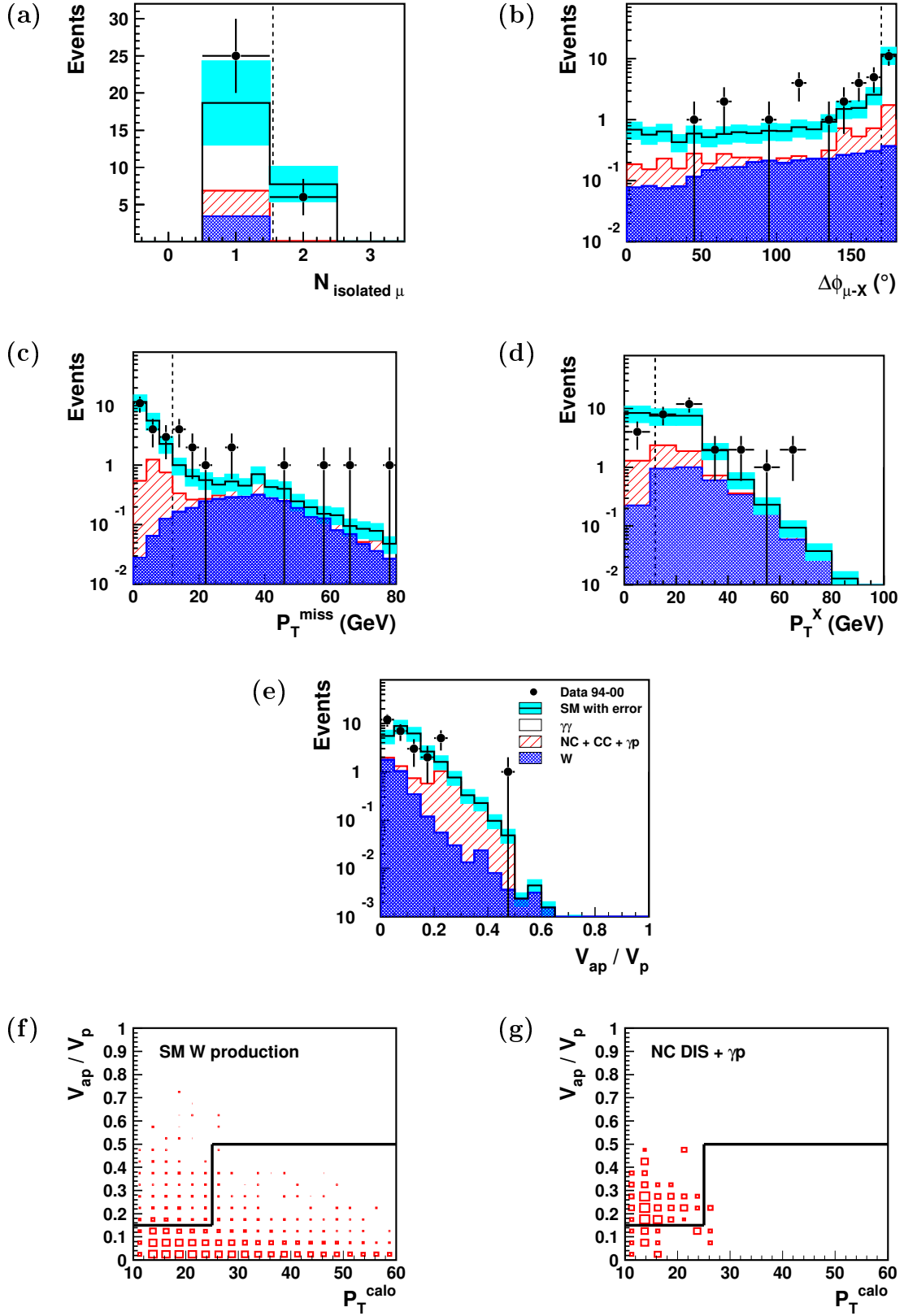


Figure 6.8: Distributions of the observables used to suppress non- $W$  background for the pre-selected muon sample. The cuts are indicated as dashed lines in the one-dimensional histograms (a)-(d) and as solid lines in the correlation plots (f) and (g).

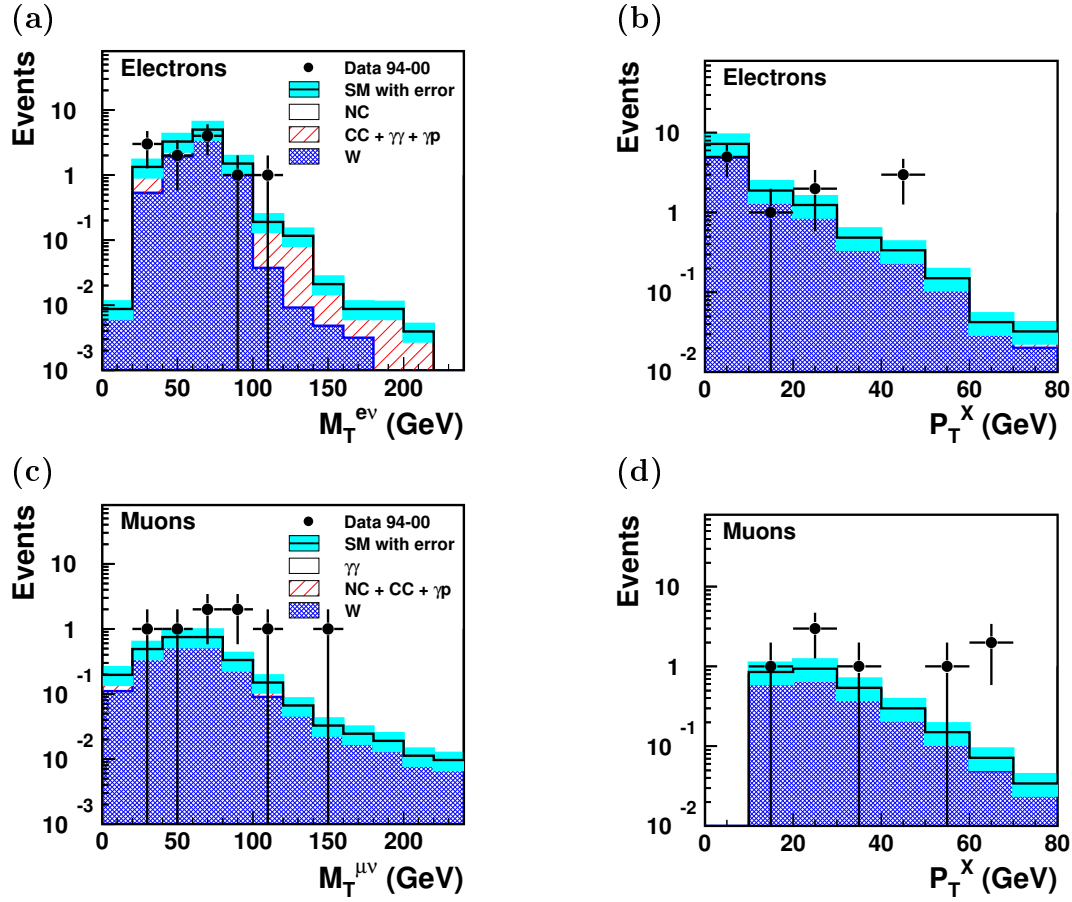


Figure 6.9: Final distributions of the transverse mass  $M_T^{\ell\nu}$  and the hadronic transverse momentum after the  $W$  selection.

Electrons	Data 94-00	SM expectation	$W$ prod.	Other processes
$0 < P_T^X < 12$ GeV	5	$7.43 \pm 1.67$	$5.01 \pm 1.50$	$2.42 \pm 0.73$
$12 < P_T^X < 25$ GeV	1	$2.18 \pm 0.50$	$1.53 \pm 0.46$	$0.65 \pm 0.20$
$25 < P_T^X < 40$ GeV	2	$1.15 \pm 0.30$	$0.95 \pm 0.29$	$0.19 \pm 0.06$
$P_T^X > 40$ GeV	3	$0.73 \pm 0.18$	$0.57 \pm 0.17$	$0.16 \pm 0.05$
Total	11	$11.48 \pm 2.63$	$8.06 \pm 2.42$	$3.42 \pm 1.03$

Table 6.3: The final event yields obtained with the  $W$  selection in the electron channel. The event numbers of the data and the Monte Carlo expectations are given for different ranges of the hadronic transverse momentum  $P_T^X$ .

### 6.3 How Likely is the Excess at high $P_T^X$ ?

The compatibility between the observed and expected  $P_T^X$  spectra for the  $W$  selection is evaluated by computing a confidence level for the hypothesis that only Standard

Muons	Data 94-00	SM expectation	$W$ prod.	Other processes
$12 < P_T^X < 25$ GeV	2	$1.21 \pm 0.31$	$1.03 \pm 0.31$	$0.18 \pm 0.05$
$25 < P_T^X < 40$ GeV	3	$1.06 \pm 0.28$	$0.94 \pm 0.28$	$0.13 \pm 0.04$
$P_T^X > 40$ GeV	3	$0.73 \pm 0.20$	$0.67 \pm 0.20$	$0.06 \pm 0.02$
Total	8	$2.99 \pm 0.80$	$2.63 \pm 0.79$	$0.37 \pm 0.11$

Table 6.4: The final event yields obtained with the  $W$  selection in the muon channel. The event numbers of the data and the Monte Carlo expectations are given for different ranges of the hadronic transverse momentum  $P_T^X$ .

Model processes account for the observed events (*background-only hypothesis*, where background means Standard Model in this case). In the following, the principles of this confidence level calculation are explained step by step. At first, the observed  $P_T^X$  spectra are used without systematic uncertainties. Later the confidence level calculation is repeated taking the uncertainty on the predicted Standard Model rate into account.

### Construction of an Estimator Distribution

As generally done in confidence level computations, an *estimator* (or *test statistic*)  $F$  is introduced to quantify the background-ness of each real and simulated event. It must be a monotonous function. As estimator, the hadronic transverse momentum  $P_T^X$  is chosen. If  $n$  events are observed in the experiment, the estimators  $F_k$  for the single events are added to form an ensemble estimator  $F$ :

$$F = \sum_{k=1}^n F_k = \sum_{k=1}^n (P_T^X)_k . \quad (6.5)$$

The probability distribution of the estimator  $F$  for an experiment with a fixed number of events needs to be constructed. The normalized  $P_T^X$  spectrum corresponds to the probability density function of  $F$  for an experiment with one event,  $\rho_1(F)$ . If there are  $n$  events in the experiment, the joint probability density function  $\rho_n(F)$  can be obtained by iterative integration. As an example, for  $n = 2$  the resulting probability density function  $\rho_2(F)$  is the convolution of  $\rho_1(F)$  with itself:

$$\rho_2(F) = \int \int \rho_1(F_1) \rho_1(F_2) \delta(F - F_1 - F_2) dF_1 dF_2 . \quad (6.6)$$

For  $n$  events this can be generalized as:

$$\rho_n(F) = \int \dots \int \prod_{k=1}^n \left( \rho_1(F_k) dF_k \right) \delta\left(F - \sum_{k=1}^n F_k\right) . \quad (6.7)$$

Since we know the expected number of events from the Standard Model simulations, we are now interested in the probability to observe a certain value of  $F$ , if the expected



number of events is  $b$ . This is achieved by weighting each joint probability density function  $\rho_n(F)$  with the Poisson probability to observe  $n$  events, if  $b$  events are expected:

$$\rho_b(F) = \sum_{n=0}^{\infty} e^{-b} \frac{b^n}{n!} \rho_n(F) . \quad (6.8)$$

Technically,  $\rho_b(F)$  is computed using two different approaches [58]:

1. *Toy Monte Carlo Experiments:*

A large number of toy Monte Carlo experiments are generated. For each event  $k$  in a toy experiment, a value of the estimator  $F_k$  is randomly chosen according to the  $P_T^X$  distribution. The number of events in each experiment is generated from a Poisson distribution with a mean corresponding to the number of expected events. With the generation of 10 000 of these toy experiments, a good approximation of the ensemble estimator distribution  $\rho_b(F)$  is reached.

2. *FFT Method:*

Using a method derived in [57], the distribution  $\rho_b(F)$  can be calculated analytically if the probability density function  $\rho_1(F)$  for a single event is given. The analytic calculation is based on Fourier transformation. The function  $\rho_n(G)$  denotes the Fourier transform of  $\rho_n(F)$ . Then the Fourier transform of a convolution of functions, such as equation 6.7, can be expressed as a product of the Fourier transforms of the functions themselves [57]. Thus  $\rho_n(G)$  can easily be expressed as a power of  $\rho_1(G)$ :

$$\overline{\rho_n(G)} = \left( \overline{\rho_1(G)} \right)^n . \quad (6.9)$$

This leads to the following relation for the ensemble estimator distribution:

$$\overline{\rho_b(F)} = \sum_{n=0}^{\infty} e^{-b} \frac{b^n}{n!} \left( \overline{\rho_1(G)} \right)^n \quad (6.10)$$

$$= e^{b(\overline{\rho_1(G)} - 1)} . \quad (6.11)$$

The application of the inverse Fourier transformation yields  $\rho_b(F)$ . The transformations are performed using a numerical Fast Fourier Transform (FFT).

The ensemble estimator distributions  $\rho_b(F)$  for the electron and muon channels are shown in figure 6.10(a) and (b). The results obtained with the FFT method (solid histogram) and the Monte Carlo experiments (dashed histogram) are in good agreement. The precision of the Monte Carlo method is limited by the number of generated toy experiments. Statistical fluctuations are clearly visible for large values of  $F$ . The FFT method has a higher precision and is less time-consuming compared to the generation of a large number of toy experiments.

### Confidence Level Computation

The confidence level for the background-only hypothesis, denoted by  $\text{CL}_b$  in the following, can now easily be obtained by integration of the ensemble estimator distributions  $\rho_b(F)$ . The confidence level  $\text{CL}_b$  is defined as the probability that the value of the estimator  $F$  for the Standard Model processes is less than the value observed in the data,  $F_{obs}$ :

$$\text{CL}_b = \int_0^{F_{obs}} \rho_b(F) dF . \quad (6.12)$$

As a result, the number  $1 - \text{CL}_b$  corresponds to the probability that the observed data are described by the Standard Model.

The integration is performed for the electron channel and the muon channel separately, and the resulting numbers for  $1 - \text{CL}_b$  are given in table 6.5. The probability of the background-only hypothesis in the electron channel is 11.0 %, in the muon channel it is  $1.1 \cdot 10^{-3}$ . The much lower probability in the muon channel is due to the fact that the three muon events with highest hadronic transverse momenta have values of  $P_T^X$  in the range 50 – 70 GeV, while the electron events with highest  $P_T^X$  have lower values between 40 – 50 GeV (see figure 6.9). In addition, the overall event yield in the electron channel is in agreement with the expectation, whereas the number of muon events lies above the expectation already from  $P_T^X > 12$  GeV on.

### Combination of Electron and Muon Channels

The combination of the electron and muon channels is achieved by adding the  $P_T^X$  distributions of both channels. The estimator distribution and the confidence level are then evaluated for the combined  $P_T^X$  spectrum. The ensemble estimator distribution  $\rho_b(F)$  for the combination is shown in figure 6.10 (c). The value of the integral over this distribution as a function of the upper integration limit  $F_{obs}$  is presented in figure (d). The value of  $F_{obs}$ , which is really observed in the data, and the corresponding confidence level  $1 - \text{CL}_b$  are marked by dashed lines. The probability that the combined electron and muon data are described by the Standard Model is  $1.4 \cdot 10^{-3}$ , neglecting systematic uncertainties.

### Results with Systematic Uncertainties

The systematic errors are dominated by the theoretical uncertainty of 30% on the  $W$  expectation and the other Standard Model processes. Therefore the systematic uncertainties are taken into account by simply scaling up the normalization of the  $P_T^X$  distributions according to the systematic uncertainties quoted in tables 6.3 and 6.4. The probability of the background-only hypothesis for the combination of electrons and muons increases from  $1.4 \cdot 10^{-3}$  without systematics to  $9.7 \cdot 10^{-3}$  with systematics. This probability is low enough to think seriously about adding a signal contribution beyond the Standard Model. One possible signal is single top production.

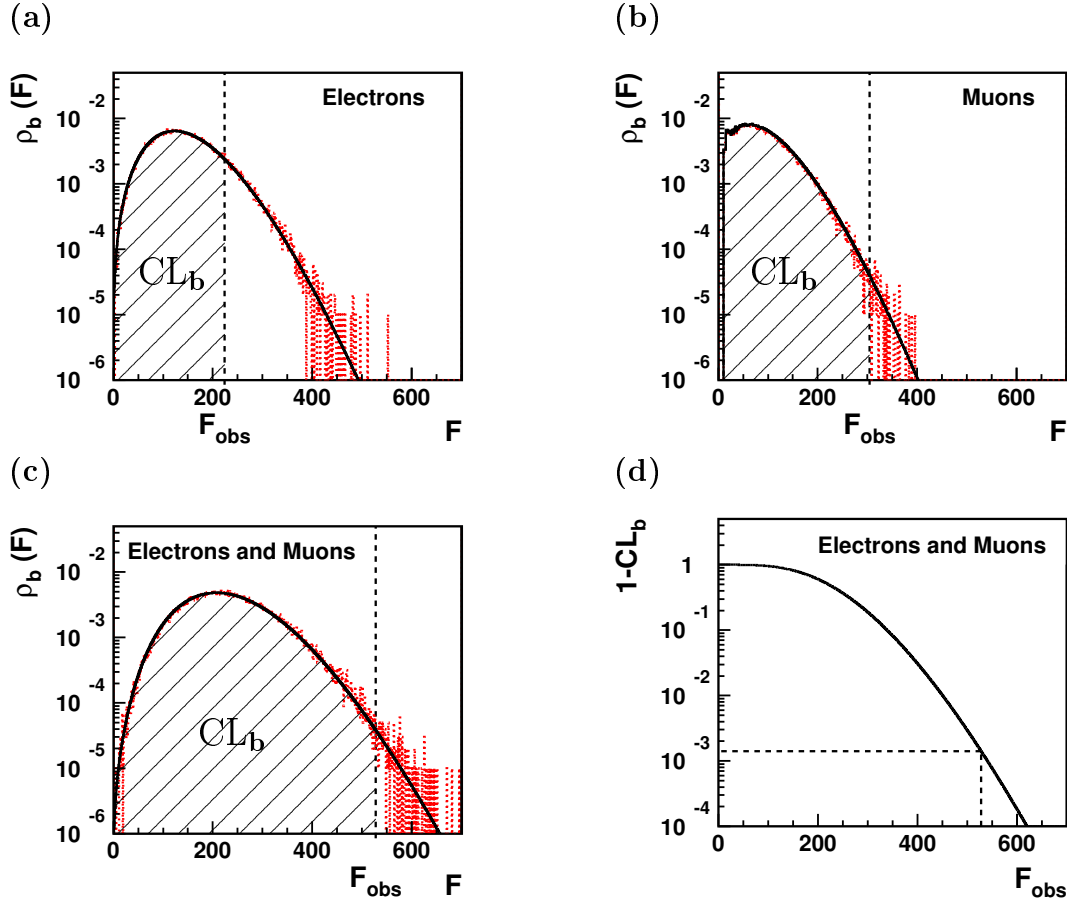


Figure 6.10: The ensemble estimator distributions,  $\rho_b(F)$ , for the electron channel (a) and the muon channel (b). The solid black histogram is calculated with the FFT-method, the dashed histogram with the Monte Carlo method. The combination of both channels yields distribution (c). In (d), the integral over this combined estimator distribution is plotted as a function of the upper integration limit,  $F_{obs}$ . It corresponds to the probability of the background-only hypothesis  $1 - CL_b$ . The confidence level  $CL_b$  is illustrated as hatched area in (a)-(c). The dashed lines correspond to the values observed in the data.

### Results for $P_T^X > 25$ GeV

For comparison, the above described confidence level calculation has been repeated using only the part of the  $P_T^X$  spectrum above 25 GeV. The confidence level is thus more concentrated on the region where the excess is observed. The results for the probability of the background-only hypothesis are also given in table 6.5.

## 6.4 Kinematic Reconstruction of Top Decays

A promising possibility to interpret the isolated lepton excess at high  $P_T^X$  is the production and decay of single top quarks. As discussed in detail in the theoretical overview in section 2.1, the Standard Model cross-section for top production at HERA is ex-

Full $P_T^X$ spectrum	$1 - \text{CL}_b$	
	w/o systematics	with systematics
Electrons	11%	23%
Muons	$1.1 \cdot 10^{-3}$	$4.5 \cdot 10^{-3}$
Electrons and Muons	$1.4 \cdot 10^{-3}$	$9.7 \cdot 10^{-3}$
$P_T^X > 25 \text{ GeV}$		
Electrons	4.5%	8.7%
Muons	$3.1 \cdot 10^{-3}$	$9.1 \cdot 10^{-3}$
Electrons and Muons	$7.4 \cdot 10^{-4}$	$4.0 \cdot 10^{-3}$

Table 6.5: The probabilities  $1 - \text{CL}_b$  that the observed data are described by the Standard Model. The confidence level calculations are carried out with and without consideration of systematic uncertainties. The results are shown for the full  $P_T^X$  spectrum and after a cut  $P_T^X > 25 \text{ GeV}$ .

tremely small and can be neglected. Single top production might, however, proceed through a flavor changing neutral current process with an anomalous  $tu\gamma$ -vertex. The top quark decays to approximately 100% into a  $b$ -quark and a  $W$  boson ( $t \rightarrow bW$ ). The  $b$ -quark is detected as hadronic jet in the calorimeter. As a result of the huge top mass, this  $b$ -jet acquires a large transverse momentum. This could explain why the excess of lepton events is situated at high  $P_T^X$ . If the  $W$  emerging from the top decay undergoes a leptonic decay ( $W \rightarrow \ell\nu$ ), only the lepton is directly measured in the detector, while the neutrino escapes detection. As a first step to obtain the full information about the top decay, it is therefore necessary to find a way to reconstruct the kinematics of the undetected neutrino.

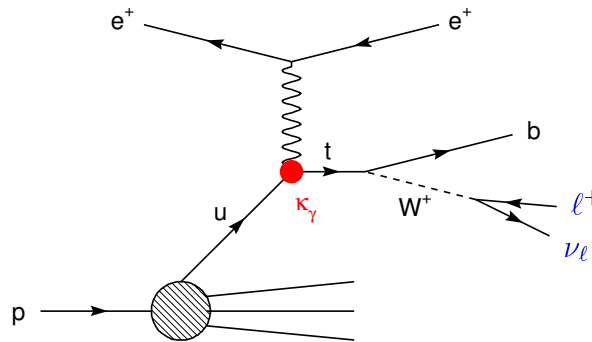


Figure 6.11: Feynman diagram of FCNC single top production at HERA with subsequent decay  $t \rightarrow bW^+ \rightarrow b\ell^+\nu_\ell$ .

### 6.4.1 Reconstruction of the Neutrino

The transverse momentum of a top quark produced in a process as shown in diagram 6.11 is generally very small and is neglected in the following. Under the assumption that there is only one neutrino in the event, the transverse momentum vector of the neutrino can then be reconstructed using the missing transverse momentum measured in the detector.

$$\vec{P}_T^\nu = \vec{P}_T^{miss} . \quad (6.13)$$

As regards the longitudinal momentum of the neutrino, two cases are treated separately:

- *Tagged events:* An event is called "tagged", if the momentum transfer  $Q^2$  is sufficiently large that the scattered beam electron is detected within the acceptance range of the H1 detector. This is the case for 30% of events from single top production (and for 25% of events from Standard Model  $W$  production) . In the muon channel, this means that the event contains an identified electron, and in the electron channel the event contains an additional electron. As single top production proceeds mostly at high values of  $y$ , the energy of the scattered electron is in general quite small. The electron with lowest transverse momentum is assumed to be the scattered electron. According to the top simulation, this assumption is correct in 95% of all tagged events. Since the scattered electron is measured in the main detector, the conservation of the total  $E - P_z$  in the event can be used to obtain the  $E - P_z$  of the neutrino via the relation:

$$(E - P_z)_\nu = 55 \text{ GeV} - (E - P_z)_{vis} . \quad (6.14)$$

Now the complete neutrino kinematics is known. In the data, this method can be applied for three of the eighteen isolated lepton events that pass the  $W$  selection. The lepton-neutrino invariant masses  $M_{\ell\nu}$  of these three tagged data events are compatible with a  $W$  interpretation ( $M_{\ell\nu} = 73_{-7}^{+7}$ ,  $79_{-12}^{+12}$  and  $86_{-9}^{+7}$  GeV). The  $M_{\ell\nu}$  distribution obtained for simulated top events are presented in figure 6.12. The muon-neutrino mass distribution is significantly broader than the electron-neutrino mass as a result of the larger uncertainty on the momentum measurement of high- $P_T$  muon tracks.

- *Untagged events:* Events are called "untagged", if the scattered beam electron is not detected. Therefore its longitudinal momentum is unknown and the constraint on  $E - P_z$  cannot be applied. Instead, another kinematic constraint can be exploited to reconstruct the full neutrino kinematics. A constraint on the invariant mass of the lepton-neutrino system ( $W$  mass constraint) is imposed:

$$M_{\ell\nu} = \sqrt{(E_\ell + E_\nu)^2 - (\vec{p}_\ell + \vec{p}_\nu)^2} = M_W = 80.4 \text{ GeV} . \quad (6.15)$$

The  $W$  mass constraint represents a quadratic equation in the neutrino energy and momentum and hence yields two possible solutions for  $(E - P_z)_\nu$ . As illustrated in figure 6.13, one of the solutions corresponds to a backward neutrino, the

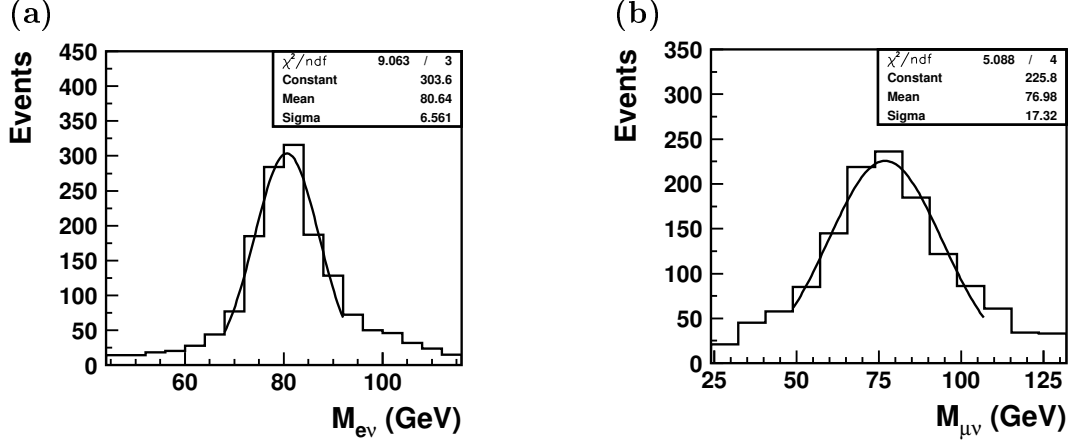


Figure 6.12: Distribution of the reconstructed lepton-neutrino invariant mass for simulated top events ( $t \rightarrow bW \rightarrow b\ell\nu$ ) with a tagged electron. The lines are Gaussian fits to the cores of the mass distributions.

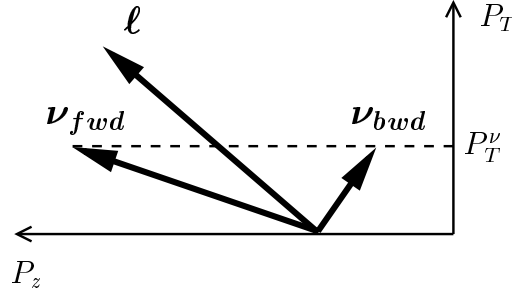


Figure 6.13: Illustration of the two possible solutions for the neutrino momentum obtained from a  $W$  mass constraint, if the transverse momentum of the neutrino is known.

other to a forward neutrino relative to the lepton direction. The two solutions will in the following be named  $\nu_{bwd}$  and  $\nu_{fwd}$ .

#### Reconstruction efficiency:

For events that do not contain a  $W$  boson, it may happen that equation 6.15 has no real solutions. The obtained solutions are then complex conjugate. Due to measurement errors, this can also happen for events that do have a  $W$  boson. In the case of complex conjugate solutions, the imaginary part of the solution is neglected, in order not to lose the event. If a solution for  $(E - P_Z)_\nu$  happens to be negative, it is rejected as being unphysical.

The  $W$  mass constraint for untagged events has a neutrino reconstruction efficiency of 99% in the electron channel and 89% in the muon channel. The loss of efficiency is due to unphysical values of  $(E - P_Z)_\nu$ , i.e. negative solutions. Since the reconstruction efficiency in the electron channel is close to optimal, the lower efficiency in the muon channel can only be a result of the larger uncertainty on the measurement of the muon track momentum compared to the calorimetric energy measurement of the electron.

In order to increase the neutrino reconstruction efficiency for muon events, a variation of the muon transverse momentum is carried out according to the uncertainty given by the measurement of the track curvature. The curvature is proportional to the inverse momentum of the track. A variation of  $\frac{1}{P_T^\mu}$  within  $2\sigma$  is performed:

$$\left(\frac{1}{P_T^\mu}\right)_{varied} = \frac{1}{P_T^\mu} \pm x \cdot \delta\left(\frac{1}{P_T^\mu}\right) \quad \text{with } x \in \{0.1, 0.2, \dots, 2.0\} . \quad (6.16)$$

If this variation yields real solutions of the  $W$  mass constraint, the event kinematics are recomputed according to the changed muon transverse momentum. For the case that real solutions exist for several values of the variation parameter  $x$ , the solution corresponding to the smallest absolute value of  $x$  is taken. The neutrino reconstruction efficiency in the muon channel is thus increased to 95%. As can be seen for simulated top events in figure 6.14, the fraction of events with unphysical negative solutions for  $(E - P_Z)_\nu$  is decreased and a better agreement between the reconstructed and generated  $(E - P_Z)_\nu$  is reached. In addition, also an improvement of the  $P_T^{miss}$  measurement in the event, and hence the transverse momentum of the neutrino, is achieved by this variation. It confirms that the variation of the muon  $P_T$  indeed yields an improved reconstruction of the event kinematics in top events.

#### Choice of the correct solution:

In 12% (7%) of untagged electron (muon) events, the  $W$  mass constraint yields complex conjugate solutions for  $(E - P_Z)_\nu$ . As mentioned before, the imaginary part of the solution is neglected in this case yielding a unique value of  $(E - P_Z)_\nu$ . If two solutions exist, however, a prescription to resolve the ambiguity needs to be given. The aim of such a prescription is to choose the solution for which the reconstructed neutrino kinematically best matches the top hypothesis.

For the top decay  $t \rightarrow b\ell\nu_\ell$ , a natural choice would be to choose the solution that yields an invariant mass of the system lepton-neutrino-hadrons closest to the top mass. The quality of this prescription is tested with simulated top events. The distance in the  $\eta - \phi$  plane between the reconstructed and the generated neutrino,  $D(\nu_{rec} - \nu_{gen})$ , is used to decide if the choice is correct. Using the “closest to the top mass prescription”, the neutrino which best matches the generated neutrino is chosen in 76% (72%) of untagged electron (muon) events that have two solutions.

Some improvement can be reached by exploiting the correlation between the lepton and the neutrino polar angles in top decays. Figure 6.15 shows that for certain regions of the lepton polar angle, one of the two solutions  $\nu_{bwd}$  and  $\nu_{fwd}$  is more likely than the other. The difference  $D(\nu_{bwd} - \nu_{gen}) - D(\nu_{fwd} - \nu_{gen})$  is used to decide which of the solution is better (i.e. yields a reconstructed neutrino that lies closer to the generated neutrino):

$$D(\nu_{bwd} - \nu_{gen}) - D(\nu_{fwd} - \nu_{gen}) \quad \begin{cases} < 0 & : \quad \nu_{bwd} \text{ better solution} \\ > 0 & : \quad \nu_{fwd} \text{ better solution} \end{cases} . \quad (6.17)$$

For small lepton polar angles, the backward neutrino is the most likely and vice versa. Therefore the choice “closest to the top mass” needs only be taken for

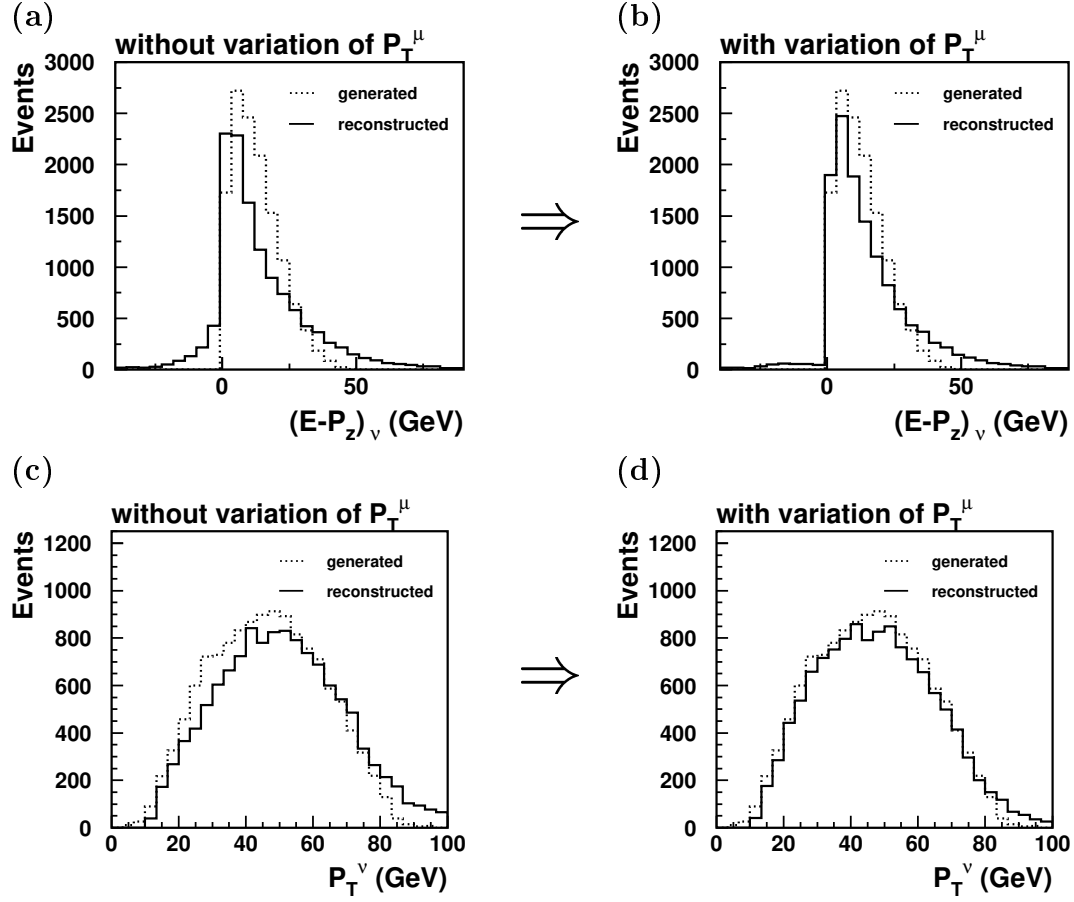


Figure 6.14: Monte Carlo distributions of the reconstructed  $(E - P_Z)_\nu$  and  $P_T^\nu$  for top events in the muon channel. The distributions are shown before and after a variation of the muon track momentum as described by equation 6.16. For events with two solutions for  $(E - P_Z)_\nu$ , one solution is chosen according to the prescription in table 6.6.

intermediate values of the lepton polar angle. The polar angles that are used to define this intermediate region were optimized to obtain the best match between the generated and the reconstructed neutrino. This leads to the prescription presented in table 6.6. The percentage of correct choices is now improved to 83% (78%) in the electron (muon) channel.

Polar angle range	Chosen Solution
$\theta_\ell < 18^\circ$	$\nu_{bwd}$
$18^\circ < \theta_\ell < 40^\circ$	$M_{\ell-\nu-jets}$ closest to top mass
$\theta_\ell > 40^\circ$	$\nu_{fwd}$

Table 6.6: Optimized prescription to choose the correct solution for the neutrino kinematics in untagged single top events.



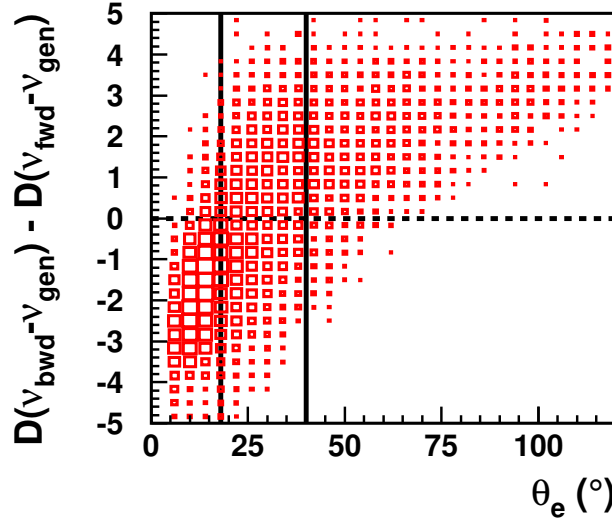


Figure 6.15: Difference of the distances between the generated and the reconstructed neutrino for the two possible neutrino choices ( $\nu_{bwd}$  and  $\nu_{fwd}$ ) as a function of the electron polar angle  $\theta_e$ , shown for untagged simulated top events ( $t \rightarrow be\nu_e$ ). Values on the ordinate less than zero mean that  $\nu_{bwd}$  is closer to the generated neutrino than  $\nu_{fwd}$ , and vice versa. The two vertical lines define the regions of  $\theta_e$ , where  $\nu_{bwd}$  (left),  $\nu_{fwd}$  (right), or the neutrino with  $M_{e-\nu-jets}$  closest to 175 GeV (in between) is the best choice.

Distributions of the reconstructed  $(E - P_z)_\nu$  for all tagged and untagged simulated top events are presented in figure 6.16. The distributions for the choice of the forward, the backward and the best-choice neutrino are shown in comparison to the generated neutrino. A good agreement is seen in the electron channel, and also a reasonable agreement could be reached in the muon channel. The tail towards high values of  $(E - P_z)_\nu$  is due to muons with an unprecise measurement of the track momentum.

### 6.4.2 Reconstruction of the $b$ -Jet and the Top Mass

In most of the cases, the fragmentation products of the  $b$ -quark form a well-collimated hadronic jet in the calorimeter. However, gluons radiated from the  $b$ -quark can produce additional jets with lower energy. These final state parton showers should be included in the kinematic reconstruction of the quark. In both the ANOTOP generator for single top production and the event generators for the Standard Model processes, final state parton showers are implemented in the leading-log approximation. Three possibilities to reconstruct the the  $b$ -quark have been studied, using:

1. The highest- $P_T$  jet
2. The sum of all jets in the event ( $P_T^{jet} > 4$  GeV, no  $\eta_{jet}$ -cut)
3. The complete hadronic final state  $X$  .

Figure 6.17 shows the energy of the reconstructed  $b$ -quark,  $E_b$ , for the three possibilities given above in comparison to the generated energy.

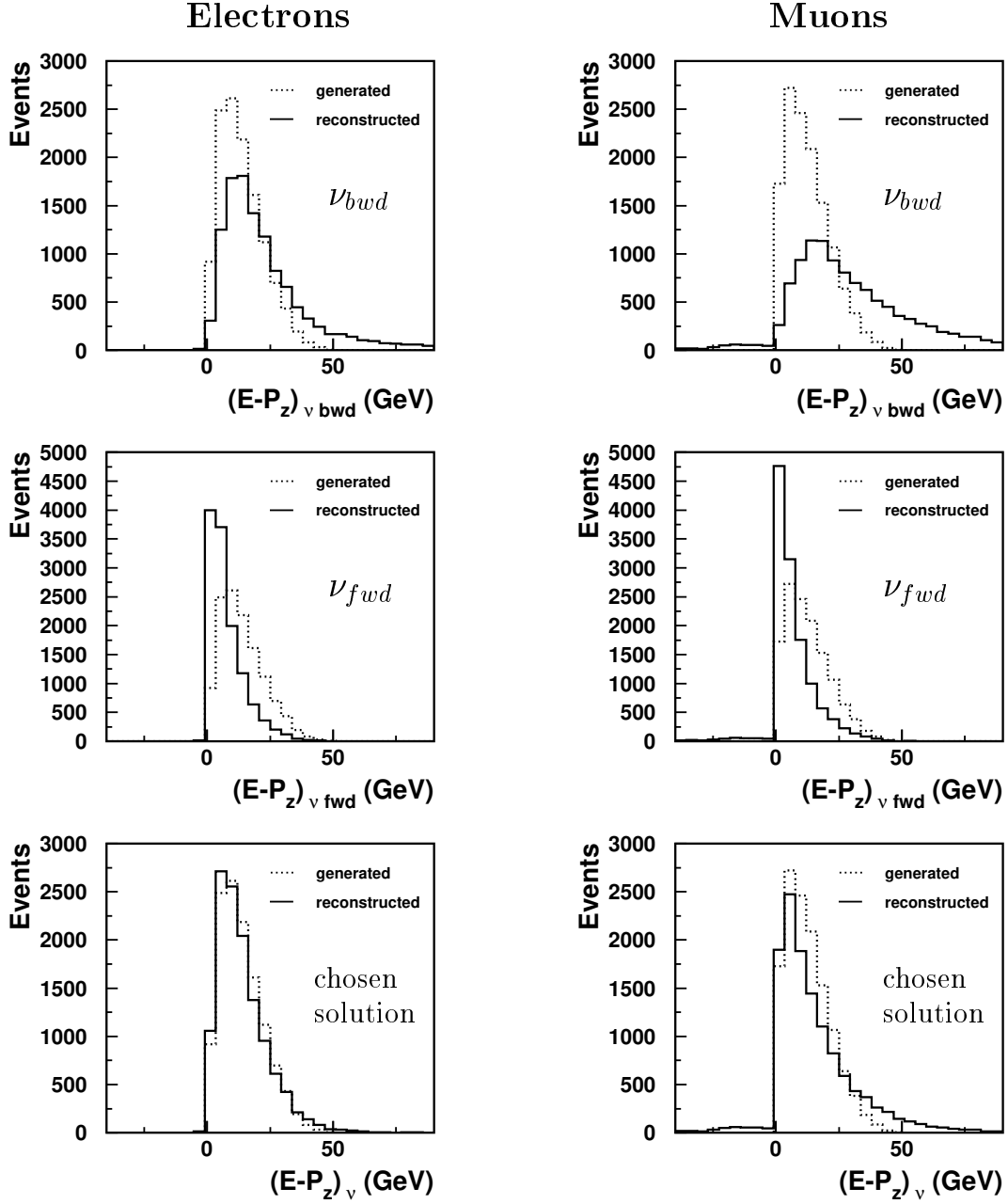


Figure 6.16: Monte Carlo distributions of the reconstructed  $(E - P_z)_\nu$  for the backward, the forward, and the best-choice neutrino obtained from a  $W$  mass constraint in simulated top events. The reconstructed distributions (solid histograms) are compared to the generated distributions (dashed histograms) in the electron channel (left) and the muon channel (right).

The best choice is obviously the sum of all jets in the event. Using only the highest- $P_T$  jet does not take parton showering into account and thus tends to underestimate the energy of the  $b$ -quark. The energy of the complete hadronic final state  $X$  is shifted towards higher values compared to the generated  $b$ -quark energy, mainly due to energy deposits of the proton remnant in the very forward region of the calorimeter.

The top mass can now be calculated as the invariant mass of the lepton, the neutrino, and all jets. Distributions of the top mass obtained for simulated top events are presented in figure 6.18. The mass resolutions taken from Gaussian fits to the  $M_{\ell-\nu-jets}$  distributions are 14.7 GeV for the electron channel and 19.7 GeV for the muon channel. Due to deviations from ideal Gaussians in the tails, only the Gaussian cores of the distributions are used in the fit.

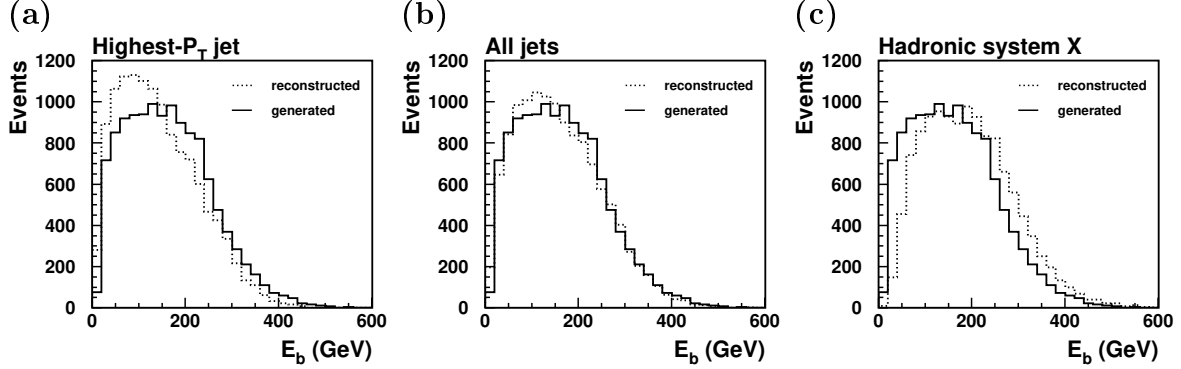


Figure 6.17: Monte Carlo distributions of the generated and reconstructed  $b$ -quark energies in simulated top events. Three different possibilities of the  $b$ -quark reconstruction are compared to each other: (a) highest- $P_T$  jet, (b) sum of all jets, (c) the full hadronic final state  $X$ .

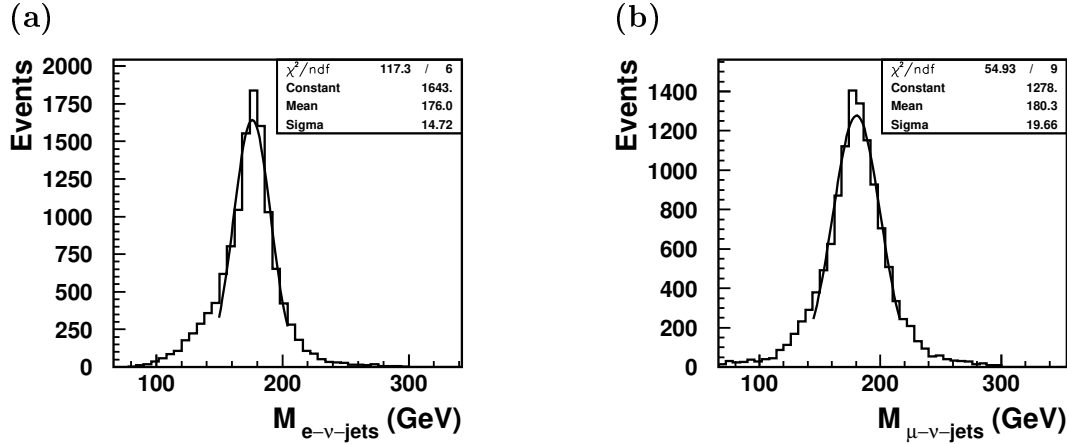


Figure 6.18: Monte Carlo distributions of the invariant mass of the system lepton-neutrino-jets for top decays in the electron channel (a) and the muon channel (b). The mass resolutions are obtained from Gaussian fits (solid lines) to the cores of the distributions.

Table 6.7 gives the reconstructed values of the transverse momentum  $P_T^{jets}$  and the invariant mass  $M_{\ell-\nu-jets}$  for the  $W$  candidate events with high hadronic transverse momentum ( $P_T^{jets} > 25$  GeV). It should be remarked that no data event in the  $W$  selection was lost in the neutrino reconstruction. If two solutions for the neutrino kinematics exist, there are of course also two solutions for the mass  $M_{\ell-\nu-jets}$ . All

solutions for the mass are shown together with the corresponding total  $E - P_z = (E - P_z)_{vis} + (E - P_z)_\nu$  in the event. The best-choice solution, chosen according to the prescription in table 6.6, is underlined. The errors quoted for the masses are obtained event by event from Gaussian variations of the lepton and hadron kinematics within  $\pm 1\sigma$  according to the resolutions of the hadronic and electromagnetic energy measurements ( $\sigma(E_{had}) = 0.7/\sqrt{E_{had}}$ ,  $\sigma(E_{em}) = 0.15/\sqrt{E_{em}}$ ) and the error of the track  $P_T$ -measurement.

Two of the events have a tagged electron and hence the reconstructed mass is unique. For comparison, also the values obtained with the untagged method are computed for these two events, pretending the scattered beam electron is not identified. For the tagged  $e^+$  event, one of the untagged solutions is perfectly consistent with the tagged solution. For the tagged  $\mu^-$  event, both masses computed with the  $W$  mass constraint are lower than for the tagged solution. The reason for this is that for the tagged solution, the reconstructed muon-neutrino invariant mass is about 6 GeV higher than the nominal  $W$  mass used in the mass constraint. However, both methods are consistent within the quoted mass errors.

Lepton	$P_T^{jets}$ (GeV)	Untagged solution $\nu_{bwd}$		Untagged solution $\nu_{fwd}$		Tagged solution	
		$M_{\ell-\nu-jets}$ (GeV)	$E - P_z$ (GeV)	$M_{\ell-\nu-jets}$ (GeV)	$E - P_z$ (GeV)	$M_{\ell-\nu-jets}$ (GeV)	$M_{\ell\nu}$ (GeV)
$e^+$	27	$187^{+17}_{-18}$	65	<u><math>144^{+14}_{-15}</math></u>	40	—	—
$e^+$	43	<u><math>155^{+7}_{-7}</math></u>	62	$135^{+6}_{-6}$	21	—	—
$e^+$	47	$375^{+18}_{-18}$	371	$168^{+8}_{-8}$	55	<u><math>168^{+11}_{-11}</math></u>	$79^{+12}_{-12}$
$e^+$	48	<u><math>160^{+6}_{-6}</math></u>	30	$160^{+6}_{-6}$	30	—	—
$\mu^+$	26	$112^{+5}_{-8}$	37	<u><math>113^{+5}_{-9}</math></u>	32	—	—
$\mu^-$	27	$146^{+9}_{-12}$	47	$136^{+6}_{-6}$	38	<u><math>159^{+6}_{-7}</math></u>	$86^{+7}_{-9}$
$\mu$	27	$123^{+16}_{-19}$	43	<u><math>147^{+52}_{-45}</math></u>	33	—	—
$\mu^+$	55	$274^{+10}_{-10}$	153	<u><math>172^{+9}_{-10}</math></u>	38	—	—
$\mu^-$	64	$164^{+9}_{-9}$	60	<u><math>169^{+11}_{-11}</math></u>	51	—	—
$\mu^+$	72	$210^{+17}_{-30}$	61	<u><math>176^{+9}_{-12}</math></u>	25	—	—

Table 6.7: Kinematics of the isolated lepton events at high hadronic transverse momentum ( $P_T^{jets} > 25$  GeV). Both untagged solutions of the  $W$  mass constraint are given for the mass  $M_{\ell-\nu-jets}$  and the total  $E - P_z = (E - P_z)_{vis} + (E - P_z)_\nu$ . In two events, the scattered beam electron is detected. For these events, the tagged method can be applied and the invariant mass of the lepton-neutrino system,  $M_{\ell\nu}$ , is computed. The chosen solution for the invariant mass is underlined.

## 6.5 Observables to Discriminate Top and $W$ Production

This section is concerned with the separation of the single top signal from Standard Model background processes. The largest background in the search for single top production at HERA is Standard Model  $W$  production. It should be noted that in contrast to the discussion of the  $W$  selection in section 6.2,  $W$  production is now no longer considered as signal, but as background process to top production. The current upper limits on single top production from experiments at LEP and the TeVatron correspond to a cross-section of  $\mathcal{O}(1 \text{ pb})$ . It is of the same order as the cross-section for Standard Model  $W$  production. In this section, different observables are studied to characterize top decays and achieve an efficient separation of the top signal and the background from  $W$  production.

### 6.5.1 Choice of Observables

The relevant degrees of freedom in a top decay are illustrated in figure 6.19. In figure (a) all particles are shown after a boost into the rest frame of the top quark, in (b) all particles are boosted into the rest frame of the  $W$ . The kinematics of top decays can be described by four observables, if the azimuthal angles of the top and the  $W$  decay are neglected. These four observables are the top mass, an angle for the decay  $t \rightarrow bW$ , the  $W$  mass, and an angle for the decay  $W \rightarrow \ell\nu$ .

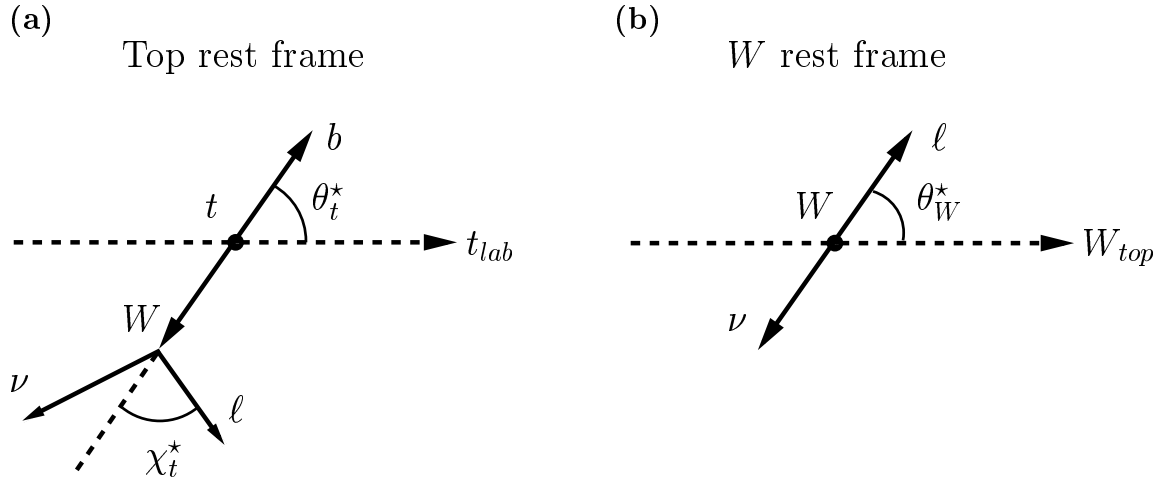


Figure 6.19: Illustrations of the top quark and  $W$  boson decays as viewed in the rest frame of the top (a) and the  $W$  (b).

- *Top Decay Angle:*

The top decay angle is chosen as the angle between the  $b$ -quark in the top rest frame and the direction of the top quark in the laboratory frame. It is denoted by  $\theta_t^*$ . Since top quarks are mainly produced with negligible transverse momentum, the top direction in the laboratory frame is to a good approximation the  $z$ -axis.

The top decay angle is strongly correlated to the transverse momentum of the  $b$ -quark:

$$P_T^b \approx (P_T^b)^* \approx E_b^* \sin(\theta_t^*), \quad (6.18)$$

where the star denotes quantities in the top rest frame. The distribution of  $\theta_t^*$  is shown in figure 6.20 (a) for generated and for reconstructed top events in comparison with reconstructed events from the  $W$  simulation. Only events that pass the  $W$  selection are shown.

Since top quarks produced in  $\gamma$ -exchange are unpolarized, there is no preferred direction for the emission of the  $b$ -quark in the top rest frame. The top decays isotropically. Therefore the cosine of the decay angle,  $\cos(\theta_t^*)$ , is expected to be flat. The observed slight deviations from a flat distribution are due to deficiencies in the neutrino reconstruction and the cuts applied in the  $W$  selection. Good agreement is seen between the generated and reconstructed top events. For Standard Model  $W$  production,  $\cos(\theta_t^*)$  exhibits sharp peaks close to -1 and 1. These peaks correspond to small values of the hadronic transverse momenta  $P_T^{jets}$ , as expected for most events from  $W$  production.

- *W Decay Angle:*

As for the  $W$  decay angle, the angle between the lepton and the direction of the  $W$  boson is chosen. In the top rest frame, it corresponds to the angle  $\chi_t^*$  of figure 6.19 (a). The thus defined angle still includes the boost of the  $W$ , which is determined by the top mass. It is more favorable to eliminate the contribution from the boost of the  $W$  by boosting the lepton and the neutrino four-vectors from the top rest frame into the  $W$  rest frame. The decay angle obtained in the  $W$  rest frame is denoted by  $\theta_W^*$ , as illustrated in figure 6.19 (b). It is the angle between the lepton in the  $W$  rest frame and the  $W$  direction in the top rest frame.

Figure 6.20 shows a good agreement between the generated and reconstructed  $W$  decay angle for top events. The shape of the  $\theta_W^*$  distribution for top events is a consequence of a specific mixture of two possible  $W$  helicity states in top quark decays and the V–A structure of the electroweak theory. A more detailed discussion can be found in appendix B and in [59, 60]. As for the discrimination between top and  $W$  production, this angle has only a rather small separation power.

A set of reconstructed observables is now chosen to separate a possible top signal from the  $W$  background, keeping in mind that the degrees of freedom in top decays is four (neglecting azimuthal angles). In semi-leptonic top decays, as discussed in this chapter, the mass of the  $W$  cannot be exploited, since a  $W$  mass constraint is needed to reconstruct the neutrino kinematics. This reduces the degrees of freedom by one. As mentioned before, the top mass is approximated by the invariant mass of the lepton-neutrino-jets system. Instead of the top decay angle, the transverse momentum of all jets,  $P_T^{jets}$ , is used, which corresponds to the transverse momentum of the  $b$ -quark and is directly measured in the detector.

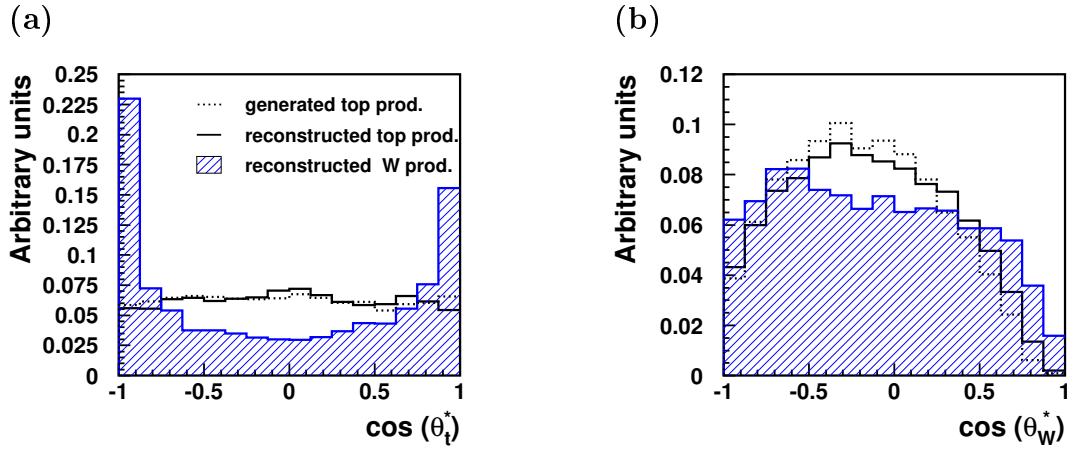


Figure 6.20: Monte Carlo distributions of the cosine of the top decay angle,  $\theta_t^*$ , in the top rest frame (a) and the  $W$  decay angle,  $\theta_W^*$ , in the  $W$  rest frame (b). The distributions are shown for generated (dashed) and reconstructed (solid) top events in the electron channel compared to reconstructed events from the simulation of  $W$  production (hatched). All distributions are normalized to unity.

The three observables used for the discrimination of top and  $W$  production are then:

1.  $P_T^{jets}$ , the transverse momentum of all jets
2.  $M_{\ell-\nu-jets}$ , the invariant mass of the lepton-neutrino-jets system (top mass)
3.  $\theta_W^*$ , the  $W$  decay angle in the  $W$  rest frame .

Distributions of these observables are shown in figure 6.21 for the data and the simulation of  $W$  production and other Standard Model processes. The histograms are normalized according to the integrated luminosity of the data. The top simulation is arbitrarily normalized to match the  $W$  expectation. The positions of the data events are marked with arrows. Concerning the separation of top and  $W$  production, one sees:

- For top events, the reconstructed  $P_T^{jets}$  distributions peak at  $\sim 65$ -70 GeV. The expected Jacobian peak for the transverse momentum of the  $b$ -quark from a top decay lies at 69 GeV. In contrast, events from  $W$  production and other Standard Model processes have mainly small values of  $P_T^{jets}$ .
- The invariant mass  $M_{\ell-\nu-jets}$  has a large separation power. Several of the isolated lepton events have masses that are compatible with the top mass distribution. It must be said, however, that the masses for all but one event lie below 175 GeV.
- The cosine of the  $W$  decay angle  $\theta_W^*$  gives only some small additional contribution to the discrimination against  $W$  production. The Standard Model processes other than  $W$  production are situated mainly at values close to -1 or 1. They make up about 30% of the background in the electron channel and 12% in the muon channel.

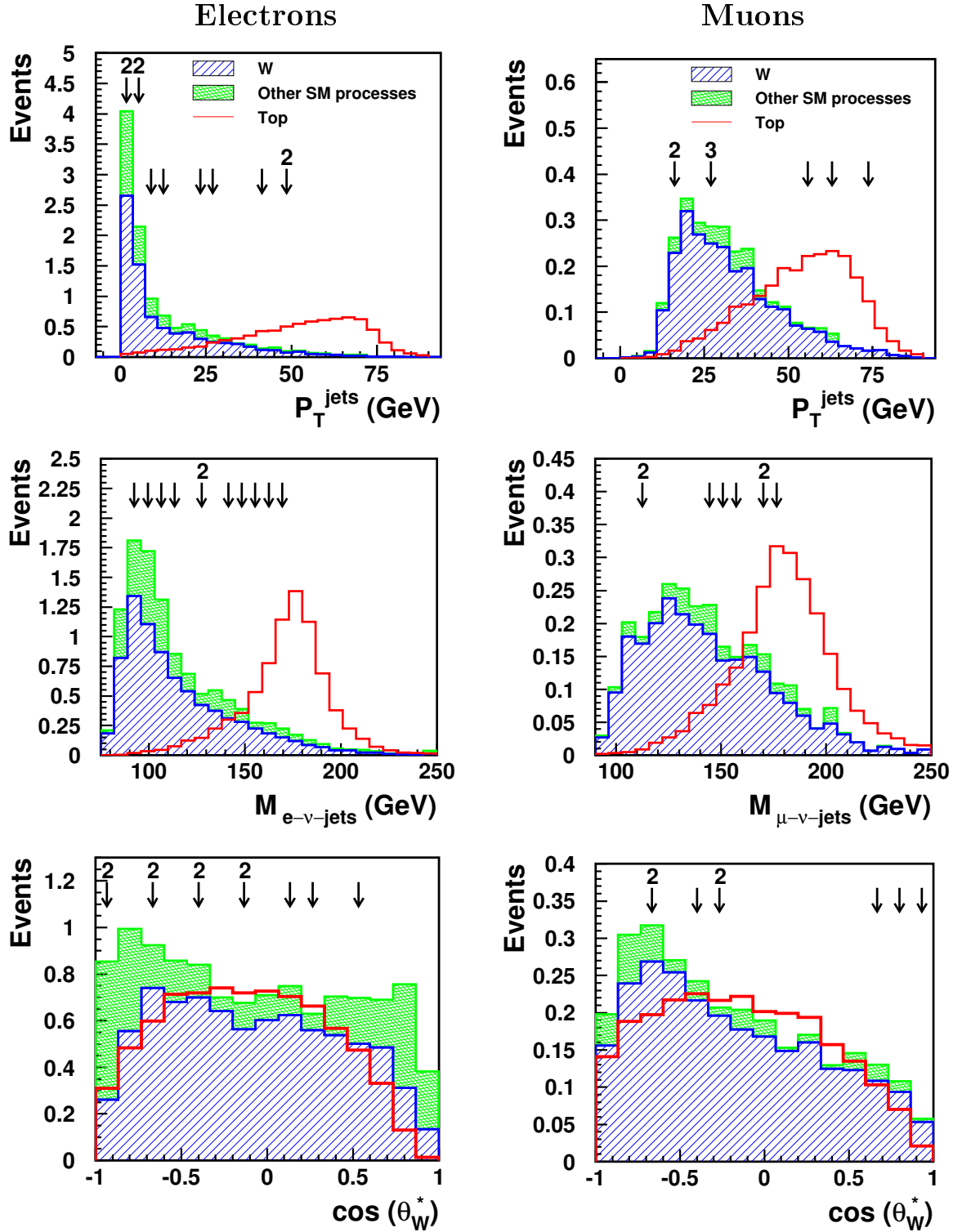


Figure 6.21: Distributions of the three discriminating observables used to separate single top production from Standard Model  $W$  production (left: electron channel, right: muon channel). The top simulation is arbitrarily normalized to the expectation from  $W$  production. The positions of the data events are marked by arrows. A number above the arrow indicates the number of data events in the corresponding bin of the distribution.



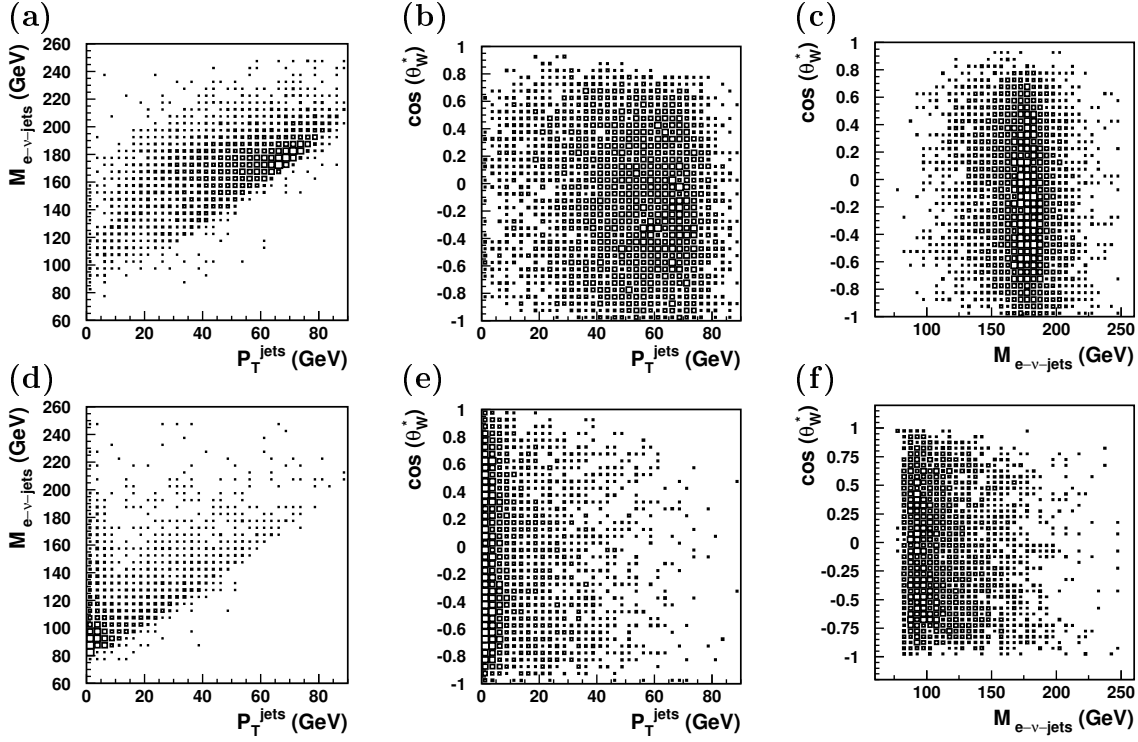


Figure 6.22: Correlations of the discriminating observables in the electron channel for the simulated top signal (upper plots (a)-(c)) and the simulated  $W$  background (lower plots (d)-(f)).

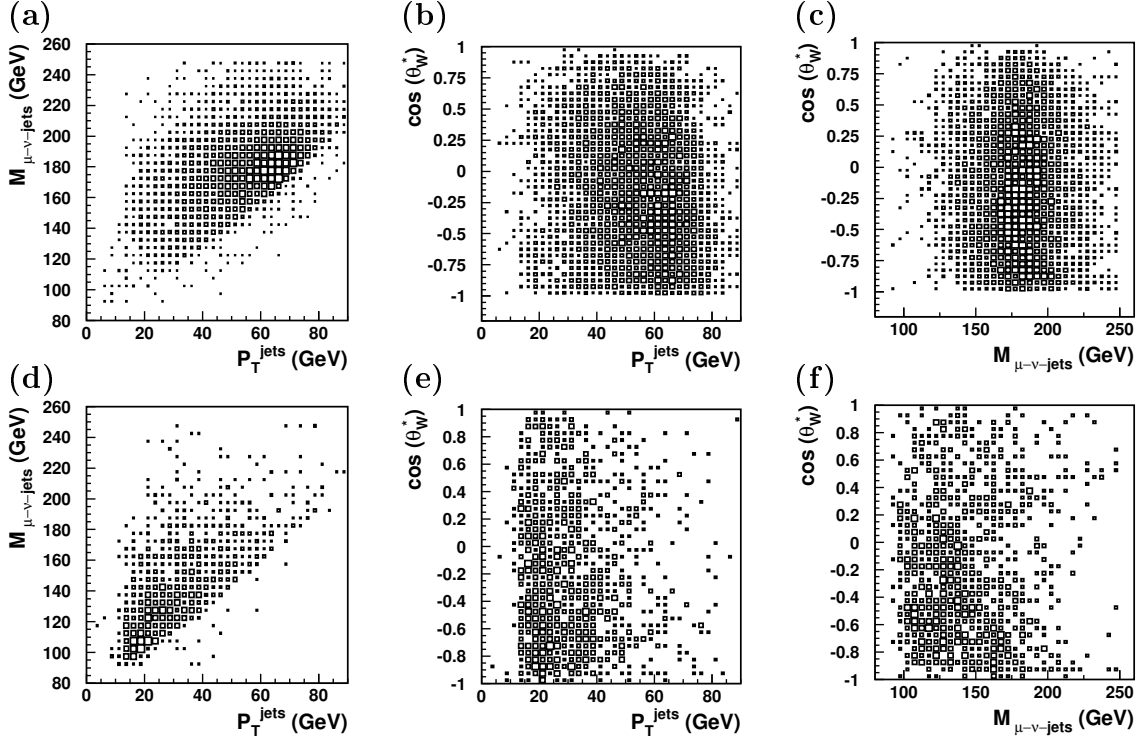


Figure 6.23: Correlations of the discriminating observables in the muon channel for the simulated top signal (upper plots (a)-(c)) and the simulated  $W$  background (lower plots (d)-(f)).

## Correlations

The correlations between the discriminating observables are shown in figures 6.22 and 6.23 for the simulated top signal (upper plots) and the Standard Model  $W$  background (lower plots). As expected, the  $W$  decay angle shows no correlation to either of the other two observables for the signal and the background simulations. The mass and the transverse momentum are clearly correlated. A large hadronic transverse momentum corresponds in general to a large invariant mass  $M_{\ell-\nu-jets}$ . In plot 6.22 (d), a band of events is visible at very small values of  $P_T^{jets}$ . It is due to events from  $W$  production, in which the quark is not scattered into the detector. Because of the cut  $P_T^X > 12$  GeV applied in the  $W$  selection for muonic decays, this band is not visible in the corresponding plot for the muon channel.

### 6.5.2 Possibility of $b$ -Quark Identification

The tagging of  $b$ -quarks is a mighty tool to identify top quark decays. A  $b$ -quark identification exploits the lifetime, mass, or semi-leptonic decay modes of  $b$ -quarks. Due to their long lifetime,  $b$ -quarks produce secondary decay vertices, which can be reconstructed with a silicon tracker. At H1, only a central silicon tracker (CST) was available before 2001. The  $b$  quarks from top decays, however, are found in the forward region most of the times, and thus outside of the CST acceptance. The large mass of the  $b$ -quark should manifest itself in a large mass of the hadronic jet measured in the detector. For the jet mass, no efficient separation from lighter quarks was seen. As for the semi-leptonic decay modes of the  $b$ -quark, only in about 10% of all  $b$ -decays a muon is produced, which can then be identified. Due to small identification efficiencies, an identification of  $b$ -quarks has not been used in this analysis. It might however be feasible with higher data statistics in the future.

### 6.5.3 Shape Analysis

As can be seen from the discriminating observables in figure 6.21, some data events fit kinematically better to single top production than to  $W$  production. Besides the observed discrepancies in the event rates between data and Standard Model prediction, it is interesting to see whether the agreement of the distributions in shape can be improved by adding a contribution from top production to the Standard Model.

To test only the shapes of the distributions, the total Standard Model background is normalized to the number of data events. The agreement in shape is checked by studying integrated distributions of the discriminating observables. Therefore, the  $P_T^{jets}$  and  $M_{\ell-\nu-jets}$  distributions are integrated bin by bin starting from the right ("signal-like") side. The leftmost bin of the integrated distribution hence gives the total number of data events.

The resulting integrated distributions are shown on in figures 6.24 and 6.25 for the electron and muon channels (left sides). It can be seen that the shapes of the  $P_T^{jets}$  and  $M_{\ell-\nu-jets}$  distributions are not well-described by the Standard Model.

In order to see if an additional contribution from single top production improves the agreement in shape, the sum of the Standard Model background and the top signal

is now normalized to the number of data events. Thereby the absolute normalization of the top contribution is chosen to best fit the observed data, as will be derived later in section 8.1. The resulting integrated distributions are presented in figures 6.24 and 6.25 (right sides). For both channels, the additional contribution from single top production gives a clearly better description of the transverse momentum and mass distributions in shape, in particular at large values of  $P_T^{jets}$  and  $M_{\ell-\nu-jets}$ .

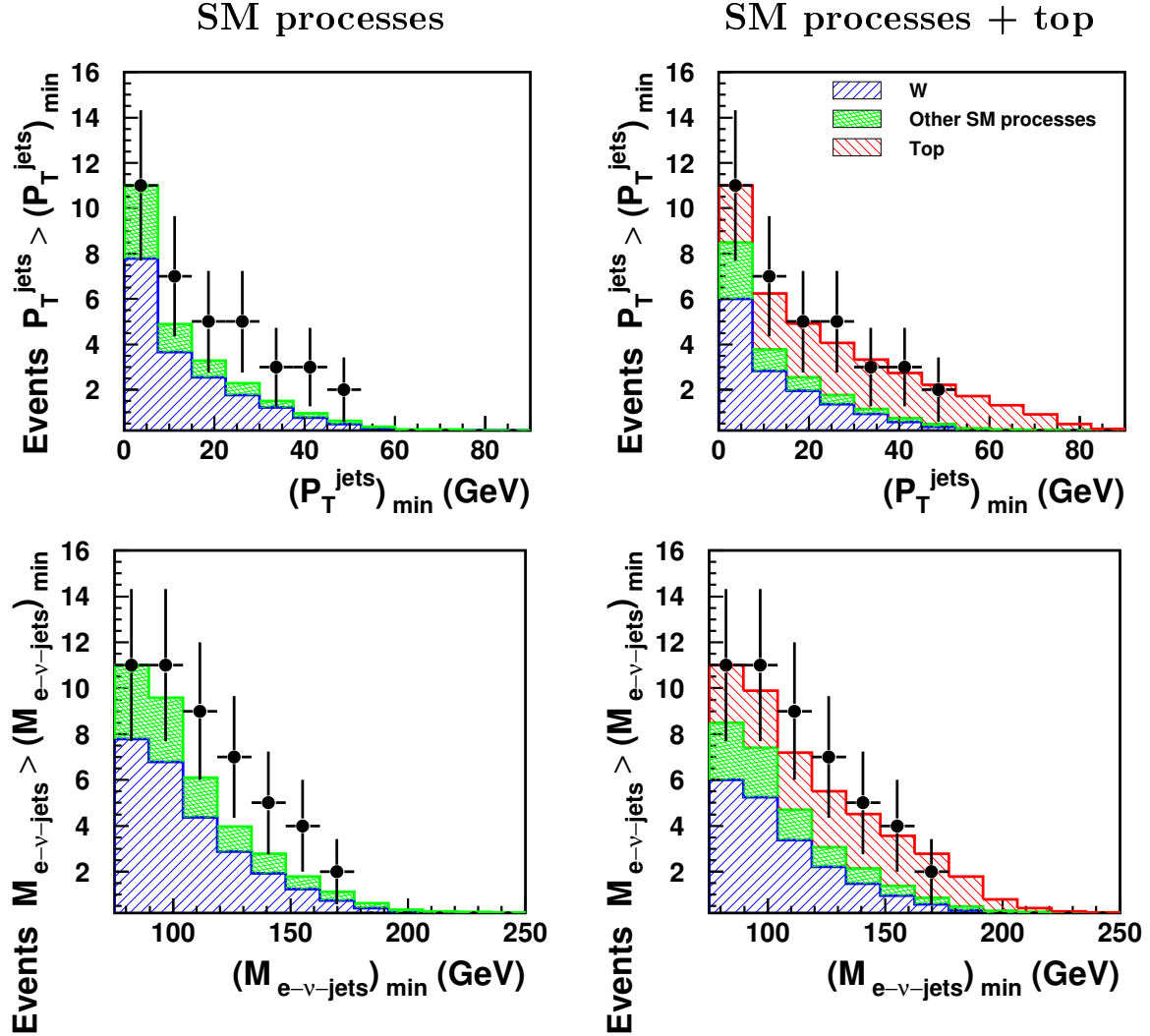


Figure 6.24: Integrated distributions of  $P_T^{jets}$  and  $M_{e-\nu-jets}$  in the electron channel. On the left side, the sum of  $W$  production and other Standard Model backgrounds is normalized to the data. On the right side, an additional contribution from top production is taken into account. The fraction of top events is chosen to best fit the observed data (see section 8.1).

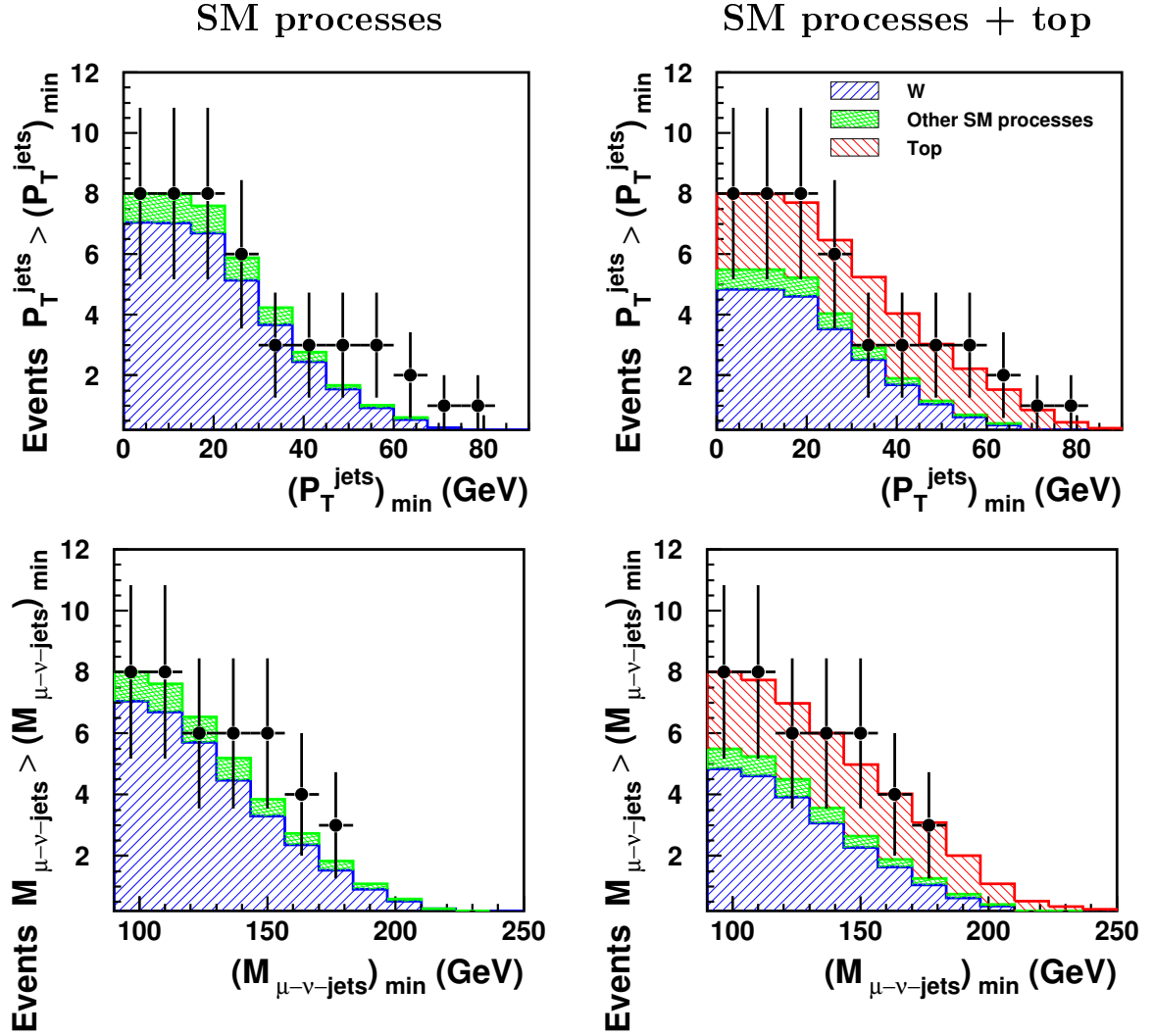


Figure 6.25: Integrated distributions of  $P_T^{jets}$  and  $M_{\mu-\nu-jets}$  in the muon channel. On the left side, the sum of  $W$  production and other Standard Model backgrounds is normalized to the data. On the right side, an additional contribution from top production is taken into account. The relative fraction of top events is chosen to best fit the observed data (see section 8.1).

## 6.6 Cut-Based Search for Top Quarks

To enhance a potential single top signal relative to the Standard Model background, both a cut-based and a more refined likelihood analysis are carried out. In this section, the straight-forward approach of applying one-dimensional cuts in the discriminating observables is pursued. The values of the cuts are chosen to reject a large fraction of the background whilst maintaining a high efficiency of about 40% for top production.

### 6.6.1 Definition of the Cuts

In the selection of top events, cuts are imposed on the transverse momentum sum of the jets,  $P_T^{jets}$ , and the mass  $M_{\ell-\nu-jets}$ . The shape of the  $W$  decay angular distribution does not allow an efficient cut to separate top from  $W$  production. It does show a nice separation from other Standard Model processes, which lie at values of  $\cos(\theta_W^*)$  close to -1 and 1, but these events have mainly low hadronic transverse momenta. They are already drastically reduced by the other two cuts on  $P_T^{jets}$  and  $M_{\ell-\nu-jets}$ . For this reason, no cut is applied on the  $W$  decay angle.

### Cut on the Charge of the Lepton

So far the charge of the lepton has not been taken into consideration. At HERA, events from single top production contain only positively charged leptons. As explained in the theoretical overview in section 2.2.2, the production of anti-top quarks, which would produce negatively charged leptons in the decay chain  $\bar{t} \rightarrow \bar{b}W^- \rightarrow \bar{b}\bar{\nu}_\ell\ell^-$ , is strongly suppressed because the  $\bar{u}$  distribution in the proton is much softer than the  $u$  distribution. For this reason, events with negatively charged leptons should be removed when selecting top events.

In order not to lose a potential top candidate due to a poor charge measurement, only leptons with a well-measured negative charge are rejected. Therefore only tracks that are reconstructed within the acceptance of the central tracking system ( $20^\circ < \theta_{track} < 160^\circ$ ) are used for the charge determination. The transverse track lengths of forward tracks are too short to allow a reliable charge measurement. In addition, the significance of the charge measurement is taken into account. The charge of a track is determined from the track curvature  $\kappa$  in the magnetic field of the solenoid. The significance of the charge determination is given by the ratio of the curvature and the error on its measurement,  $\frac{\kappa}{\delta\kappa}$ . It is plotted in figure 6.26 (a) for lepton tracks from top decays and in (b) for tracks from  $W^\pm$  decays. The cut indicated by a dashed line rejects all negative charges measured with an accuracy of at least  $2\sigma$ .

As can be seen in figure 6.26 (a), only a negligible fraction of top events is removed by this cut. The  $\frac{\kappa}{\delta\kappa}$  distribution for Standard Model  $W$  production shows two peaks. The right peak belongs to  $W^+$  production, the left peak to  $W^-$  production. The production of negative  $W$ 's makes up  $\sim 40\%$  of the total  $W$  cross-section at HERA. In about 50% of these  $W^- \rightarrow \ell^- \nu$  events, the lepton lies within the acceptance of the Central Jet Chambers. Altogether, the cut on the lepton charge reduces the  $W$  background by 20%. The other Standard Model processes are reduced by 30-40%.

A summary of the top selection cuts is given in table 6.8. The same cuts are used for the electron and the muon channels.

### 6.6.2 Systematic Uncertainties and Results

Before the final results of the cut-based selection of top candidates is presented, the effect of systematic uncertainties is discussed. Various systematic uncertainties can

---

<sup>1</sup>According to the sign convention of the curvature, a negative curvature corresponds to a positive charge and vice versa. Hence the quantity defined as  $\frac{\kappa}{\delta\kappa}$  is greater (less) than zero for tracks with positive (negative) charge

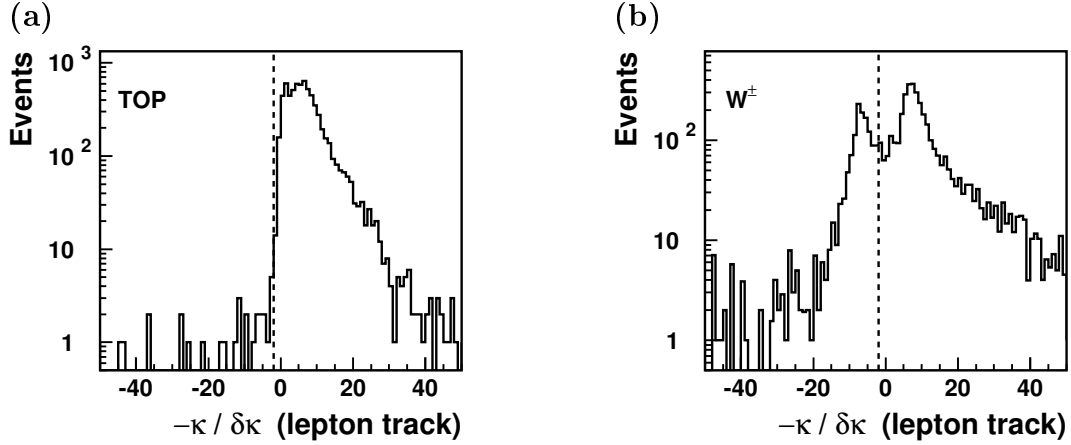


Figure 6.26: The significance of the charge determination of lepton tracks for (a) simulated top production and (b) simulated Standard Model  $W^\pm$  production. Positively charged tracks have values of  $\frac{-\kappa}{\delta\kappa}$  above zero, negatively charged tracks below zero. In (b) the two contributions from  $W^+$  and  $W^-$  production are clearly separated. The cut on the lepton charge applied in the top analysis is indicated as a dashed line.

	Top selection cuts
Transverse momentum	$P_T^{jets} > 30 \text{ GeV}$
Mass	$M_{\ell-\nu-jets} > 140 \text{ GeV}$
Lepton charge	$Q_\ell = +1$ for $\frac{ \kappa }{\delta\kappa} > 2$ and $20^\circ < \theta_\ell < 160^\circ$

Table 6.8: Definition of the cuts used in the cut-based top selection.

have an impact on the results of the top selection. These uncertainties originate either from an imperfect understanding of the detector, for instance the knowledge of the absolute calibration of energies measured in the calorimeter, or theoretical calculations for the processes implemented in the Monte Carlo generators. The following uncorrelated systematic error sources have been studied:

### Experimental Systematic Uncertainties

- *Lepton measurement:* The electromagnetic energy scale is given a 3% uncertainty. The muon energy scale is given a 5% uncertainty. The measurement of the lepton angles is attributed an uncertainty of 3 mrad for the polar angle  $\theta_\ell$  and 1 mrad for the more precisely measured azimuthal angle  $\phi_\ell$ .
- *Hadron measurement:* The hadronic energy scale has a 4% error. The measurement of the jet angles are attributed an uncertainty of 20 mrad for  $\theta_{jets}$  and  $\phi_{jets}$ . This uncertainty has been checked with a standard selection of neutral current DIS events by comparison of the measured inclusive hadron polar angle with the angle predicted from the energy and the polar angle of the electron (“electron

method”). The result of this comparison is presented in figure 6.27. For the top analysis, mainly the forward-to-central region, roughly between  $10^\circ$  and  $70^\circ$ , is of interest. An uncertainty of 20 mrad ( $= 1.1^\circ$ ) seems to be a conservative choice.

- *Lepton identification:* The efficiency of the electron identification is assigned an uncertainty of 2%. The uncertainty on the association of a track to the electron cluster is 3%. The muon identification is assigned an uncertainty of 5%.
- *Trigger efficiency:* The uncertainty on the trigger efficiency in the muon channel varies from 16% at lowest  $P_T^X$  to 4% for  $P_T^X > 40$  GeV [45]. The trigger efficiency in the electron channel is  $\sim 100\%$ , no uncertainty is assumed.
- *Luminosity measurement:* The accuracy of the luminosity determination is 1.5%.

Table 6.9 summarizes the experimental systematic uncertainties on the expected event yield after the top selection. The quadratic sum of all uncertainties gives a total experimental systematic uncertainty of 6% for electron events and 8% for muon events.

Experimental systematic	$\Delta N_{SM}/N_{SM}$ after top cuts	
	Electrons	Muons
Leptonic energy scale	$\pm 3\%$	$\pm 4\%$
$\theta$ lepton	$\pm 2\%$	$\pm 1\%$
$\phi$ lepton	$\pm 0.5\%$	$\pm 0.5\%$
Hadronic energy scale	$\pm 2\%$	$\pm 2\%$
$\theta$ hadron	$\pm 2\%$	$\pm 2\%$
$\phi$ hadron	$\pm 1\%$	$\pm 1\%$
Trigger efficiency	$\pm 0\%$	$\pm 2\%$
Lepton identification	$\pm 4\%$	$\pm 5\%$
Luminosity	$\pm 1.5\%$	$\pm 1.5\%$
Total	$\pm 6\%$	$\pm 8\%$

Table 6.9: Effect of the experimental systematic uncertainties on the Standard Model expectation,  $N_{SM}$ , for the cut-based top selection.

### Uncertainties on the Predicted Rates for Standard Model Processes

- *W production:* An error of 30% percent is quoted in [25] for the calculation of the  $W$  production cross-section used in EPVEC. It is mainly due to uncertainties on the scale used for the calculation and the uncertainty in the photon parton distributions.
- *Other Standard Model processes:* As already mentioned, an uncertainty of 30% is estimated in [55] for the background rates of neutral current DIS, charged current DIS, and photon-photon interactions modeled by the generators RAPGAP, DJANGO, and LPAIR.

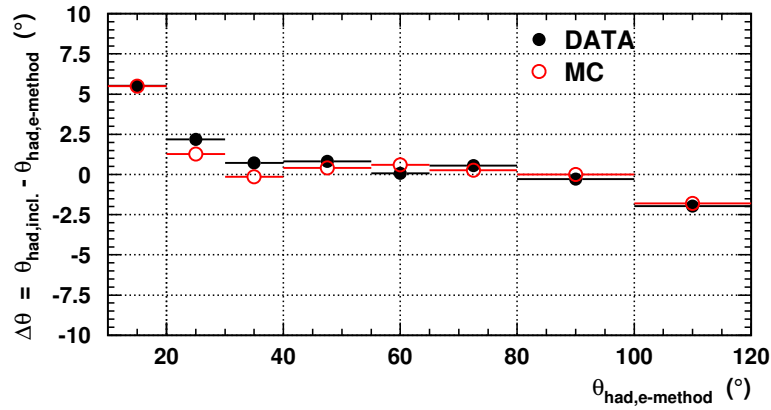


Figure 6.27: The difference  $\Delta\theta$  of the reconstructed inclusive hadron polar angle and the polar angle of the hadron calculated using the measurements of the electron energy and polar angle ("electron-method") in a standard selection of neutral current DIS events. The  $\Delta\theta$  distribution is shown for data and Monte Carlo simulation (DJANGO).

The uncertainties of the Monte Carlo predictions are large compared to the total experimental uncertainty and thus dominate the systematics.

## Results

After the cut-based top selection, three electron events and two muon events are found as top candidates. The Standard Model expectations with systematic uncertainties are given in table 6.10. The combined result for both channels yields five top candidates in the data for a Standard Model expectation of  $1.61 \pm 0.42$  events. The data show therefore an excess of events selected as top candidates. The efficiencies of the top selection are obtained with the ANOTOP generator. They are 40% in the electron channel and 42% in the muon channel.

Top selection	Data 94-00	SM expectation	SM $W$ prod.	Top efficiency
Electrons	3	$0.78 \pm 0.20$	$0.68 \pm 0.20$	40%
Muons	2	$0.83 \pm 0.22$	$0.74 \pm 0.22$	42%
Electrons and muons	5	$1.61 \pm 0.42$	$1.42 \pm 0.42$	41%

Table 6.10: The observed and expected event yields after all top selection cuts.

## 6.7 Likelihood Discriminator

In this section, a multivariate likelihood method is discussed, which provides an alternative to the simple application of one-dimensional cuts. It should allow to improve



the signal and background separation and takes into account correlations between the different discriminating observables.

In a likelihood analysis, a single discriminator distribution is constructed by combining the information from the discriminating observables in an optimal way. In contrast to the cut-based analysis, the likelihood analysis exploits the full distributions of the input observables. Distributions which show only moderate differences in shape for the signal and background processes (e.g. the angular distribution in figure 6.21), and thus do not allow an effective one-dimensional cut without losing too much signal efficiency, can still give some additional contribution to the signal and background separation in a likelihood analysis. In the following two sections, the principles of the likelihood methods used in this thesis are explained. The results and performance of their application to semi-leptonic top decays are presented in section 6.7.3.

### 6.7.1 Likelihood Method

In a likelihood analysis, a decision is taken to classify an event as signal or background candidate on the basis of a single discriminator  $L$ . The measurements of  $n$  observables  $x_i$  in one event are combined in an  $n$ -dimensional vector of measurements  $\mathbf{x} = (x_1, \dots, x_n)$ . The likelihood discriminator is then defined as:

$$L = \frac{P_{signal}(\mathbf{x})}{P_{signal}(\mathbf{x}) + P_{bkg}(\mathbf{x})} \quad , \quad (6.19)$$

where  $P_{signal}(\mathbf{x})d^n x$  and  $P_{bkg}(\mathbf{x})d^n x$  are the probabilities to produce measurements  $\mathbf{x}$  in a volume element  $d^n x$  for a signal and background event, respectively.

By definition, the likelihood discriminator can take on values in the range  $0 \leq L \leq 1$ . Signal events tend to have values close to one, while background events tend to be close to zero. The exact limits zero and one are only reached for values of  $\mathbf{x}$ , for which one of the probability densities vanishes:

$$L = \begin{cases} 0 & \Leftrightarrow P_{signal}(\mathbf{x}) = 0 \\ 1 & \Leftrightarrow P_{bkg}(\mathbf{x}) = 0 \end{cases} \quad . \quad (6.20)$$

In the *standard likelihood method*, the joint probability density  $P(\mathbf{x})$  for both signal and background events are approximated by the product of the one-dimensional probability density functions  $p_i(x_i)$  for each single observable:

$$P(\mathbf{x}) = \prod_{i=1}^n p_i(x_i) \quad . \quad (6.21)$$

Technically, the probability densities functions  $p_i(x_i)$  correspond to the normalized distributions (histograms) of the discriminating observables  $x_i$  for the signal and background Monte Carlo samples. For strongly correlated observables, equation 6.21 can

be a poor approximation. The factorization is only correct, if the observables are uncorrelated or follow Gaussian distributions. The standard method thus neglects any correlations between the observables.

### Review of Some Statistical Quantities

The definitions of a few statistical quantities, that are used in the following discussion of the treatment of correlations, are briefly reviewed.

The function  $f(x)$  is the *probability density* of a continuous random variable  $x$ . The probability of finding  $x$  in the interval  $[x; x + dx]$  is given by  $f(x)dx$ .

The *expectation value* of the random variable  $x$  is then defined as:

$$E(x) = \hat{x} = \int_{-\infty}^{\infty} x f(x) dx . \quad (6.22)$$

The *variance* of  $x$  corresponds to the mean deviation of  $x$  from its expectation value:

$$\text{var}(x) = \sigma^2 = \int_{-\infty}^{\infty} (x - \hat{x})^2 f(x) dx . \quad (6.23)$$

The *covariance* of two random variables  $x_i$  and  $y_i$  is a measure of the dependence between  $x_i$  and  $y_i$ :

$$\text{cov}(x_i, x_j) = \sigma_{ij} = \int_{-\infty}^{\infty} (x_i - \hat{x}_i)(x_j - \hat{x}_j) f_i(x_i) f_j(x_j) dx_i dx_j . \quad (6.24)$$

The above definitions can be generalized for  $n$  variables. The covariance can then be written in form of a  $n \times n$  matrix:

$$(\sigma_{ij}) = \begin{pmatrix} \sigma_1^2 & \sigma_{12} & \dots & \sigma_{1n} \\ \sigma_{21} & \sigma_2^2 & \dots & \sigma_{2n} \\ \vdots & \vdots & \ddots & \vdots \\ \sigma_{n1} & \sigma_{n2} & \dots & \sigma_n^2 \end{pmatrix} . \quad (6.25)$$

Finally, the *correlation coefficients* are defined as:

$$\rho(x_i, y_i) = \rho_{ij} = \frac{\sigma_{ij}}{\sigma_i \sigma_j} , \quad (6.26)$$

which can be combined in a *correlation matrix*  $(\rho_{ij})$  in analogy to 6.25.

### 6.7.2 Approximation of Correlations

For strongly correlated observables, the approximation of the probability densities  $P_{sig}(\mathbf{x})$  and  $P_{bkg}(\mathbf{x})$  according to equation 6.21 artificially shifts events towards very low or very high values of the likelihood. False peaks close to  $L = 0$  and  $L = 1$  are created. These erroneous peaks disappear if the correlations are properly taken into account and the correct probability densities are used.

A modification of the standard likelihood method was developed in [61] (*PTC-method*<sup>2</sup>) to obtain an improved description of the joint probability density  $P(\mathbf{x})$  by taking correlations into account.

The observables  $x_i$  are transformed to Gaussian distributed variables  $y_i$ . The joint probability density for  $\mathbf{y} = (y_1, \dots, y_n)$  can then be well approximated by an  $n$ -dimensional Gaussian distribution:

$$G(\mathbf{y}) = \frac{1}{(2\pi)^{n/2}} |V|^{-1/2} e^{-\frac{1}{2}\mathbf{y}^T V^{-1} \mathbf{y}} , \quad (6.27)$$

where  $V$  denotes the  $n \times n$  covariance matrix  $(\sigma_{ij})$  of the  $y_i$ , and  $|V|$  its determinant.

The following monotonic mapping is used for the parameter transformation of the observables  $x_i \rightarrow y_i$ :

$$y_i(x_i) = \sqrt{2} \operatorname{erf}^{-1}(2F(x_i) - 1) . \quad (6.28)$$

Here  $\operatorname{erf}^{-1}$  denotes the inverse error function and  $F(x_i)$  the cumulative distribution function, defined by:

$$F(x_i) = \int_{-\infty}^{x_i} p(x'_i) dx'_i . \quad (6.29)$$

After this transformation, the  $y_i$  follow Gaussian distributions of mean zero and variance one. As a result, the covariances  $\sigma_{ij}$  of the variables  $y_i$  are equal to their correlation coefficients  $\rho_{ij}$ . The approximation of the  $n$ -dimensional probability density for  $\mathbf{y}$  by the  $n$ -dimensional Gaussian  $G(\mathbf{y})$  is not necessarily exact, since only the projections of this distribution onto each variable axis are Gaussian. However, it is a much better approximation than provided by the standard method.

In the PTC-method, a discriminator  $L'$  is constructed in analogy to equation 6.19, but using the improved probability density  $P'(\mathbf{x})$ , which are obtain by transforming  $G(\mathbf{y})$  back into the  $\mathbf{x}$ -space:

$$P'(\mathbf{x}) = G(\mathbf{y}) \frac{d^n y}{d^n x} = G(\mathbf{y}) \prod_{i=1}^n \frac{\partial y_i}{\partial x_i} = G(\mathbf{y}) \prod_{i=1}^n \frac{p(x_i)}{g(y_i)} , \quad (6.30)$$

where the functions  $g(y_i)$  are one-dimensional unit Gaussians of mean zero. The improved probability density can be related to the product probability density  $P(\mathbf{x})$ , as used in equation 6.21 for the standard method, by a correction factor  $c(\mathbf{x})$ :

$$P'(\mathbf{x}) = c(\mathbf{x})P(\mathbf{x}) = c(\mathbf{x}) \prod_{i=1}^n p_i(x_i) . \quad (6.31)$$

The correction factor is equal to the ratio of the  $n$ -dimensional Gaussian  $G(\mathbf{y})$  and the product of the  $n$  one-dimensional unit Gaussians  $g(y_i)$ :

$$c(\mathbf{x}) = \frac{G(\mathbf{y})}{\prod_{i=1}^n g(y_i)} = |V|^{-1/2} e^{-\frac{1}{2}\mathbf{y}^T (V^{-1} - I) \mathbf{y}} \quad (I = \text{identity matrix}) . \quad (6.32)$$

---

<sup>2</sup>PTC stands for Projection Transformation Correlation.

A detailed derivation of this relation and of the parameter transformation can be found for instance in [62].

Since the correlations between the observables  $x_i$  are in general different for signal and background events, a set of transformations  $x_i \rightarrow y_i$  and  $x_i \rightarrow z_i$  is needed to calculate  $P'_{signal}(\mathbf{x})$  and  $P'_{bkg}(\mathbf{x})$ , respectively. The improved likelihood discriminator is then defined by:

$$L = \frac{P'_{signal}(\mathbf{x})}{P'_{signal}(\mathbf{x}) + P'_{bkg}(\mathbf{x})} \quad . \quad (6.33)$$

### 6.7.3 Performance and Results

The improved likelihood method is applied to the single top analysis in the semi-leptonic channel, and its performance is tested. The distributions of all three discriminating observables  $x_i$  ( $i = 1, 2, 3$ ) in figure 6.21 serve as input to the likelihood analysis. Since only the shapes of these input distributions are of relevance for the construction of the likelihood discriminator, they are normalized to unity to obtain the probability densities  $p(x_i)$ .

To achieve the best discrimination between single top and Standard Model  $W$  production, the likelihood discriminator is constructed using the probability distributions of the top signal and the  $W$  background only. It is thus designed to test the  $W$  hypothesis versus the top hypothesis. The other Standard Model processes are interpreted as additional small contribution, that may be classified either as more  $W$ -like or as more top-like.

At first, no cut on the lepton charge is imposed. Although only positive charges are expected from single top production, it is instructive to see how the events with negative leptons are kinematically classified in the likelihood analysis.

#### Treatment of Correlations (Application of the PTC-Method)

To avoid a possible bias in the likelihood analysis, two statistically independent Monte Carlo samples for each process are used in the generation of the likelihood discriminator  $L$ . Therefore each Monte Carlo sample is split up in two subsamples of equal size. The first subsample is used to calculate the probability densities  $P'(\mathbf{x})$ , i.e. to compute the covariance matrices and the parameter transformations. The second subsample is then used to obtain the distribution of  $L$  according to equation 6.33.

The Gaussian transformed variables  $y_i$  for the signal and  $z_i$  for the background ( $i = 1, 2, 3$ ) are presented in appendix C. Fits to their distributions show that they agree well with Gaussians of mean zero and standard deviation one. The deviations from these ideal values are smaller than  $\sim 4\%$  for the mean and the standard deviation. Hence the covariance matrices of the transformed observables  $y_i$  and  $z_i$  are to a good approximation equal to their correlation matrices. The covariance matrices are used to approximate the joint probability density by a three-dimensional Gaussian distribution (see equation 6.27). The accuracy of the description of the correlations with the PTC-method can be checked by comparison of the correlation matrices before and after the transformation to Gaussian distributed variables. All correlation matrices are given in appendix C. Overall, a good agreement of the correlations for the untransformed and transformed observables is seen in the signal and background Monte Carlo samples.

The obtained likelihood discriminator  $L$  is presented in figure 6.28 for both the standard method (left) and the PTC-method (right). In these plots, all likelihood distributions are normalized to unity in order to visualize the separation. The additional background from other Standard Model processes has not yet been added. Since the standard method disregards any correlations, erroneous peaks appear at zero (one) for the signal (background) Monte Carlo. The improved likelihood distributions show that the approximation of correlations with the PTC-method reduces these false peaks and restores the true value of the likelihood.

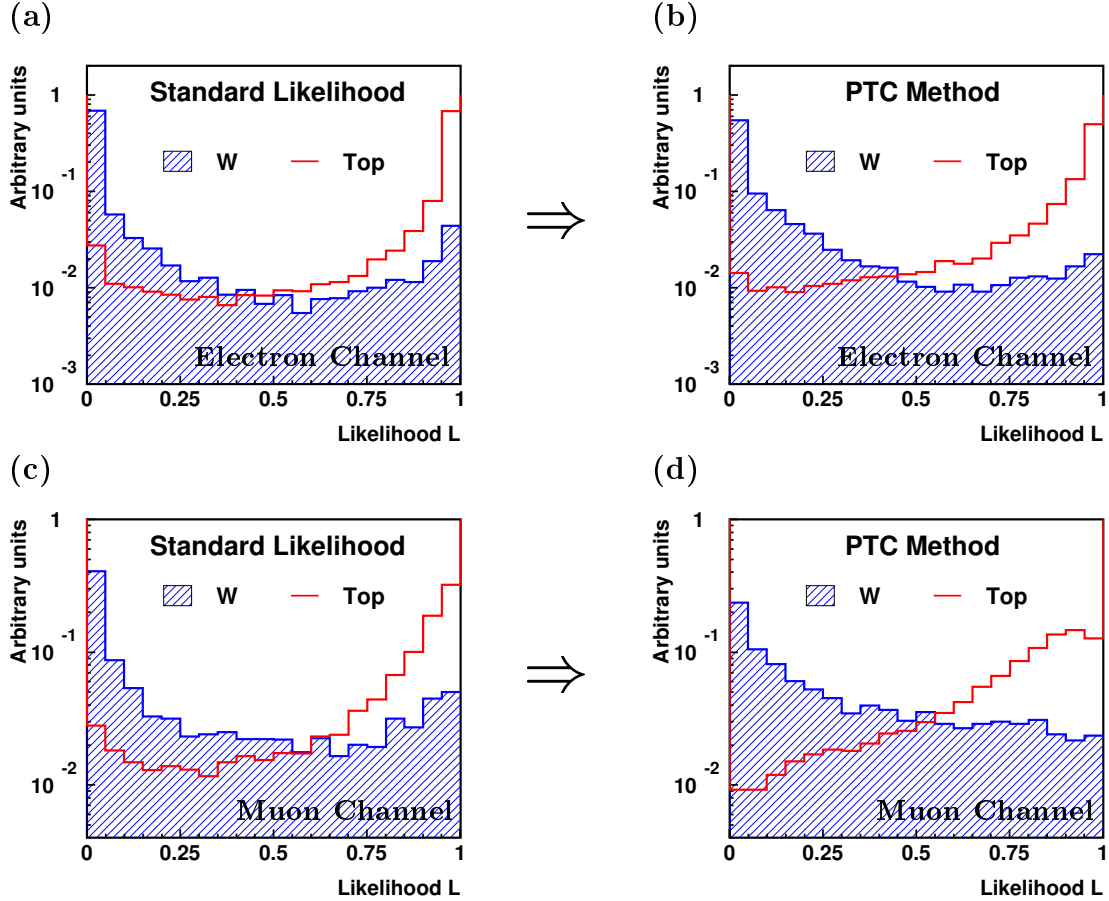


Figure 6.28: The likelihood discriminators obtained with the standard method (left) and the PTC-method (right) for Monte Carlo events from single top and  $W$  production. Upper plots: electron channel, lower plots: muon channel. All distributions are normalized to unity.

In figure (b) for the electron channel, a slight rise is still visible for large values of  $L$ , even after applying the PTC-method. Though very small in absolute size, it is interesting to see where it comes from. It has been checked that this rise is not due to an insufficient description of the correlations. Instead, it is an effect of the specific shapes of the discriminating distributions in the electron channel. Since no cut on  $P_T^X$  is applied in the  $W$  selection for electron events, the normalized  $P_T^{jets}$  and mass distributions exhibit long tails, which correspond already to a very small background

probabilities in the regions where the top signal peaks. Hence background events in these regions tend to have values of  $L$  close to one. The slight rise can thus be considered as an effect of the large kinematic range of the observables  $P_T^{jets}$  and  $M_{e-\nu-jets}$ . It has been studied that applying a cut  $P_T^X > 12$  GeV also in the electron channel would cause this effect to disappear. A discriminator distribution similar to the one in the muon channel would be obtained.

### Results without Cut on the Charge of the Lepton

Figure 6.29 shows the likelihood spectra of the Monte Carlo simulations compared to the observed data events. The additional background contributions from non- $W$  processes is now included. The Standard Model background is normalized according to the luminosity of the analyzed data. The top simulation is arbitrarily normalized to the expectation from  $W$  production. The total event numbers seen in the likelihood distributions correspond to the ones obtained with the  $W$  selection, reduced by the number of events lost in the neutrino reconstruction, i.e. events for which no physical solution of the  $W$  mass constraint is found. The event numbers are given in tables 6.12 and 6.13.

Looking at the likelihood distributions, it is obvious that in both channels the data contain a fraction of events that has more  $W$ -like kinematics and another fraction with clearly more top-like kinematics.

In the electron channel, four events are observed in a region where the top hypothesis is favored to the  $W$  hypothesis. The other seven electron events at lower likelihood are consistent with the  $W$  hypothesis. Their number is slightly lower than the total Standard Model expectation of  $11.23 \pm 2.58$  events ( $7.96 \pm 2.39$  from  $W$  production). Considering the statistical and systematic uncertainties, it corresponds to an agreement on the  $1.1 \sigma$  level. Two data events contain an electron with a well-measured negative charge (as marked in the likelihood distribution). These two events are consistent with the 2.40 events expected from Standard Model processes for negative charges.

In the muon channel, three data events are observed in the top-like region of the likelihood. In contrast to the electron channel, the other five more  $W$ -like muon events overshoot the total Standard Model expectation of  $2.83 \pm 0.76$  ( $2.49 \pm 0.75$  from  $W$  production). Due to the large statistical error, this overshoot also corresponds to a  $1 \sigma$  deviation only. Amongst the observed muon events, there are two with a well-measured negative charge for 0.69 expected. It should be noted that one of these two events lies at  $L = 0.80$ . Kinematically it thus fits better to the top hypothesis.

### Results with Cut on the Charge of the Lepton

Since only positive leptons are expected from top production at HERA, the likelihood analysis is carried out a second time. This time all events with negative lepton charges are removed by applying the cut defined in table 6.8.

The resulting distributions of the discriminating observables are very similar to the ones in figure 6.21 without any cut on the lepton charge. For completeness they are shown in appendix D. Since the spectra of the discriminating observables are only subject to marginal changes, also the shapes of the likelihood discriminators have

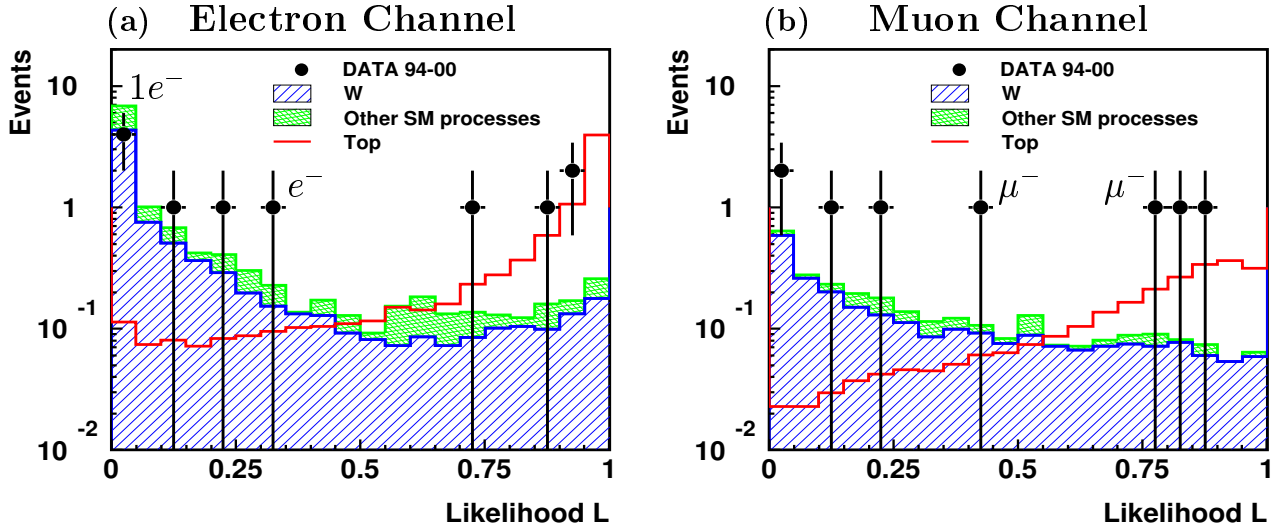


Figure 6.29: The likelihood discriminators obtained with the PTC-method without cut on the lepton charge. The electron and muon events with well-measured negative lepton charges ( $> 2\sigma$ ) are marked. The top simulation is normalized to the expectation from  $W$  production.

changed only slightly. The improved likelihood distributions are shown in figures 6.30 and 6.31 for the electron and muon channels. The event yields after the cut on the lepton charge can be found in table 6.12 for electron events and table 6.13 for muon events. As mentioned earlier, the  $W$  background is reduced by 20% and the other Standard Model backgrounds by 30–40%, without any significant loss of top efficiency.

The rejection of events with a negatively charged lepton removes two  $W$ -like data events in the electron channel. In the muon channel, also two events are cut, but at significantly higher likelihood values.

In the electron channel, the likelihood distribution after the cut on the lepton charge still shows four events in the data with high likelihood  $L$ . The electron event at highest  $L$  is a tagged event, i.e. it contains the scattered beam electron in the Liquid Argon Calorimeter, and thus allows a direct measurement of the lepton-neutrino invariant mass. It is measured as  $79^{+12}_{-12}$  GeV and is thus perfectly consistent with the  $W$  mass.

In the muon channel, two events remain at high  $L$ . They are situated directly in the maximum of the single top likelihood distribution and have very top-like kinematics. Their invariant masses  $M_{\ell-\nu-jets}$  are  $172^{+9}_{-10}$  GeV and  $176^{+9}_{-12}$  GeV. In addition, one of these events has a muon in the jet, measured in the forward muon system (see figure A.8 in appendix A), which increases the probability that this jet comes from a heavy quark. In about 10% of  $b$ -quark decays, a muon in or close to the hadronic jet is expected.

### Comparison to Cut-Based Analysis

A way to compare the performance of the likelihood to the cut-based analysis is imposing a cut on the likelihood discriminator that yields the same top efficiency as the

cut-based selection. In the electron channel, this cut is  $L = 0.70$ , in the muon channel, where the phase space is already much more restricted due to the cut  $P_T^X > 12$  GeV, it is  $L = 0.40$ . The resulting event yields are shown in tables 6.12 and 6.13 and compared to the one obtained with the top cuts. In the electron channel, the performances of the likelihood cut and the top cuts are almost identical. In the muon channel, an improvement of  $\sim 10\%$  in the background reduction is achieved.

In contrast to the cut-based analysis exploiting several one-dimensional cuts, the likelihood discriminator allows an easy optimization of the cut to maximize the signal sensitivity. As a measure of the sensitivity of a cut on the likelihood, the ratio of the signal expectation and the square root of the background expectation,  $N_{SM}$ , can be used. Since the normalization of the top signal is unknown, the top efficiency,  $\epsilon_{top}$ , is used instead. Hence the ratio  $\epsilon_{top}$  over  $\sqrt{N_{SM}}$  defines the sensitivity of the cut. This sensitivity is plotted as a function of the top efficiency in figures 6.30 and 6.31 (c).

In the electron channel, no maximum of the sensitivity curve is reached before the last bin of the likelihood. The optimal cut is found to be  $L > 0.95$ , which leaves a top efficiency of 24%, and removes all data candidates. In the muon channel, the sensitivity curve reaches its maximum for a top efficiency of 29%, corresponding to a cut  $L > 0.75$ . Two data events remain. The event rates can again be seen in tables 6.12 and 6.13.

Later in the statistical evaluation of the likelihood analysis (section 8.1), the signal fraction in the data will be obtained in a maximum likelihood fit exploiting the full likelihood spectrum. The likelihood discriminator is ideally suited for such a fit, because it contains the combined information of all discriminating observables in one distribution.

### Confidence Level for Background-Only Hypothesis

As is done in section 6.3, a confidence level for the background-only hypothesis (i.e. assuming only Standard Model processes to be present) is now computed using the background likelihood spectrum instead of the  $P_T^X$  spectrum. The results obtained for the confidence level  $1 - \text{CL}_b$  are presented in table 6.11. Systematic uncertainties are again included by scaling up the background normalization according to the size of the total systematic uncertainty. Since the event numbers have changed compared to section 6.3, mainly because of the cut on the lepton charge, the confidence level calculation using only the  $P_T^X$  spectrum has also been performed another time and is compared to the one using the likelihood spectrum.

In the electron channel, the likelihood spectrum yields smaller probabilities for the Standard Model to describe the data than the  $P_T^X$  spectrum. In the muon channel, it is the other way around. However, the fact that the value of  $1 - \text{CL}_b$  in the muon channel is larger for the likelihood spectrum than for the  $P_T^X$  spectrum, does not mean that it has a worse separation power than the  $P_T^X$  spectrum, since the signal distribution is not taken into account here. It was shown in the previous section that the likelihood discriminator gives a better separation of signal and background. Comparing the confidence level for the muon channel to the one obtained in section 6.3, one sees that the value of  $1 - \text{CL}_b$  increases from  $4.5 \cdot 10^{-3}$  to 1.9%, because the cut on the lepton charge eliminates two events at high  $P_T^X$ . Hence the background-only hypothesis for the muon channel is a little more likely in the top analysis than in the



	1 - CL <sub>b</sub> (Likelihood)		1 - CL <sub>b</sub> ( $P_T^X$ spectrum)	
	w/o syst.	with syst.	w/o syst.	with syst.
Electrons	2.4%	5.6%	5.2%	11.9%
Muons	3.4%	6.3%	0.7%	1.9%
Electrons and Muons	0.4%	1.6%	0.3%	1.3%

Table 6.11: Probability  $1 - \text{CL}_b$  of the background-only hypothesis. The confidence level calculations are shown for the likelihood spectrum and the  $P_T^X$  spectrum after the cut on the lepton charge. Results are given with and without inclusion of systematic uncertainties.

analysis of all isolated muon events.

## 6.8 Summary

The selection of isolated lepton events and candidates for  $W$  boson production shows an excess of electron and muon events at high hadronic transverse momenta. The distribution of the lepton-neutrino transverse mass indicates that these events may indeed all contain  $W$  bosons. The probability for the Standard Model to describe the electron and muon excess at high  $P_T^X$  was evaluated and found to be  $9.7 \cdot 10^{-3}$  ( $4.0 \cdot 10^{-3}$ ) for the full  $P_T^X$  spectrum ( $P_T^X > 25$  GeV), including all systematic uncertainties.

As a possible interpretation in terms of new physics, the anomalous production of single top quarks has been studied in the semi-leptonic decay channel. After reconstructing the full event kinematics, five top candidates (three electrons and two muons) are selected in a cut-based analysis for a background expectation of  $1.61 \pm 0.42$  events.

A nice way of improving and visualizing the separation between the top signal and Standard Model  $W$  production is achieved in a likelihood analysis. It serves as a test of the top hypothesis versus the  $W$  hypothesis and shows that the data contain a fraction of events that favors the  $W$  hypothesis, and another fraction of events that favors the top hypothesis. The most top-like electron event has invariant masses  $M_{\ell-\nu-jets} = 168$  GeV and  $M_{\ell\nu} = 79$  GeV. The two top candidates in the muon channel have invariant masses  $M_{\ell-\nu-jets}$  of 172 GeV and 176 GeV, respectively.

The probability that the Standard Model describes the data excess is again evaluated for the likelihood spectrum of the Standard Model background, after rejection of events with negative charge of the lepton. Now the probability amounts to 1.6%, including systematic uncertainties.

Electrons	Data 94-00	SM expectation	SM $W$ prod.	Top efficiency
$W$ selection	11	$11.48 \pm 2.63$	$8.06 \pm 2.42$	50%
$\nu$ reconstruction	11	$11.23 \pm 2.58$	$7.96 \pm 2.39$	49%
Cut on lepton charge	9	$8.83 \pm 2.08$	$6.54 \pm 1.96$	49%
Top cuts	3	$0.78 \pm 0.20$	$0.68 \pm 0.20$	40%
Cut $L > 0.70$	3	$0.76 \pm 0.19$	$0.63 \pm 0.19$	40%
Optim. cut $L > 0.95$	0	$0.17 \pm 0.05$	$0.16 \pm 0.05$	24%

Table 6.12: Summary of the event yields in the electron channel for the different steps of the top analysis. Beginning with the  $W$  selection, in the upper half of the table the consecutive decrease of the event numbers for the neutrino reconstruction and the cut on the lepton charge is presented. In the lower half of the table, the results of the cut-based top selection are compared to the results obtained by using either a likelihood cut with comparable top efficiency or the likelihood cut that optimizes the signal sensitivity.

Muons	Data 94-00	SM expectation	SM $W$ prod.	Top efficiency
$W$ selection	8	$2.99 \pm 0.80$	$2.63 \pm 0.79$	50%
$\nu$ reconstruction	8	$2.83 \pm 0.76$	$2.49 \pm 0.75$	47%
Cut on lepton charge	6	$2.15 \pm 0.58$	$1.93 \pm 0.58$	47%
Top cuts	2	$0.83 \pm 0.22$	$0.74 \pm 0.22$	42%
Cut $L > 0.40$	2	$0.74 \pm 0.20$	$0.68 \pm 0.20$	42%
Optim. cut $L > 0.75$	2	$0.28 \pm 0.08$	$0.26 \pm 0.08$	29%

Table 6.13: Summary of the event yields in the muon channel for the different steps of the top analysis. For further explanations see the caption of table 6.12.

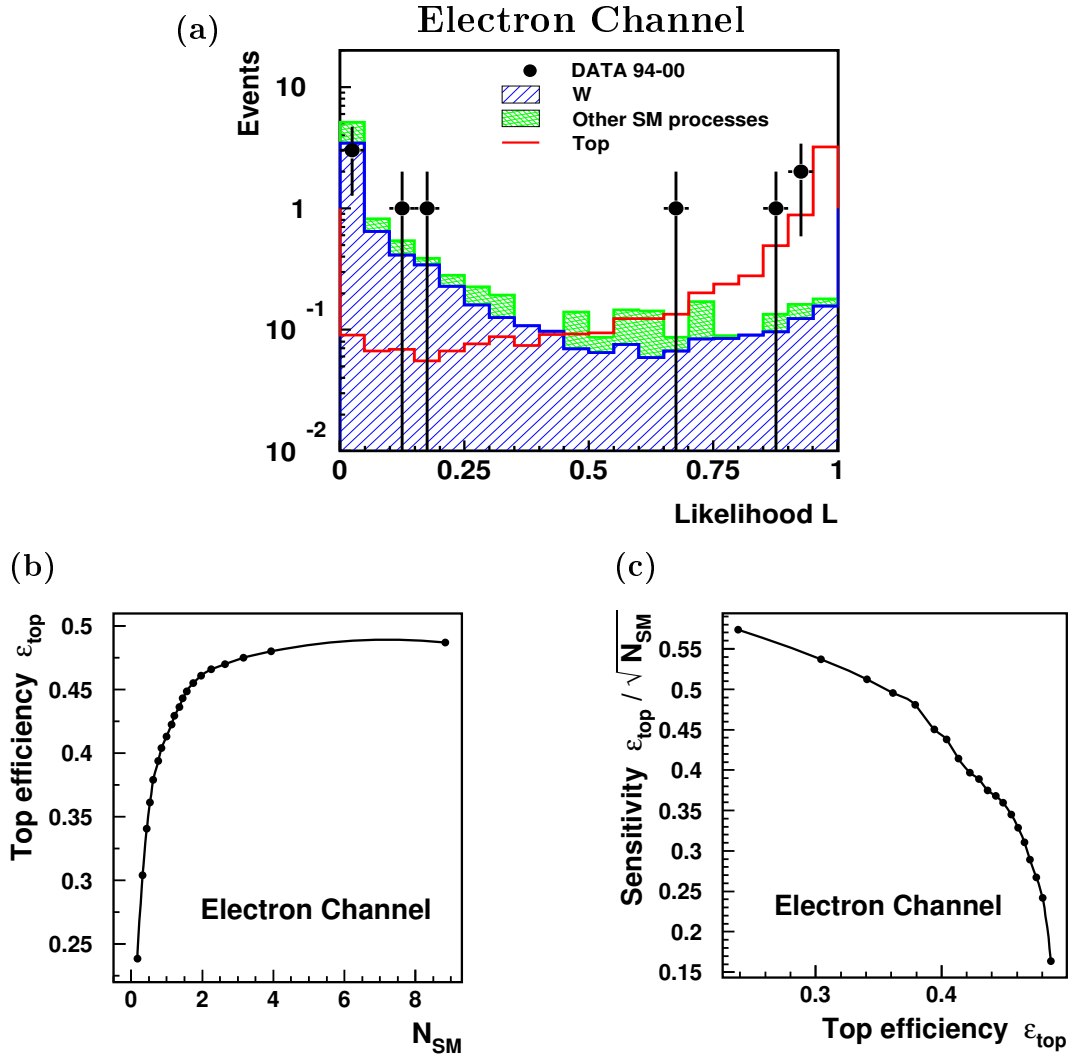


Figure 6.30: The likelihood discriminator in the electron channel, obtained with the PTC-method after imposing the cut on the electron charge. Events with negative electron charge are removed. The top simulation is normalized to the expectation from  $W$  production. In (b) the top efficiency,  $\epsilon_{top}$ , is shown as a function of the remaining Standard Model background,  $N_{SM}$ . Plot (c) shows a signal sensitivity curve, evaluated for the likelihood discriminator in (a). The dots on the curves correspond to the bin borders of the likelihood.

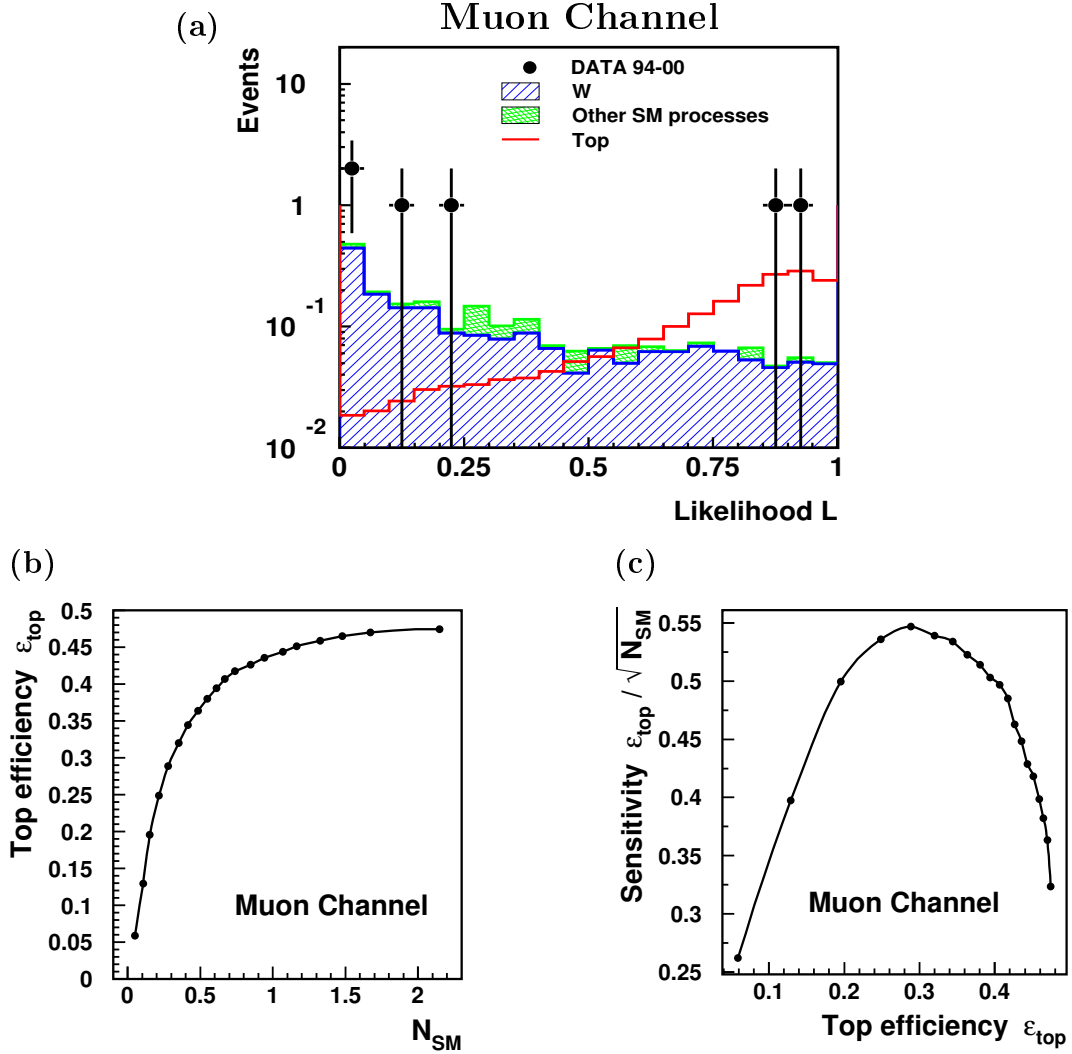


Figure 6.31: The likelihood discriminator in the muon channel, obtained with the PTC-method after imposing the cut on the muon charge. Events with negative muon charge are removed. The top simulation is normalized to the expectation from  $W$  production. In (b) the top efficiency,  $\epsilon_{top}$ , is shown as a function of the remaining Standard Model background,  $N_{SM}$ . Plot (c) shows a signal sensitivity curve, evaluated for the likelihood discriminator in (a). The dots on the curves correspond to the bin borders of the likelihood.

# Chapter 7

## Top Search in the Hadronic Decay Channel

A search for single top production is also performed for top quark decays, where the  $W$  decays hadronically. The decay cascade  $t \rightarrow bW \rightarrow bq\bar{q}'$  typically yields events with at least three high- $P_T$  jets. The jets are expected mainly in the forward region of the detector. In contrast to the semi-leptonic decay channel, where the Standard Model rate is low, the background expectation in the hadronic channel is much higher because QCD processes leading to multi-jet signatures have large cross-sections. These multi-jet final states appear in higher orders of the strong coupling constant  $\alpha_s$ . Unfortunately, the currently available QCD generators can only give approximate descriptions of these higher order processes in the leading-log parton shower approximation.

As a first step, a pre-selection of events with at least three jets is carried out. In this pre-selected event sample, the agreement between kinematic distributions of the data and the QCD simulations is tested. For the top analysis, the phase space is restricted to a region of high transverse momenta and events are required to contain a candidate for the decay  $W \rightarrow q\bar{q}'$ . A set of variables is chosen to effectively separate the top signal from the bulk of QCD events. In correspondence to the analysis in the semi-leptonic decay channel, first a selection of top candidates using one-dimensional cuts is accomplished. The selection is then refined in a likelihood analysis and the two methods are compared to each other.

### 7.1 Pre-Selection of Multi-Jet Events

The search for multi-jet events is performed using an inclusive  $k_T$  algorithm as described in section 5.2.2. Only jets in the pseudorapidity range  $-0.5 < \eta_{jet} < 2.5$  are selected. The restricted  $\eta$ -range ensures that the jets are well-contained in the Liquid Argon Calorimeter. In order to remove electrons that are mis-identified as hadronic jets, each jet is required to either have an energy fraction in the electromagnetic calorimeter of less than 90% of its total energy or a size in the  $\eta - \phi$  plane larger than 0.1. These criteria define the hadronic jets in each event.

For the pre-selection of top candidates, only events with at least three hadronic jets are selected that fulfill the transverse momentum criteria  $P_T^{jet1} > 25$  GeV,  $P_T^{jet2} > 20$  GeV,  $P_T^{jet3} > 15$  GeV. The jets are ordered according to decreasing transverse momentum. Additional jets are accepted if their transverse momenta are larger than 4 GeV. With these requirements, the pre-selected multi-jet sample contains 1473 data events.

### 7.1.1 Standard Model Background and Background Normalization

The main Standard Model background to hadronic top decays is the electro- and photoproduction of high- $P_T$  multi-jets. The photoproduction and low- $Q^2$  regime with momentum transfers  $Q^2 < 4$  GeV<sup>2</sup> is modeled with the PYTHIA generator. Neutral current DIS events with momentum transfers  $Q^2 > 4$  GeV<sup>2</sup> are simulated with the RAPGAP generator.

It is seen that the predicted multi-jet rates for the Standard Model background do not agree with the data after normalization to their integrated luminosity. This difference is at the level of 30-40%, and it could be explained by the fact that the parton shower approximation in the Monte Carlo simulations does not correctly describe next-to-leading order corrections. The background simulations are therefore normalized to the observed number of data events. It remains to be checked, if the shapes of kinematic distributions are well described. The normalization factors are derived separately for the different  $Q^2$  regimes modeled by PYTHIA and by RAPGAP.

- **Normalization of RAPGAP:**

A subsample of multi-jet events that contain an electron candidate is selected. Therefore, in addition to the multi-jet preselection, an electromagnetic cluster with energy  $E_{em.cluster}$  above 5 GeV and an associated track in the main detector are required. The thus defined sample contains 372 data events. A nice example event is presented in figure 7.1. The RAPGAP normalization is now derived from the data in the polar angle region  $50^\circ < \theta_{em.cluster} < 165^\circ$  of the electromagnetic cluster, where the contribution from PYTHIA is completely negligible.

- **Normalization of PYTHIA:**

The normalization of the PYTHIA Monte Carlo is derived from a subsample of events, in which no electron candidate is found. This sample contains 1101 data events. Here, in turn, the contribution from RAPGAP is small.

Compared to a normalization according to the integrated luminosity of the data, the normalization derived for RAPGAP (PYTHIA) corresponds to a scaling factor of 1.4 (1.29). Figure 7.2 shows the transverse momentum and polar angle distribution of the electromagnetic cluster for the multi-jet subsample with an electron candidate. At very large polar angles, the transition from the PYTHIA simulation to the RAPGAP simulation at  $Q^2 = 4$  GeV<sup>2</sup> is visible. For very small polar angles (forward region), an accumulation of events can be seen. They are due to photons or hadrons that are falsely identified as electron. In the case of photons, the required associated track

originates from conversions in the dead material of the forward tracker or in the end caps of the central jet chamber. These electron mis-identifications are seen to be well described by the normalized Monte Carlo simulations.

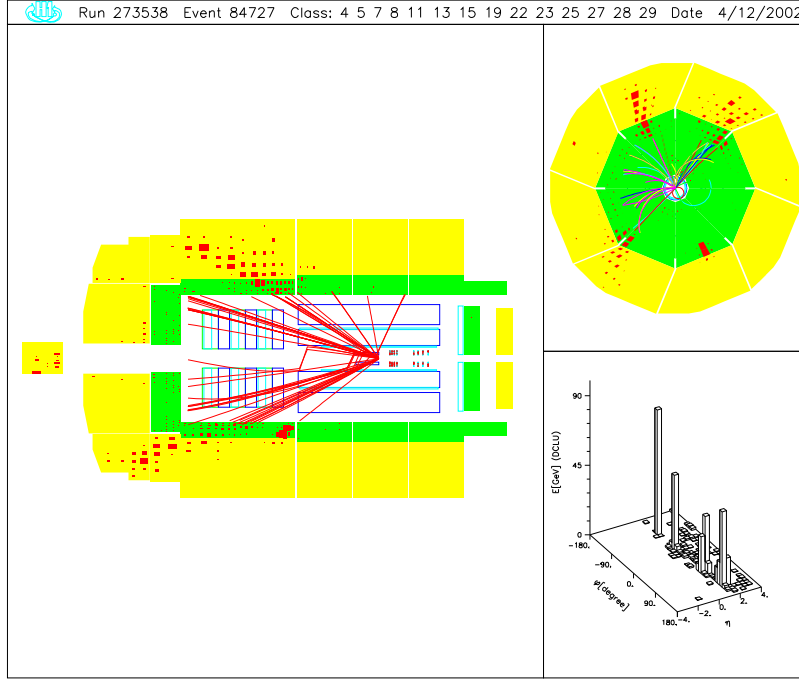


Figure 7.1: Pre-selected multi-jet event with tagged electron.

$$P_T^{jet1,2,3} = 47, 45, 42 \text{ GeV} \quad , \quad P_T^e = 51 \text{ GeV}.$$

### 7.1.2 Control Distributions

In figure 7.3, control distributions for the multi-jet pre-selection are presented. The normalized PYTHIA and RAPGAP Monte Carlos now represent the Standard Model QCD background. The  $z$ -vertex distribution of the data is seen to be well described by the simulation. Also the  $E - P_z$  distribution and the number of jets are well described. Roughly 30% of the events contain more than three jets. The transverse momentum distributions of the three highest- $P_T$  jets are shown as well as the transverse momentum of a possible fourth jet and the total transverse momentum measured in the calorimeter,  $E_T^{tot}$ . The shapes of all studied distributions are in reasonable agreement with the simulation.

The displayed error band corresponds to a 15% uncertainty on the total Standard Model expectation, as derived later in section 7.4.2. For now it should only give an impression of the size of systematic uncertainties involved in the analysis of the hadronic channel.

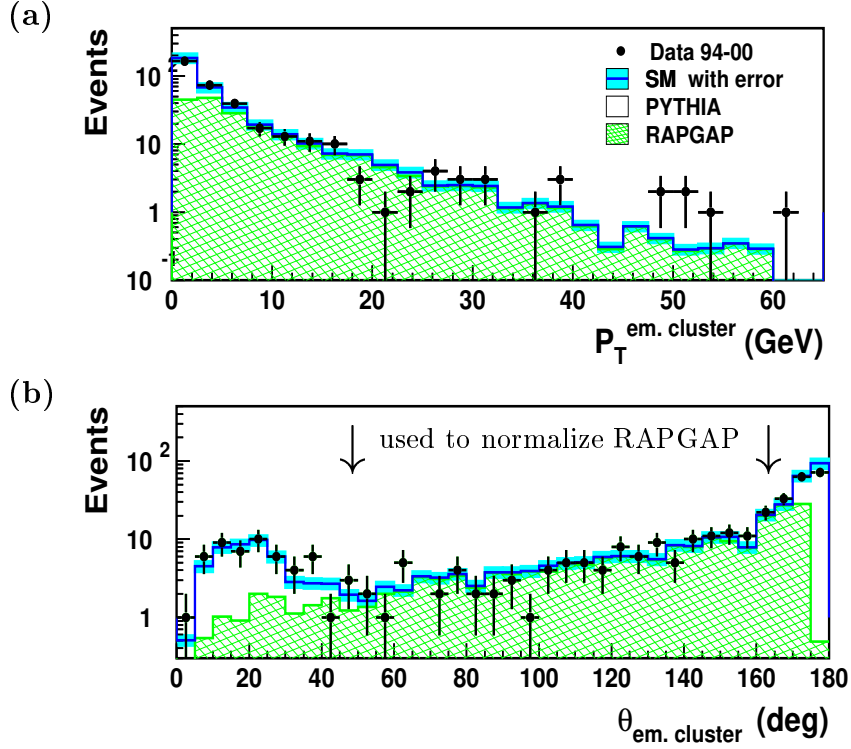


Figure 7.2: Polar angle and transverse momentum of the electromagnetic cluster in the pre-selected multi-jet events that contain an electron candidate. The polar angle region used to derive the RAPGAP normalization is marked by arrows.

## 7.2 Selection of Events with High $E_T$ and a $W$ Candidate

To enhance a possible top signal relative to the QCD background, the phase space is further restricted to a region of higher jet transverse momenta. Moreover, candidate events for top production are required to have the signature of a  $W$  boson in the event.

### Transverse Momentum Requirements

The two highest- $P_T$  jets must have transverse momenta  $P_T^{\text{jet1}} > 40$  GeV and  $P_T^{\text{jet2}} > 30$  GeV. In top events, the two highest- $P_T$  jets correspond to the  $b$ -quark and to the quark from the  $W$  decay that is emitted in the direction of the  $W$  boost. The pre-selection requirement for the third jet,  $P_T^{\text{jet3}} > 15$  GeV, is already quite harsh and is not increased further. Due to the high top mass, a large amount of transverse energy is expected in events from top production. Thus the total transverse energy  $E_T^{\text{tot}}$  is required to be above 110 GeV. The applied cuts are indicated as dashed lines in the control distributions of figure 7.3.



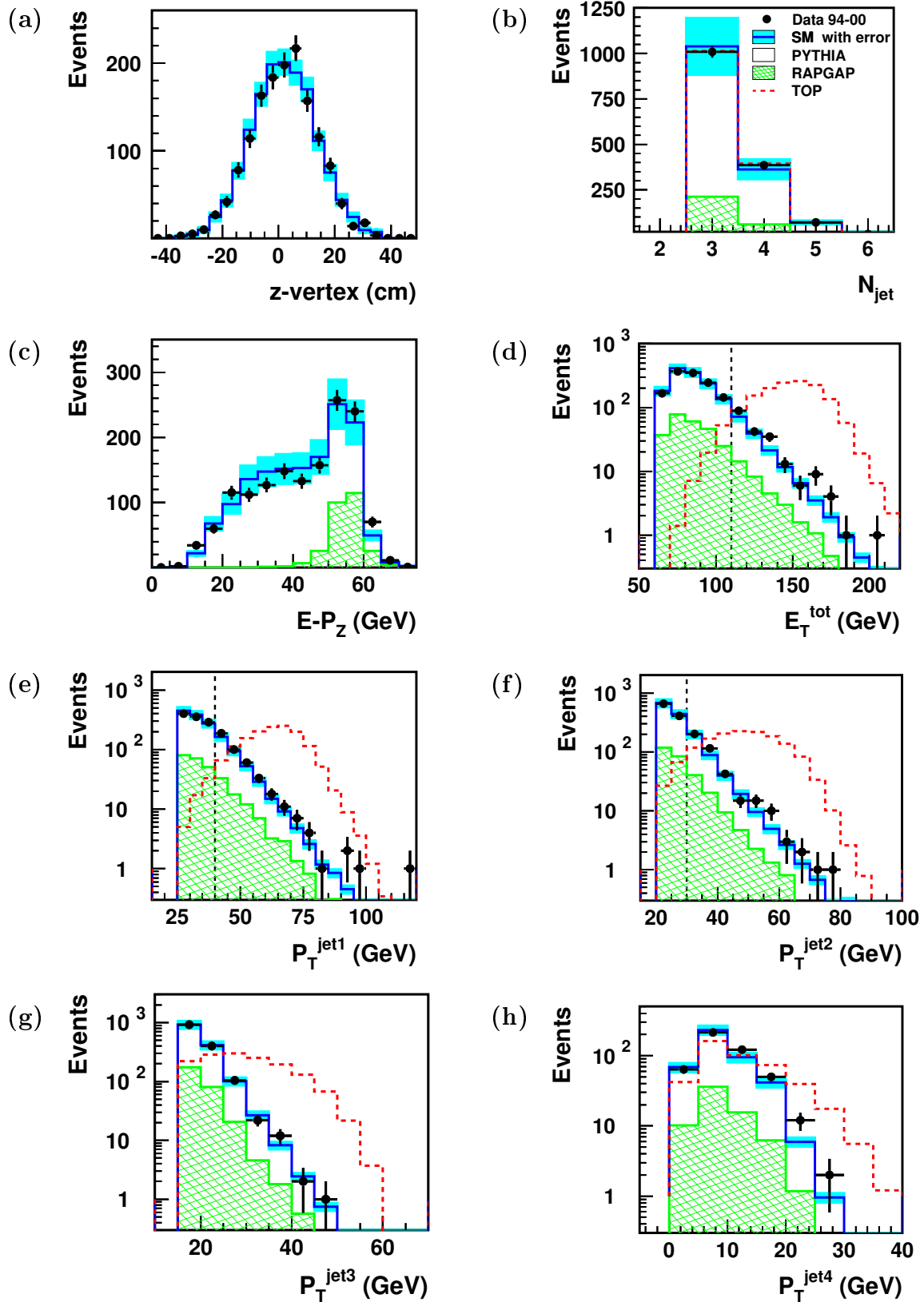


Figure 7.3: Control distributions of the multi-jet pre-selection. The error band corresponds to a 15% uncertainty on the Standard Model distribution, represented by the scaled PYTHIA ( $\times 1.29$ ) and RAPGAP ( $\times 1.4$ ) simulations. For the transverse energy,  $E_T^{\text{tot}}$  and the transverse momenta of the jets also the top simulation is shown as dashed histogram, normalized to the same area as the Standard Model background. The dashed lines indicate the cuts used in the selection of high- $E_T$  multi-jet events.

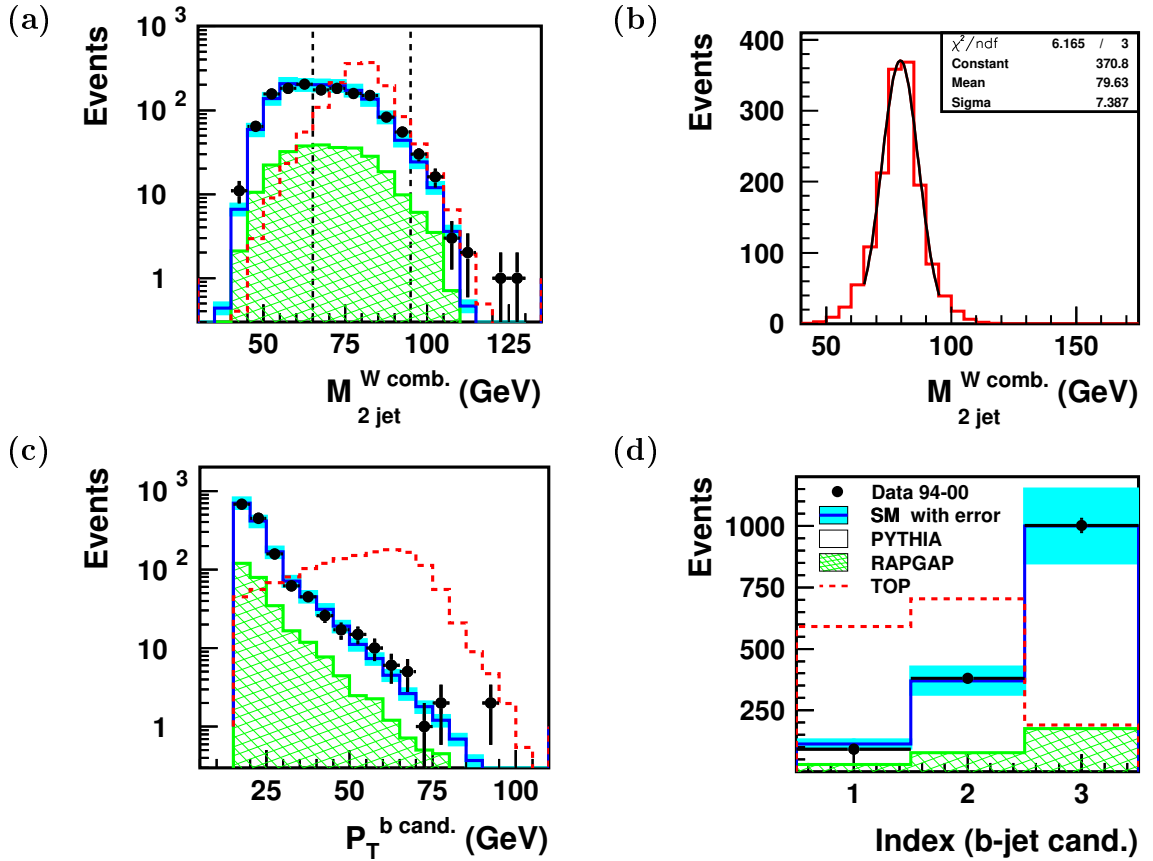


Figure 7.4: Control distributions of the multi-jet pre-selection representing the event decomposition that is used to identify the  $b$ -jet and the two jets from the  $W$  decay. The distributions are shown for both background and top simulations. The top simulation is arbitrarily normalized to the same area as the Standard Model background. The dashed lines in (a) represent the mass window applied on the di-jet mass closest to the  $W$  mass,  $M_{2jet}^{W comb.}$ , in order to select events with a  $W$  candidate. The results of a Gaussian fit to the  $M_{2jet}^{W comb.}$  distribution for simulated top events is shown in (b). Plots (c) and (d) show the transverse momentum and the index of the candidate  $b$ -jet (index=1 means highest- $P_T$  jet).

### Event Decomposition to Identify the $b$ -Quark and the $W$ Decay Products

In contrast to the semi-leptonic decay channel, where the lepton is unambiguously identified, it is not obvious for hadronic top decays, which of the jets correspond to the  $q\bar{q}'$  pair from the  $W$  decay, and which to the  $b$ -quark. The three highest- $P_T$  jets are associated to the  $b$ -quark and to the hadronic decay of the  $W$  according to the following procedure:

- The two jets with an invariant mass closest to the  $W$  mass are assigned to the  $W$  decay products. The invariant mass of these two jets is denoted with  $M_{2jet}^{W comb.}$ .
- The remaining jet among the three highest- $P_T$  jets is assigned to the  $b$ -quark from the top decay.

This hypothesis identifies the correct  $b$ -jet in about 70% of simulated top events. As can be seen in figure 7.4, the results of this event decomposition is well described by the Monte Carlo simulations. In top decays, the  $b$ -jet is found to be the jet with second highest- $P_T$  in most of the cases.

### $W$ Mass Requirement

As a sign of a  $W$  boson in the event, one of the invariant masses of the different di-jet combinations must have a value close to the nominal  $W$  mass. To select events with potential  $W$  candidates, a mass window is set around the mass of the di-jet combination closest to the  $W$  mass:

$$65 \text{ GeV} < M_{2jet}^{Wcomb.} < 95 \text{ GeV}. \quad (7.1)$$

The mass resolution obtained for simulated top events is 7.4 GeV (see figure 7.4 (b)). The width of the mass window corresponds to about twice the  $W$  mass resolution.

The selection of multi-jet events with high  $E_T$  and a  $W$  candidate yields 92 data events for a Standard Model expectation of 92.4 events. The efficiency for single top production is 42%. The expected contribution from Standard Model  $W$  production amounts to only 4.0 events. Table 7.1 summarizes the event yields for the data and the Standard Model expectations.

The normalization factors for the PYTHIA and RAPGAP Monte Carlos are again checked after the high- $E_T$  and  $W$  mass requirements, following the same strategy as described for the pre-selection. The factors of 1.29 for PYTHIA and 1.4 for RAPGAP are found to be also valid in this more restricted phase space. Distributions of the transverse momenta and pseudorapidities of the jets are displayed in figure 7.5. Also the distributions of a possible fourth jet are shown. The shapes of all distributions are in agreement with the Standard Model prediction.

Hadronic channel	Data 94-00	SM	PYTHIA	RAPGAP	$W$ prod.	$\epsilon_{top}$
Multi-jet pre-selection	1473	normalized to data			10.0	54%
High- $E_T$ and $W$ cand.	92	92.4	68.7	19.8	4.0	42%

Table 7.1: Observed and predicted event yields for the multi-jet pre-selection and the harsher selection of multi-jet events with high- $E_T$  and a  $W$  candidate. PYTHIA is scaled by 1.29, RAPGAP by 1.4.

## 7.3 Observables to Discriminate Top and QCD Background

The available kinematic degrees of freedom in top decays were discussed in section 6.5.1. From the four degrees of freedom, neglecting the azimuthal angles of the top and  $W$

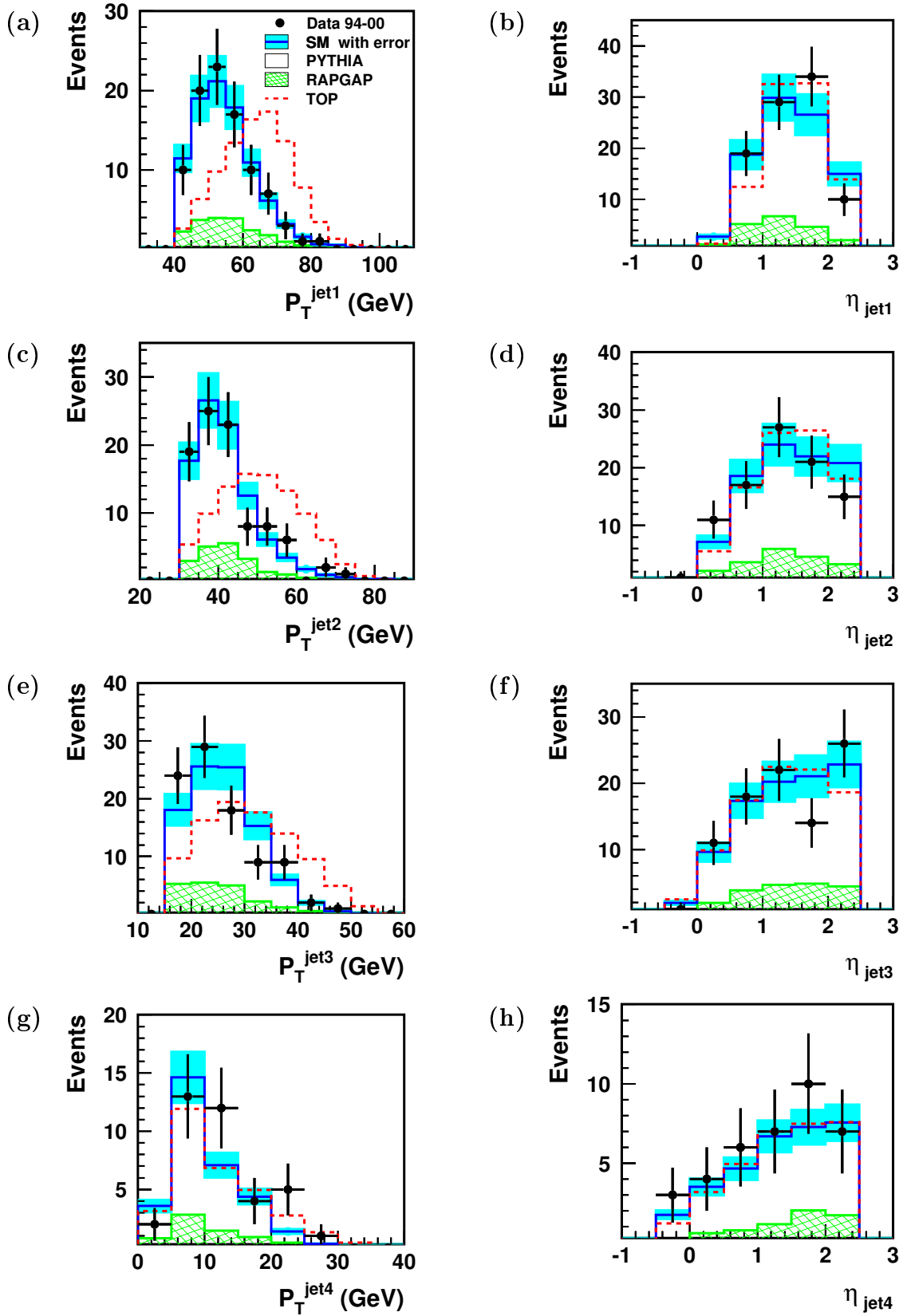


Figure 7.5: Distributions of the jet transverse momenta and pseudorapidities for the selection of multi-jet events with high  $E_T$  and a  $W$  candidate. The error band corresponds to a 15% uncertainty on the total Standard Model prediction. The top simulation is arbitrarily normalized to the same area as the Standard Model background.

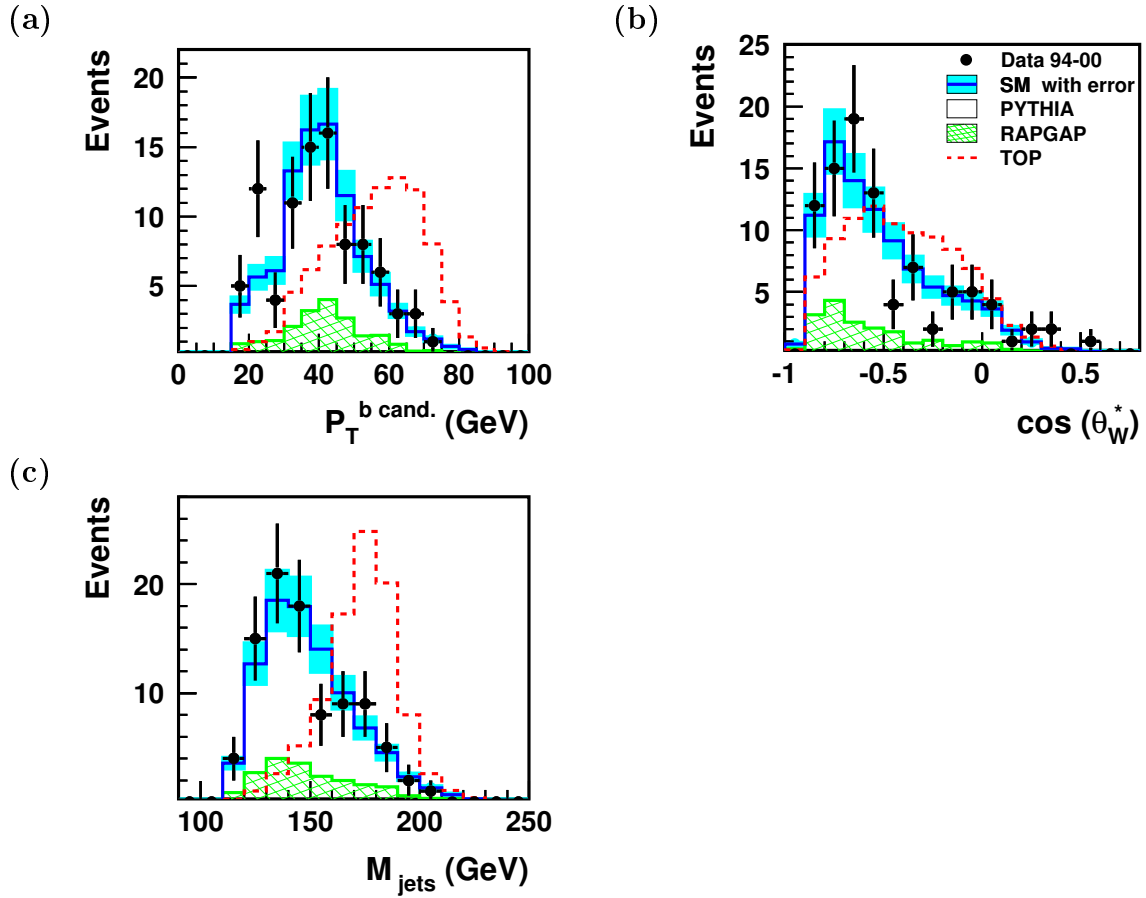


Figure 7.6: Distributions of the three observables used to discriminate the top signal from the Standard Model background. The error band corresponds to a 15% uncertainty on the total Standard Model expectation. The top simulation is arbitrarily normalized to the same area as the Standard Model background.

decays, the  $W$  mass has already been exploited in the previous selection step. Thus three observables remain. They are chosen corresponding to the semi-leptonic decay channel:

1.  $P_T^{b \text{ cand.}}$ , the transverse momentum of the candidate  $b$ -jet.
2.  $M_{\text{jets}}$ , the invariant mass of all selected jets in the event.
3.  $\cos(\theta_W^*)$ , the  $W$  decay angle (see figure 6.19). It is defined as the angle between the lower- $P_T$  jet of the two jets assigned to the  $W$  decay in the  $W$  rest frame and the direction of the  $W$  in the top rest frame. In the hadronic channel, no distinction between the quark and the anti-quark jet emerging from the  $W$  decay is possible. Since always the lower- $P_T$  jet is used to define this angle, the angular distribution differs from the one in figure 6.20 for the semi-leptonic channel. A lower transverse momentum favors large angles between the jet and the  $W$  direction, which leads to a depopulation of positive  $\cos(\theta_W^*)$  values.

As can be seen in figure 7.6, all three observables exhibit a good discrimination between the top signal and the QCD background. The  $P_T^{b \text{ cand.}}$  distribution shows the

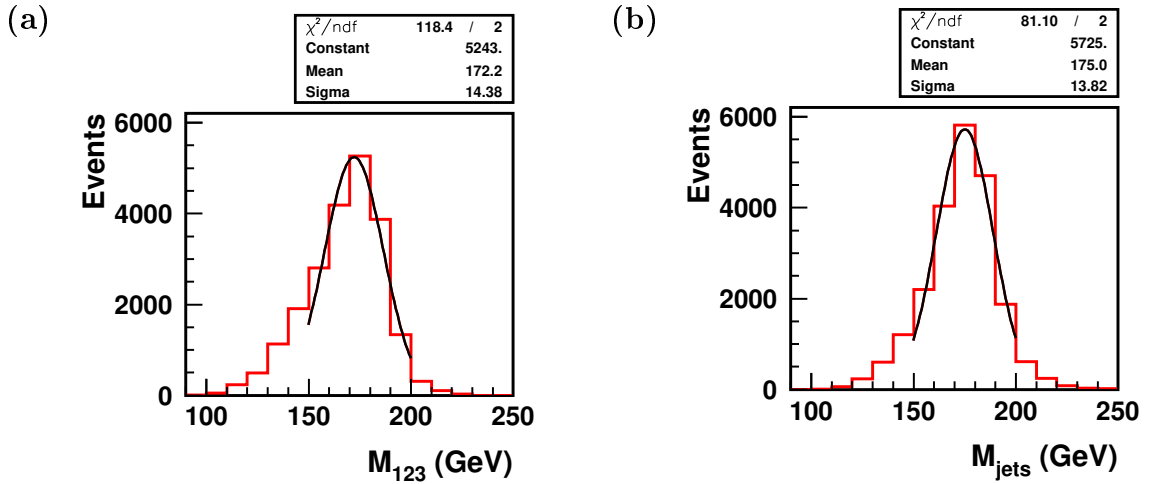


Figure 7.7: Monte Carlo distributions of the invariant mass of the three highest- $P_T$  jets (a) and of all jets (b) for simulated top events. The lines correspond to Gaussian fits to the cores of the mass distributions.

Jacobian at 69 GeV expected for top decays, while the QCD background exhibits a steeply falling  $P_T^{b\text{-}cand.}$  spectrum. The angular distribution for QCD processes peaks at larger angles than for top production. This is also reflected in the lower transverse momentum of the third jet (see figure 7.5 (e)). As for the reconstruction of the top mass, the 3-jet invariant mass,  $M_{123}$ , and the invariant mass of all selected jets,  $M_{\text{jets}}$ , are compared for simulated top events in figure 7.7. The 3-jet invariant mass peaks at 172 GeV and exhibits a tail toward smaller masses. This tail is mainly due to the neglecting of final state parton showers. It is therefore more favorable to reconstruct the top mass as the mass of all selected jets. The  $M_{\text{jets}}$  distribution shows a peak at the nominal top mass, a more Gaussian shape, and a slightly improved mass resolution of 13.8 GeV.

The correlations of the three discriminating observables are displayed in figure 7.8. As expected, the decay angle shows no significant correlation to the other two observables, while the transverse momentum of the candidate  $b$ -jet and the invariant mass of the jets are clearly correlated.

## 7.4 Cut-Based Top Search

The final selection of top candidates in the hadronic channel is performed using both a simple cut-based analysis and a likelihood analysis. In this section, the selection cuts and the results of the cut-based analysis, as well as the effect of systematic uncertainties are discussed.

### 7.4.1 Definition of the Cuts

Table 7.2 shows the top selection cuts imposed on the three discriminating observables. Due to the much larger background expectation from Standard Model processes,

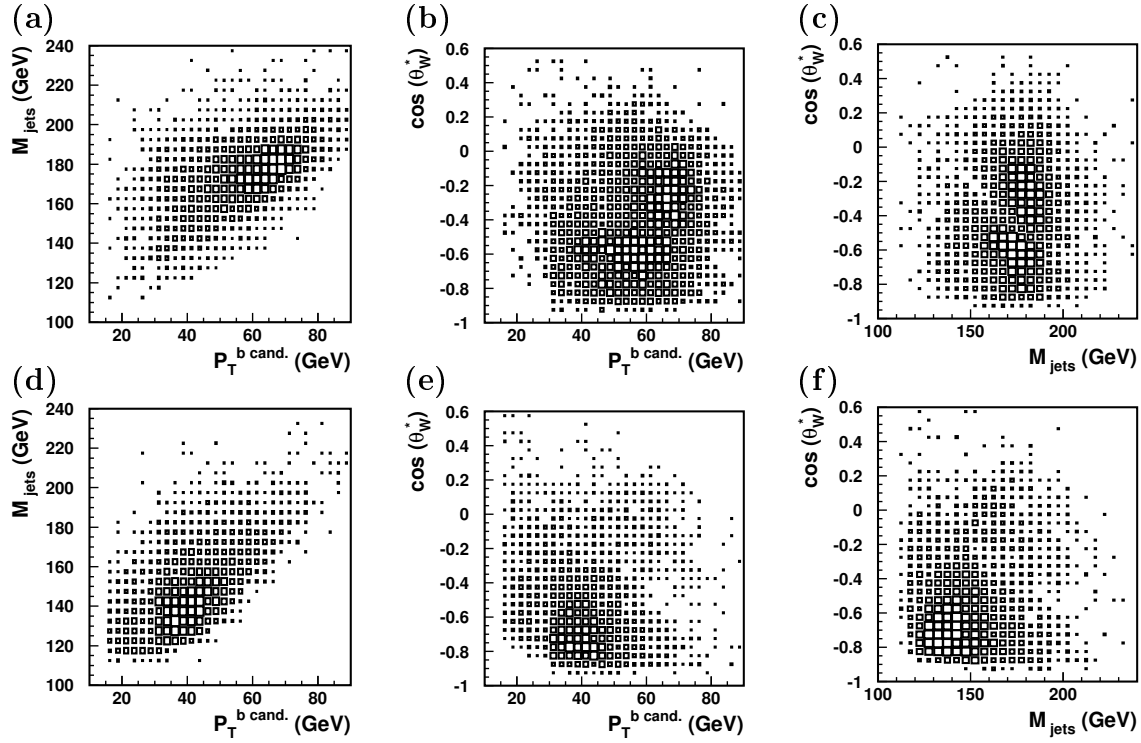


Figure 7.8: Correlations of the discriminating observables in the hadronic channel for the simulations of the top signal (upper plots (a)-(c)) and the background from photoproduction (lower plots (d)-(f)).

harsher cuts have to be applied compared to the semi-leptonic channel. The cut values are designed to maintain an efficiency of 30% for top events.

Hadronic Channel	Top selection cuts
Transverse momentum of $b$ -candidate	$P_T^{b-cand.} > 40 \text{ GeV}$
$W$ decay angle	$\cos(\theta_W^*) > -0.75$
Top mass window	$150 \text{ GeV} < M_{jets} < 210 \text{ GeV}$

Table 7.2: Summary of the cuts used in the cut-based selection of hadronic top decays.

### 7.4.2 Systematic Uncertainties

Uncertainties on the experimental measurements as well as uncertainties on the theoretical predictions for multi-jet production can have an impact on the normalization and the shape of the distributions used in the cut-based top selection. The theoretical uncertainty on the Standard Model prediction should give an estimate of how well the approximation of parton showers by the leading order PYTHIA model can simulate for instance a 3-jet process ( $\mathcal{O}(\alpha_s^2)$ ).

### Uncertainty on the Standard Model Prediction

Since the Monte Carlo simulations have been normalized to the data, the uncertainty on the Standard Model normalization is given by the statistical uncertainty of the data events. It is taken from the number of events in the sample, where the final top selection is carried out, i.e. the high- $E_T$  sample with a  $W$  candidate. It contains 92 data events, and thus yields an uncertainty on the Standard Model normalization of 10%. At this stage one assumes of course that the data are dominated by Standard Model background.

Figure 7.9 shows the data over Monte Carlo ratio for the distributions of the total transverse energy,  $E_T^{tot}$ , and the invariant mass  $M_{jets}$  for the high- $E_T$  sample with a  $W$  candidate. Both distributions show no significant slope within statistical uncertainties. Thus no additional uncertainty is assumed for the shape of the Standard Model distributions and the extrapolation into the signal region.

Studies of kinematic distributions for multi-jet production can be found in [63, 64, 65, 66]. For instance, the analysis of multi-jet distributions in photoproduction published by the ZEUS Collaboration in [63] showed, that next-to-leading order corrections,  $\mathcal{O}(\alpha_s^2)$ , cause a 30-40% increase of the leading order cross-section. This increase is consistent with the normalization factors derived in this analysis. The shape of the multi-jet invariant mass distribution was shown to be in good agreement with both the  $\mathcal{O}(\alpha_s^2)$  calculations and the prediction of the leading-log parton shower model PYTHIA.

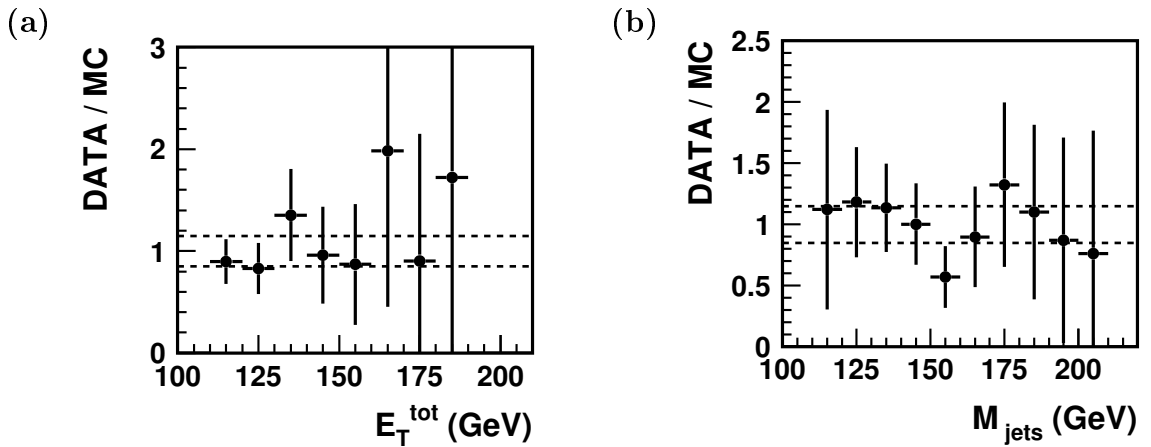


Figure 7.9: Ratio of the observed (DATA) and predicted (MC) number of events for the distributions of the total transverse energy,  $E_T^{tot}$ , and the invariant mass  $M_{jets}$  in the selected sample of multi-jet events with high- $E_T$  and a  $W$  candidate.

### Experimental Systematic Uncertainties

The main experimental systematic uncertainty in the hadronic channel are due to the uncertainties in the absolute hadronic energy calibration of the calorimeter and the measurement of the polar angles of the jets. The uncertainties on the azimuthal angle of the jets is found to be negligible. The large amount of calorimetric energy in the selected multi-jet events assures that the events are triggered with an efficiency of  $\sim 100\%$ . The uncertainty resulting from trigger inefficiencies can therefore be neglected. The uncertainty on the luminosity measurement is 1.5%.



The effect of the experimental systematic uncertainties are evaluated through variation of the hadronic energy scale by  $\pm 4\%$  and a simultaneous variation of all jet polar angles by  $\pm 20$  mrad. The impact of these variations on the overall Monte Carlo prediction is already included in the 10% normalization uncertainty discussed above. Only the effect on the slope of the distributions must still be taken into account. Therefore the change in overall normalization is effectively subtracted from the uncertainty leaving only the contribution from the change in slope.

Experimental Systematic	$\delta N_{SM}$ after top cuts (slope uncertainty)
Hadronic energy scale	$\pm 6\%$
Jet polar angles	$\pm 9\%$
Luminosity	$\pm 1.5\%$
Total	$\pm 11\%$

Table 7.3: Summary of the experimental systematic uncertainties in the hadronic channel. The total uncertainty is the quadratic sum of all experimental uncertainties.

The effect of the variation of the jet polar angles is relatively large. Besides migrations of events in and out of the restricted  $\eta_{jet}$  range, a variation by  $\pm 20$  mrad for a forward jet with pseudorapidity  $\eta_{jet} = 2.5$  also corresponds to a change in its transverse momentum of roughly 10%.

The normalization uncertainty and the uncorrelated experimental uncertainties are added in quadrature. The resulting total systematic uncertainty is 15%.

### 7.4.3 Results

In the cut-based analysis, 18 data events are selected as top candidates. The observed data events agree well with the Standard Model expectation of  $20.2 \pm 3.0$  events (see table 7.4). The uncertainty of 3.0 events on the Standard Model expectation corresponds to the 15% obtained above. Figure 7.10 (a) shows the distribution of the invariant mass  $M_{jets}$  after all top selection cuts. The top simulation is normalized to the same area as the background. No excess of events as a signal of top production is observed. In plots (b) and (c) of figure 7.10 the full invariant mass spectrum can be seen, i.e. without imposing the top mass window. In (b) the top Monte Carlo is normalized to the number of events that would correspond to a potential top signal in the semi-leptonic channel, as evaluated later in section 8.1. It is obvious that a signal of this size would not be very significant in the hadronic channel. In plot (c), however, the top normalization corresponds to the combined LEP limit on anomalous top production [67]. It shows that the H1 top analysis is sensitive enough to improve the exclusion limits obtained by other experiments.

The compatibility between both channels and the derivation of an exclusion limit on the cross-section for anomalous top production will be discussed in detail in chapter 8.

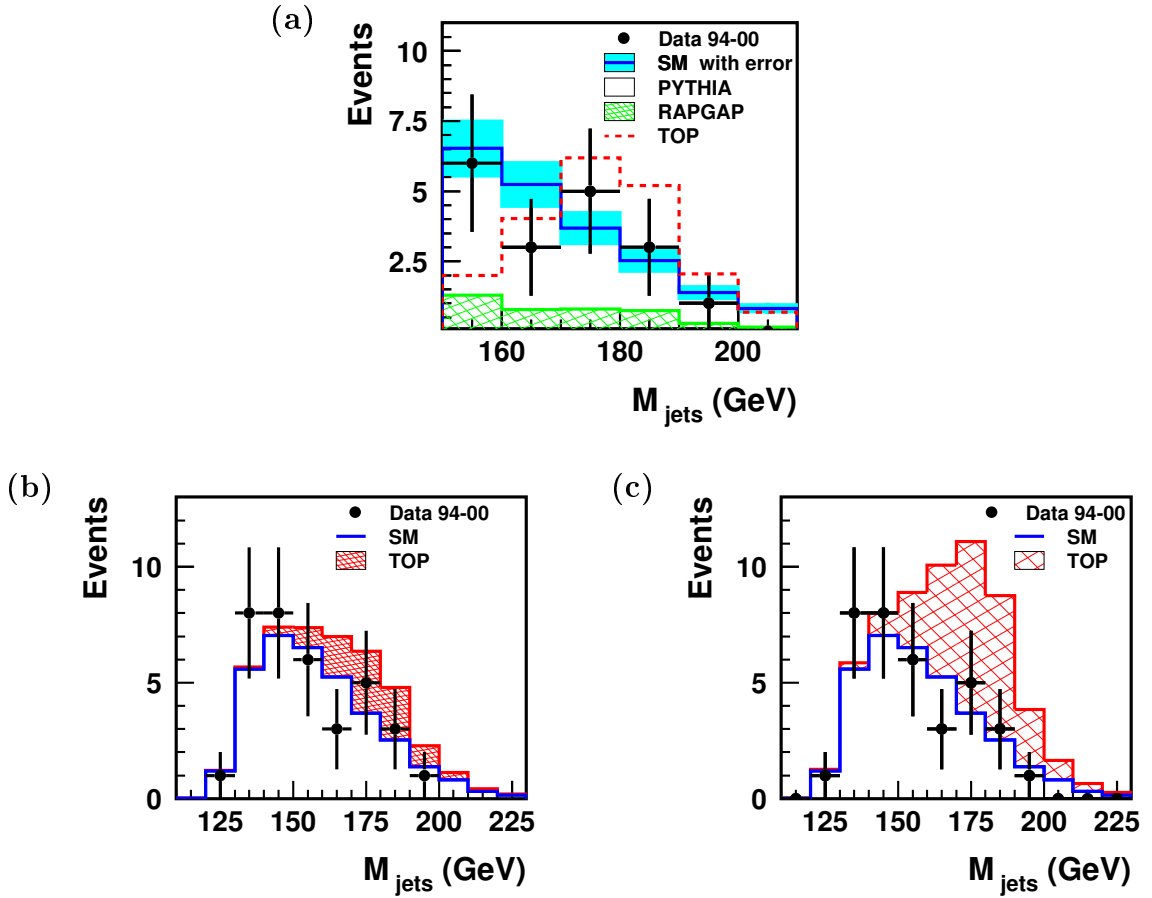


Figure 7.10: (a): The  $M_{jets}$  distribution after the cut-based top selection in the hadronic channel. The error band corresponds to a 15% error on the total Standard Model expectation. The top simulation is arbitrarily normalized to the same area as the Standard Model background. (b) and (c): The full  $M_{jets}$  distribution after the cut-based top selection without imposing the top mass window. Here the top simulation is added to the Standard Model histogram. In (b) the top simulation is normalized according to a top interpretation of the isolated lepton excess seen in H1. The top normalization in (c) represents the current limit on the anomalous top production cross-section obtained by the LEP collaboration.

## 7.5 Likelihood Discriminator

The likelihood method described in section 6.7.2 is applied to combine the discriminating observables in a single likelihood discriminator and improve the sensitivity of the top selection. The three observables in figure 7.6 serve as input to the likelihood analysis. In contrast to the semi-leptonic channel, where the top hypothesis was tested versus the  $W$  hypothesis as dominant background, the background in the hadronic channel comes mainly from non- $W$  processes. All background processes are combined and the combination is used for the construction of the likelihood discriminator. Hence in the hadronic likelihood analysis, the top hypothesis is tested versus the combined Standard Model hypothesis.

### 7.5.1 Application of the Likelihood Method

Correlations between the observables are again taken into account by using the PTC-method described in section 6.7.2. The distributions of the Gaussian transformed observables for the signal and background samples are displayed in appendix C. The deviations of the mean (standard deviation) of the obtained Gaussian distributions from zero (one) are less than 8% (3%). The correlations matrices of the observables before and after the Gaussian transformations are also shown.

The resulting likelihood discriminator is presented in figure 7.11. To visualize the separation between signal and background, the top simulation is normalized to the same area as the total Standard Model background. The relative background contributions from different Standard Model processes (photoproduction, neutral current DIS, and  $W$  production) are shown as separate histograms. The PTC-method removes the small erroneous peaks produced by the standard method at  $L = 0$  for the signal and at  $L = 1$  for the background through a proper treatment of correlations, leading to a higher purity for the signal.

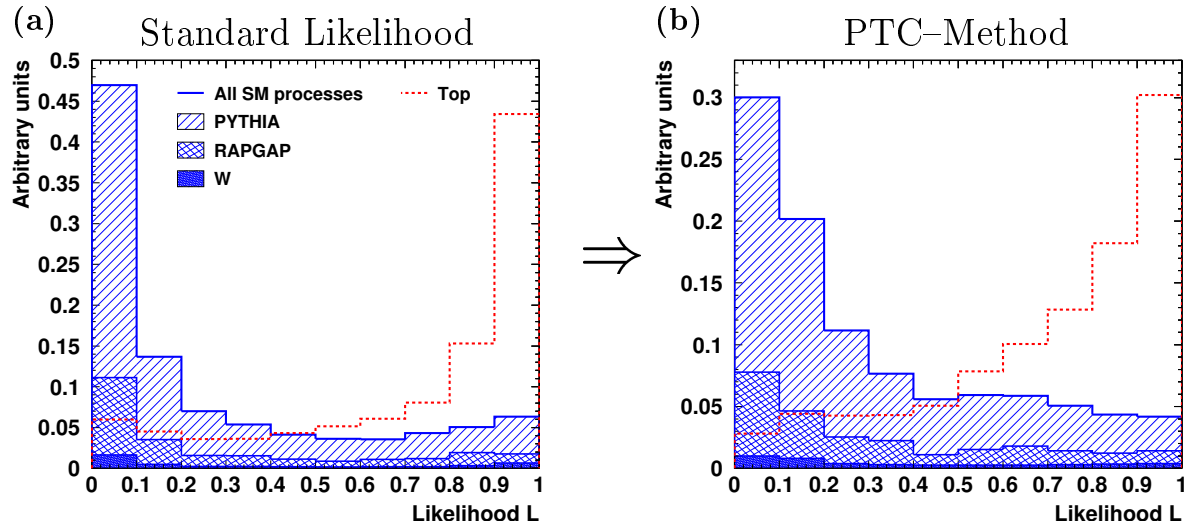


Figure 7.11: The likelihood discriminators obtained with the standard method (a) and the PTC-method (b) for Monte Carlo events of the top signal and the QCD background. The signal and total background distributions are normalized to unity. The relative background contributions from photoproduction, neutral current DIS and Standard Model  $W$  production are displayed as different hatching types (see legend).

### 7.5.2 Results and Comparison to Cut-Based Analysis

The likelihood distributions of the data and the Monte Carlo simulations are compared in figure 7.12. The data agree well with the likelihood distribution of the Standard Model simulation, consistent with the result obtained in the cut-based analysis. The top signal is again displayed with two different normalizations, one corresponding to

Hadronic Channel	Data 94-00	SM	PYTHIA	RAPGAP	W prod.	$\epsilon_{top}$
Top cuts	18	$20.2 \pm 3.0$	14.7	4.0	1.4	30%
Cut $L > 0.60$	18	$18.0 \pm 2.7$	12.6	4.2	1.2	30%
Optim. cut $L > 0.80$	9	$7.9 \pm 1.2$	5.4	1.8	0.7	21%

Table 7.4: Summary of the observed and predicted number of events for the cut-based top analysis and for two different cuts on the likelihood discriminator  $L$ . The total Standard Model expectation is shown with a systematic uncertainty of 15%. The contributions from photoproduction, neutral current DIS and  $W$  production are shown separately. For each selection, also the top efficiency,  $\epsilon_{top}$ , is given.

the excess in the semi-leptonic channel, the other corresponding to the current LEP limit on anomalous top production.

The performance of the likelihood discriminator compared to the selection exploiting a set of one-dimensional cuts is again studied by comparison of the Standard Model expectation for the cut-based analysis with the expectation for a likelihood cut that yields the same signal efficiency of 30%. As can be seen in table 7.4 and figure 7.12 (b), a cut at  $L = 0.60$  leaves a top efficiency of 30% and a background expectation of 18.0 events. It corresponds to a background reduction of  $\sim 10\%$  compared to the cut-based analysis.

The signal sensitivity of the likelihood discriminator, represented by a plot of the ratio  $\epsilon_{top} / \sqrt{N_{SM}}$  as a function of  $\epsilon_{top}$ , is displayed in figure 7.12 (c). The most sensitive likelihood cut is thus found to be at  $L = 0.80$ , corresponding to a top efficiency of 21%. This optimized cut yields nine data events in agreement with the expectation of  $7.9 \pm 1.2$  events. The kinematic properties of the nine data events are shown in table 7.5.2. One of these events is rejected by the cut-based analysis because of a too low transverse momentum of the candidate  $b$ -jet. In the likelihood analysis, the low value of  $P_T^{b-cand.}$  is compensated by values of  $\cos(\theta_W^*)$  and  $M_{jets}$  for which the Standard Model expectation is low. Event displays of some of these top candidates can be found in appendix E.

As already mentioned in the discussion of the likelihood analysis in the semi-leptonic channel, the likelihood discriminator is ideally suited to determine the top fraction in the data using a maximum-likelihood fit. Such a fit and the statistical evaluation of its results are presented in the following chapter.

### Confidence Level for Background-Only Hypothesis

As done for the likelihood spectra in the semi-leptonic channel, a confidence level for the background-only hypothesis is now computed for the hadronic channel. As estimator, the likelihood discriminator in figure 7.12 (a) for the Standard Model background is used. The results obtained for the confidence level  $1 - CL_b$  are:

$$1 - CL_b = 64\%_{-30\%}^{+10\%} . \quad (7.2)$$

The systematic uncertainties are again evaluated by scaling up the background normalization according to the size of the total systematic uncertainty (15%). As expected, the data are in good agreement with the Standard Model.

Likelihood $L$	$P_T^{b-cand.}$	$M_{jets}$	$M_{2jet}^{Wcomb.}$	$\cos(\theta_W^*)$
0.82	69.1	170.8	71.2	-0.75
0.83	59.5	173.7	80.7	-0.60
0.85	56.2	156.3	78.1	-0.03
0.85 <sup>†</sup>	21.3 <sup>†</sup>	180.3	90.4	-0.183
0.88	49.1	179.1	68.2	-0.07
0.86	68.3	186.4	84.9	-0.75
0.94	61.2	186.3	70.3	-0.30
0.94	62.8	181.0	69.8	0.09
0.95	68.1	179.8	74.7	0.04

Table 7.5: Kinematics of the nine top candidates in the hadronic channel that pass the optimized likelihood cut  $L > 0.8$ . The event marked with a dagger <sup>†</sup> is rejected by the cut-based top selection defined in table 7.2.

## 7.6 Summary

The study of multi-jet distributions showed that the leading-log parton shower model PYTHIA provides a good description of the kinematics of multi-jet events at high transverse momenta. However, it fails to describe the overall normalization of the data. The selection of top candidates is carried out on the basis of a multi-jet sample with high total transverse energy and a candidate for the decay  $W \rightarrow q\bar{q}'$  in the event. Both a top selection using one-dimensional cuts and a likelihood analysis showed good agreement between the observed multi-jet events and the Standard Model prediction. No sign of single top production could be found for hadronic decays of the  $W$ . However, due to the large QCD background, the results in the hadronic channel are not in contradiction with a possible top interpretation of the excess in the semi-leptonic channel. This will be studied in more detail in the next chapter. Moreover, it was shown that the hadronic channel has a large sensitivity to anomalous top production beyond the current limits from other experiments.

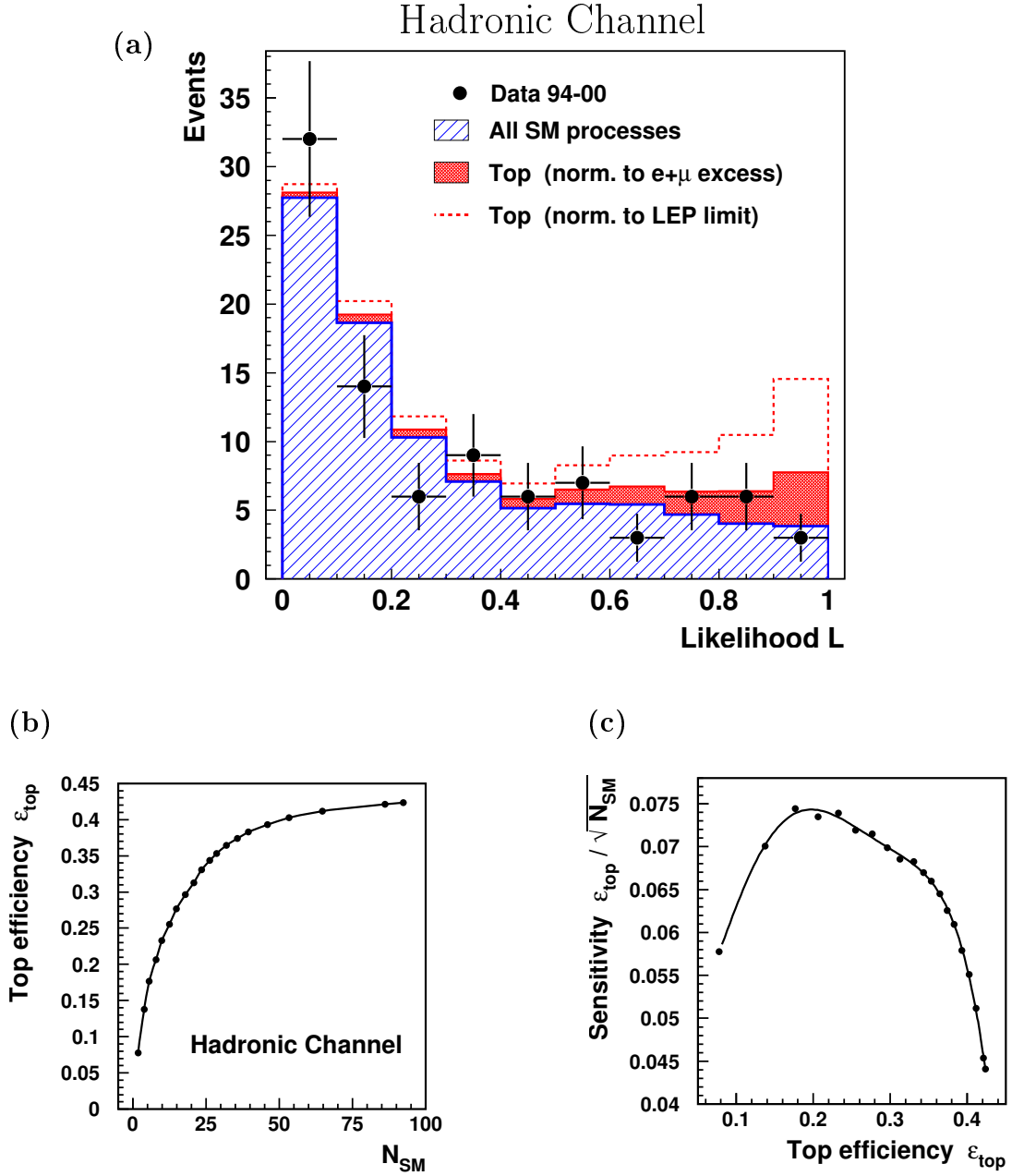


Figure 7.12: The likelihood discriminator  $L$  obtained with the PTC-method for the data and the Monte Carlo simulation in the hadronic channel. The top simulation is shown with two different normalizations. The full histogram is normalized according to the top interpretation of the isolated lepton excess. The normalization of the open dashed histogram represents the current limit on the anomalous top production cross-section obtained by the LEP collaboration. Plot (b) shows the top efficiency,  $\epsilon_{top}$ , as a function of the Standard Model expectation,  $N_{SM}$ . Plot (c) represents the signal sensitivity of the likelihood discriminator, defined as  $\epsilon_{top}/\sqrt{N_{SM}}$ , as a function of the top efficiency. The dots in (b) and (c) correspond to steps in  $L$  of size 0.05.

# Chapter 8

## Statistical Evaluation of the Likelihood Analyses

In this chapter, a statistical evaluation of the likelihood spectra obtained in the analyses of the semi-leptonic and hadronic decay channels of the top quark are presented. Under the assumption that anomalous single top production exists, the fraction of top events in the data is determined using a maximum-likelihood fit to the discriminator spectra. The compatibility of the different search channels and the probability of the top interpretation are discussed. Due to the presently small number of top candidates, exclusion limits are set on the single top production cross-section and the anomalous coupling of the top quark to an up-quark and a photon. Finally, the results are compared to single top searches carried out by other experiments.

### 8.1 Maximum-Likelihood Fit of the Top Signal

In searches for new physics, fits to spectra of kinematic observables or to discriminator distributions, obtained in a likelihood analysis or with a neural network, have frequently been used to extract signal fractions in the data. In this analysis, a maximum-likelihood fit of the top contribution in the data is performed. It provides the maximal sensitivity to the signal.

#### 8.1.1 Description of the Maximum-Likelihood Fit

The likelihood discriminators shown in figures 8.1 are used as input for the maximum-likelihood fit.

A *likelihood function*,  $\mathcal{L}$ , is introduced as the product of Poisson probabilities of observing  $n_k$  data events in each bin  $k$  of the discriminator spectrum:

$$\mathcal{L} = \prod_{k=1}^{n_{\text{bin}}} e^{-\mu_k} \frac{\mu_k^{n_k}}{n_k!}, \quad (8.1)$$

where  $\mu_k = B_k + S_k$  is the sum of the signal  $S_k$  and expected background  $B_k$  in bin  $k$ .

The signal normalization which best matches the data can be obtained by maximizing the likelihood function, or correspondingly by minimizing the negative *log-likelihood*

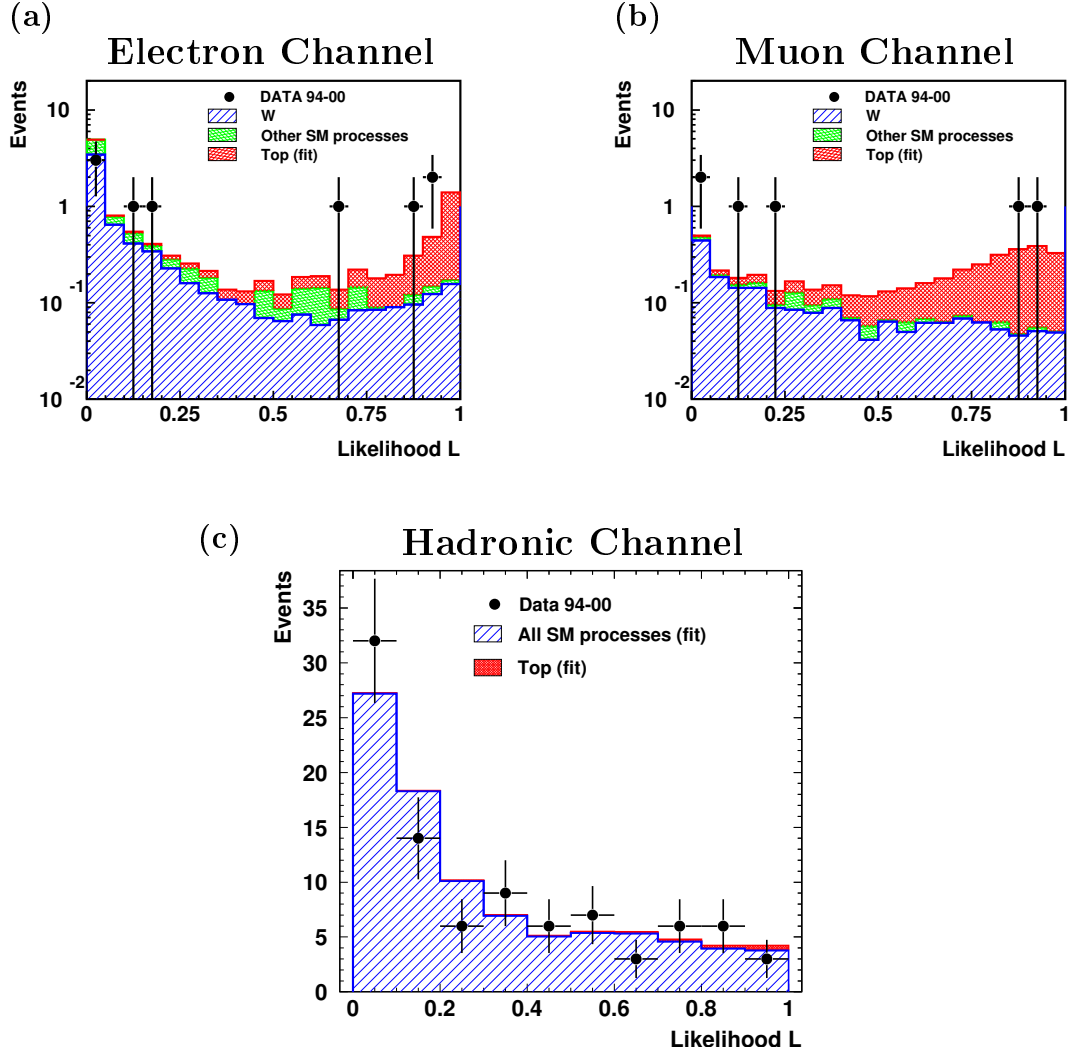


Figure 8.1: Distributions of the likelihood discriminator spectra for the electron (a), muon (b) and hadronic (c) channels. The simulated top signal is added to the Standard Model background. It is normalized according to the a maximum-likelihood fit to the data. In (a) and (b), the background is normalized to the number of events predicted by the Monte Carlo simulation. In (c), also the background normalization is obtained from the fit to the data.

function  $-2 \log(\mathcal{L})$ . By using the factor 2, the log-likelihood function corresponds to a  $\chi^2$  function (in the Gaussian limit).

In order to express the log-likelihood as a function of the signal normalization, the signal  $S_k$  in each bin is written as product of the overall signal normalization  $S$  and the signal shape  $\hat{s}_k$  (i.e. the signal spectrum normalized to unity):

$$S_k = S \cdot \hat{s}_k . \quad (8.2)$$

If the data statistics is large enough, one can fit also the background normalization as free parameter. The background  $B_k$  is then analogously written as  $B_k = B \cdot \hat{b}_k$ , with the overall background normalization  $B$  and the background shape  $\hat{b}_k$ , and the



log-likelihood is minimized as a function of the two parameters  $S$  and  $B$ .

To allow an easy interpretation of the log-likelihood function, its minimum value is subtracted, leading to:

$$-2 \Delta \log(\mathcal{L}) := -2 (\log(\mathcal{L}) - \log(\mathcal{L})_{min}) = \Delta \chi^2 . \quad (8.3)$$

If  $-2 \Delta \log(\mathcal{L})$  is plotted as a function of  $S$ , the ordinate corresponds to the deviation from the best fit value for  $S$  in terms of standard deviations squared ( $\sigma^2$ ). The width of this function at  $-2 \Delta \log(\mathcal{L}) = 1$  corresponds to the statistical uncertainty in terms of one standard deviation,  $\delta S_{stat}$ , on the fitted number of signal events. The position of its minimum is the best signal normalization,  $S_{fit}$ .

### Conversion to Single Top Cross-Section

The fitted number of signal events in each channel is translated into a cross-section for anomalous top production by dividing through the signal efficiency ( $\epsilon_{top}$ ), the decay branching ratio ( $BR$ ) and the integrated data luminosity ( $L_{tot}$ ) for each individual channel. Since the analyzed data sets were recorded with two different  $ep$  center-of-mass energies (1994-1997:  $\sqrt{s} = 300$  GeV, 1998-2000:  $\sqrt{s} = 320$  GeV), the obtained cross-section is valid for an effective center-of-mass energy,  $\sqrt{s_{eff}}$ :

$$\sigma_{eff} = \sigma(ep \rightarrow etX, \sqrt{s_{eff}}) = \frac{S_{fit}}{\epsilon_{top} \cdot BR \cdot L_{tot}} . \quad (8.4)$$

It is then converted into a cross-section at  $\sqrt{s} = 320$  GeV using the cross-section ratio for  $\sqrt{s} = 300$  GeV and 320 GeV ( $\sigma_{300}/\sigma_{320} = 0.68$ ) [19]:

$$\sigma_{320} = \sigma(ep \rightarrow etX, \sqrt{s} = 320 \text{ GeV}) = \sigma_{eff} \cdot \frac{L_{tot}}{0.68 \cdot L_{300} + L_{320}} . \quad (8.5)$$

### 8.1.2 Results of the Maximum-Likelihood Fit

The maximum-likelihood fit is carried out for each of the three search channels. In this section, the results of the fits are presented for the individual channels and for their combinations. The inclusion of systematic errors is described and the compatibility between the different channels is discussed.

#### Semi-Leptonic Channel

In the electron and muon channels, the background normalization is taken from the Monte Carlo predictions for  $W$  production and the various other Standard Model processes. Only the signal normalization is fitted as free parameter.

The log-likelihoods with respect to  $S$  are displayed in figure 8.2 for both channels. Due to the small data statistics, they are asymmetric and the statistical uncertainties are large. The maximum-likelihood fits yield  $S_{fit} = 2.5^{+2.4}_{-1.7}$  top events in the electron channel and  $S_{fit} = 2.3^{+2.2}_{-1.4}$  top events in the muon channel. These very similar results show a good agreement between the two channels in view of a top interpretation of the isolated lepton excess. The cross-sections corresponding to the fitted numbers of signal events are  $0.45^{+0.44}_{-0.31}$  pb for the electron channel and  $0.42^{+0.41}_{-0.26}$  pb for the muon channel.

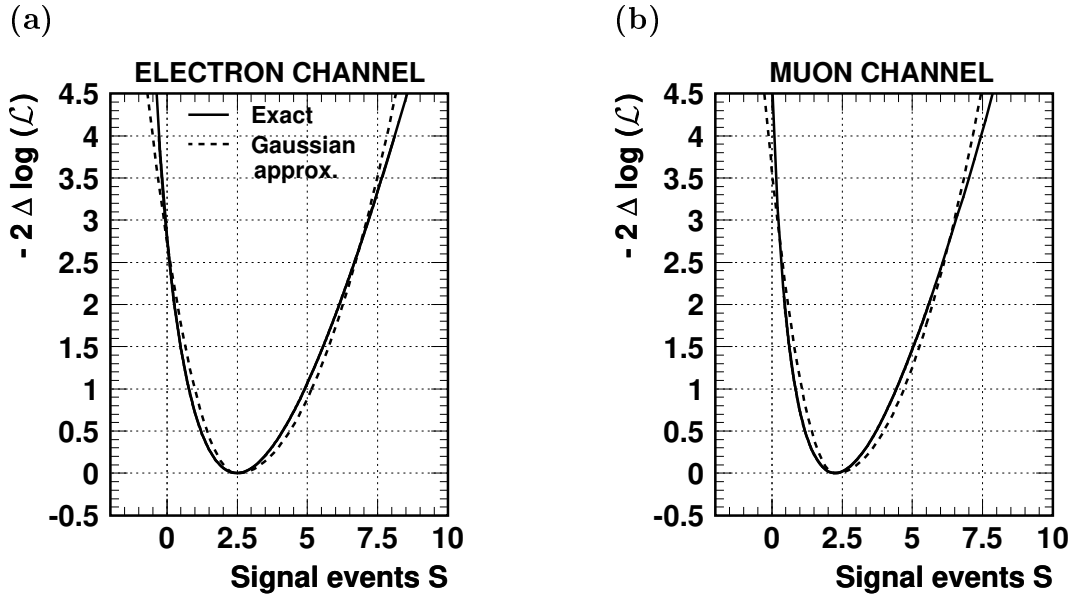


Figure 8.2: The log-likelihood functions of the signal fit in the electron (a) and muon (b) channels. They are shown as functions of the signal normalization. The exact log-likelihoods (solid lines) are compared to approximations (dashed lines) consisting of two half parabolas for each function (one on each side of the minimum).

### Hadronic Channel

The larger number of data events in the hadronic channel allows also the background normalization to be used as free fit parameter. A two-parameter fit of  $S$  and  $B$  is performed. The maximum-likelihood fit to the discriminator spectrum yields  $B_{fit} = 90.7^{+11.8}_{-11.0}$  background events and  $S_{fit} = 1.3^{+6.9}_{-5.9}$  events from top production in the 92 selected multi-jet events. The log-likelihood function is plotted in figure 8.3 (a). Within statistical errors, the data are well compatible with the QCD background and thus consistent with no top signal. The corresponding cross-section for single top production is  $0.05^{+0.23}_{-0.20}$  pb.

Since the background normalization is used as free parameter, the width of the log-likelihood function also includes the uncertainty on  $S$  resulting from the statistical uncertainty on the background normalization  $B$ . Figure 8.3 (c) shows the  $1\sigma$  contour of the log-likelihood as function of  $S$  and  $B$  and illustrates the increase of the uncertainty on  $S$  due to the additional fit parameter.

As a test, also a one-parameter fit of  $S$  only is performed, using a fixed background normalization of  $B = B_{fit}$ . In figure 8.3 (b), the log-likelihood for this one-parameter fit is compared to the two-parameter fit. The effect of the uncertainty on the background normalization on the statistical error of  $S$  is obvious.

### 8.1.3 Inclusion of Systematic Errors

So far, the log-likelihood functions do not include any systematic uncertainties. To allow for an inclusion of systematic errors, each log-likelihood function is approximated by a function  $f(S)$  consisting of two half parabolas, one on each side of the minimum

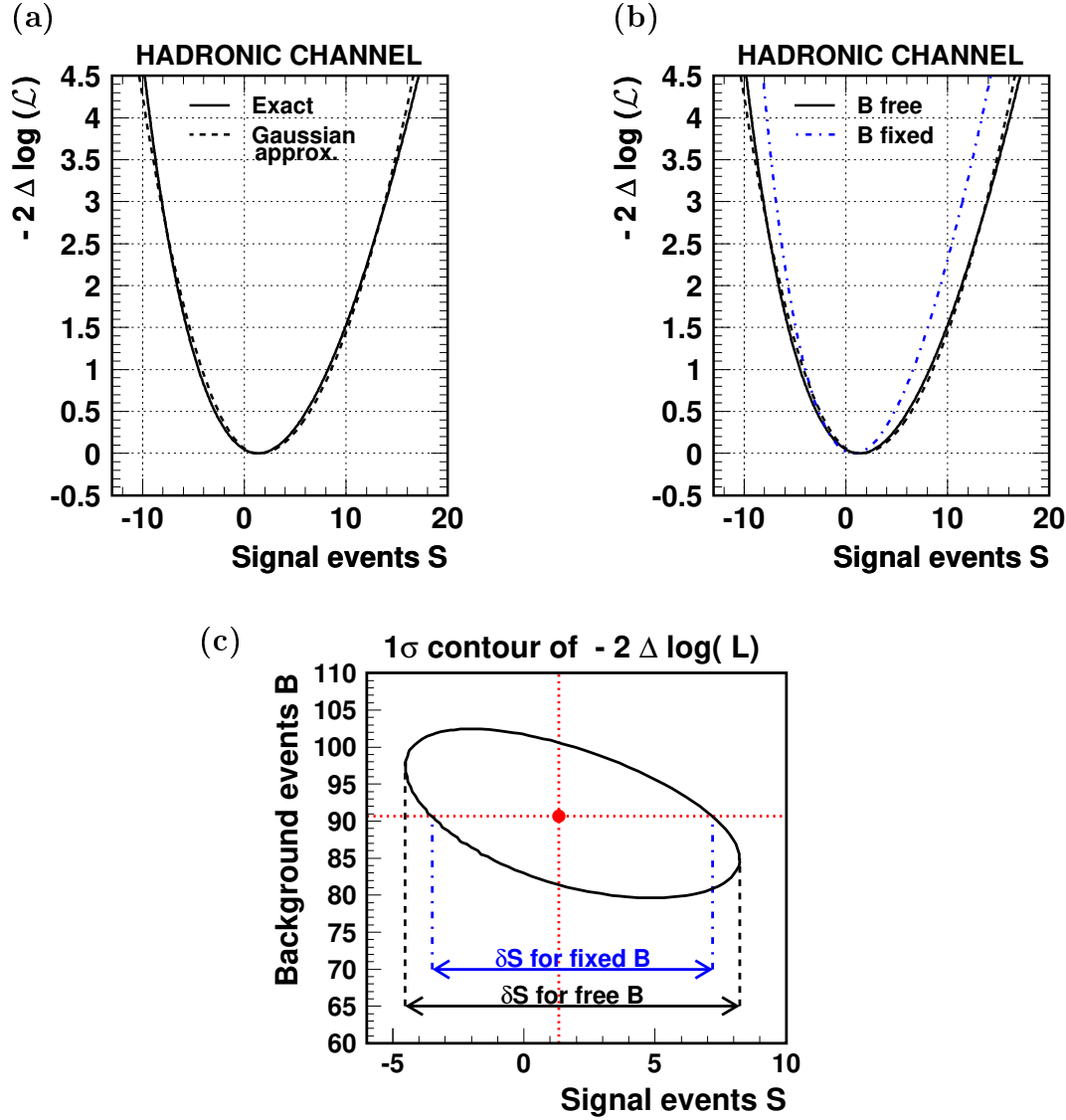


Figure 8.3: The log-likelihood functions of the signal+background fit in the hadronic channel, shown as a function of the signal normalization  $S$  in (a) and (b) and as a function of the signal and the background normalizations,  $S$  and  $B$ , in (c). Plots (b) and (c) illustrate the different widths of the log-likelihoods obtained by performing a one-parameter fit of the signal ( $B$  fixed) or a two-parameter fit of the signal and background ( $B$  free). Plot (c) shows the  $1\sigma$  contour of the two-parameter fit. The central fit result is marked by a dot.

at  $S = S_{fit}$ :

$$f(S) = (S - S_{fit})^2 \cdot \begin{cases} \frac{1}{(\delta S_{stat}^+)^2} & \text{for } S \geq S_{fit} \\ \frac{1}{(\delta S_{stat}^-)^2} & \text{for } S < S_{fit} \end{cases} \quad (8.6)$$

Here the half widths of the parabolas correspond to the upper and lower statistical errors on the fitted signal events,  $\delta S_{stat}^+$  and  $\delta S_{stat}^-$ . This "two-parabola" approximation represents a Gaussian approximation of the log-likelihood on both sides of its minimum, but preserves its asymmetry.

The functions  $f(S)$  are shown as dashed lines in figure 8.2 for the electron and muon channels and in figure 8.3 for the hadronic channel. They provide good approximations of the exact log-likelihood functions in the region relevant for the evaluation of this analysis<sup>1</sup>. It is clear that for very large deviations of  $S$  from the minimum, these approximations become poor.

Systematic uncertainties on the number of signal events  $S$  can now easily be included by increasing the width of the approximated log-likelihood function according to:

$$\delta S^\pm = \delta S_{stat}^\pm \oplus \delta S_{sys}^\pm . \quad (8.7)$$

The effect of systematic uncertainties on the number of signal events obtained in the maximum-likelihood fit is evaluated using the following procedure:

- Each quantity affected by a systematic uncertainty is randomly smeared around its central value according to a Gaussian distribution with a width corresponding to the systematic uncertainty (at least 200 variations per systematic are performed).
- The full analysis is carried out under these changed conditions. New likelihood discriminator spectra are obtained for the signal and the background. The data events, whose kinematics are left unchanged, are reanalyzed in the modified likelihood spectra.
- The maximum-likelihood fit is performed as described above.
- Each smearing yields a fitted number of signal events. The width of their distribution is obtained in a Gaussian fit and used as resulting uncertainty.

The distributions of the fitted numbers of signal events obtained by Gaussian smearing can be found in appendix F for each systematic. The resulting uncertainties are translated into uncertainties on the single top cross-section. They can be found in table 8.1.

Figure 8.4 shows the effect of the systematic uncertainties on the log-likelihood functions for each channel. It can be seen that the electron and muon channels are completely dominated by statistics. The systematic errors are small compared to the statistical errors. In the hadronic channel, the systematic errors are no more negligible compared to the statistical error. However, it can be seen that the log-likelihood function in the hadronic channel has the smallest width of all three channels (even after inclusion of systematics). With the present data statistics it thus possesses the largest sensitivity to the top signal, due to the large branching ratio for  $W \rightarrow q\bar{q}'$ .

Table 8.2 summarizes the fitted numbers of signal events and the corresponding single top cross-sections for all three channels.

---

<sup>1</sup>In fact, to reach a good approximation of the log-likelihoods in the region corresponding to  $\sim 2\sigma$ , the widths  $\delta S_{stat}^\pm$  of the two parabolas used in equation 8.6 are taken at  $-2\Delta\log(\mathcal{L}) = 2.7$  instead of one. Moreover, this also guarantees a good approximation for the value of the log-likelihood later needed to extract the 95% exclusion limit on single top production.

Systematic	Syst. error on single top cross-section, $\delta\sigma_{320,syst}$		
	Electron channel	Muon channel	Hadronic channel
Leptonic energy scale	$\pm 0.03$ pb	$\pm 0.02$ pb	–
$\theta$ lepton	$\pm 0.02$ pb	$\pm 0.01$ pb	–
$\phi$ lepton	$\pm 0.02$ pb	$\pm 0.01$ pb	–
Hadronic energy scale	$\pm 0.02$ pb	$\pm 0.02$ pb	$\pm 0.06$ pb
$\theta$ hadron	$\pm 0.02$ pb	$\pm 0.03$ pb	$\pm 0.11$ pb
$\phi$ hadron	$\pm 0.01$ pb	$\pm 0.02$ pb	–
Trigger efficiency	$\pm 0.00$ pb	$\pm 0.01$ pb	–
Background normalization	$\pm 0.10$ pb	$\pm 0.06$ pb	included in $\delta\sigma_{320,stat}$ <sup>†</sup>
Total	$\pm 0.11$ pb	$\pm 0.08$ pb	$\pm 0.13$ pb

Table 8.1: Effect of the experimental systematic uncertainties and the uncertainty of the background normalization on the single top cross-section. The uncertainties of the luminosity measurement and the lepton identification are included in the background normalization. <sup>†</sup> In the hadronic channel, the background normalization is fitted, therefore its uncertainty is propagated into the statistical uncertainty on the signal cross-section.

Max.-likelihood fit	$S \pm \delta S$	$\delta S_{stat}$	$\delta S_{syst}$	$\sigma_{320} \pm \delta\sigma_{320}$	$\delta\sigma_{320,stat}$	$\delta\sigma_{320,syst}$
Electron channel	$2.5^{+2.5}_{-1.8}$	$^{+2.4}_{-1.7}$	$\pm 0.6$	$0.45^{+0.45}_{-0.33}$ pb	$^{+0.44}_{-0.31}$ pb	$\pm 0.11$ pb
Muon channel	$2.3^{+2.2}_{-1.5}$	$^{+2.2}_{-1.4}$	$\pm 0.4$	$0.42^{+0.41}_{-0.27}$ pb	$^{+0.41}_{-0.26}$ pb	$\pm 0.08$ pb
Hadronic channel	$1.3^{+7.8}_{-6.9}$	$^{+6.9}_{-5.9}$	$\pm 3.7$	$0.05^{+0.27}_{-0.24}$ pb	$^{+0.23}_{-0.20}$ pb	$\pm 0.13$ pb

Table 8.2: The number of signal events and the corresponding single top cross-section at  $\sqrt{s} = 320$  GeV obtained by the maximum-likelihood fit. Statistical and systematic uncertainties are shown separately. The total uncertainty  $\delta S$  ( $\delta\sigma_{320}$ ) is the quadratic sum of the statistical and systematic uncertainties.

### 8.1.4 Combination of Channels

Because likelihoods can be multiplied, the different search channels can be combined by adding their log-likelihood functions. Due to the different efficiencies and branching ratios for each channel, the combined functions are shown with respect to the single top cross-section. Their minima correspond to the best combined value of the cross-section for single to production.

At first, the two lepton channels are combined. The log-likelihood for the combined electron and muon channels is shown in figure 8.4 (d). In the following, this combination is frequently referred to as the semi-leptonic channel. The width of the combined log-likelihood is slightly smaller than for the hadronic channel, reflecting a higher sensitivity of the combination. The combination of all three channels is shown in figure 8.5. The

obtained values for the single top cross-sections in the semi-leptonic channel and for all channels combined can be found in table 8.3.

Max.-likelihood fit	$\sigma_{320} \pm \delta\sigma_{320}$
Semi-leptonic channel ( $e + \mu$ )	$0.43^{+0.33}_{-0.18}$ pb
All channels	$0.31^{+0.16}_{-0.15}$ pb

Table 8.3: The single top cross-section obtained by the maximum-likelihood fit for the (combined) semi-leptonic channel and for the combination of all channels.

### 8.1.5 Compatibility of Semi-Leptonic and Hadronic Channels

As good agreement with the Standard Model is seen in the hadronic channel, whereas some top candidates exist in the semi-leptonic channel, it is necessary to check the level of compatibility between these two channels.

The compatibility is obtained by comparing the difference of the single top cross-sections determined in the semi-leptonic and hadronic channels with respect to their total uncertainties<sup>2</sup>. It can thus be evaluated as:

$$\text{Compatibility} = \frac{\sigma_{320}(lep.) - \sigma_{320}(had.)}{\sqrt{(\delta\sigma_{320}^-(lep.))^2 + (\delta\sigma_{320}^+(had.))^2}} \approx 1.2 . \quad (8.8)$$

Here  $\delta\sigma_{320}^-(lep)$  ( $\delta\sigma_{320}^+(had)$ ) denote the total lower (upper) uncertainty on the single top cross-section measured in the semi-leptonic (hadronic) channel. Compatibility is seen at the  $1.2 \sigma$  level. This means that the semi-leptonic and the hadronic channel are not in contradiction.

---

<sup>2</sup>Since the systematic errors in the semi-leptonic channel are small, correlations of experimental systematic errors (e.g. the hadronic energy scale) between the different channels can be neglected.

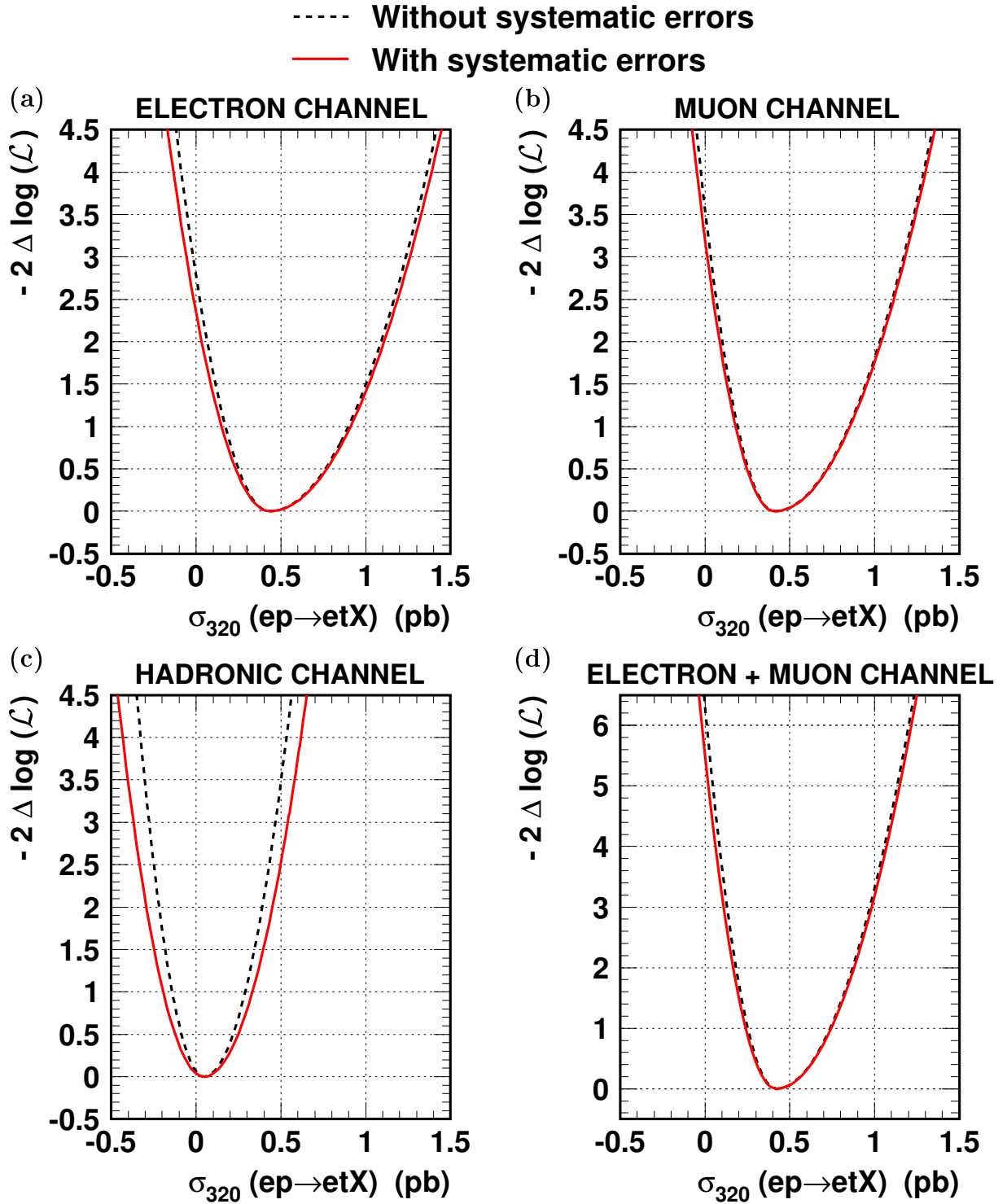


Figure 8.4: The log-likelihood functions of the signal fit in the electron (a), muon (b) and hadronic (c) channels, and for the combination of the electron and muon channels (d). They are shown as functions of the single top cross-section. The inner dashed lines correspond to the log-likelihoods neglecting systematic errors, the outer solid lines represent the inclusion of systematic errors.

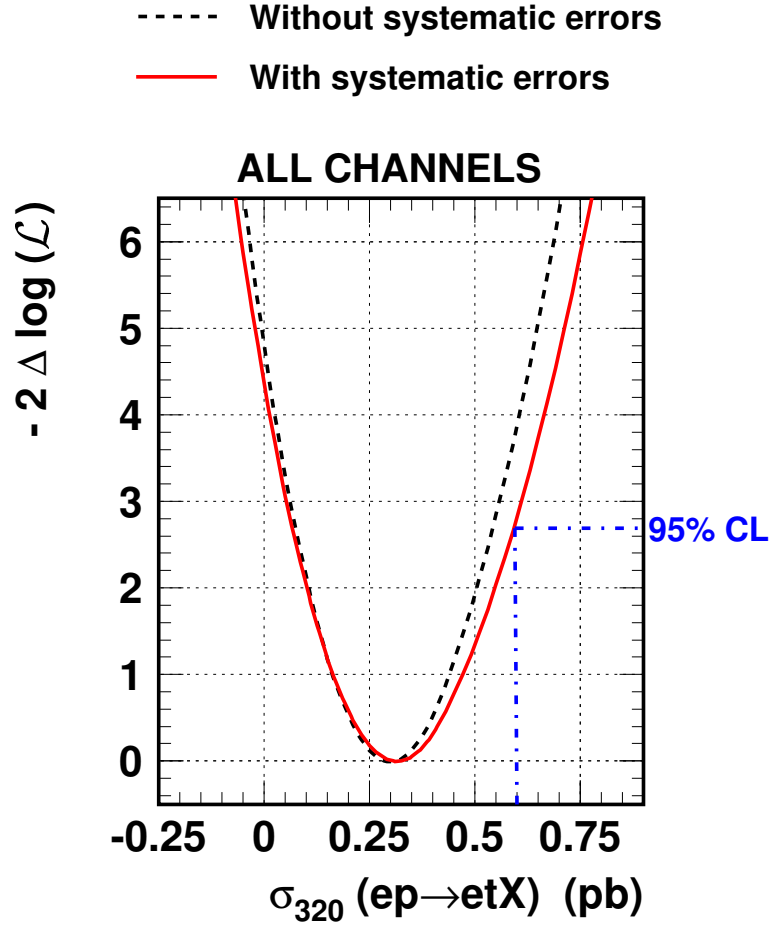


Figure 8.5: The log-likelihood function obtained for the combination of all three channels, shown as a function of the single top cross-section. The inner dashed line corresponds to the log-likelihood neglecting systematic errors, the outer solid line represents the inclusion of systematic uncertainties. The dashed-dotted line indicates the point on the log-likelihood, that corresponds to a 95% (upper) exclusion limit on the cross-section.

## 8.2 Probability of the Top Interpretation

In the previous chapters, confidence levels for the *background-only* hypothesis ( $CL_b$ ) were computed for each channel. The value of  $1 - CL_b$  corresponds to the probability that the Standard Model describes the observed data. Now the probability of the top interpretation needs to be studied.

To find out how well the background together with the fitted signal contribution describes the data, confidence levels for the *signal+background* hypothesis ( $CL_{s+b}$ ) are computed for each channel. The value of the likelihood function 8.1 (which corresponds to a total Poisson probability summed over all bins of the discriminator spectrum) is used to determine the consistency between the signal+background and data distributions:

$$\mathcal{L} = \prod_{k=1}^{n_{\text{bin}}} e^{-(S_k + B_k)} \frac{(S_k + B_k)^{n_k}}{n_k!} . \quad (8.9)$$



The value of  $\mathcal{L}$  is evaluated for the following cases:

1. The signal+background distribution is normalized according to the central result of the maximum-likelihood fit:  $S = S_{fit}$  ( $B = B_{fit}$ ). The obtained value of  $\mathcal{L}$  is labeled  $\mathcal{L}_{fit}$ .
2. Toy Monte Carlo experiments are generated by forcing each bin of the signal+background distribution to fluctuate around its central value according to a Poisson probability. For each Monte Carlo experiment, a value of  $\mathcal{L}$  is obtained.

All toy Monte Carlo experiments that yield a likelihood  $\mathcal{L}$  smaller than  $\mathcal{L}_{fit}$  are less consistent with the data than the result of the maximum-likelihood fit. The probability  $1 - \text{CL}_{s+b}$ , defined as:

$$1 - \text{CL}_{s+b} = P(\mathcal{L} < \mathcal{L}_{fit}) = \frac{\# \text{ toy experiments with } \mathcal{L} < \mathcal{L}_{fit}}{\# \text{ toy experiments}}, \quad (8.10)$$

can thus be considered as a measure of consistency between the fitted top+background distribution and the data. The probabilities  $1 - \text{CL}_{s+b}$  obtained for the different channels are given in table 8.4 and compared to the probabilities for the background-only hypothesis.

In all three channels, the additional single top contribution is consistent with the data. In the electron and muon channels, the signal+background hypothesis gives a clearly better description of the data than the background-only hypothesis. Since in the hadronic channel no significant top contribution is observed, the two hypotheses have approximately the same probability.

In order to perform the confidence level computation for certain combinations of channels, the corresponding value of the top cross-section obtained in the combined log-likelihood is used to normalize the signal distribution. The sum in equation 8.9 now runs over all bins of the discriminator distributions in all channels. For the semi-leptonic channel, the signal+background hypothesis shows the largest improvement compared to the Standard Model alone, as expected. Also for the combination of all channels, the signal+background hypothesis is found to be consistent with the observation and gives an improved description of the data.

### 8.3 Exclusion Limit on Top Cross-Section and FCNC Coupling

Because of the small number of top candidates, it is at present not yet possible to make a definite statement, whether they originate from a Standard Model fluctuation or indeed from top production. For this reason, also a limit is set on the cross-section for anomalous single top production. The branching  $t \rightarrow bW$  is assumed to be 100%, which represents a safe approximation considering the existing limits on radiative top decays into  $q\gamma$  [18].

For the combination of all channels, the exclusion limit can directly be taken from the log-likelihood function in figure 8.5. A one-sided (upper) bound at 95% confidence level (CL) corresponds to a value of the log-likelihood of  $-2 \Delta \log(\mathcal{L}) = 2.69$  [5].

	$1 - \text{CL}_{s+b}$	$1 - \text{CL}_b$ w/o syst.	$1 - \text{CL}_b$ with syst.
Electron channel	43%	2.4%	5.6%
Muon channel	33%	3.4%	6.3%
Hadronic channel	65%	64%	64% <sup>†</sup>
Semi-leptonic channel ( $e + \mu$ )	36%	0.4%	1.6%
All channels	34%	12%	16%

Table 8.4: Probabilities  $1 - \text{CL}_{s+b}$  for the signal+background hypothesis and  $1 - \text{CL}_b$  for the background-only hypothesis (with and without inclusion of systematic uncertainties). <sup>†</sup> Since in the hadronic channel good agreement with the Standard Model is seen, no value of  $1 - \text{CL}_b$  for a systematic change of the background normalization is given.

Including systematic uncertainties, the resulting upper bound on the single top cross-section at  $\sqrt{s} = 320$  GeV is:

$$\sigma(ep \rightarrow etX, \sqrt{s} = 320 \text{ GeV}) < 0.60 \text{ pb} \quad \text{at 95\% CL} . \quad (8.11)$$

This cross-section limit can now be translated into an upper exclusion limit on the coupling strength of the anomalous  $tu\gamma$  magnetic coupling <sup>3</sup>, giving:

$$\kappa_{tu\gamma} < 0.25 \quad \text{at 95\% CL} . \quad (8.12)$$

Table 8.5 summarizes the exclusion limits obtained for the combination of all channels, as well as for the semi-leptonic and the hadronic channels alone. The strongest limit comes from the hadronic channel. The limit from the semi-leptonic channel is of course much weaker because of the observed data excess. The bounds obtained for  $\kappa_{tu\gamma}$  are also illustrated in figure 8.6. Since the single top cross-section strongly depends on the top mass,  $m_t$ , the precision on its measured value needs to be considered. In figure 8.6, the effect of a variation of  $m_t$  by  $\pm 5$  GeV is displayed as error band on the combined limit from all channels. It changes the cross-section by  $\sim 20\%$  and thus represents the largest systematic uncertainty.

---

<sup>3</sup>The single top cross-section in equation 2.13 is given for  $\kappa_{tu\gamma} = 0.1$ . The coupling strength, which corresponds to the cross-section limit obtained in this thesis, is derived by exploiting that the cross-section scales with  $\kappa_{tu\gamma}^2$ .

Exclusion limits at 95% CL	$\sigma_{320}(t \rightarrow etX)$	$\kappa_{tu\gamma}$
Semi-Leptonic channel ( $e + \mu$ )	$< 0.96$ pb	$< 0.32$
Hadronic channel	$< 0.51$ pb	$< 0.23$
All channels	$< 0.60$ pb	$< 0.25$

Table 8.5: . Exclusion limits at 95% CL on the single top cross-section at  $\sqrt{s} = 320$  GeV and the  $tu\gamma$ -coupling.

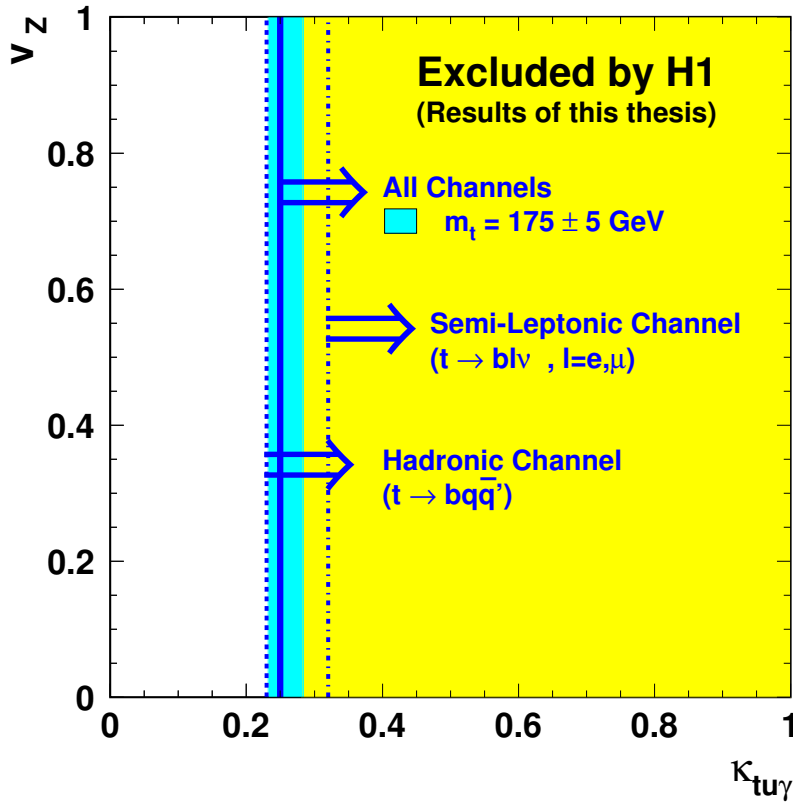


Figure 8.6: The exclusion limits (at 95% CL) on the anomalous  $tu\gamma$ -coupling obtained with this analysis for the semi-leptonic channel, the hadronic channel and the combination of all channels. For the latter, the effect of a variation of the top mass is indicated as error band. The limits are shown in the  $v_Z - \kappa_{tu\gamma}$  plane ( $v_Z$  = vector coupling of the top quark to a  $Z$  boson and a light quark,  $\kappa_{tu\gamma}$  = magnetic coupling of the top quark to a photon and an  $u$ -quark). The HERA experiments are only sensitive to the  $tu\gamma$ -coupling.

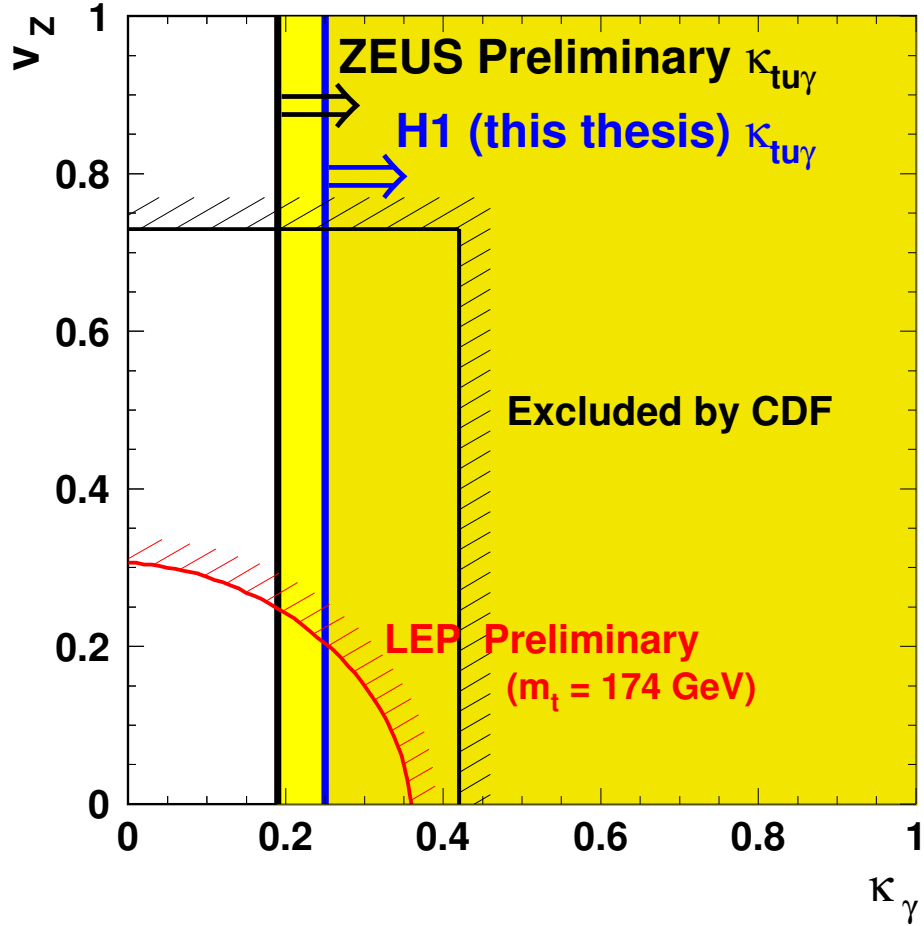


Figure 8.7: The current status of constraints on the anomalous magnetic coupling of the top quark to a photon and a light quark ( $\kappa_\gamma = \kappa_{tq\gamma}$ ,  $q = u, c$ ) and on the anomalous vector coupling of the top quark to a  $Z$  boson and a light quark ( $v_Z = v_{tqZ}$ ,  $q = u, c$ ). The exclusion limits from HERA, LEP and TeVatron are shown. The HERA experiments (H1 and ZEUS) are only sensitive to the  $tu\gamma$ -coupling, for which they set the strongest limits.

## 8.4 Comparison with Other Experiments

At present, there are three high energy physics facilities that provide a sufficiently large center-of-mass energy for the production of top quarks. This section summarizes the existing searches for single top quarks at the TeVatron and LEP colliders and the other HERA collider experiment ZEUS. The current status of constraints on FCNC couplings involving the top quark is presented in figure 8.7.

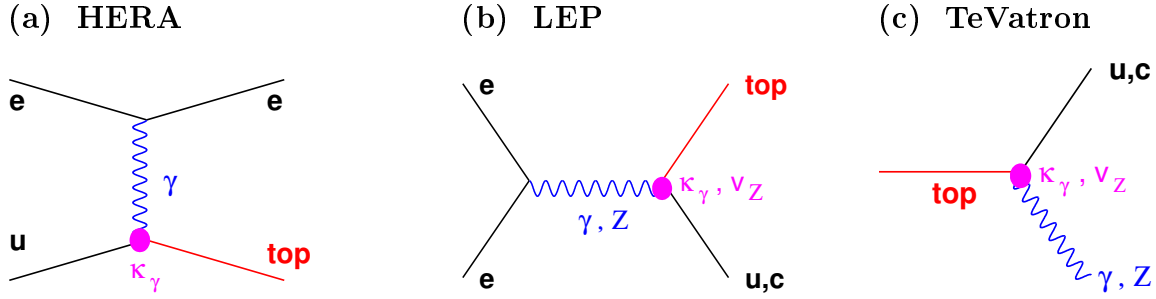


Figure 8.8: Diagrams for FCNC single top production and decay at HERA, LEP, and the TeVatron.

### 8.4.1 Single Top at TeVatron

The CDF collaboration at the TeVatron performed a search for radiative top decays  $t \rightarrow q\gamma$  and  $t \rightarrow qZ$  ( $Z \rightarrow e^+e^-, \mu^+\mu^-$ ) in  $p\bar{p}$  collisions at  $\sqrt{s} = 1.8$  TeV. The corresponding diagram is illustrated in figure 8.8 (c). In the Standard Model, branching ratios of  $10^{-10}$  or smaller are expected for these decays [18, 68]. The main background to single top production at the TeVatron is  $t\bar{t}$  production.

The CDF collaboration reports one event in the  $t \rightarrow q\gamma$  channel and one event in the  $t \rightarrow qZ$  channel, both consistent with the background expectation. Exclusion limits are obtained for the branchings  $BR(t \rightarrow u\gamma) + BR(t \rightarrow c\gamma) < 3.2\%$  and  $BR(t \rightarrow uZ) + BR(t \rightarrow cZ) < 33\%$  [18]. They can be translated into bounds on the anomalous couplings  $\kappa_\gamma < 0.42$  and  $v_z < 0.73$  [67]. The limit on  $\kappa_\gamma$  is valid for both  $tu\gamma$ - and  $tc\gamma$ -couplings. Considering only the coupling to the  $u$ -quark, the CDF limit is much weaker than the one obtained by H1.

Also the Standard Model electroweak production of single top quarks in  $W$ -gluon fusion or  $W^*$  processes has been searched for with the CDF and D0 experiments [6, 7]. Assuming  $|V_{tb}| = 1$ , the predicted cross-sections for  $Wg$  and  $W^*$  are 1.7 pb [69] and 0.7 pb [70], respectively (compared to 5.1 pb for  $t\bar{t}$  production [71]). Due to low signal efficiencies, the CDF and D0 analyses of Run I data ( $\sim 110 \text{ pb}^{-1}$ ) showed no sensitivity to electroweak single top production. For TeVatron Run II, the signal might be within reach.

### 8.4.2 Single Top at LEP

Single top production in association with a light quark ( $q = u, c$ ) in the process  $e^+e^- \rightarrow t\bar{q}(\bar{t}q)$  (illustrated in figure 8.8 (b)) has actively been searched for at the LEP2 collider,

since its center-of-mass energy exceeds the top production threshold. It corresponds to the crossed process compared to diagram (a) relevant for HERA. Since  $e^+e^-$  collisions also provide sensitivity to anomalous  $tqZ$ -couplings, the couplings to the photon ( $\kappa_\gamma$ ) and to the  $Z$  boson ( $v_Z$ ) have been investigated simultaneously.

The preliminary results of the four experiments using data with  $\sqrt{s}$  up to 209 GeV, corresponding to an integrated luminosity of approximately 600 pb<sup>-1</sup> per experiment, were combined in [67]. No evidence for single top production has been observed in the final state  $bWq$  with the  $W$  decaying leptonically or hadronically. The exclusion limits obtained in this preliminary LEP combination are  $\kappa_\gamma < 0.36$  and  $v_z < 0.31$  at 95% CL for a top quark mass of  $m_t=174$  GeV (figure 8.7). These limits represent the currently strongest constraints on the anomalous couplings from colliders other than HERA. The ALEPH, L3, and OPAL collaborations have recently published their final results in [72, 73, 74].

### 8.4.3 Isolated Leptons and Single Top at ZEUS

The ZEUS collaboration, the other HERA collider experiment besides H1, has also carried out a search for isolated lepton events and single top production [75]. In the hadronic channel, the analysis is similar to the cut-based analysis presented in this thesis, and the preliminary results of both experiments are consistent (see figure 8.9 (d)).

In the semi-leptonic channel, ZEUS carries out a more inclusive selection with a larger expectation of non- $W$  background (see figure 8.9 (a) and (b)) and a selection dedicated to look for  $W$  bosons and top quarks at high  $P_T^X$  (see table 8.6). ZEUS sees no excess of isolated lepton events above the Standard Model expectation. In particular, they see no isolated electron or muon event with a hadronic transverse momentum  $P_T^X > 40$  GeV. Even though extensive comparisons between both experiments have been undertaken, e.g. restricting the phase space to reach comparable acceptances for both analyses, the discrepancy in the yield of electron and muon events at high  $P_T^X$  persists and remains a puzzle. Only HERA II data will be able to shed light on this discrepancy and decide whether it comes from a statistical fluctuation or not.

The ZEUS collaboration has recently presented a search for isolated tau leptons [76]. In the tau channel, they report two candidates with large  $P_T^X \sim 40$  GeV for a low Standard Model expectation (see figure 8.9 (c) and table 8.6). These two events possess similar kinematic properties as the outstanding isolated electron and muon events observed by H1. The extension of the H1 single top analysis to the tau channel is currently in work.

ZEUS preliminary $e^\pm p$ (130.5 pb <sup>-1</sup> )	Electrons obs./exp.	Muons obs./exp.	Taus obs./exp.
$P_T^X > 25$ GeV	1 / $1.14 \pm 0.06$	1 / $1.29 \pm 0.16$	2 / $0.12 \pm 0.02$
$P_T^X > 40$ GeV	0 / $0.46 \pm 0.03$	0 / $0.50 \pm 0.08$	1 / $0.06 \pm 0.01$

Table 8.6: Observed and expected event yields of the ZEUS isolated lepton analysis. Numbers taken from [75, 76].

A comparison of the H1 and ZEUS isolated lepton results for the combination of electron, muon (and tau) channels is shown in table 8.7. On the basis of these numbers, the compatibility between the two experiments has been evaluated for the following two signal hypotheses:

1. No signal exists.
2. The signal lies between the H1 and ZEUS results (a mean signal of 4.4 events is used, deduced from the sum of the H1 and ZEUS event numbers, without making any assumptions on the nature of the signal).

For each experiment, a confidence level for the signal+background hypothesis is computed, which corresponds to the probability that the obtained result is consistent with the signal+background expectation. The compatibility between the H1 and ZEUS results is then evaluated as the probability that two measurements would give results that are less consistent with the signal+background expectation than the H1 and ZEUS results [77]. This probability is found to be  $\sim 2\%$  in absence of a signal, and  $\sim 10\%$  for a mean signal.

Isolated Leptons	observed / expected
H1 ( $e + \mu$ )	11 / $3.67 \pm 0.96$
ZEUS ( $e + \mu + \tau$ )	4 / $2.55 \pm 0.24$

Table 8.7: Comparison of the H1 and ZEUS results on isolated leptons at  $P_T^X > 25$  GeV.

As for the single top cross-section and the  $tu\gamma$ -coupling, ZEUS reports the following exclusion limits at 95%CL (tau channel not included):

$$\sigma(ep \rightarrow etX, \sqrt{s} = 320 \text{ GeV}) < 0.25 \text{ pb} \quad \text{and} \quad \kappa_{tu\gamma} < 0.19.$$

These limits are stricter than the H1 limits due to the absence of top candidates in the electron and muon channels. In the preliminary ZEUS results, systematic errors are not yet taken into account.

#### 8.4.4 Outlook for FCNC Single Top Production

The sensitivity of the HERA and TeVatron colliders to FCNC processes will significantly increase with the large luminosities expected in the near future. Both TeVatron Run II and HERA II have started taking data.

The goal of HERA II is to collect an integrated luminosity of  $\sim 1 \text{ fb}^{-1}$  in five years, which would suffice to either gather enough isolated lepton candidates to claim a discovery or to improve the current exclusion limit on the FCNC coupling by roughly a factor of three to  $\kappa_{tu\gamma} < 0.07$ .

The search for radiative top decays  $t \rightarrow q\gamma$  in TeVatron Run IIa ( $2 \text{ fb}^{-1}$ ) has been estimated to yield  $\kappa_{tu\gamma} < 0.13$  [78]. It will also allow a test of the FCNC coupling to the gluon. After 2007, the LHC will be able to study all above mentioned anomalous couplings of the top quark with much higher sensitivity.

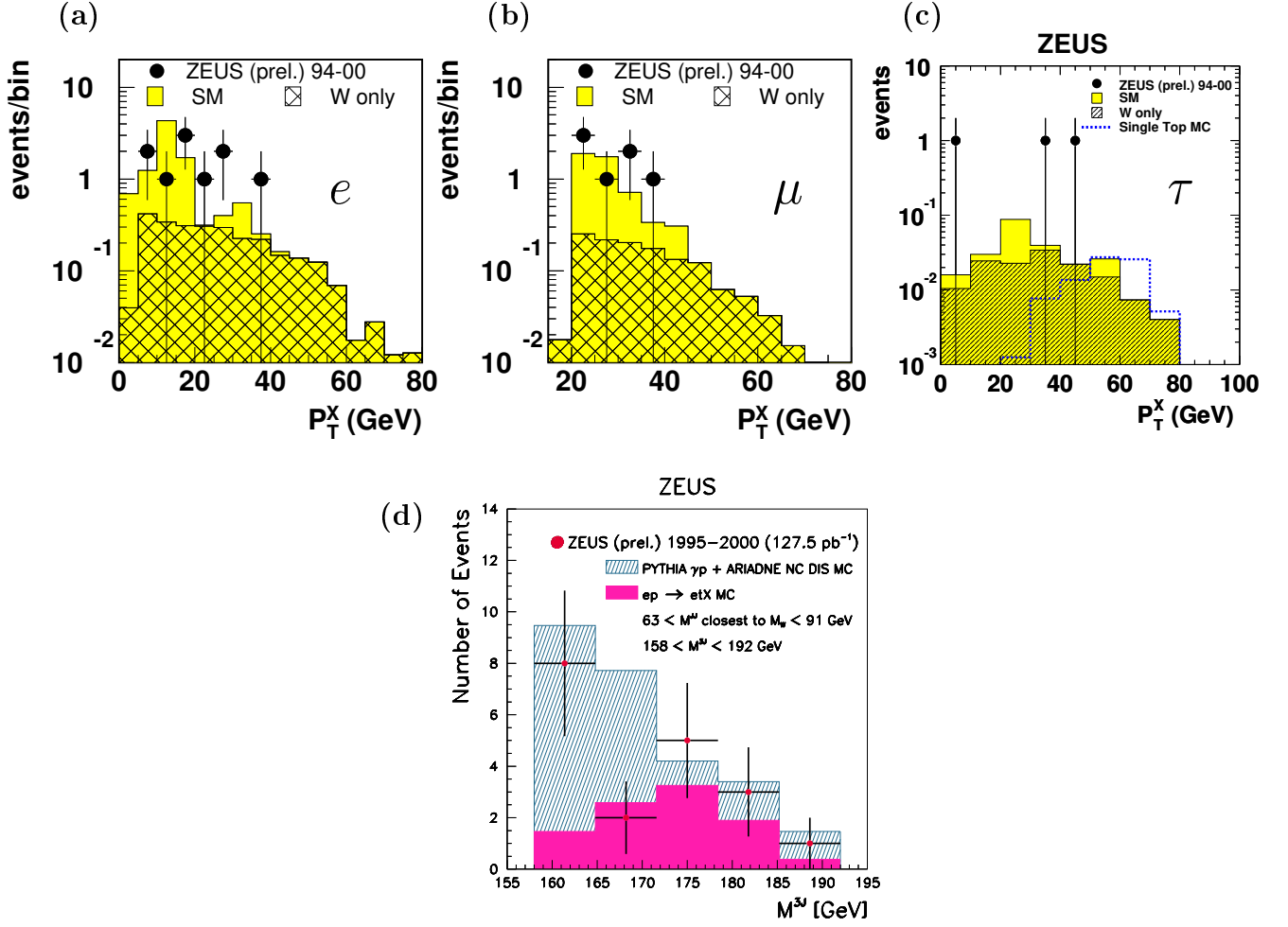


Figure 8.9: Preliminary results on isolated leptons and single top production obtained by the ZEUS collaboration. Shown are the hadronic transverse momentum distributions in the electron channel (a), muon channel (b), tau channel (c) and the 3-jet mass distribution in the hadronic channel (d). In (c) and (d), the top simulation is shown with arbitrary normalization. Taken from [75, 76].

## 8.5 Summary

For each analyzed decay channel of the top quark, a possible fraction of signal events in the data is obtained in a maximum-likelihood fit. Single top cross-sections of  $\sigma_{320} = 0.43^{+0.33}_{-0.18}$  ( $0.05^{+0.27}_{-0.24}$ ) pb are derived for the semi-leptonic (hadronic) channel. The two results are found to be consistent within  $1.2\sigma$ , taking statistical and systematic uncertainties into account. The additional contribution from single top production to the Standard Model background, as obtained from the fit, significantly increases the compatibility between data and simulation compared to the background-only hypothesis. However, for the combination of all channels, the probability that the data are still consistent with the Standard Model is still sizeable (16%). Therefore exclusion limits are set on the single top cross-section ( $\sigma_{320}(ep \rightarrow etX) < 0.60$  pb) and the  $tu\gamma$ -coupling ( $\kappa_{tu\gamma} < 0.25$ ).



The comparison with searches for FCNC top production at other experiments has shown that:

1. the HERA experiments have a large sensitivity the FCNC single top production via photon exchange, beyond the reach of other experiments at LEP and TeVatron.
2. there is a discrepancy in the yields of isolated electron and muon events observed by H1 and ZEUS. More data statistics will be needed to clarify this disagreement. Since ZEUS sees no excess of events at high  $P_T^X$ , they set a stricter exclusion limit on the cross-section for single top production. However, ZEUS observes two candidates at high  $P_T^X$  in the tau channel. Comparing the results on isolated leptons from H1 and ZEUS (including taus), they are found to be compatible with a probability of  $\sim 2\%$  ( $\sim 10\%$ ) assuming no signal (a mean signal) .



# Chapter 9

## Summary and Outlook

In this thesis, a search for the production of single top quarks in  $ep$  collisions is presented. This search is motivated by the observation of outstanding events with an isolated electron or muon and missing transverse momentum in the H1 detector. In addition, some of these events possess an unexpectedly large hadronic transverse momentum  $P_T^X$ . The dominant Standard Model process that produces similar final states is the production of real  $W$  bosons. However, the observed rate of the isolated lepton events together with their kinematical properties, mainly their large hadronic transverse momentum, make an interpretation as events from  $W$  production or other Standard Model processes unlikely.

The probability that the isolated electron and muon events are consistent with the Standard Model is  $9.7 \cdot 10^{-3}$  ( $4.0 \cdot 10^{-3}$ ) obtained from a confidence level computation using the full  $P_T^X$ -spectrum (only  $P_T^X > 25$  GeV). Systematic uncertainties are taken into account by scaling up the Standard Model prediction accordingly. These probabilities are low enough to seriously consider processes beyond the Standard Model as possible interpretation of the observed data candidates.

One interpretation is single top production. The predicted cross-section for Standard Model top production at HERA is of the order  $\mathcal{O}(1 \text{ fb})$  and thus too small to allow an observable rate of top events. However, in several extensions of the Standard Model, flavor changing neutral current couplings can be considerably enhanced, which would increase the production cross-section. In this analysis, a comprehensive search for singly produced top quarks is carried out assuming a model with flavor changing neutral current interactions involving a coupling of the top quark to a  $u$ -quark in the proton and a photon. Top quark decays into a  $b$ -quark and a  $W$  boson are considered in both the leptonic and the hadronic decay modes of the  $W$ . The full HERA I data recorded with the H1 experiment, corresponding to an integrated luminosity of  $118 \text{ pb}^{-1}$ , are analyzed.

An optimized set of observables is used for the discrimination of the top signal and the Standard Model background. In each decay channel, first a cut-based selection of top candidates is carried out. In the semi-leptonic channel, this selection yields five top candidates for a Standard Model expectation of  $1.61 \pm 0.42$  events. The dominant background is  $W$  production. Obviously a part of the observed data events fits kinematically better to single top production than to the Standard Model. Three of the selected top candidates have invariant masses close to and compatible with the top

mass ( $M_{\ell-\nu-jets} = 168^{+11}_{-11}, 172^{+9}_{-10}, 176^{+9}_{-12}$  GeV). In the hadronic channel, the cut-based top selection yields 18 events for  $20.2 \pm 3.0$  events expected. Therefore no deviation from the Standard Model is seen. In contrast to the semi-leptonic channel, the expected background from QCD processes is however large.

In a second step, a likelihood analysis is carried out to maximize the sensitivity to the signal. By constructing a likelihood discriminator, an improved signal and background separation is reached. The discriminator spectra are used for a maximum-likelihood fit of the signal normalization to the data. The results obtained in each channel are evaluated on a statistical basis. The maximum-likelihood fit results in a cross-section for single top production of  $0.43^{+0.33}_{-0.18}$  ( $0.05^{+0.27}_{-0.24}$ ) pb for the combined semi-leptonic channel (hadronic channel) at  $\sqrt{s} = 320$  GeV. Both channels are compatible within  $1.2 \sigma$  taking statistical and systematic uncertainties into account. A combination of all three channels gives the combined single top cross-section of  $0.31^{+0.16}_{-0.15}$  pb. The compatibility of the fitted signal+background distribution with the data has been evaluated and compared to the compatibility with the background-only hypothesis. The results presented in table 9.1 show that the signal+background fit gives a much better description of the data than the Standard Model background alone.

	$1 - \text{CL}_{s+b}$	$1 - \text{CL}_b$ w/o syst.	$1 - \text{CL}_b$ with syst.
Semi-leptonic channel ( $e + \mu$ )	36%	0.4%	1.6%
All channels	34%	12%	16%

Table 9.1: Probabilities  $1 - \text{CL}_{s+b}$  for the signal+background hypothesis and  $1 - \text{CL}_b$  for the background-only hypothesis (with and without inclusion of systematic uncertainties).

These result can be summarized by stating that the H1 data are best described in rate and distributions by a combination of the Standard Model prediction with a signal from new physics. Such a new signal could very well be single top production. However, the number of observed top candidates is still small and the probability of a Standard Model background fluctuation still sizeable. Hence the obtained results are also translated into exclusion limits on the single top production cross-section and the corresponding strength of the FCNC coupling. The obtained bounds at 95% CL are:

$$\sigma(ep \rightarrow etX, \sqrt{s} = 320 \text{ GeV}) < 0.60 \text{ pb} \quad , \quad \kappa_{t\gamma} < 0.25 \quad . \quad (9.1)$$

A comparison with searches for single top production or rare top quark decays carried out by other experiments shows that the HERA experiments have the largest sensitivity to the anomalous  $tu\gamma$ -coupling and set the strongest limit. As opposed to the H1 results, the ZEUS collaboration reports no excess of electron or muon events, but sees two candidates at high  $P_T^X$  in the tau channel. Comparing the results of both experiments for  $P_T^X > 25$  GeV assuming a mean signal rate, both experiments are compatible with each other with a probability of  $\sim 10\%$ . Assuming that no signal exists, the compatibility decreases to  $\sim 2\%$ .

## Outlook

Due to the small number of data events, the presented search for top quarks is dominated by statistical uncertainties, in particular in the semi-leptonic channel. Therefore more statistics is needed to be able to decide if the isolated lepton excess is only an (unlikely) statistical fluctuation. HERA II is currently starting a phase of operation at higher luminosity, aiming at collecting data corresponding to an integrated luminosity of  $1 \text{ fb}^{-1}$  in the next five years. This increase of the integrated luminosity by a factor of  $\sim 10$  should either turn the isolated lepton excess into a discovery or significantly improve the limit on the FCNC coupling  $\kappa_{tu\gamma}$  (by roughly a factor of three to 0.07).

Besides higher statistics, also the following aspects will be relevant for the single top analysis in the future:

- During the shutdown in 2001, various components of the H1 detector have been upgraded or newly installed. The new forward tracker will hopefully allow an improved tracking in the forward region, where most of the particles from top decays are expected. Also a new silicon tracker (FST) was installed in the forward region of the detector. Together with the central silicon tracker (CST), the acceptance will be significantly increased. This may allow an efficient tagging of  $b$ -quarks in top events.
- The single top analysis at H1 is currently being extended to include the tau channel. Hadronic tau decays are identified as narrow jets with one or three tracks in the detector. Tau candidates at high  $P_T^X$ , as the two candidates observed by ZEUS, could nicely complement the observations in the electron and muon channels.
- A next-to-leading order calculation for the  $W$  production cross-section in  $ep$  collisions has recently been published [79]. It could unfortunately not be included in this thesis. The calculated leading order cross-section corresponds within a few percent to the prediction of the EPVEC generator, as used in this analysis. The systematic uncertainty on the predicted cross-section is reduced from 30% to 15%, which would have some impact on the probabilities (including systematics) evaluated in this thesis.
- Although single top production seems to kinematically fit quite well to the isolated lepton excess, there are other interpretations that may be worthwhile to be studied. One example is the production of stop quarks in supersymmetric models with R-parity violation. A possible stop decay  $\tilde{t} \rightarrow \tilde{b}W^+ \rightarrow d\bar{\nu}_e\mu^+\nu_\mu$  (assuming the sbottom is lighter than the stop) would yield signatures similar to the ones of the isolated lepton events.



# Appendix A

## Event Displays of Isolated Leptons at High Hadronic $P_T$

This appendix contains event displays of all ten isolated lepton events selected as  $W$  candidates that have a high hadronic transverse momentum ( $P_T^{jets} > 25$  GeV). First the four electron events are presented in increasing order of  $P_T^{jets}$ , then the six muon events. The five events selected in the cut-based top analysis are marked as **top candidates**.

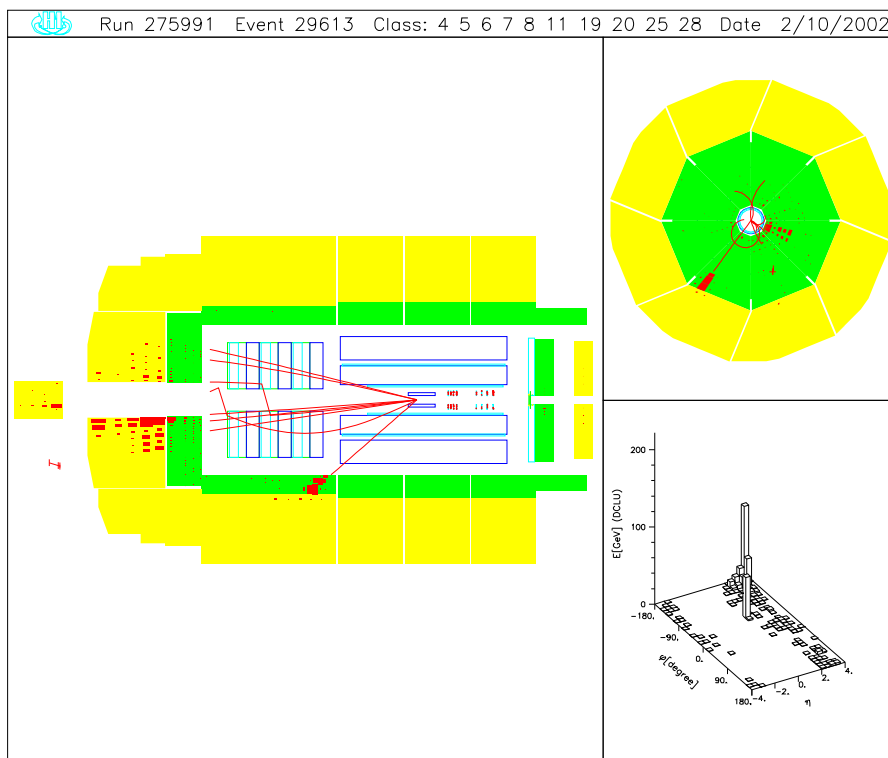


Figure A.1:  $W \rightarrow e^+ \nu$  candidate.

$P_T^e = 38$  GeV ,  $P_T^{miss} = 42$  GeV ,  $P_T^{jets} = 27$  GeV ,  $M_{e-\nu-jets} = 144$  GeV .

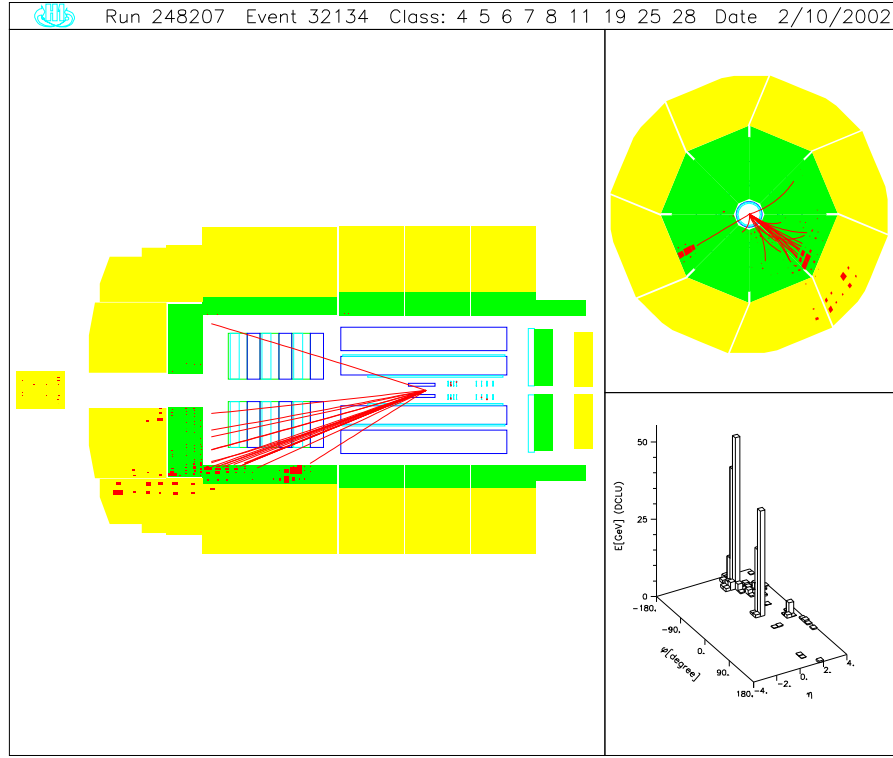


Figure A.2:  $W \rightarrow e^+ \nu$  candidate. (**top candidate**)

$P_T^e = 32$  GeV ,  $P_T^{miss} = 44$  GeV ,  $P_T^{jets} = 43$  GeV ,  $M_{e-\nu-jets} = 155$  GeV.

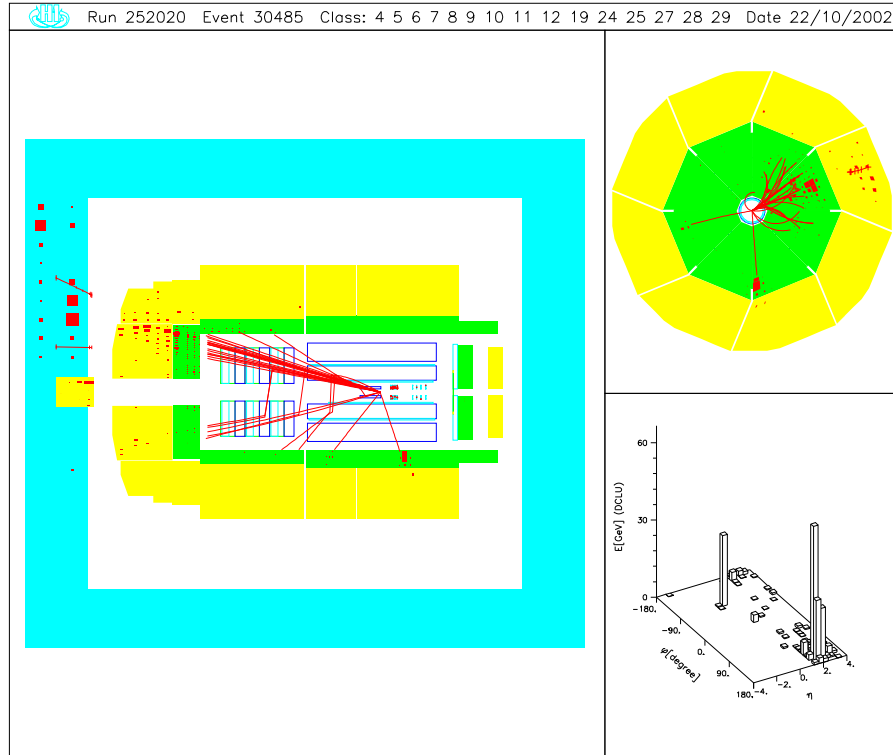


Figure A.3:  $W \rightarrow e^+ \nu$  candidate with tagged scattered electron. (**top candidate**)  
 $P_T^e = 25$  GeV ,  $P_T^{miss} = 40$  GeV ,  $P_T^{jets} = 47$  GeV ,  $M_{e-\nu-jets} = 168$  GeV ,  
 $M_{e\nu} = 79$  GeV.



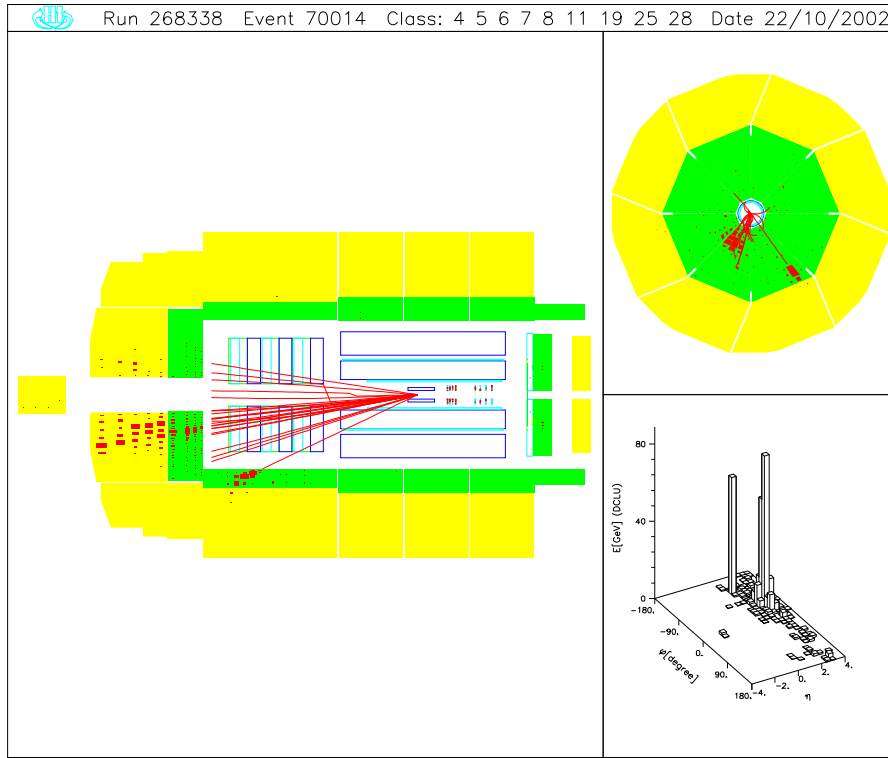


Figure A.4:  $W \rightarrow e^+ \nu$  candidate. (**top candidate**)  
 $P_T^e = 32$  GeV ,  $P_T^{miss} = 67$  GeV ,  $P_T^{jets} = 48$  GeV ,  $M_{e-\nu-jets} = 160$  GeV.

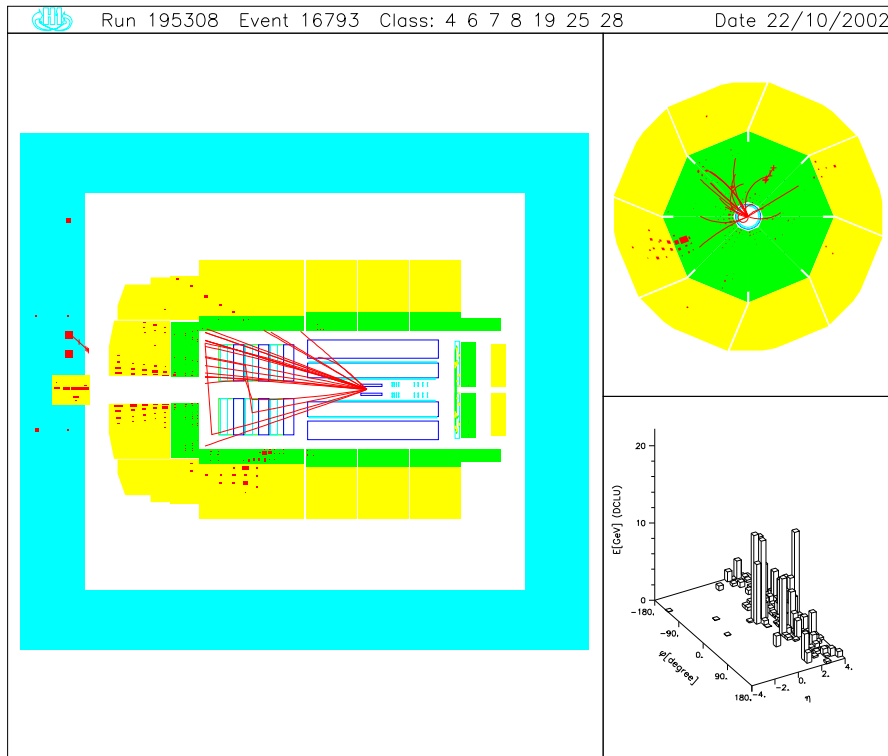


Figure A.5:  $W \rightarrow \mu^+ \nu$  candidate.  
 $P_T^\mu = 60_{-12}^{+19}$  GeV ,  $P_T^{miss} = 31$  GeV ,  $P_T^{jets} = 26$  GeV ,  $M_{e-\nu-jets} = 113$  GeV.

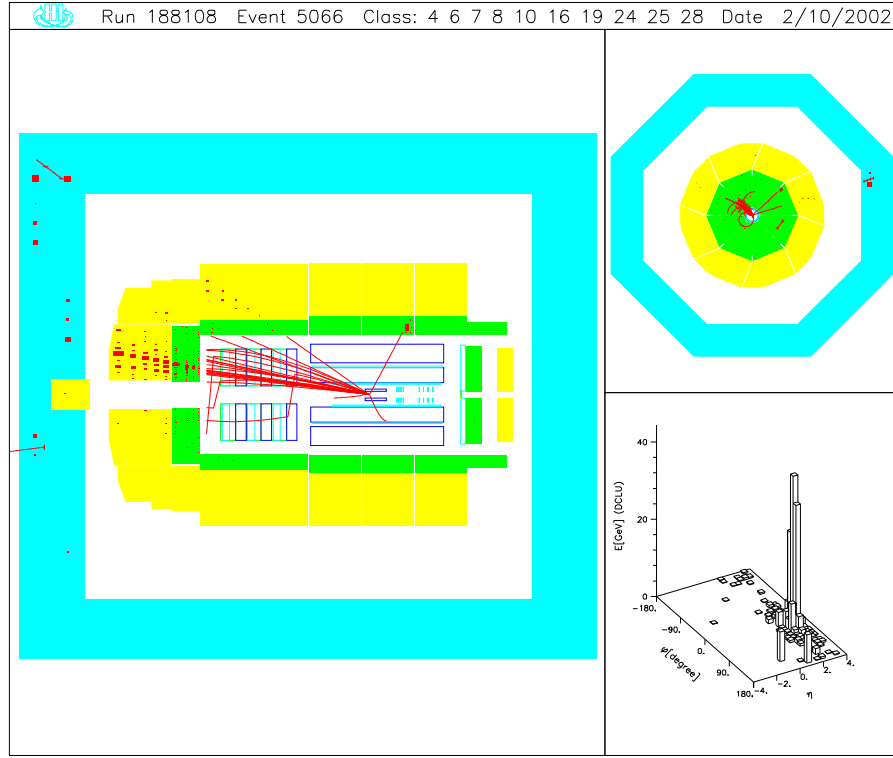


Figure A.6:  $W \rightarrow \mu^- \nu$  candidate with tagged scattered electron.

$P_T^\mu = 41_{-4}^{+6}$  GeV ,  $P_T^{miss} = 45$  GeV ,  $P_T^{jets} = 27$  GeV ,  $M_{e-\nu-jets} = 159$  GeV ,  $M_{\mu\nu} = 79$  GeV.

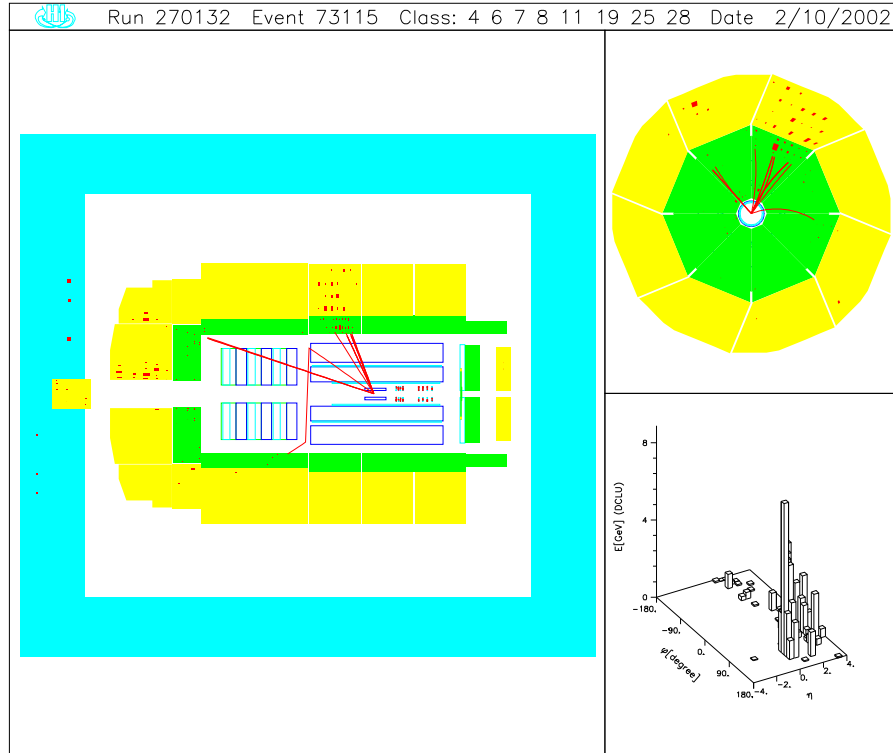


Figure A.7:  $W \rightarrow \mu\nu$  candidate. The muon charge is undetermined.

$P_T^\mu = 64_{-38}^{+55}$  GeV ,  $P_T^{miss} = 79$  GeV ,  $P_T^{jets} = 27$  GeV ,  $M_{e-\nu-jets} = 147$  GeV.

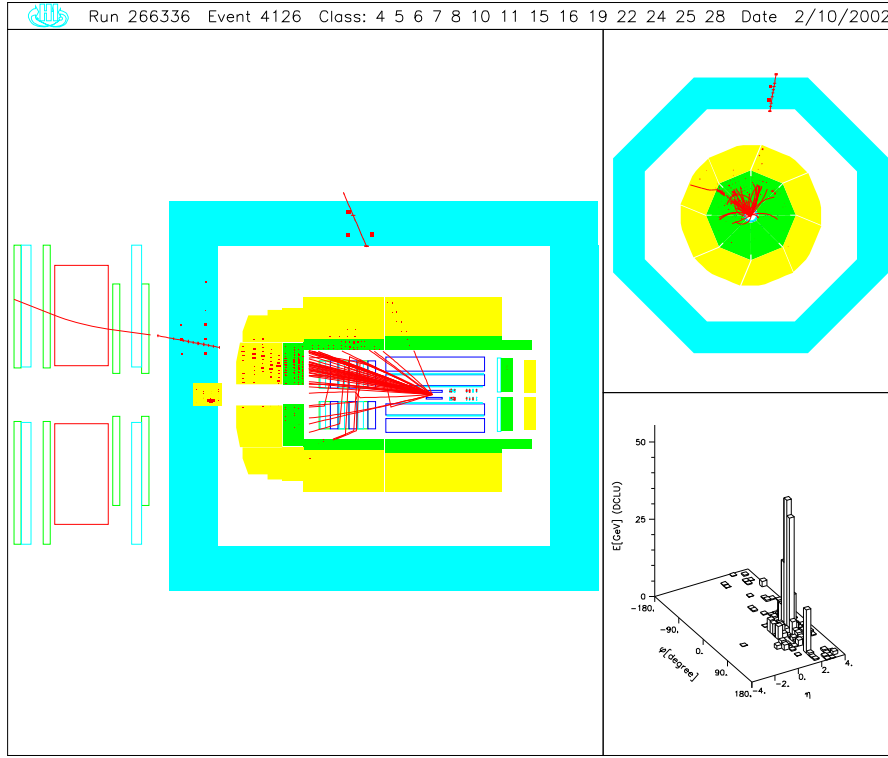


Figure A.8:  $W \rightarrow \mu^+ \nu$  candidate with a second muon in the jet. (**top candidate**)  
 $P_T^\mu = 20_{-1}^{+1}$  GeV ,  $P_T^{miss} = 67$  GeV ,  $P_T^{jets} = 55$  GeV ,  $M_{e-\nu-jets} = 172$  GeV.

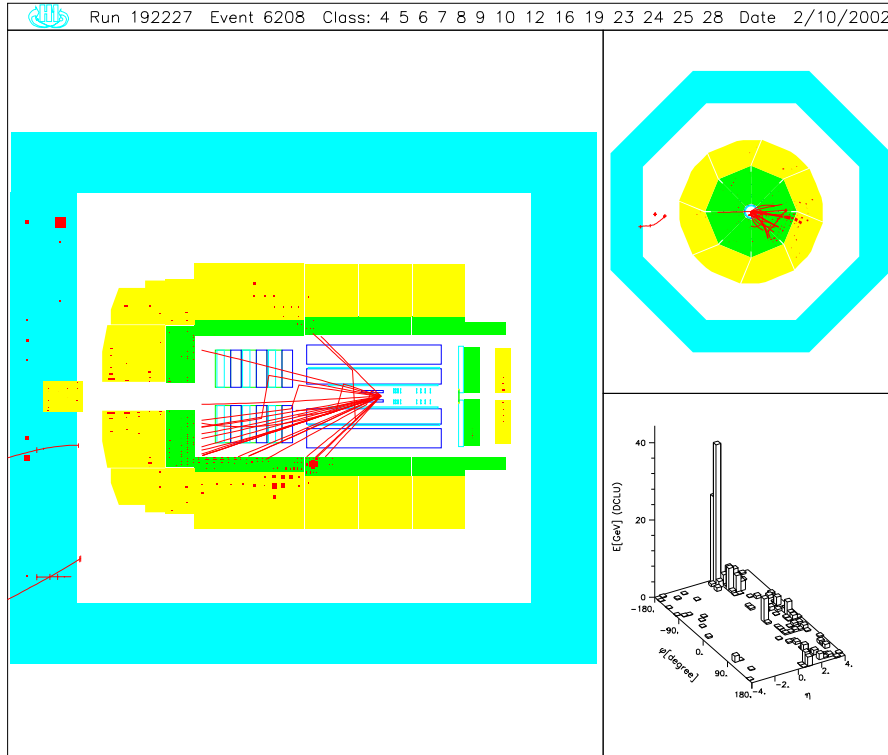


Figure A.9:  $W \rightarrow \mu^- \nu$  candidate.  
 $P_T^\mu = 73_{-9}^{+12}$  GeV ,  $P_T^{miss} = 22$  GeV ,  $P_T^{jets} = 64$  GeV ,  $M_{e-\nu-jets} = 169$  GeV.

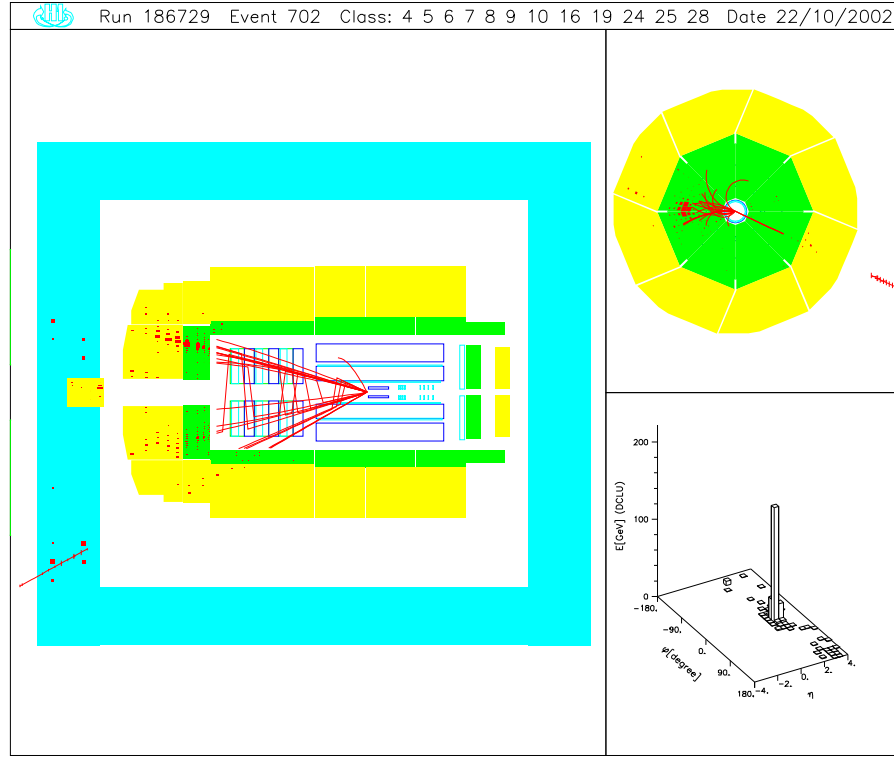


Figure A.10:  $W \rightarrow \mu^+ \nu$  candidate. (**top candidate**)

$P_T^\mu = 51_{-11}^{+17}$  GeV ,  $P_T^{miss} = 28$  GeV ,  $P_T^{jets} = 72$  GeV ,  $M_{e-\nu-jets} = 176$  GeV.

# Appendix B

## Spin Correlations in Top Quark Decays

In this chapter, the correlations between the spin of the top quark and the spin of the  $W$  boson are discussed for top quark decays  $t \rightarrow bW \rightarrow b\ell\nu$ .

The shape of the  $\cos(\theta_W^*)$  distribution presented in figure 6.20 is a consequence of a specific mixture of  $W$  helicities in top quark decays. To recall, the  $W$  decay angle  $\theta_W^*$  is defined as the angle between the lepton in the  $W$  rest frame and the  $W$  direction in the top rest frame. As illustrated in B.1 (a) and (b), only two helicities states are possible for  $W$  bosons emerging from top decays. The right-handed helicity state is absent, while the left-handed and longitudinal helicity states occur in the ratio [59]:

$$W_{left} : W_{long} = 2M_W^2 : M_{top}^2 \approx 30\% : 70\%. \quad (\text{B.1})$$

The reason for this is the V-A structure of the electro-weak theory. Due to the V-A coupling of the  $W$  to quarks and the negligible  $b$ -quark mass compared to its energy obtained in the top decay, the left-handed chirality of the  $tbW$ -vertex leads to a left-handed helicity of the  $b$ -quark. When the  $W$  is emitted in the direction of the top quark spin, angular momentum conservation tells us that the spin of the  $W$  has to be perpendicular to the spin of the top and the  $b$ -quark (longitudinal  $W$ ). Similarly, the spin of the  $W$  has to point in the same direction as the spin of the top quark for a  $W$  emitted in the opposite direction (left-handed  $W$ ).

How is the  $W$  spin direction now related to the direction of the lepton? This becomes clear by looking at figure B.1 (c). Single top production at HERA yields  $W^+$  bosons and thus positively charged leptons in the subsequent leptonic decays of the  $W^+$ . Due to the left-handedness of the neutrino, the positively charged lepton must be emitted in the direction of the  $W$  spin. Therefore the contribution to  $\cos(\theta_W^*)$  from left-handed  $W$ 's is a term  $\propto (1 - \cos(\theta_W^*))^2$  and from longitudinal  $W$ 's a term  $\propto \sin^2(\theta_W^*)$ . The angular distribution has the following form:

$$\frac{dN}{d(\cos(\theta_W^*))} \approx 0.3 \cdot \frac{1}{4}(1 - \cos(\theta_W^*))^2 + 0.7 \cdot \frac{1}{2}\sin^2(\theta_W^*). \quad (\text{B.2})$$

This equation is also valid for unpolarized top quarks, as implemented in the generator ANOTOP. The  $\cos(\theta_W^*)$  distribution obtained for ANOTOP events on parton level

is shown in figure B.2 together with the individual contributions expected from left-handed and longitudinal  $W$ 's.

As a side remark, it should be mentioned that as a consequence of the lepton direction with respect to the  $W$  spin and the two possible  $W$  helicities in top decays, the transverse momentum of the neutrino in the top decay chain tends to be larger than the transverse momentum of the lepton. The difference comes from the left-handed  $W$  component. For left-handed  $W$ 's, the lepton is emitted opposite to the direction of motion of the  $W$  in the laboratory frame, while the neutrino is emitted in the  $W$  direction, and thus obtains a larger transverse momentum than the electron.

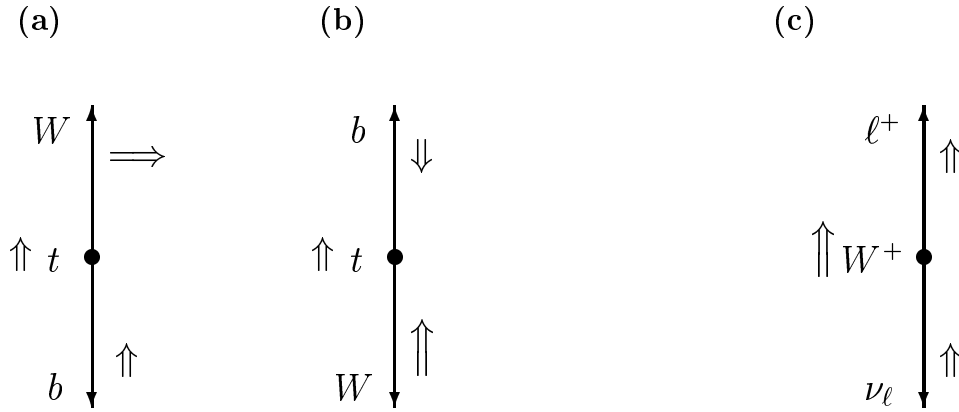


Figure B.1: Illustrations of the spin correlations in top decays (a) and (b) and in  $W^+$  decays (c).

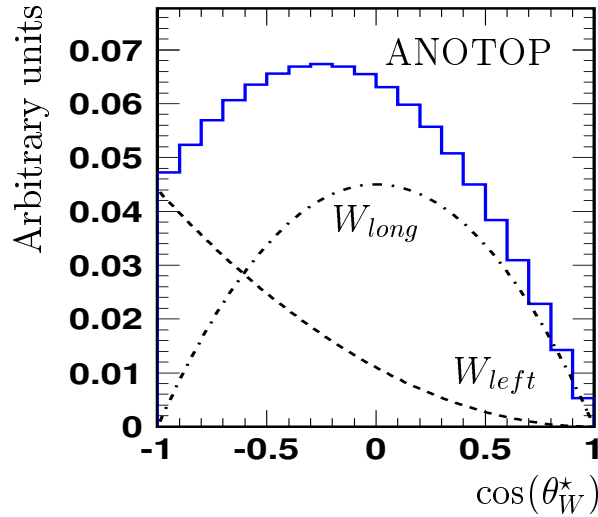


Figure B.2: Distribution of the cosine of the  $W$  decay angle,  $\theta_W^*$ , for generated top events (ANOTOP) on parton level. The angular distribution consists of a contribution from left-handed  $W$  bosons and a contribution from longitudinal  $W$  bosons, drawn as dashed and dashed-dotted lines.

# Appendix C

## Transformed Observables and Correlation Matrices

In this appendix, the input variables for the likelihood analyses are shown after their transformation to Gaussian distributed variables by the PTC-method. In addition, all correlation (covariance) matrices of these variables are given for the top signal and the background Monte Carlo samples before and after the transformation.

## C.1 Electron Channel

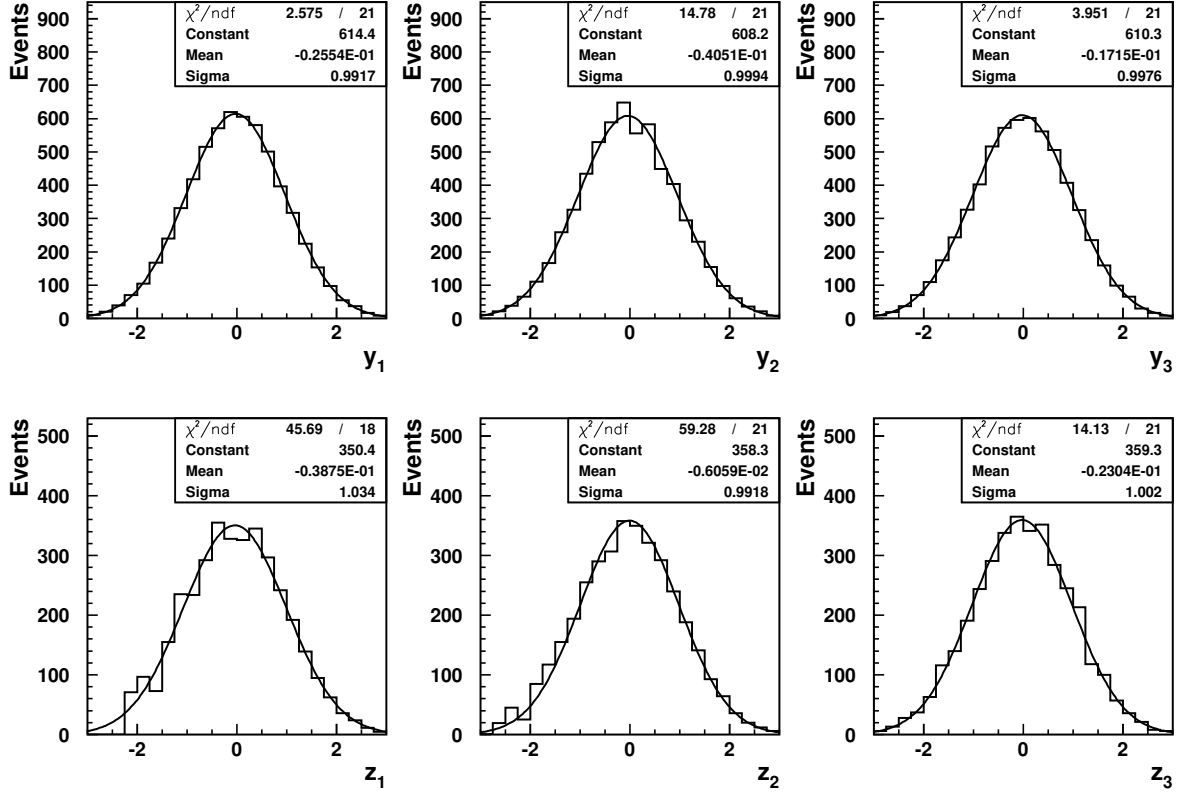


Figure C.1: Distributions of the Gaussian transformed variables  $y_i$  for the top signal (upper plots) and  $z_i$  for the background (lower plots). Gaussian fits to the distributions are shown as solid lines.

### Signal Sample

	$P_T^{jets}$	$M_{e-\nu-jets}$	$\cos(\theta_W^*)$
$P_T^{jets}$	1.00	0.61	-0.11
$M_{e-\nu-jets}$	0.61	1.00	-0.12
$\cos(\theta_W^*)$	-0.10	-0.12	1.00

Table C.1: Correlation matrix of the untransformed variables.

	$y_1$	$y_2$	$y_3$
$y_1$	0.97	0.59	-0.11
$y_2$	0.59	1.00	-0.12
$y_3$	-0.11	-0.12	0.99

Table C.2: Covariance matrix of the transformed variables.

### Background Sample

	$P_T^{jets}$	$M_{e-\nu-jets}$	$\cos(\theta_W^*)$
$P_T^{jets}$	1.00	0.64	-0.01
$M_{e-\nu-jets}$	0.64	1.00	-0.03
$\cos(\theta_W^*)$	-0.01	-0.03	1.00

Table C.3: Correlation matrix of the untransformed variables.

	$z_1$	$z_2$	$z_3$
$z_1$	0.98	0.63	-0.01
$z_2$	0.63	1.04	-0.02
$z_3$	-0.01	-0.02	1.00

Table C.4: Covariance matrix of the transformed variables.



## C.2 Muon Channel

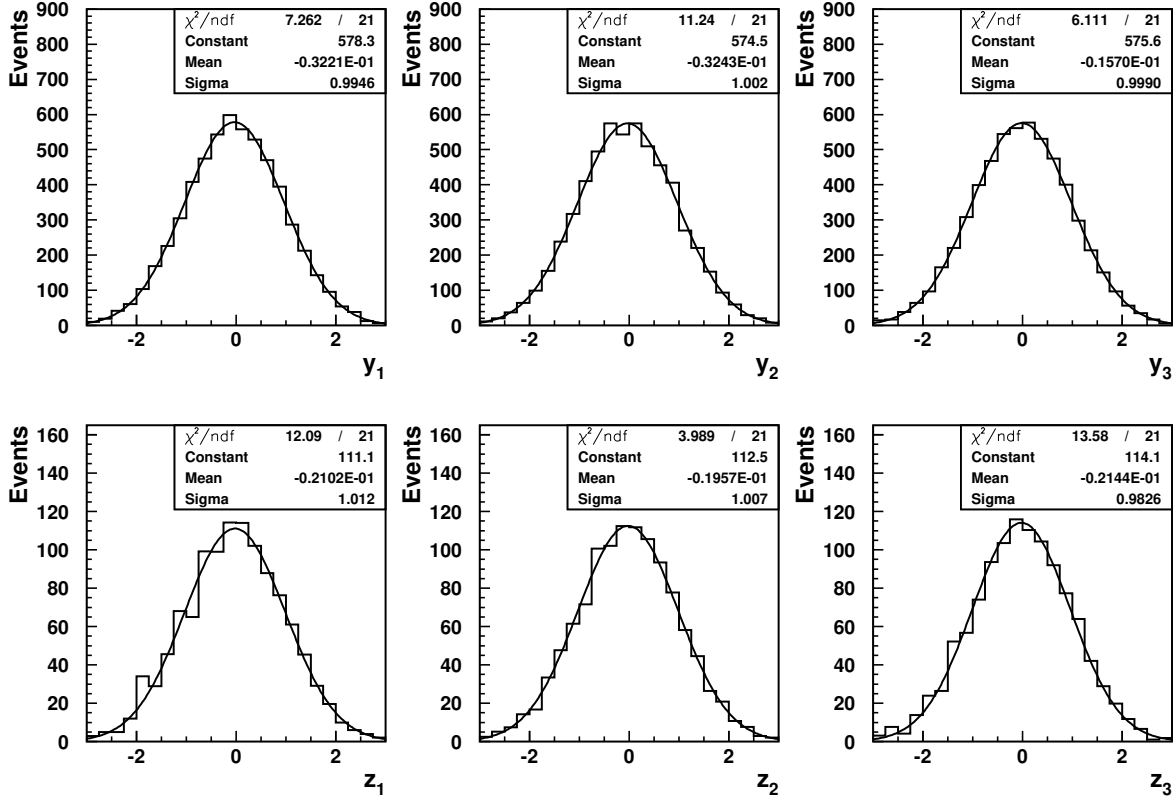


Figure C.2: Distributions of the Gaussian transformed variables  $y_i$  for the top signal (upper plots) and  $z_i$  for the background (lower plots). Gaussian fits to the distributions are shown as solid lines.

### Signal Sample

	$P_T^{jets}$	$M_{e-\nu-jets}$	$\cos(\theta_W^*)$
$P_T^{jets}$	1.00	0.54	-0.13
$M_{e-\nu-jets}$	0.54	1.00	-0.05
$\cos(\theta_W^*)$	-0.13	-0.05	1.00

Table C.5: Correlation matrix of the untransformed variables.

	$y_1$	$y_2$	$y_3$
$y_1$	1.06	0.56	-0.13
$y_2$	0.56	1.03	-0.06
$y_3$	-0.13	-0.06	1.04

Table C.6: Covariance matrix of the transformed variables.

### Background Sample

	$P_T^{jets}$	$M_{e-\nu-jets}$	$\cos(\theta_W^*)$
$P_T^{jets}$	1.00	0.68	0.02
$M_{e-\nu-jets}$	0.68	1.00	0.04
$\cos(\theta_W^*)$	0.02	0.04	1.00

Table C.7: Correlation matrix of the untransformed variables.

	$z_1$	$z_2$	$z_3$
$z_1$	1.15	0.77	0.06
$z_2$	0.77	1.15	0.02
$z_3$	0.06	0.02	1.15

Table C.8: Covariance matrix of the transformed variables.

### C.3 Hadronic Channel

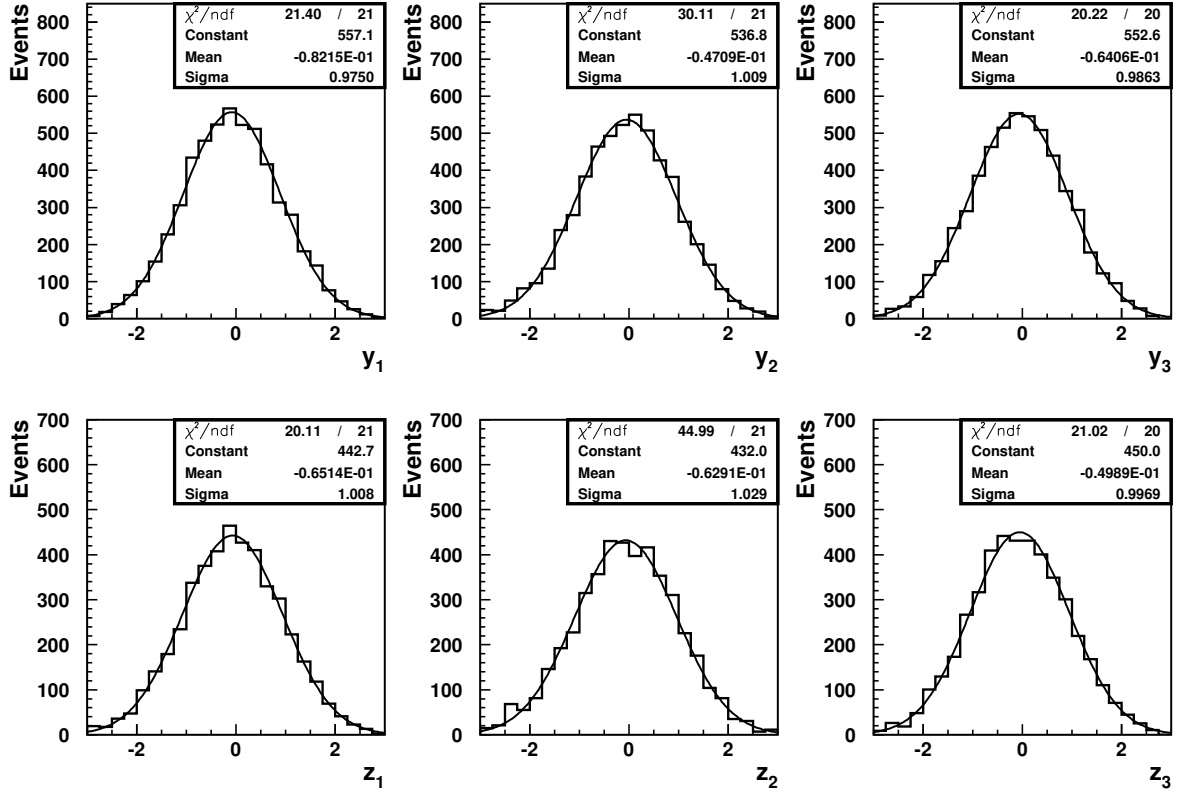


Figure C.3: Distributions of the Gaussian transformed variables  $y_i$  for the top signal (upper plots) and  $z_i$  for the photoproduction background (lower plots). Gaussian fits to the distributions are shown as solid lines.

#### Signal Sample

	$P_T^{jets}$	$M_{e-\nu-jets}$	$\cos(\theta_W^*)$
$P_T^{jets}$	1.00	0.53	0.07
$M_{e-\nu-jets}$	0.53	1.00	0.04
$\cos(\theta_W^*)$	0.07	0.04	1.00

Table C.9: Correlation matrix of the untransformed variables.

	$y_1$	$y_2$	$y_3$
$y_1$	1.02	0.53	0.07
$y_2$	0.53	1.01	0.04
$y_3$	0.07	0.04	1.10

Table C.10: Covariance matrix of the transformed variables.

#### Background Sample

	$P_T^{jets}$	$M_{e-\nu-jets}$	$\cos(\theta_W^*)$
$P_T^{jets}$	1.00	0.60	0.05
$M_{e-\nu-jets}$	0.60	1.00	-0.16
$\cos(\theta_W^*)$	0.05	-0.16	1.00

Table C.11: Correlation matrix of the untransformed variables.

	$z_1$	$z_2$	$z_3$
$z_1$	0.91	0.51	0.02
$z_2$	0.51	0.83	-0.12
$z_3$	0.02	-0.12	0.93

Table C.12: Covariance matrix of the transformed variables.

## Appendix D

# Discriminating Observables after Cut on the Lepton Charge

This appendix shows the observables used to discriminate the top signal from  $W$  production in the electron and muon channels, after rejecting all events that have a lepton with well-measured negative charge ( $> 2\sigma$ ).

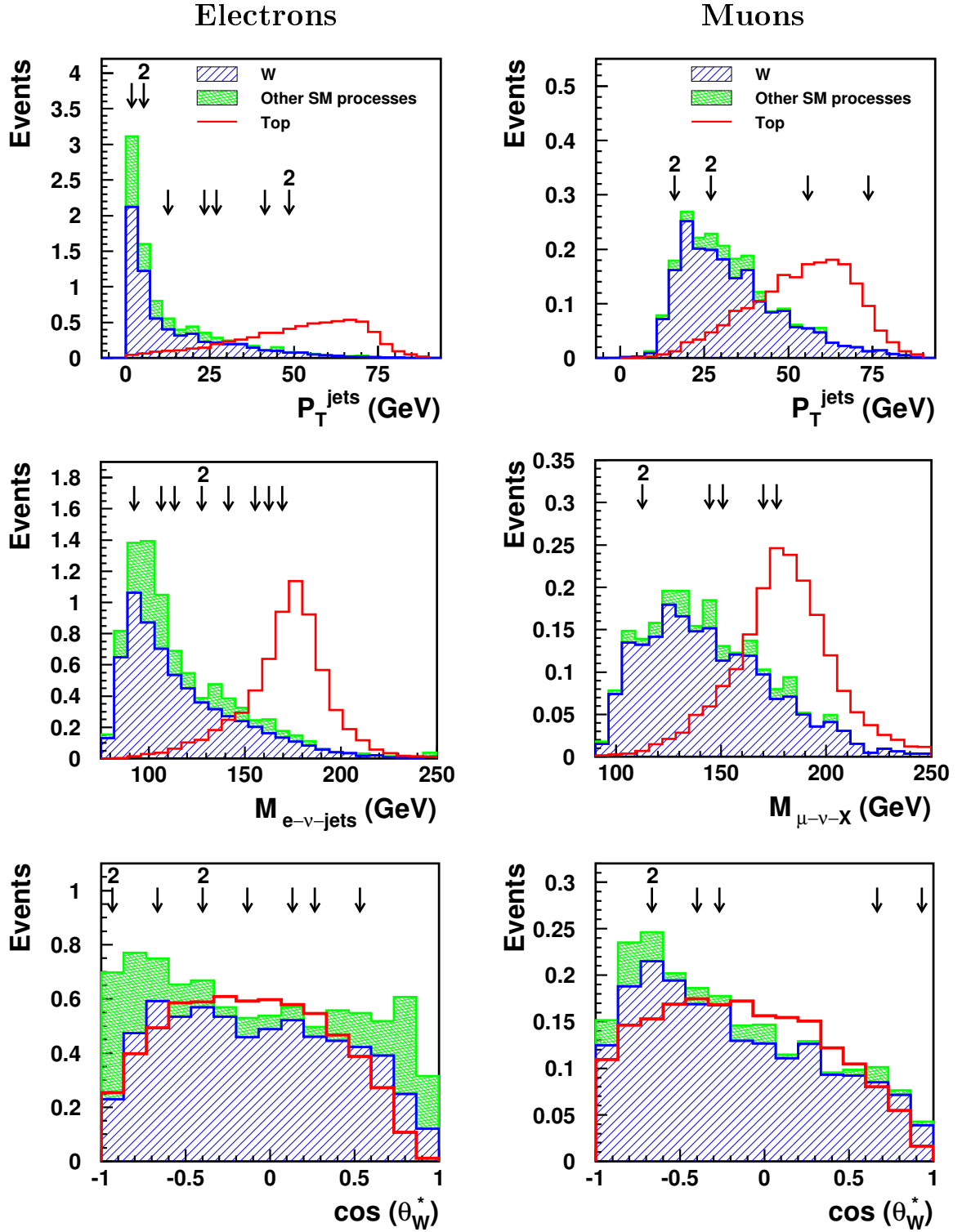


Figure D.1: Distributions of the three discriminating observables used to separate single top production from Standard Model  $W$  production (left: electron channel, right: muon channel). The distributions are shown after applying a cut on the lepton charge, that rejects all events with well-measured negative leptons. The top simulation is arbitrarily normalized to the expectation from  $W$  production. The positions of the data events are marked by arrows. A number above the arrow indicates the number of data events in the corresponding bin of the distribution.

# Appendix E

## Event Displays of Top Candidates in the Hadronic Channel

This appendix presents event displays of selected multi-jet events that pass the top selection.

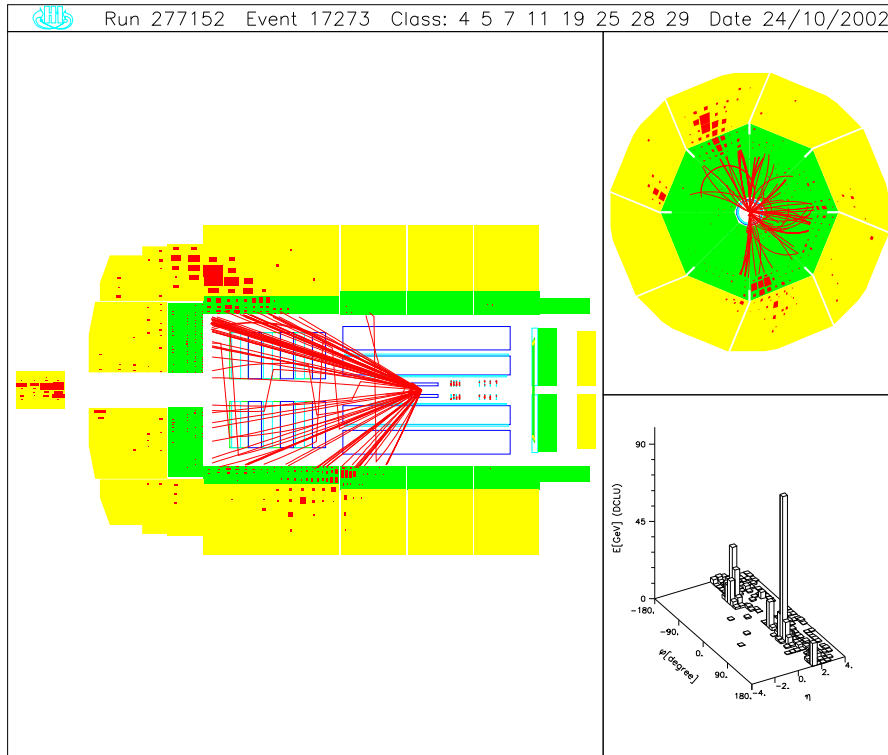
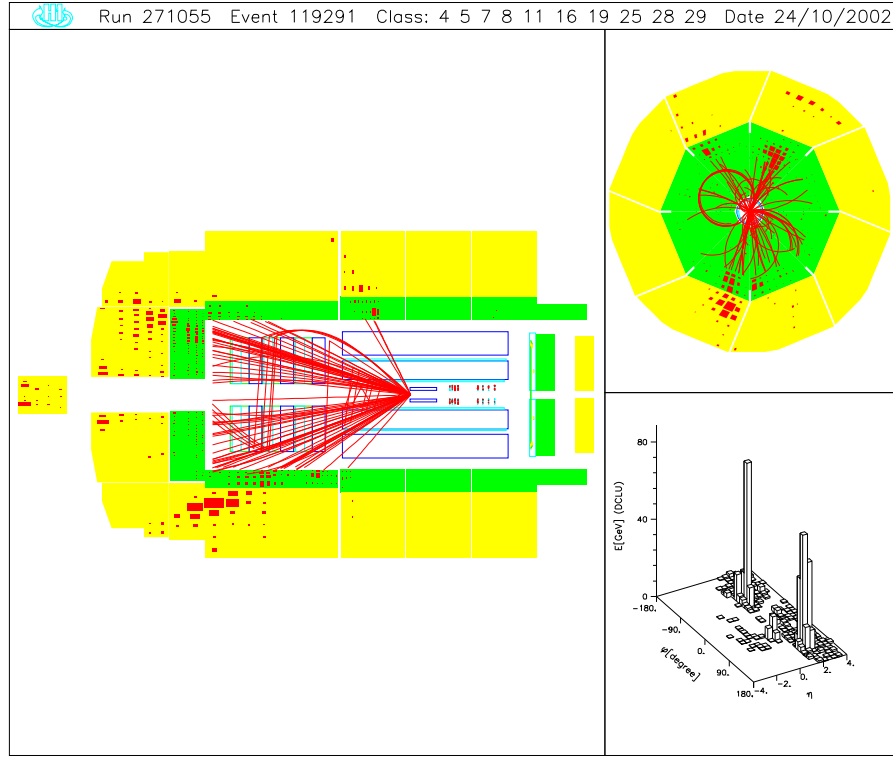
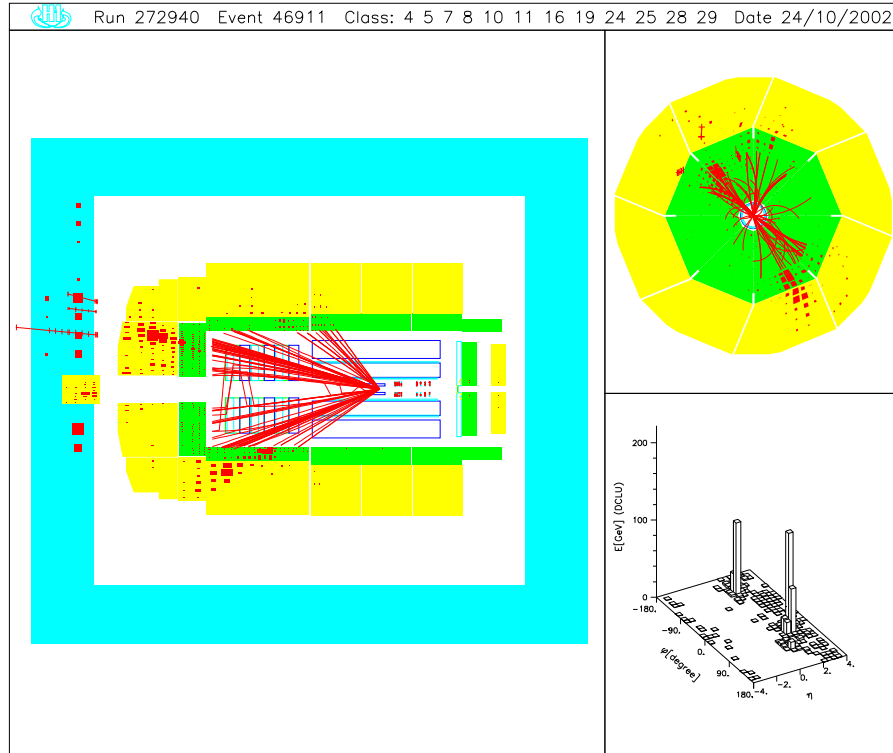


Figure E.1:  $t \rightarrow bW \rightarrow bq\bar{q}'$  candidate.

$P_T^{jet1,2,3} = 70, 69, 21$  GeV ,  $M_{jets} = 171$  GeV ,  $M_{2jet}^{Wcomb.} = 71$  GeV.

Figure E.2:  $t \rightarrow bW \rightarrow bq\bar{q}'$  candidate.
$$P_T^{jet1,2,3} = 70, 60, 22 \text{ GeV} , M_{jets} = 174 \text{ GeV} , M_{2jet}^{Wcomb.} = 81 \text{ GeV} .$$
Figure E.3:  $t \rightarrow bW \rightarrow bq\bar{q}'$  candidate.
$$P_T^{jet1,2,3} = 75, 68, 24 \text{ GeV} , M_{jets} = 186 \text{ GeV} , M_{2jet}^{Wcomb.} = 85 \text{ GeV} .$$

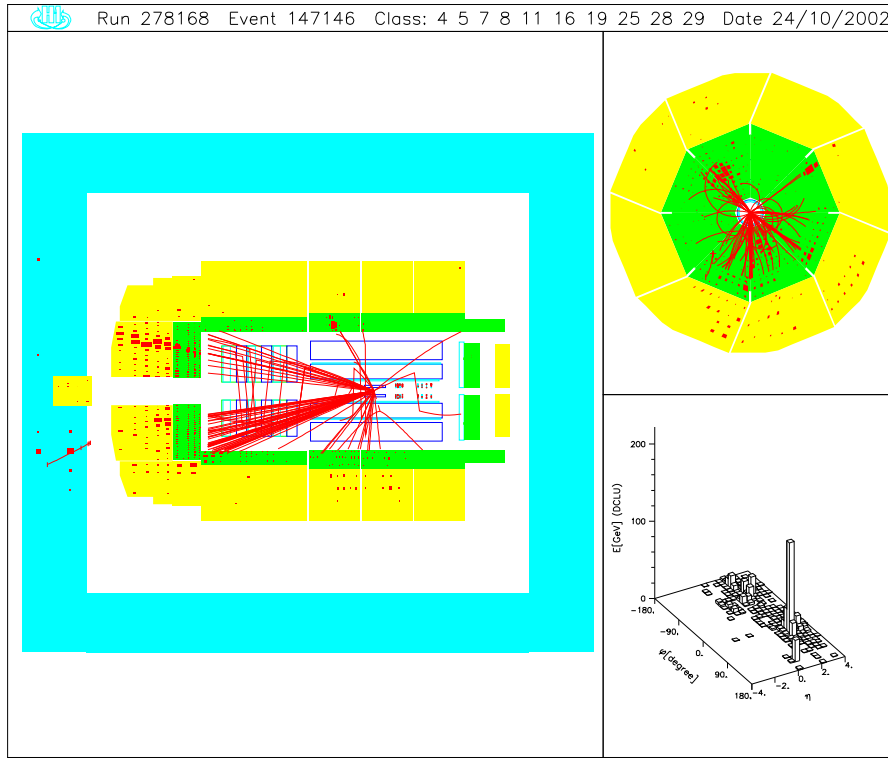


Figure E.4:  $t \rightarrow bW \rightarrow bq\bar{q}'$  candidate.  
 $P_T^{jet1,2,3} = 63, 43, 23$  GeV ,  $M_{jets} = 181$  GeV ,  $M_{2jet}^{Wcomb.} = 70$  GeV.

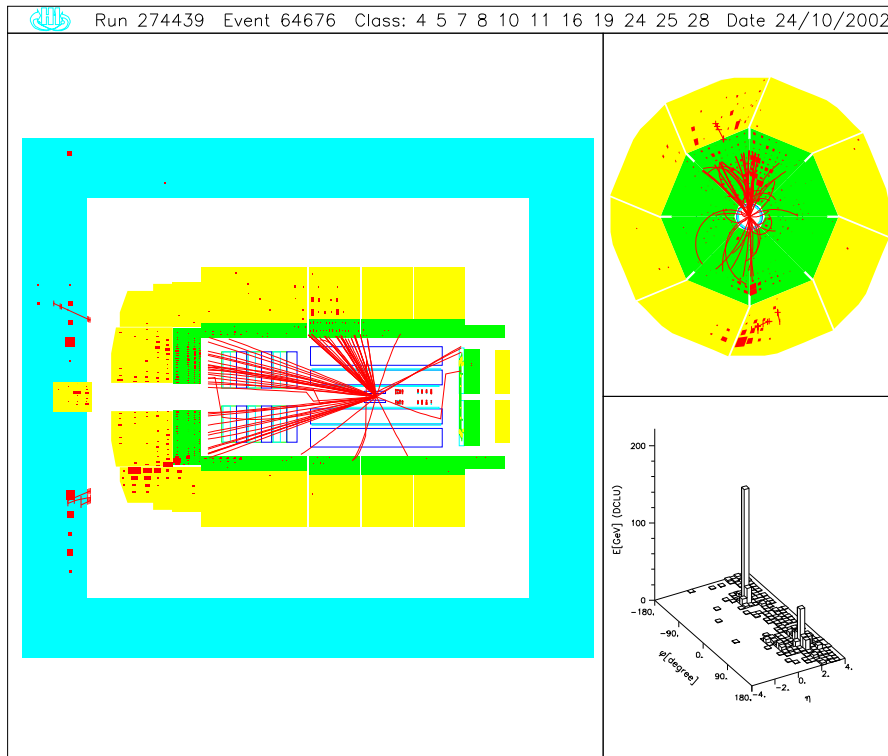


Figure E.5:  $t \rightarrow bW \rightarrow bq\bar{q}'$  candidate.  
 $P_T^{jet1,2,3} = 68, 42, 36$  GeV ,  $M_{jets} = 180$  GeV ,  $M_{2jet}^{Wcomb.} = 75$  GeV.

# Appendix F

## Study of Systematic Uncertainties for the Signal Fit

In this appendix, the distributions of the fitted numbers of top signal events are shown after a Gaussian smearing of the different quantities affected with a systematic uncertainty. Each distribution contains (at least) 200 entries. The uncertainty on the number of signal events is obtained by applying Gaussian fits to these distributions. The results of the fits are shown.

### F.1 Hadronic Channel

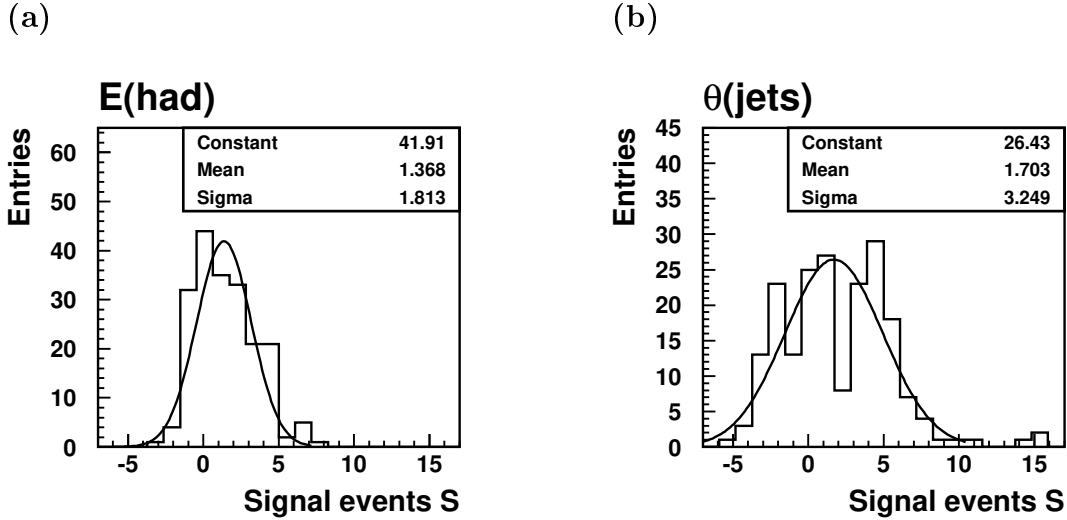


Figure F.1: Systematic uncertainty on the number of signal events due to different experimental uncertainties in the hadronic channel.



## F.2 Electron Channel

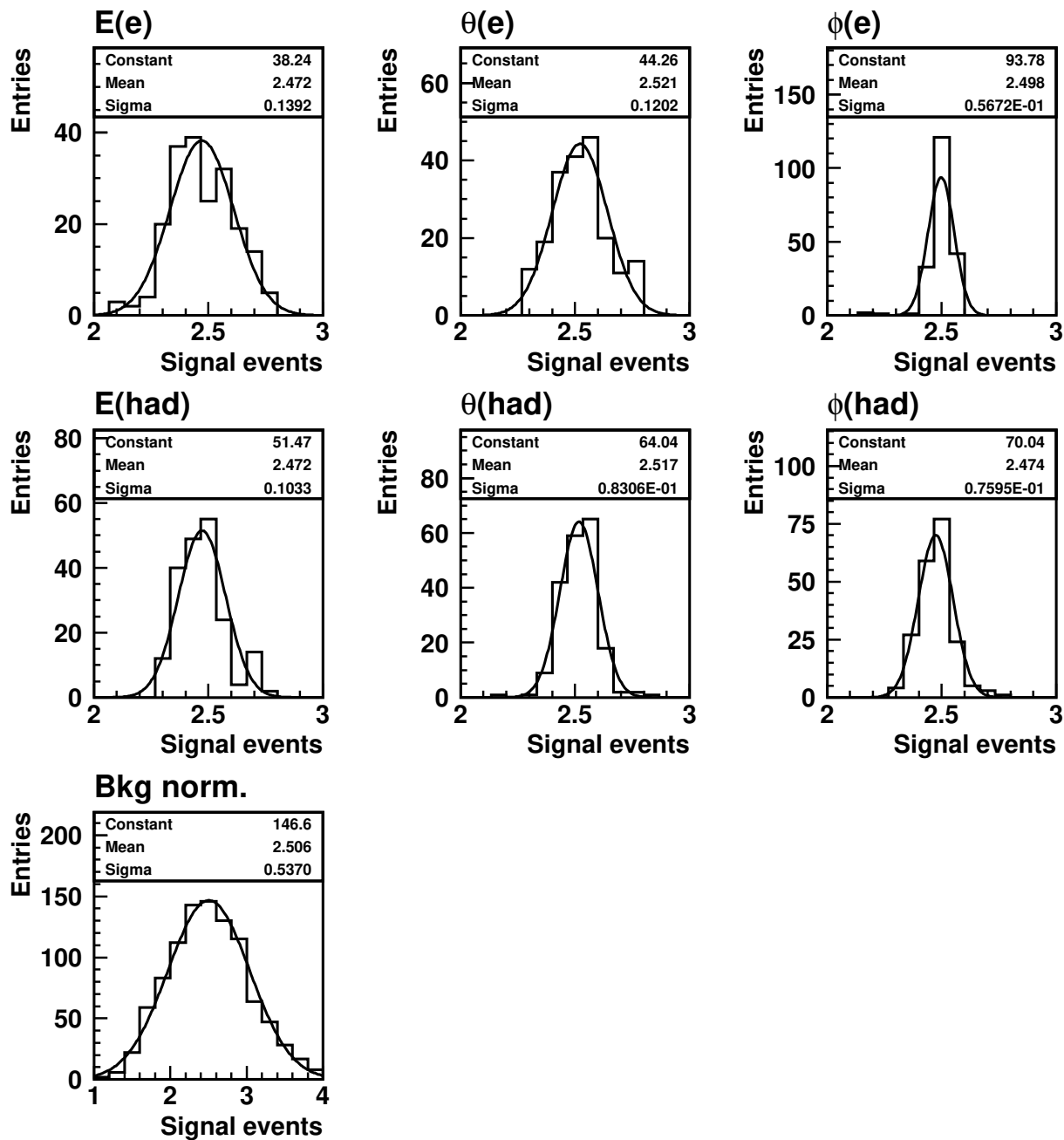


Figure F.2: Systematic uncertainty on the number of signal events due to different experimental uncertainties in the electron channel.

### F.3 Muon Channel

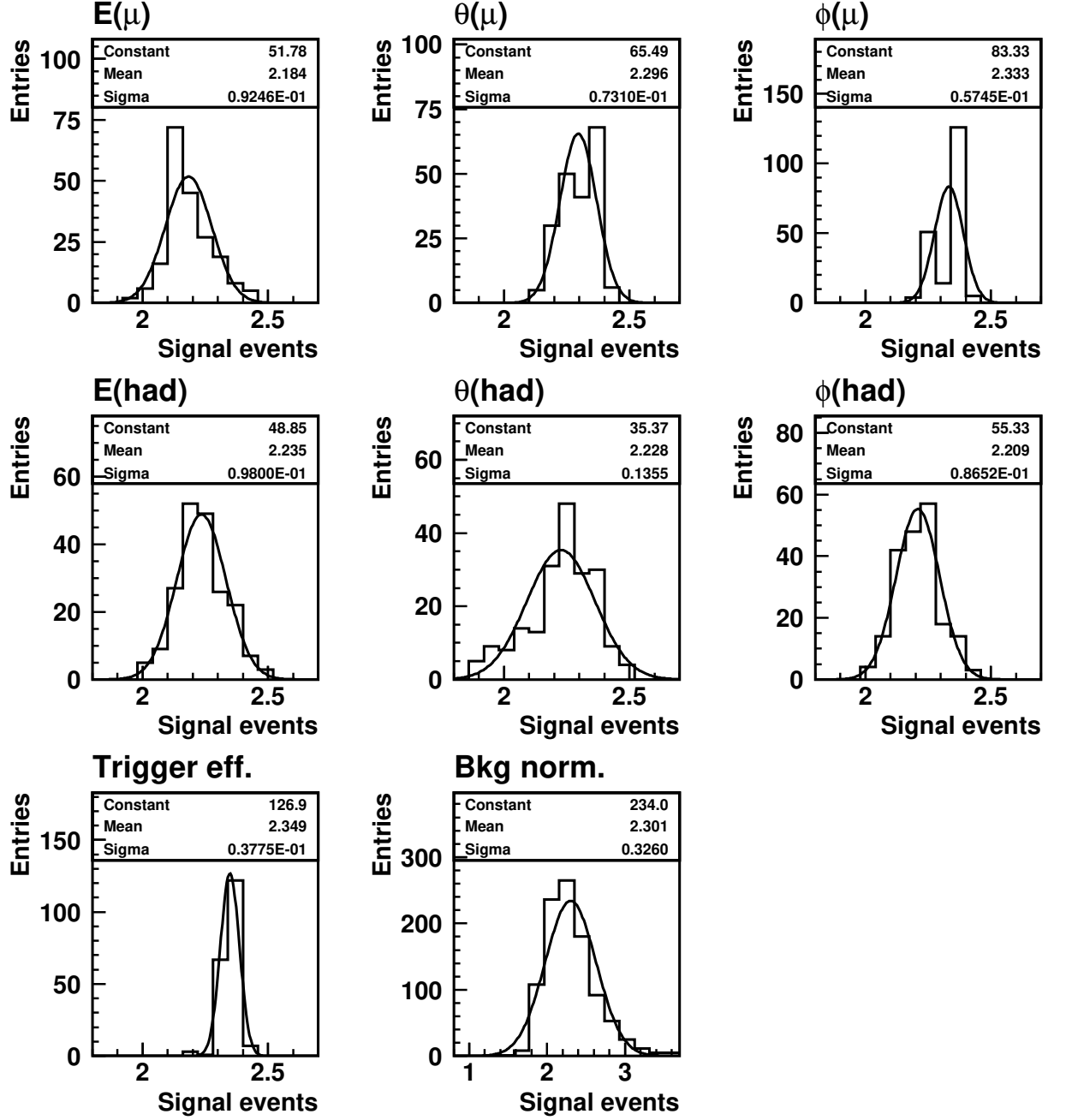


Figure F.3: Systematic uncertainty on the number of signal events due to different experimental uncertainties in the muon channel.

# List of Figures

2.1	Diagram for Standard Model single top production at HERA . . . . .	4
2.2	Diagrams of processes with effective FCNC couplings . . . . .	6
2.3	Diagram of FCNC top production at HERA . . . . .	7
2.4	Generated kinematic distributions of top events . . . . .	9
2.5	Single top cross-section calculations . . . . .	10
2.6	Dominant diagram for $W$ production . . . . .	12
2.7	Generated quark transverse momentum in $W$ and top production . . .	12
2.8	Leading order diagrams for $W$ production . . . . .	13
2.9	Dominant diagram for lepton-pair production . . . . .	14
2.10	Deep inelastic scattering . . . . .	15
2.11	Diagrams for photoproduction processes . . . . .	18
2.12	Diagrams for 3-jet production . . . . .	19
3.1	The HERA collider . . . . .	22
3.2	The H1 detector . . . . .	24
3.3	Longitudinal section of Liquid Argon Calorimeter . . . . .	25
3.4	Transverse section of Liquid Argon Calorimeter . . . . .	26
3.5	Longitudinal section of tracking system . . . . .	28
3.6	Transverse section of tracking system . . . . .	29
5.1	Mean fractional energy shift from absolute electromagnetic energy scale	38
5.2	Cluster-track and electron finding efficiencies . . . . .	39
5.3	$P_T$ -balance plots . . . . .	44
6.1	Isolated muon event with high hadronic transverse momentum . . . . .	46
6.2	Calorimetric missing transverse momentum in neutral current DIS events	49
6.3	Control Distributions of the $W$ selection in the electron channel . . . .	51
6.5	Illustration of the quantities $E - P_z$ and $\Delta\phi(\ell, X)$ . . . . .	51
6.4	Control distributions of the $W$ selection in the muon channel . . . . .	52
6.6	Distributions of the electron channel after the NC suppression . . . . .	54
6.7	Distributions of the observables for further background suppression in the electron channel . . . . .	56
6.8	Distributions of the observables to suppress background in the muon channel . . . . .	58
6.9	Transverse mass and hadronic transverse momentum distributions for the final $W$ selection . . . . .	59
6.10	Ensemble estimator distributions . . . . .	63

6.11	Feynman diagram of FCNC single top production at HERA . . . . .	64
6.12	Distribution of lepton-neutrino invariant mass . . . . .	66
6.13	Illustration of the two solutions of a $W$ mass constraint . . . . .	66
6.14	Reconstructed $P_T^\nu$ and $(E - P_z)_\nu$ for variation of the muon transverse momentum . . . . .	68
6.15	Illustration of the correlation between lepton polar angle and correct neutrino choice . . . . .	69
6.16	Reconstructed $(E - P_z)_\nu$ for three different neutrino choices . . . . .	70
6.17	Reconstruction of the $b$ -quark energy . . . . .	71
6.18	Invariant mass of the system lepton-neutrino-jets . . . . .	71
6.19	Illustration of top quark and $W$ decay in the top and $W$ rest frames . .	73
6.20	Distributions of the top and $W$ decay angle . . . . .	75
6.21	Observables to discriminate top and $W$ production . . . . .	76
6.22	Correlations of the discriminating observables in the electron channel .	77
6.23	Correlations of the discriminating observables in the muon channel . .	77
6.24	Integrated distributions of $P_T^{jets}$ , $M_{e-\nu-jets}$ in the electron channel . .	79
6.25	Integrated distributions of $P_T^{jets}$ , $M_{\mu-\nu-jets}$ in the muon channel . . .	80
6.26	Significance of lepton charge determination . . . . .	82
6.27	Study of systematic uncertainty on hadron angle . . . . .	84
6.28	Likelihood discriminators with the standard method and the PTC-method	89
6.29	Likelihood discriminator without cut on lepton charge . . . . .	91
6.30	Likelihood discriminator in the electron channel . . . . .	95
6.31	Likelihood discriminator in the muon channel . . . . .	96
7.1	3-jet neutral current DIS event . . . . .	99
7.2	Distribution of electron transverse momentum and polar angle . . . . .	100
7.3	Control distributions of the multi-jet pre-selection . . . . .	101
7.4	Control distributions to illustrate the event decomposition in the hadronic channel . . . . .	102
7.5	Jet transverse momenta and pseudorapidities in the high- $E_T$ sample with a $W$ candidate . . . . .	104
7.6	Discriminating observables in the hadronic channel . . . . .	105
7.7	3-jet and total invariant mass . . . . .	106
7.8	Correlations of the discriminating observables in the hadronic channel .	107
7.9	Data/MC ratio for $E_T^{tot}$ and $M_{jets}$ . . . . .	108
7.10	Top mass distribution . . . . .	110
7.11	Likelihood discriminators for the standard and the PTC-method in the hadronic channel . . . . .	111
7.12	Likelihood discriminator in the hadronic channel . . . . .	114
8.1	Likelihood discriminators for all three channels . . . . .	116
8.2	Log-likelihood functions in electron and muon channels . . . . .	118
8.3	Log-likelihood functions in the hadronic channel . . . . .	119
8.4	Log-likelihood functions including systematics . . . . .	123
8.5	Log-likelihood function for the combination of all channels including systematics . . . . .	124

8.6	Exclusion limits on $tu\gamma$ -coupling . . . . .	127
8.7	Exclusion limits on $\kappa_\gamma$ and $v_Z$ from different experiments . . . . .	128
8.8	Diagrams for FCNC single top production and decay . . . . .	129
8.9	ZEUS results on isolated leptons and single top production . . . . .	132
A.1	$W \rightarrow e\nu$ candidate . . . . .	139
A.2	$W \rightarrow e\nu$ candidate . . . . .	140
A.3	$W \rightarrow e\nu$ candidate . . . . .	140
A.4	$W \rightarrow e\nu$ candidate . . . . .	141
A.5	$W \rightarrow \mu\nu$ candidate . . . . .	141
A.6	$W \rightarrow \mu\nu$ candidate . . . . .	142
A.7	$W \rightarrow \mu\nu$ candidate . . . . .	142
A.8	$W \rightarrow \mu\nu$ candidate . . . . .	143
A.9	$W \rightarrow \mu\nu$ candidate . . . . .	143
A.10	$W \rightarrow \mu\nu$ candidate . . . . .	144
B.1	Spin correlations in top decays . . . . .	146
B.2	$W$ decay angle and contributions from different helicities . . . . .	146
C.1	Gaussian transformed variables for the electron channel . . . . .	148
C.2	Gaussian transformed variables in the muon channel . . . . .	149
C.3	Gaussian transformed variables in the hadronic channel . . . . .	150
D.1	Discriminating observables after cut on the lepton charge . . . . .	152
E.1	$t \rightarrow bW \rightarrow bq\bar{q}'$ candidate . . . . .	153
E.2	$t \rightarrow bW \rightarrow bq\bar{q}'$ candidate . . . . .	154
E.3	$t \rightarrow bW \rightarrow bq\bar{q}'$ candidate . . . . .	154
E.4	$t \rightarrow bW \rightarrow bq\bar{q}'$ candidate . . . . .	155
E.5	$t \rightarrow bW \rightarrow bq\bar{q}'$ candidate . . . . .	155
F.1	Systematic uncertainties for the signal fit in hadronic channel . . . . .	156
F.2	Systematic uncertainties for the signal fit in the electron channel . . . . .	157
F.3	Systematic uncertainties for the signal fit in muon channel . . . . .	158



# List of Tables

2.1	Estimates for the branching $t \rightarrow cV$ ( $V = \gamma, Z$ ) in different theories . . .	7
2.2	Top quark and $W$ decay branching ratios . . . . .	10
3.1	Spatial resolution of the H1 central tracker . . . . .	28
4.1	Summary of H1 data sets . . . . .	34
5.1	Selection criteria for a neutral current check sample . . . . .	43
6.1	Summary of the $W$ selection cuts in the electron channel . . . . .	55
6.2	Summary of the $W$ selection cuts in the muon channel . . . . .	57
6.3	Event yields of the $W$ selection in the electron channel . . . . .	59
6.4	Event yields of the $W$ selection in the muon channel . . . . .	60
6.5	Probabilities $1 - \text{CL}_b$ for the background-only hypothesis using the $P_T^X$ spectra . . . . .	64
6.6	Prescription for the choice of the neutrino . . . . .	68
6.7	Kinematics of the isolated lepton events at high $P_T^X$ . . . . .	72
6.8	Top selection cuts . . . . .	82
6.9	Experimental systematics in semi-leptonic channel . . . . .	83
6.10	Results of the top selection in the semi-leptonic channel . . . . .	84
6.11	Probability $1 - \text{CL}_b$ of the background-only hypothesis after cut on the lepton charge . . . . .	93
6.12	Summary of all selection steps in the electron channel . . . . .	94
6.13	Summary of all selection steps in the muon channel . . . . .	94
7.1	Event yields of the multi-jet pre-selection and the high- $E_T$ selection with a $W$ candidate . . . . .	103
7.2	Top selection cuts in the hadronic channel . . . . .	107
7.3	Experimental systematics in the hadronic channel . . . . .	109
7.4	Event yields of the top selection cuts in the hadronic channel . . . . .	112
7.5	Kinematics of the multi-jet top candidates . . . . .	113
8.1	Systematic uncertainties on the signal cross-section . . . . .	121
8.2	Fitted number of signal events and single top cross-section . . . . .	121
8.3	Single top cross-section for combinations of channels . . . . .	122
8.4	Probabilities $1 - \text{CL}_{s+b}$ for the signal+background hypothesis and $1 - \text{CL}_b$ for the background-only hypothesis . . . . .	126
8.5	Exclusion limits on single top cross-section . . . . .	127

---

8.6	ZEUS isolated lepton event yields . . . . .	130
8.7	H1 and ZEUS isolated leptons at $P_T^X > 25$ GeV . . . . .	131
9.1	Review of probabilities for background-only and signal+background hy- potheses . . . . .	136
C.1	Correlation matrix of untransformed variables in electron channel . . .	148
C.2	Covariance matrix of transformed variables in electron channel . . . . .	148
C.3	Correlation matrix of untransformed variables in electron channel . . .	148
C.4	Covariance matrix of transformed variables in electron channel . . . . .	148
C.5	Correlation matrix of untransformed variables in muon channel . . . . .	149
C.6	Covariance matrix of transformed variables in muon channel . . . . .	149
C.7	Correlation matrix of untransformed variables in muon channel . . . . .	149
C.8	Covariance matrix of transformed variables in muon channel . . . . .	149
C.9	Correlation matrix of untransformed variables in hadronic channel . . .	150
C.10	Covariance matrix of transformed variables in hadronic channel . . . . .	150
C.11	Correlation matrix of untransformed variables in hadronic channel . . .	150
C.12	Covariance matrix of transformed variables in hadronic channel . . . . .	150



# Bibliography

- [1] H1 Collaboration,  
*Search for Single Top Quark Production in  $e^{\pm}p$  collisions at HERA*,  
contributed paper 1024, ICHEP 2002 (Amsterdam).
- [2] J. Dingfelder, *on behalf of the H1 and ZEUS collaborations*,  
*Searches for signatures of physics beyond the Standard Model with high- $P_T$  leptons at HERA*,  
in the proceedings to ICHEP 2002 (Amsterdam).
- [3] CDF Collaboration, *Observation of top quark production in anti- $p$   $p$  collisions*,  
*Phys. Rev. Lett.* **74** (1995) 2626.
- [4] D0 Collaboration, *Observation of the top quark*,  
*Phys. Rev. Lett.* **74** (1995) 2632.
- [5] K. Hagiwara *et al.*,  
*Review of Particle Physics*,  
*Physical Review D* **66**, 010001 (2002).
- [6] CDF Collaboration,  
*Search for Single-Top-Quark Production in  $p\bar{p}$  Collisions at  $\sqrt{s} = 1.8$  TeV*,  
*FERMILAB-PUB-01/ 318-E* (2001).
- [7] D0 Collaboration,  
*Search for single top quark production at D0 using neural networks*,  
*Phys.Lett.* **B 517** (2001) 282, hep-ex/0106059.
- [8] E.E. Boos *et al.*,  
SNUTP-94-116, hep-ph/9503280;  
E.E. Boos *et al.*,  
Proceedings of the Xth Int. Workshop on High Energy Physics and Quantum Field Theory, QFTHEP-95, (Moscow, 1995), Eds. B. Levtchenko and V. Savrin, p 101.
- [9] T. Han and J.L. Hewett, *Top-Charm Associated Production in High Energy  $e^+e^-$  Collisions*,  
*Phys. Rev.* **D 60** (1999) 074015.
- [10] W. Buchmüller, D. Wyler,  
*Effective Lagrangian Analysis*,  
*Nucl.Phys.* **B 268** (1986) 621.

- [11] B. A. Arbuzov and M. Yu. Osipov, *An enhancement of neutral  $tc$  transitions in the model of dynamical breaking of the electroweak symmetry*, *Phys.Atom.Nucl.* **62** (1999) 485.
- [12] H. Fritzsch and D. Holtmannspötter, *The Production of Single  $t$ -Quarks at LEP and HERA*, *Phys. Lett.* **B 457** (1999) 1199.
- [13] E. Perez,  
*Private communication*,  
Hamburg, Germany (2002).
- [14] G.M. Divitiis, R. Petronzio and L. Silvestrini,  
*Flavour changing top decays in supersymmetric extensions of the standard model*, *Nucl. Phys.* **B 504** (1997) 45.
- [15] J.M. Yang et al,  
*Flavor changing top quark decays in  $R$  parity violating SUSY*, *Phys Rev* **D 58** (1998) 055001.
- [16] DELPHI Collaboration,  
*Search for single top quark production in the framework of  $R$ -parity violation*,  
contributed paper, ICHEP 2002 (Amsterdam).
- [17] F. del Aguila, J. A. Aguilar-Saavedra,  
*Constraints on top couplings in models with exotic quarks*, *Phys.Rev.Lett.* **82** (1999) 1628.
- [18] CDF Collaboration, F. Abe *et al.*, *Search for flavor changing neutral current decays of the top quark in  $p$  anti- $p$  collisions at  $s^{*(1/2)} = 1.8$ -TeV*, *Phys. Rev. Lett.* **80** (1998) 2525.
- [19] A. Belyaev and N. Kidonakis,  
*QCD corrections to FCNC single top production at HERA*,  
FSU-HEP-20010205 (2001) , hep-ph/0102072.
- [20] H1 Collaboration,  
*Observation of isolated leptons with missing  $P_T$  and comparison to  $W$  production at HERA*,  
contributed paper 1022, ICHEP 2002 (Amsterdam).
- [21] U. Bassler und G. Bernardi,  
*Structure Function Measurements and Kinematic Reconstruction at HERA*,  
DESY **97-137** (1997).
- [22] V.N. Gribov and L.N. Lipatov, *Sov. Journ. Nucl. Phys.* **15** (1972) 78;  
G. Altarelli and G. Parisi, *Nucl. Phys.* **B 126** (1977) 298;  
Y.L. Dokshitzer, *JETP* **46** (1977) 641.
- [23] S. Kawabata, *Comp. Phys. Comm.* **41** (1986) 127.

- [24] A.D. Martin, R.G. Roberts, W.J. Stirling and R.S. Thorne,  
*Euro. Phys. J. C* **4** (1998) 463.
- [25] U. Baur, J.A.M. Vermaseren, D. Zeppenfeld,  
*Electroweak vector boson production in high-energy ep collisions*,  
*Nucl. Phys. B* **375** (1992) 3.
- [26] S. Baranov *et al.*,  
Proc. of the Workshop Physics at HERA, W. Buchmüller and G. Ingelman (Editors), (October 1991, DESY-Hamburg) Vol. 3, p. 1478;  
J.A.M. Vermaseren,  
*Nucl. Phys. B* **229** (1983) 347.
- [27] H. Jung, *Comp. Phys. Comm.* **86** (1995) 147,  
RAPGAP program manual (1998), unpublished.
- [28] DJANGO 2.1;  
G.A. Schuler and H. Spiesberger,  
Proceedings of the Workshop Physics at HERA, W. Buchmüller and G. Ingelman (Editors), (October 1991, DESY-Hamburg), vol. 3 p. 1419.
- [29] HERACLES 4.4;  
A. Kwiatkowski, H. Spiesberger and H.-J. Möhring,  
*Comput. Phys. Commun.* **69** (1992) 155.
- [30] G. Gustafson and U. Pettersson,  
*Nucl. Phys. B* **306** (1988) 746;  
*idem*,  
*addendum* Lund University preprint LU-TP-87-19, (October 1987) 4pp.;  
B. Andersson *et al.*,  
*Z. Phys. C* **43** (1989) 625.
- [31] ARIADNE 4.0;  
L. Lönnblad,  
*Comput. Phys. Commun.* **71** (1992) 15.
- [32] JETSET 7.4;  
T. Sjöstrand,  
Lund Univ. preprint LU-TP-95-20 (August 1995) 321pp;  
*idem*,  
CERN preprint TH-7112-93 (February 1994) 305pp.
- [33] PYTHIA 5.7;  
T. Sjöstrand,  
CERN-TH-6488 (1992), *Comp. Phys. Comm.* **82** (1994) 74.
- [34] M. Glück, E.Reya and A Vogt,  
*Phys. Rev. D* **45** (1992) 3986;  
*idem*,  
*Phys. Rev. D* **46** (1992) 1973.

- 
- [35] I. Abt,  
*Manual to IJRAY, Monte Carlo generator shell to produce  $eP$  events for H1*,  
H1 internal note-290 (1993).
- [36] H1 Collaboration (I. Abt et al.):  
*The H1 detector at HERA*,  
Nuclear Instruments and Methods in Physics Research **A 386** (1997), 310-347.
- [37] H1 Collaboration (I. Abt et al.):  
*The tracking, calorimeter and muon detectors of the H1 experiment at HERA*,  
Nuclear Instruments and Methods in Physics Research **A 386** (1997), 348-396.
- [38] H1 Collaboration (I. Abt et al.):  
*The H1 Liquid Argon Calorimeter System*,  
Nuclear Instruments and Methods **A 336** (1993), 460-498
- [39] H1 Calorimeter Group,  
*Results from pion calibration runs for the H1 LAr calorimeter and comparisons with simulations*,  
Nuclear Instruments and Methods **A 336** (1993), 499-509.
- [40] H1 Calorimeter Group,  
*Beam tests and calibration of the H1 LAr calorimeter with electrons*,  
Nuclear Instruments and Methods **A 350** (1994), 57-72.
- [41] H. Bethe, W. Heitler,  
Proc. Roy. Soc. A 146 (1934), 83
- [42] CERN Computing and Networks Division,  
*GEANT Detector Description and Simulation Tool*,  
CERN Program Library W5013 (1993).
- [43] E. Chabert and C. Diaconu, S. Kermiche, I. Négri, C. Vallée,  
*QBGFMAR – An Updated Phan Package for Cosmic and Halo Muon Topological Rejection in High  $P_T$  Physics Analysis*,  
H1 Note H1-11/98-556 (1998)
- [44] P. Bruel,  
*Reherchee d’interactions au-dela du Modele Standard a HERA*,  
Dissertation, Orsay, France (1998).
- [45] H1 Collaboration, C. Adloff *et al.*,  
*Measurement of Neutral and Charged Current Cross-Sections in Positron-Proton Collisions at Large Momentum Transfer*,  
*Eur. Phys. J. C* **13** (2000) 609 , hep-ex/9908059.
- [46] M.H. Seymour  
*Searches for new particles using cone and cluster jet algorithms: a comparative study*,  
*Z. Phys. C* **62**, 127-138 (1994)

- 
- [47] M. Ellerbrock,  
*Measurement of the Neutral Current Cross Sections and Search for Contact Interactions with the H1 Experiment at HERA*,  
Dissertation in preparation, Heidelberg.
- [48] H1 Collaboration, C. Adloff *et al.*,  
*diffraction dissociation in photoproduction at HERA*,  
*Z. Phys. C* **74**, (1997) 221.
- [49] F.-P. Schilling,  
*Diffraction Jet Production in Deep-Inelastic  $e^+p$  Collisions at HERA*,  
Dissertation, Heidelberg (2001).
- [50] S. Catani, Y. L. Dokshitzer, M. H. Seymour and B. R. Webber,  
*Nucl. Phys. B* **406** (1993) 187.
- [51] S. D. Ellis and D. E. Soper,  
*Phys. Rev. D* **48** (1993) 3160.
- [52] M. Jacquet, Z. Zhang and V. Brisson, S. Kermiche, C. Vallee,  
*Absolute hadronic jet calibration of the H1 liquid Argon calorimeter*,  
H1-04/99-571 (1999).
- [53] H1 Collaboration, T. Ahmed *et al.*,  
*Observation of an  $e^+p \rightarrow \mu^+X$  Event with High Transverse Momenta at HERA*,  
*DESY* **94-248** (1994).
- [54] H1 Collaboration, C. Adloff *et al.*,  
*Observation of Events with an Isolated High Energy Lepton and Missing Transverse Momentum at HERA*,  
*Eur. Phys. J. C* **5** (1998) 575
- [55] H1 Collaboration,  
*Observation of isolated leptons in events with missing  $P_T$  and comparison to Standard Model  $W$  production at HERA*,  
to be published.
- [56] M. Schneider,  
*Recherche d'événements contenant un lepton isolé et une impulsion transverse manquante sur le collisionneur HERA avec le détecteur H1*,  
Dissertation in preparation, Marseille.
- [57] H. Hu, J. Nielsen,  
*Analytic Confidence Level Calculations Using the Likelihood Ratio and Fourier Transform*,  
in a CERN Yellow Book ...
- [58] E. Perez,  
*Private communication.*, Hamburg, Germany (2001).

- [59] G. Mahlon,  
*Observing Spin Correlations in Single Top Production and Decay*,  
hep-ph/0011349.
- [60] R. Frey *et al.*,  
*Top Quark Physics: Future Measurements*,  
hep-ph/9704243.
- [61] D. Karlen,  
*Using projections and correlations to approximate probability distributions*,  
*Computers in Physics* **12** (1998) 380.
- [62] G. Frising,  
*Eine Likelihood-Analyse der H1 Jet-Daten*,  
Diploma Thesis, Technische Hochschule Aachen, Germany (2000).
- [63] ZEUS Collaboration, J. Breitweg *et al.*,  
*Measurement of Three-jet Distributions in Photoproduction at HERA*,  
*Phys. Lett. B* **443** (1998) 394, hep-ex/9810046.
- [64] P. Bate,  
*High Transverse Momentum 2-Jet and 3-Jet Cross Section Measurements in Photoproduction*,  
Dissertation, University of Manchester, England (1999).
- [65] S. Caron,  
*Jets in Photoproduction at HERA*,  
Dissertation, Technische Hochschule Aachen, Germany (2002).
- [66] H1 Collaboration, C. Adloff *et al.*,  
*Three-Jet Production in Deep-Inelastic Scattering at HERA*,  
DESY **01-073** (2001)
- [67] ALEPH, DELPHI, L3, OPAL and the LEP EXOTICA Working Group,  
*Search for single top production via flavour changing neutral currents: preliminary combined results of the LEP experiments*,  
contributed paper submitted to summer 2001 conferences, LEP Exotica WG 2001-01, ALEPH 2001-055 CONF 2001-035, DELPHI 2001-119 CONF542, L3 Note 2706, OPAL TN698.
- [68] S. Parke,  
Proceedings of the 1994 Meeting of the American Physical Society, Division of Particles and Fields, pp. 726-730.
- [69] T. Stelzer, Z. Sullivan, and S. Willenbrock,  
*Phys. Rev. D* **58**, 0904021 (1998).
- [70] M. C. Smith and S. S. Willenbrock,  
*Phys. Rev. D* **54**, 6696 (1996).

- [71] R. Bonciani *et al.*,  
*Nucl. Phys.* **B 529**, 424 (1998).
- [72] ALEPH Collaboration, A. Heister *et al.*,  
*Search for single top production in  $e^+ e^-$  collisions at  $s^{**}(1/2)$  up to 209-GeV*,  
*Phys.Lett.* **B 543** (2002) 173, hep-ex/0206070.
- [73] L3 Collaboration, P. Achard *et al.*,  
*Search for single top production at LEP*,  
*Phys.Lett.* **B 549** (2002) 290, hep-ex/0210041.
- [74] OPAL Collaboration, G. Abbiendi *et al.*,  
*Search for single top quark production at LEP-2*,  
*Phys.Lett.* **B 521** (2001) 181, hep-ex/0110009.
- [75] ZEUS Collaboration,  
*Search for single top production in ep collisions at HERA*,  
contributed paper 650, EPS 2001 (Budapest).
- [76] ZEUS Collaboration,  
*Search for events with isolated tau leptons and large missing transverse momentum in ep collisions at HERA*,  
contributed paper 909, ICHEP 2002 (Amsterdam).
- [77] P. Bock,  
*Private communication*, Heidelberg, Germany (2002).
- [78] S. Dusini,  
*Single top production and FCNC processes*,  
*Nucl.Phys.Proc.Suppl.* **109** (2002) 262.
- [79] K.-P. O. Diener, C. Schwanenberger, M. Spira,  
*Photoproduction of W Bosons at HERA: QCD Corrections*,  
*Eur.Phys.J.* **C 25** (2002) 405, hep-ph/0203269.





# Acknowledgments

First of all I am thankful to everyone in the H1 Collaboration. The last few years have been a great experience for me. My special thanks go to:

- My supervisor Prof. Franz Eisele, for his excellent guidance and support during my time in Heidelberg. I am very thankful for his commitment and interest in my work.
- Prof. Christof Wetterich, for his friendly willingness to act as second referee of this thesis.
- Olaf Behnke, for everything he has done for me. He has contributed a great deal to this analysis. Thank you for being an excellent tutor and friend.
- All my colleagues in the H1 group Heidelberg: Jörg Marks, Malte Ellerbrock, Christian Gerlich, Christoph Werner, Gerhard Brandt, Johannes Haller, Sebastian Schätzel, Matthias Mozer, Stefan Schenk, David Emschermann for their support and a good teamwork. It has been fun working with you. Also everyone in the LHCb and OPAL groups. I would like to especially thank Prof. Bock for his help with statistical problems.
- Emmanuelle Perez, Cristi Diaconu and Mireille Schneider, who have been working with me on the single top analysis. Thanks a lot for a great cooperation, your readiness to help and discuss many details of this analysis, and in particular for your friendship, which I appreciate a lot.
- The convenors and members of the ex-BSM and ex-HIP groups and all my colleagues at DESY. In particular, I would like to say thank you to Frank-Peter Schilling, Nicolas Keller, André Schöning, Peter Schleper, and the top referees Martin Erdmann, Hinrich Meyer.
- All my friends and family members, for their patience and understanding when I did not have time.
- Tina, for the beautiful time I have spent with her.
- Last but certainly not least, my parents and my brother for their love, support and for always being there for me. Without you this thesis would not have been possible.

This thesis was funded by the Graduiertenkolleg “Experimental Methods of Nuclear and Particle Physics” of the German Research Society (DFG).

